

ON ISOTOPICALLY SELECTIVE COLLISIONAL ENERGY TRANSFER AND INFRARED MULTIPLE PHOTON ABSORPTION BY VIBRATIONALLY HIGHLY EXCITED MOLECULES

THÈSE N° 3298 (2005)

PRÉSENTÉE À LA FACULTÉ SCIENCES DE BASE

Institut des sciences et ingénierie chimiques

SECTION DE CHIMIE ET GÉNIE CHIMIQUE

ÉCOLE POLYTECHNIQUE FÉDÉRALE DE LAUSANNE

POUR L'OBTENTION DU GRADE DE DOCTEUR ÈS SCIENCES

PAR

Richard BOSSART

ingénieur physicien diplômé EPF
de nationalité suisse et originaire de Sursee (LU)

acceptée sur proposition du jury:

Prof. Th. Rizzo, directeur de thèse

Prof. B. Abel, rapporteur

Dr G. Seyfang, rapporteur

Prof. H. van den Bergh, rapporteur

Lausanne, EPFL
2005

Richard Bossart

On Isotopically Selective Collisional Energy Transfer and Infrared Multiple Photon
Absorption by Vibrationally Highly Excited Molecules

PhD Thesis

<http://library.epfl.ch/theses/?nr=3298>

Contents

Abstract	IX
Version abrégée	XI
Kurzfassung	XIII
1 Introduction	3
1.1 A new laser isotope separation scheme called OP-IRMPD	4
1.2 Aim of this work	8
1.3 Structure of this work	12
Bibliography	13
2 Background information	19
2.1 Spectroscopy and intramolecular dynamics of CF ₃ H	19
2.2 IR multiple photon dissociation (IRMPD)	41
2.3 Collisional vibrational relaxation	52
Bibliography	72
3 Experimental setup	87
3.1 Optical setup of our experiments	87
3.2 Working pressure	96
3.3 Synthesis of ¹³ CF ₃ H	99
Bibliography	104
4 Experimental investigations	105
4.1 Introduction	105

4.2	State specificity of the increase of isotopic selectivity upon leaving a time-delay between the pre-excitation and the dissociation lasers	110
4.3	Properties of collision-free IRMPD of excited molecules: photofragment excitation spectrum and dissociation selectivity of vibrationally excited CF_3H	114
4.4	Separation of different mechanisms changing the wavelength of the dissociation laser	127
4.5	Separation of different mechanisms using a carbon-13 enriched sample	133
4.6	Discussion and conclusion	148
	Bibliography	151
5	Numerical simulations of V-V energy transfer and IRMPD of CF_3H	153
5.1	Absorption and emission spectra of an excited molecule	154
5.2	Numerical simulations of vibrational energy transfer between excited and ground state molecules	165
5.3	Numerical simulations of IRMPD in the presence of collisions	187
	Bibliography	222
6	Conclusions and Outlook	229
6.1	Isotopically selective collisional vibrational relaxation	229
6.2	Enhancement of isotopic selectivity in our MLIS process	231
	Bibliography	232
	APPENDICES	233
A	Development of formulae for pumping molecules through a low density regime (“case C”)	235
A.1	Qualitative explanations	236
A.2	Calculations details	238
A.3	Attempts to generalise case C calculations	240
	Bibliography	242
B	Collisional quenching of LIF	243
	Bibliography	245

C	CO₂ laser fluence control and measurement	247
C.1	Attenuation of the CO ₂ laser beam	247
C.2	Calculation of the fluence	248
D	CO₂ laser fluence dependence of the decay rate	253
E	The numerical codes for the calculation of IRMPD in the presence of collisions	257
E.1	Generalities	257
E.2	The code	258
	Notations and abbreviations	271
	List of tables	280
	List of figures	283
	Acknowledgements	289
	Curriculum vitae	291

Abstract

This study focuses on an interesting and important phenomenon that was employed in a new approach to laser isotope separation that has been recently proposed and developed in our laboratory for highly selective separation of carbon isotopes. This approach consists of pre-exciting CF_3H molecules with the desired isotope to a low vibrational overtone of the CH-stretch with a subsequent selective infrared multiple photon dissociation (IRMPD) of only the pre-excited molecules by a CO_2 -laser pulse. Significant isotopic shifts of the employed CH overtone bands already allow high selectivity at the pre-excitation step. This selectivity, however, can be further greatly increased by increasing the pressure of the sample gas and/or the delay between the two laser pulses; that is, by increasing the number of molecular collisions during the process. At first glance, the observed effect contradicts the general expectations that the isotopic selectivity of such a process should drop with an increase in the number of collisions because of vibrational energy transfer between different isotopic species. In this work we have studied this phenomenon and found its physical origins.

We propose the contribution of two different mechanisms to the observed enhancement of isotopic selectivity by collisions. First, the vibrational collisional relaxation itself is isotopically selective, that is vibrationally excited $^{12}\text{CF}_3\text{H}$ relax on the bath of cold, $^{12}\text{CF}_3\text{H}$, molecules faster than the excited $^{13}\text{CF}_3\text{H}$ do on the same bath. The primary reason for such a selectivity could be a significant isotopic shift of the vibration (CF-stretch, we believe) that mediates the energy transfer.

A second mechanism arises from the difference between the IRMPD probabilities of the two isotopic species by the CO_2 laser tuned to a particular wavelength that enhances the dissociation yield of the targeted, carbon-13, species. As collisional deactivation of

both species increases the number of photons they have to absorb to be dissociated, this difference in dissociation probability increases as well, yielding an additional isotopic selectivity of the process.

We perform a set of experiments and numerical simulations to investigate these two mechanisms. Experimentally we find that, indeed, collisional vibrational deactivation of CF_3H is isotopically selective. This is, perhaps, the first direct observation of isotopically selective collisional relaxation of highly excited medium-sized molecules. At low pressures and increased time-delay between the lasers both suggested mechanisms contribute equally to the enhancement of isotopic selectivity (with a slight dominance of the IRMPD step). We also perform numerical simulations of vibrational energy transfer (VET) between highly excited and cold CF_3H of both isotopic species. The model we employ includes V-V energy transfer due to long-range dipole-dipole interactions and V-V',T,R energy transfer due to head-on collisions between two molecules. The results reproduce well the measured isotopic selectivity in vibrational energy transfer. At the next step, we propose a model for the simulation of the laser isotope separation process. We solve the master equations including vibrational energy transfer and absorption and stimulated emission of IR photons. The main improvement of our calculations with respect to existing models is that we introduce a dependence of the absorption/emission rates on the frequency of the laser, the internal energy of the molecule and its isotopic species. We are able to reproduce our experiments numerically and thus gain information on the laser isotope separation process. In particular, we find that at high sample pressures the mechanism of isotopically selective IRMPD rates prevails over the mechanism of different collisional relaxation rates.

Version abrégée

Notre étude se concentre sur un phénomène intéressant et important qui a été utilisé dans une nouvelle approche de séparation isotopique par laser qui a été proposée et développée dans notre laboratoire pour la séparation hautement sélective de carbone-13. Cette approche consiste à exciter des molécules de CF_3H avec l'isotope désiré via un overtone de la vibration CH suivi d'une dissociation sélective des molécules excitées par absorption multiple de photons infrarouges (IRMPD, "Infrared multiple photon dissociation") provenant d'un laser CO_2 . Une grande sélectivité est obtenue à l'excitation initiale qui est due à un déplacement isotopique important de l'overtone de la vibration CH. Cette sélectivité peut être largement augmentée en augmentant la pression du gaz et/ou la durée entre les deux impulsions laser utilisées, ce qui augmente le nombre de collisions moléculaires pendant le processus. À première vue, cet effet est en contradiction avec la diminution attendue de la sélectivité isotopique lorsque le nombre de collisions augmente, à cause du transfert d'énergie vibrationnelle entre les différentes espèces isotopiques. Dans ce travail, nous avons étudié cet effet et trouvé ses origines physiques.

Nous proposons la contribution de deux mécanismes différents à l'augmentation de la sélectivité due aux collisions. Premièrement, la relaxation vibrationnelle par collisions est isotopiquement sélective en elle-même, c'est-à-dire que des molécules $^{12}\text{CF}_3\text{H}$ excitées se désactivent sur les molécules $^{12}\text{CF}_3\text{H}$ non excitées environnantes plus vite que des molécules $^{13}\text{CF}_3\text{H}$ excitées. La raison principale de cette sélectivité pourrait être un déplacement isotopique important de la vibration qui est à l'origine de ce transfert d'énergie (probablement la vibration CF).

Un deuxième mécanisme est dû à une différence de l'efficacité de l'IRMPD des deux

espèces isotopiques par le laser CO_2 fixé à une longueur d'onde particulière qui augmente le rendement de dissociation du $^{13}\text{CF}_3\text{H}$. Puisque la relaxation par collisions des deux espèces isotopiques augmente le nombre de photons qu'elles doivent absorber pour être dissociées, cette différence de probabilité de dissociation est aussi augmentée, ce qui mène à une plus grande sélectivité isotopique du processus.

Nous conduisons des expériences et des simulations numériques afin d'étudier ces deux mécanismes. Expérimentalement, nous observons que la relaxation vibrationnelle par collisions de CF_3H est isotopiquement sélective. Ceci est, peut-être, la première observation directe de relaxation par collisions isotopiquement sélective de molécules de taille moyenne hautement excitées. À basses pressions et avec un plus grand intervalle de temps entre les lasers les deux mécanismes contribuent de manière égale à l'augmentation de la sélectivité isotopique (avec une légère dominance de l'IRMPD sélective). Nous effectuons des simulations numériques du processus de transfert d'énergie vibrationnelle (VET, "vibrational energy transfer") entre des molécules CF_3H des deux espèces isotopiques hautement excitées et non excitées. Le modèle utilisé comprend le transfert d'énergie V-V dû à l'interaction dipôle-dipôle à longue distance et le transfert d'énergie V-V',T,R dû à des collisions frontales entre deux molécules. Les résultats reproduisent bien la sélectivité du transfert d'énergie vibrationnelle mesurée expérimentalement. Dans une deuxième étape, nous proposons un modèle pour la simulation du processus de séparation isotopique par laser. Nous résolvons les équations maîtresses incluant la relaxation vibrationnelle, ainsi que l'absorption et l'émission stimulée de photons infrarouges. L'amélioration principale de notre approche par rapport aux modèles existants est l'introduction d'une dépendance des vitesses d'absorption et d'émission en fonction de la fréquence du laser, de l'énergie interne et de l'espèce isotopique de la molécule. Nous sommes en mesure de reproduire nos expériences de manière numérique et ainsi d'obtenir des informations sur le processus de séparation isotopique par laser. Nous constatons notamment qu'à hautes pressions, le mécanisme de la différence d'efficacité de l'IRMPD prévaut sur celui de la désactivation par collisions isotopiquement sélective.

Kurzfassung

Diese Untersuchung ist einem interessanten und wichtigen Phänomen gewidmet, welches in einer neuen Methode zu einer hochselektiven Isotopentrennung mit Lasern ausgenutzt wird, das wir in unserem Laboratorium entwickelt haben. Der Ansatz dazu ist, CF_3H Moleküle mit dem gewünschten Isotop via einen Oberton der CH Schwingung anzuregen, um sie anschliessend mit Absorption mehrerer Infrarot-Photonen die angeregten Moleküle selektiv zu dissoziieren (IRMPD, “Infrared multiple photon dissociation”). Grosse isotopische Verschiebungen der CH Schwingung erlauben bereits eine hohe Selektivität. Diese Selektivität kann sehr gesteigert werden, indem der Probendruck oder die Verzögerung zwischen den Laser-Pulsen erhöht wird. Dadurch wird die Anzahl molekularer Stösse erhöht. Diese Beobachtung steht im Widerspruch zu der allgemeinen Erwartung, dass die isotopische Selektivität in einem solchen Prozess wegen der vibrationeller Energieübertragung fallen sollte. In dieser Arbeit studierten wir dieses Phänomen und haben dessen physikalischen Ursprünge entdeckt.

Wir schlagen den Beitrag zweier verschiedener Mechanismen für den beobachteten Anstieg der isotopischer Selektivität wegen der Stössen vor. Erstens, die vibrationelle Energieübertragung in den Stössen ist isotopisch selektiv, d.h. die angeregten $^{12}\text{CF}_3\text{H}$ Moleküle verlieren ihre Energie schneller als angeregte $^{13}\text{CF}_3\text{H}$ Moleküle in den Stössen mit kalten $^{12}\text{CF}_3\text{H}$ Molekülen. Der Grund für diese Selektivität ist die isotopische Verschiebung der CF Schwingung, welche für die Energieübertragung verantwortlich ist.

Ein zweiter Mechanismus gründet auf den verschiedenen Geschwindigkeiten, mit welchen die Moleküle die Infrarot-Photonen absorbieren. Die Energie dieser Photonen ist dermassen optimiert, dass sie mit den Kohlenstoff-13 haltigen Molekülen möglichst in Resonanz sind. Da die Anzahl der zu absorbierenden Photonen wegen der Stösse erhöht

wird, wird dadurch der Unterschied in der Dissoziationswahrscheinlichkeit zusätzlich erhöht, was zu einer gesteigerten isotopischen Selektivität führt.

Wir führen mehrere Experimente und numerische Simulationen durch, um die zwei Mechanismen zu untersuchen. Experimentell erkennen wir, dass die Energieübertragung in Stößen in der Tat isotopisch selektiv ist. Dies ist wahrscheinlich die erste direkte Beobachtung von isotopisch selektiver Energieübertragung in Stößen von hochangeregten, mittelgrossen Molekülen. Bei tiefen Probedrücken und erhöhter Verzögerung ist der Beitrag der beiden Mechanismen zu der Erhöhung der isotopischen Selektivität ungefähr gleich gross (mit einer leichten Dominanz der verschiedenen IRMPD Dissoziationsgeschwindigkeiten). Wir haben auch Simulationen zu der Übertragung von vibrationeller Energie in Stößen (VET, “vibrational energy transfer”) zwischen hochangeregten und kalten CF_3H verschiedener isotopischer Spezies durchgeführt. Das Modell baut einerseits auf vibrationeller V-V Energieübertragung über grosse Distanzen auf, welche auf der Dipol-Dipol-Wechselwirkung beruht, andererseits auf Wechselwirkungen über kurze Distanzen, die zu V-V', T, R Energieübertragung führen. Die Resultate geben die experimentell beobachteten isotopische Selektivität überzeugend wieder. In einem zweiten Schritt schlagen wir ein Modell für die Simulation unseres Systems zur Isotopentrennung mit Lasern vor. Wir haben die Hauptgleichungen gelöst, die sowohl die vibrationelle Energieübertragung in Stößen als auch die Absorption und die stimulierte Emission von IR-Photonen beinhaltet. Die wichtigste Verbesserung unserer Simulationen gegenüber existierenden Modellen besteht darin, dass wir für die Absorptions- und Emissionswahrscheinlichkeiten eine Abhängigkeit von der Wellenlänge des Lasers, der vibrationellen Energie des Moleküls und der isotopischen Zusammensetzung des Moleküls berücksichtigen. Wir können so unsere experimentelle Beobachtungen numerisch reproduzieren und auf diese Weise Informationen über den Prozess der Isotopentrennung mit Lasern gewinnen. Insbesondere finden wir, dass bei erhöhten Probedrücken der Mechanismus der verschiedenen IRMPD Wahrscheinlichkeiten wichtiger ist als der Mechanismus von isotopischer selektiver Energieübertragung.

THE THESIS

Chapter 1

Introduction

Isotopes are atoms of a chemical element whose nuclei have the same atomic number (number of protons) but different atomic weights (i.e. different number of neutrons). The word “isotope”, meaning at the same (Greek, “iso”) place (Greek, “topos”), comes from the fact that isotopes are located at the same place on the periodic table^{1, 2}. The first isotopes were discovered experimentally in the early 1930’s³.

Numerous applications in different areas require isotopically pure materials. For example, a recent medical test called “Urea breath test” (UBT⁴⁻⁶) has been developed in order to detect a peptic ulcer disease caused by a helicobacter pylori^{7, 8} infection in the body. For this, the patient swallows a capsule containing carbon-13 enriched $(\text{NH}_2)_2\text{CO}$ (urea). In the presence of the helicobacter pylori this molecule is broken down; one of the products is CO_2 which is later exhaled by the patient. The infection can be diagnosed by measuring the isotopic ratio of the carbon species in the exhaled CO_2 ; in this case an excess of carbon-13 can be observed.

The production of isotopically pure material is done by gas centrifuge, gaseous diffusion, chemical exchange, electro-magnetic separation or low temperature distillation⁹. An alternative lies in laser isotope separation (LIS¹⁰⁻¹³) which is based on spectroscopic differences between different isotopic species. Here, one distinguishes between atomic vapour laser isotope separation (AVLIS), where atoms are directly ionised, molecular laser isotope separation (MLIS), where molecules are dissociated via infrared multiple photon excitation (IRMPE) and chemical reaction by isotope selective laser activation

(CRISLA) in which case the excited molecules react chemically.

1.1 A new laser isotope separation scheme called OP-IRMPD

Traditional approaches to MLIS consist of irradiating a sample gas with a laser in the $10\mu\text{m}$ wavelength region, typically by CO_2 or NH_3 lasers, in order to selectively dissociate the molecules with the desired isotope.

Recently, an original approach to molecular laser isotope separation was proposed in our laboratory¹⁴⁻²¹. A key point of this new approach is the ability of IRMPD to perform a selective dissociation of vibrationally pre-excited molecules without significant dissociation of the ground state species under some specific circumstances. This specific feature of IRMPD was first demonstrated for hydrated hydronium cluster ions²² $\text{H}_3\text{O}^+ \cdot (\text{H}_2\text{O})_n$ ($n=1, 2, 3$), and later it was used in a successful development of a spectroscopic technique for detecting weak vibrational overtone transitions²³. The same feature, combined with isotopically selective vibrational overtone pre-excitation and collisional enhancement of isotopic selectivity, comprises the new approach for isotope separation. We first describe this spectroscopic technique called “IRLAPS” which led to the invention of the new approach to molecular laser isotope separation, then we will give some details about the MLIS technique itself.

1.1.1 IRLAPS detection scheme

The spectroscopic technique we present here is called “Infrared laser assisted photofragment spectroscopy” (IRLAPS). Figure 1.1 describes the idea of this technique using the CF_3H molecule as an example.

In the first step of this process a tunable dye laser pre-excites the molecule to a vibrational overtone level - it is the measurement of the spectrum resulting from this transition that is the goal of the experiment. The number of pre-excited molecules is a function of the frequency of the pre-excitation laser, and in the absence of saturation it is simply proportional to the absorption cross section $\sigma(\nu)$. To detect this absorption, the pre-excited molecules are dissociated by IRMPD and the resulting fragments are detected spectroscopically by laser induced fluorescence (LIF). Scanning the excitation

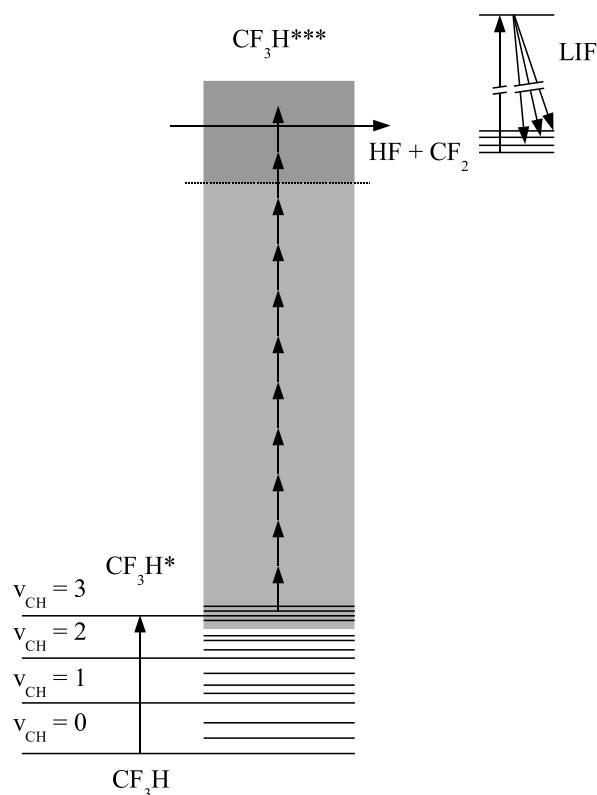


Figure 1.1: IRLAPS detection scheme.

laser while monitoring the LIF intensity produces the excitation spectrum that mirrors the vibrational overtone absorption spectrum. Because the overtone transitions are weak, one wants to dissociate selectively only the pre-excited molecules and not a large excess of ground state molecules, since the products resulting from the dissociation of the latter would mask any change due to the overtone excitation. To avoid dissociation of ground state molecules the three following properties of the IRMPD process can be used.

1. The laser intensity dependence. Multiple photon excitation through the region of lower vibrational levels is facilitated by power broadening which occurs at high laser intensity (energy per unit area per unit time). On the other hand, excitation of the molecules pre-excited to the region of vibrational quasicontinuum depends mostly on the integral fluence of the dissociation laser pulse (energy per unit area)^{24, 25}. Thus, using moderate laser intensities may prevent dissociation of

the ground-state molecules, whereas pre-excited molecules still may be efficiently dissociated provided the fluence of the dissociation laser is sufficient.

2. Anharmonic red-shift of the absorption spectrum of excited molecules^{23, 26}. Because of this red-shift, applying a dissociation laser wavelength detuned to the red side from the maximum of the absorption spectrum of ground-state molecules will result in preferential multiple photon excitation of pre-excited molecules.
3. Fluence dependence. The initial energy level of the multiple photon excitation process for pre-excited molecules lies higher than the one for ground state molecules. It means that pre-excited molecules need to collect less infrared photons from the dissociation laser to reach its dissociation threshold. Thus, the laser fluence required for dissociation of pre-excited molecules is lower^{26, 27}. The correct choice of the dissociation laser fluence may further increase the discrimination between the ground-state and pre-excited molecules.

The advantage of the IRLAPS method as a spectroscopic technique is its high sensitivity which allows the detection of extremely weak vibrational overtone transitions under molecular jet expansion conditions. Since its development in the beginning of 1990's, the IRLAPS method has been applied for obtaining high resolution overtone spectra of a number of molecules, contributing to understanding the dynamics of intramolecular vibrational energy redistribution (IVR) process^{23, 28-34}.

1.1.2 OP-IRMPD system for isotope separation

Two findings in the experiments, where IRLAPS was applied for the detection of highly excited molecules, have lead to the development of our isotope separation process:

1. Excitation of high vibrational overtones can be isotopically selective.
2. The dissociation of molecules in the ground state can be suppressed in an effective way by appropriately adjusting the fluence and the wavelength of the dissociation laser.

The new approach consists of two major steps: in the first step, a near-infrared laser pulse pre-excites molecules containing the desired isotope via a low vibrational overtone transition of a high frequency vibrational mode. In the second step, a CO₂ laser

pulse selectively dissociates the pre-excited molecules. Finally, the dissociation products enriched in the desired isotope are chemically converted to a stable molecule ($\text{CF}_2 + \text{CF}_2 \rightarrow \text{C}_2\text{F}_4$) that is different from the parent molecule and physically separated from the latter, for instance, by distillation. This method is called ‘‘Overtone Pre-excitation - Infrared Multiple Photon Dissociation’’ (OP-IRMPD). In this scheme, the isotopic composition of the products is mainly determined by the selectivity of the pre-excitation step. Although the pre-excitation laser is tuned in such a way that a maximum amount of $^{13}\text{CF}_3\text{H}$ molecules is pre-excited, some of the $^{12}\text{CF}_3\text{H}$ molecules are pre-excited as well, because a P-branch of the absorption feature for $^{12}\text{CF}_3\text{H}$ overlaps with the Q-branch of the absorption feature for $^{13}\text{CF}_3\text{H}$.

We show in figure 1.2 an IRLAPS action spectrum of CF_3H around 8800 cm^{-1} which is obtained by measuring the total amount of LIF as a function of the pre-excitation energy. The small feature at $\sim 8753\text{ cm}^{-1}$ is due to the carbon-13 isotopomer of CF_3H . In our MLIS scheme we excite the molecules at this wavelength.

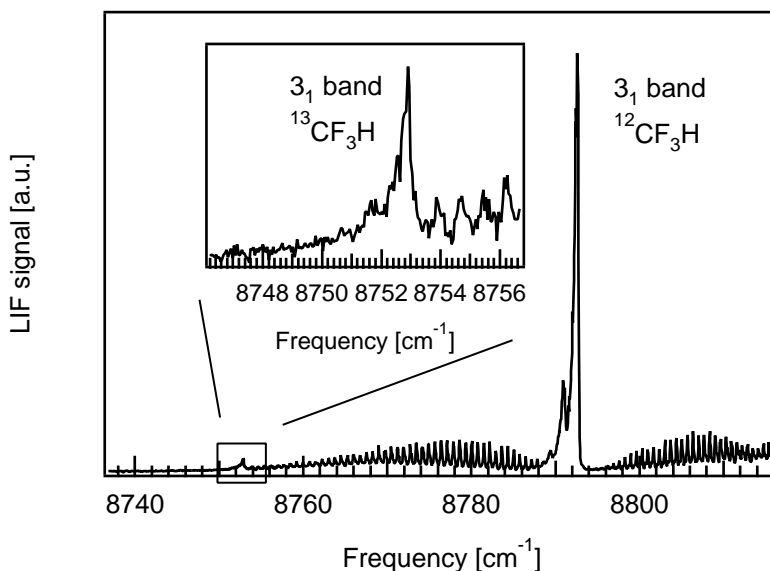
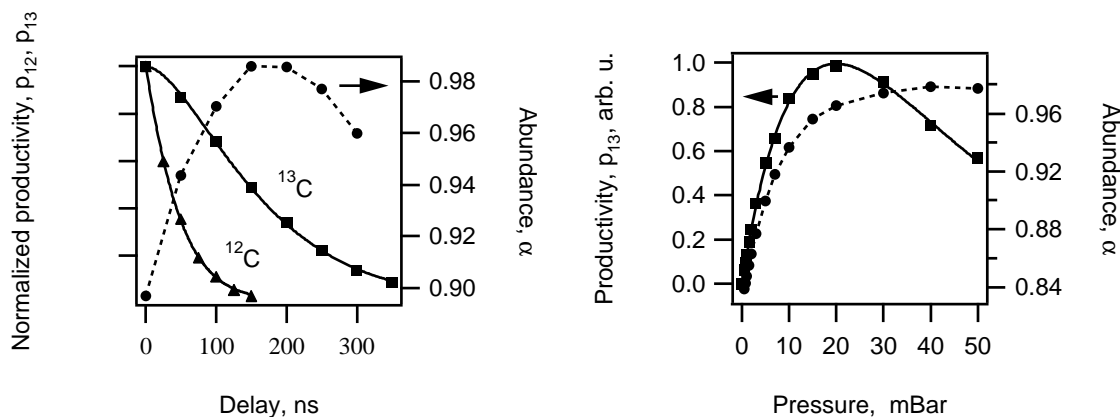


Figure 1.2: Spectrum of the 3_1 transition in CF_3H . The large peak at $\sim 8793\text{ cm}^{-1}$ is assigned to the $^{12}\text{CF}_3\text{H}$ isotopomer, the small peak at $\sim 8753\text{ cm}^{-1}$ is assigned to the $^{13}\text{CF}_3\text{H}$ isotopomer. The sample is in its natural isotopic abundance.

1.2 Aim of this work

Experimentally it has been observed, that the isotopic abundance in the products depends on the sample pressure and on the delay between the two lasers used in this scheme^{15, 16}. Figure 1.3 shows the observed effect.



(a) Isotopic selectivity and productivity as a function of the time-delay between the two lasers.

(b) Isotopic selectivity and productivity of ^{13}C containing products as a function of the sample pressure.

Figure 1.3: Observed effect we study in this thesis. It shows the \bullet isotopic enrichment of the products (right axes) and the productivity of \blacktriangle ^{12}C and \blacksquare ^{13}C containing products (left axes). The isotopic selectivity *increases* as the delay between the two lasers (left) or the sample pressure (right) is increased. Data from Boyarkin¹⁶.

The experimental observations shown in figure 1.3 have been explained by an effect of collisional relaxation occurring between the pre-excited molecules and the surrounding molecules. At first glance, this increase of selectivity contradicts normal expectations. Indeed, collisional vibrational energy transfer between the two different isotopic species should scramble initial isotopic selectivity gained in the pre-excitation step. Many previous works with other MLIS schemes have been performed at low pressures in order not to scramble isotopic selectivity of the process^{35–40}. Some authors have reported a slight increase of isotopic selectivity in IRMPD experiments upon an increase of the sample pressure^{41, 42} or the time-delay between two IR lasers^{43, 44}. Although not complete, some tentative explanations have been delivered. For example, competition between IRMPD

and collisional relaxation⁴² or isotopically selective collisional relaxation⁴⁴ have been proposed.

Figure 1.4 shows the processes occurring when a time-delay between the two lasers is left and/or when the sample pressure is increased. The molecules are allowed to undergo collisional relaxation, lowering their vibrational energy. Because of this, the molecules have to absorb additional photons in order to reach the dissociation limit.

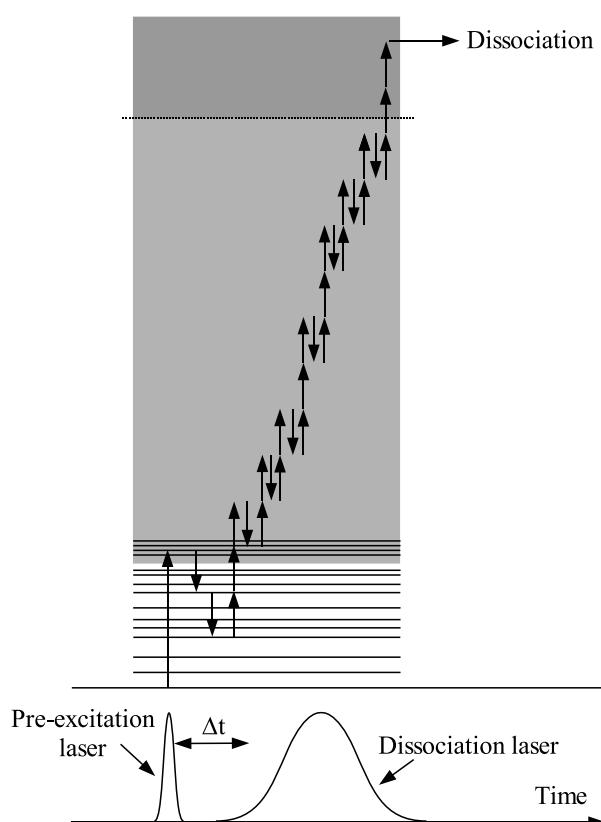


Figure 1.4: Collisions between the lasers and during IRMPD lower the vibrational energy of the molecules \downarrow , which have to absorb more photons \uparrow in order to reach the dissociation limit.

In what follows we demonstrate with a simple model which mechanisms can potentially lead to the increased isotopic selectivity due to the additional collisions. This selectivity S is defined as the ratio of dissociation probabilities of $^{12}\text{CF}_3\text{H}$ and $^{13}\text{CF}_3\text{H}$:

$$S := \frac{{}^{13}D}{{}^{12}D} \quad (1.1)$$

and the enhancement of isotopic selectivity is defined by

$$E := \frac{S}{S_0} = \frac{{}^{13}D/{}^{12}D}{{}^{13}D_0/{}^{12}D_0}, \quad (1.2)$$

where the dissociation probabilities ${}^x D$ at a higher sample pressure or a large time-delay between the lasers are compared to the dissociation probabilities ${}^x D_0$ at a zero time-delay between the lasers and a low sample pressure.

For the purpose of the demonstration below we will assume the up-pumping rates of the molecules κ_u due to the dissociation laser radiation such as the collisional relaxation rates κ_d independent on the vibrational energy of the molecule, which is not strictly true, but demonstrates the underlying physical ideas. If a pre-excited ${}^x \text{CF}_3\text{H}$ molecule ($x=12, 13$) has a dissociation probability ${}^x D_0$ at a zero time-delay between the lasers and at low pressures, then the dissociation probability ${}^x D$ in a situation given in figure 1.4 is given by

$${}^x D \approx {}^x D_0 \cdot \sigma^x N, \quad (1.3)$$

where $\sigma \approx \kappa_u \cdot \Phi < 1$ is the probability of the molecule absorbing a photon of the laser radiation field, Φ is the fluence of the dissociation laser pulse and N is the number of additional photons to be absorbed in order to compensate for the loss of vibrational energy in collisions. The enhancement E of the isotopic selectivity S of the process is hence given by

$$\begin{aligned} E &= \frac{S}{S_0} \\ &= \frac{{}^{13}D}{{}^{12}D} / \frac{{}^{13}D_0}{{}^{12}D_0} \\ &= \frac{({}^{13}\kappa_u \cdot \Phi)^{{}^{13}N}}{({}^{12}\kappa_u \cdot \Phi)^{{}^{12}N}}. \end{aligned} \quad (1.4)$$

The enhancement of isotopic selectivity E can be different from 1 in two cases: both in the case that the up-pumping rates via IRMPD are different (${}^{12}\kappa_u \neq {}^{13}\kappa_u$) and in the case of different numbers of additional photons to be absorbed (${}^{12}N \neq {}^{13}N$). This number of additional photons is proportional to the collisional relaxation rate:

$${}^x N \approx {}^x \kappa_d \cdot p \cdot (\Delta t + \tau_d), \quad (1.5)$$

where ${}^x \kappa_d$ is the relaxation rate, p the sample pressure, Δt the time-delay between the two lasers and τ_d the typical time for a molecule to be dissociated[‡].

We hence propose two mechanisms which can lead to the enhancement of isotopic selectivity:

${}^{12}\kappa_u \neq {}^{13}\kappa_u$	Different IRMPD rates
${}^{12}\kappa_d \neq {}^{13}\kappa_d$	Different vibrational relaxation rates

Using these two ideas, “*Isotopically selective IRMPD rates*” and “*Isotopically selective vibrational relaxation rates*”, the goal of this thesis is to quantify the relative influences of the two mechanisms to the enhancement of isotopic selectivity upon an increase of either the time-delay between the laser pulses or the sample pressure.

For this, fundamental properties such as the interaction between molecules and laser radiation (infrared multiple photon dissociation - IRMPD) and vibrational energy transfer (VET) between two colliding molecules are studied. By means of this fundamental research we both gain understanding of the phenomena under investigation and understand the OP-IRMPD process better.

In addition to this, we will be interested in knowing to what extent any differences in vibrational relaxation rates and/or up-pumping through IRMPD is a general feature of vibrationally excited CF_3H , or whether this is accidentally caused through different couplings of the excited vibrational states in ${}^{12}\text{CF}_3\text{H}$ and ${}^{13}\text{CF}_3\text{H}$ to the other vibrational modes of the molecule. It is known that the state to which the molecules are initially excited are mixed with other (unidentified) close lying states, and that the couplings are not equally strong³⁰. It is possible, that because of this the overall energy redistribution in the molecule takes place on different time-scales for the two isotopomers which hinders or enhances the first steps of collisional relaxation or IRMPD. Can we treat the vibrational energy of a molecule in a statistical manner (i.e. the energy is completely

[‡] τ_d depends on the isotopic species, but for simplicity we set them equal. This does not change the reasonings.

randomised over the molecule) or do we have to take into account the exact state the molecules are prepared in ?

In order to investigate on the contributions of the two mechanisms to the increase of isotopic selectivity, the work is performed as follows:

- For time-delayed lasers at a low sample pressure: the determination is done experimentally, as the two mechanisms occur temporally separated allowing a clear discrimination of the two mechanisms.
- For an increased sample pressure: the determination is done in numerical simulations, as an experimental approach is more difficult to realise.

1.3 Structure of this work

This work is divided into five chapters.

- In this chapter we have stated the problem we wish to study.
- For the convenience of the reader, chapter 2 gives some background information relevant to the subject of our study. It consists of three sections: the first one describes the spectroscopy and intramolecular dynamics of CF_3H , the second one describes theoretical approaches for a treatment of IR multiple photon dissociation (IRMPD), and in the third section we give an overview of the field of collisional energy transfer (CET).
- In the third chapter we propose detailed descriptions of our experimental setup.
- In chapter 4 we give an overview of different experiments we perform in order to investigate the phenomenon described above. This is organised as follows: after a brief introduction, a first small section describe some experiments performed in order to address the question of accidental resonances between the 3_1 and an other (unidentified) one. Then, we describe experiments performed under collision-free conditions, where any dissociation selectivity is obtained because of different IRMPD efficiencies. Then we propose two sets of experiments where we try to separate the different mechanisms leading to an increased isotopic selectivity: first,

we change the wavelength of the dissociation laser radiation and then we work with isotopically enriched CF_3H . The chapter is concluded by a discussion of the experimental results.

- Chapter 5 is dedicated to numerical simulations. There are essentially two important sections: simulations of vibrational energy transfer, and simulations of the overall processes in our MLIS process. A separate chapter treats the absorption and emission spectrum of vibrationally excited CF_3H .
- Finally, we conclude with the take home message of this work.

Bibliography

- [1] F. Soddy. Infra-atomic charge. *Nature*, 92:399–400, 1913.
- [2] F. Soddy. The radio-elements and the periodic law. *Chemical News*, 107:97–99, 1913.
- [3] Harold C. Urey, F. G. Brickwedde, and G. M. Murphy. A Hydrogen Isotope of Mass 2 . *Phys. Rev.*, 39:164–165, 1932.
- [4] Barry J. Marshall. Methods for the diagnosis of gastrointestinal disorders . US Patent Number 4,830,010 (May 16, 1989).
- [5] S. Koletzko, M. Haisch, I. Seeboth, B. Braden, K. Hengels, B. Koletzko, and P. Hering. Isotope selective nondispersive infrared spectrometry for detection of helicobacter-pylori infection with C-13-Urea Breath Test . *Lancet*, 345(8955):961–962, 1995.
- [6] Graham, Malaty, Cole, Martin, and Klein. Simplified ^{13}C -Urea Breath Test for Detection of Helicobacter pylori Infection . *The American Journal of Gastroenterology*, 96:1741–1745, 2001.
- [7] Author unknown. ‘Guinea pig’ doctor uncovers new cause of ulcers - and the cure . *The Star*, A copy can be obtained upon request from the author of this thesis., 1984.

-
- [8] Harry L.T. Mobley, George L. Mendz, and Stuart L. Hazell, editors. *Helicobacter pylori : physiology and genetics*. Washington, D.C. : ASM Press, 2001.
- [9] J.-M. Cavedon. La séparation isotopique . *Ann. Phys. Fr.*, 25(2):327–341, 2000.
- [10] V. S. Letokhov. Use of lasers to control selective chemical reactions. *Science*, 180:451–458, 1973.
- [11] V. S. Letokhov. Laser isotope separation. *Nature*, 277:605–610, 1979.
- [12] V. S. Letokhov. Laser-induced processes in spectroscopy, isotope separation, and photochemistry. *Sov. Phys. Uspekhi*, 29:70–81, 1986.
- [13] V. Y. Baranov, editor. *Isotopes: properties, production, applications*. IzdAT, Moscow, 2000 (in Russian).
- [14] Thomas R. Rizzo and Oleg V. Boiarkine. Laser Isotope Separation Method Employing Isotopically Selective Collisional Relaxation . US Patent Number 6,653,587 (Nov. 25, 2003).
- [15] Monika Kowalczyk. *Highly Selective Molecular Laser Isotope Separation of Carbon-13* . PhD thesis, Ecole polytechnique fédérale de Lausanne, Switzerland, 2000.
- [16] O. V. Boyarkin, M. Kowalczyk, and T. R. Rizzo. Collisionally Enhanced Isotopic Selectivity in Multiphoton Dissociation of vibrationally excited CF₃H . *J. Chem. Phys.*, 118(1):93–103, 2003.
- [17] Mikhail N. Polianski. *Overtone pre-excitation - Infrared Multiple Photon Dissociation Under Collisional Conditions. New Potential for Laser Isotope Separation* . PhD thesis, Ecole polytechnique fédérale de Lausanne, Switzerland, 2004.
- [18] M. Polianski, O. V. Boyarkin, and T.R. Rizzo. Collisionally-assisted, highly-selective laser isotope separation of carbon-13 . *J. Chem. Phys.*, 121(23):11771–11779, 2004.
- [19] M. Polianski, O. V. Boyarkin, and T. R. Rizzo. to be published . 2005.
- [20] R. Bossart, O. V. Boyarkin, A. A. Makarov, and T. R. Rizzo. Isotopically selective collisional energy transfer of vibrationally excited CF₃H (in preparation) . 2005.

- [21] R. Bossart, O. V. Boyarkin, and T. R. Rizzo. in preparation . 2005.
- [22] L. I. Yeh, M. Okumura, J. D. Myers, J. M. Price, and Y. T. Lee. Vibrational spectroscopy of the hydrated hydronium cluster ions $\text{H}_3\text{O}^+ \cdot (\text{H}_2\text{O})_n$ ($n=1, 2, 3$) . *J. Chem. Phys.*, 91(12):7319–7330, 1989.
- [23] R. D. F. Settle and T. R. Rizzo. CO_2 laser assisted vibrational overtone spectroscopy . *J. Chem. Phys.*, 97(4):2823–2825, 1992.
- [24] T. B. Simpson, J. G. Black, I. Burak, E. Yablonovitch, and N. Bloembergen. Infrared multiphoton excitation of polyatomic molecules. *J. Chem. Phys.*, 83:628–640, 1985.
- [25] O. V. Boyarkin, T. R. Rizzo, D. S. Rueda, M. Quack, and G. Seyfang. Nonlinear intensity dependence in the infrared multiphoton excitation and dissociation of methanol preexcited to different energies . *J. Chem. Phys.*, 117(21):9793–9805, 2002.
- [26] V. N. Bagratashvili, V. S. Letokhov, A. A. Makarov, and E. A. Ryabov. *Multiple Photon Infrared Laser Photophysics and Photochemistry*. Harwood, Amsterdam, 1985.
- [27] M. C. Gower and T. K. Gustafson. Collisionless dissociation of SF_6 using two resonant frequency CO_2 laser fields. *Optics Commun.*, 23:69–72, 1977.
- [28] O. V. Boyarkin and T. R. Rizzo. Rotational state selected vibrational overtone spectroscopy of jet-cooled molecules. *J. Chem. Phys.*, 103:1985–1988, 1995.
- [29] O. V. Boyarkin, R. D. F. Settle, and T. R. Rizzo. Vibrational Overtone Spectra of Jet-Cooled CF_3H by Infrared Laser Assisted Photofragment Spectroscopy . *Ber. Bunsenges. Phys. Chem.*, 99(3):504–513, 1995.
- [30] O. V. Boyarkin and T. R. Rizzo. Secondary time scales of intramolecular vibrational energy redistribution in CF_3H studied by vibrational overtone spectroscopy . *J. Chem. Phys.*, 105(15):6285–6292, 1996.
- [31] O. V. Boyarkin, L. Lubich, R. D. F. Settle, D. S. Perry, and T. R. Rizzo. Intramolecular energy transfer in highly vibrationally excited methanol. I. Ultrafast dynamics . *J. Chem. Phys.*, 107(20):8409–8422, 1997.

- [32] O. V. Boyarkin and T. R. Rizzo. Intramolecular energy transfer in highly vibrationally excited methanol. II. Multiple time scales of energy redistribution . *J. Chem. Phys.*, 110(23):11346–11358, 1999.
- [33] O. V. Boyarkin, T. R. Rizzo, and David S. Perry. Intramolecular energy transfer in highly vibrationally excited methanol. III. Rotational and torsional analysis . *J. Chem. Phys.*, 110(23):11359–11367, 1999.
- [34] Andrei Chirokolava, David S. Perry, O. V. Boyarkin, M. Schmid, and T. R. Rizzo. Intramolecular energy transfer in highly vibrationally excited methanol. IV. Spectroscopy and dynamics of $^{13}\text{CH}_3\text{OH}$. *J. Chem. Phys.*, 113(22):10068–10072, 2000.
- [35] R. V. Ambartzumian, N. P. Furzikov, Yu. A. Gorokhov, and V. S. Letokhov. Isotope-selective dissociation of the OsO_4 molecule by two pulses of infrared radiation at different frequencies . *Opt. Lett.*, 1(1):22–24, 1977.
- [36] Joe J. Tjee and Curt Wittig. IR photolysis of SeF_6 : Isotope separation and dissociation enhancement using NH_3 and CO_2 lasers . *J. Chem. Phys.*, 69(11):4756–4761, 1978.
- [37] P. Rabinowitz, A. Kaldor, A. Gnauck, R. L. Woodin, and J. S. Gethner. Two-color infrared isotopically selective decomposition of UF_6 . *Optics Lett.*, 7(5):212–214, 1982.
- [38] J.-M. Zellweger, J.-M. Philippoz, P. Melinon, R. Monot, and H. van den Bergh. Isotopically selective condensation and infrared laser assisted gas dynamic isotope separation . *Phys. Rev. Lett.*, 52(7):522–525, 1984.
- [39] Sam A. Tuccio and Donald F. Heller. Sequential multiphoton excitation method . US Patent Number 4,461,686 (July 24, 1984).
- [40] L. Pateopol and J. A. O’Neill. *Laser Isotope Separation*, volume 1859, chapter Two color multiple-photon dissociation of CF_3T , pages 210–218. editors: Jeffrey A. Paisner, Lawrence Livermore National Lab., Livermore, CA, USA. SPIE Proceedings, 1993.

-
- [41] Pheihua Ma, Kyoko Sugita, and Shigeyoshi Arai. Highly selective ^{13}C Separation by CO_2 -laser-induced IRMPD of $\text{CF}_2\text{Cl}_2/\text{HI}$ and $\text{CF}_2\text{ClBr}/\text{HI}$ Mixtures . *Appl. Phys. B*, 49(6):503–512, 1989.
- [42] M. Gauthier, C. G. Cureton, P. A. Hackett, and C. Willis. Efficient Production of $^{13}\text{C}_2\text{F}_4$ in the Infrared Laser Photolysis of CHClF_2 . *Appl. Phys. B*, 28:43–50, 1982.
- [43] A. V. Evseev, V. S. Letokhov, and A. A. Puretzky. Highly Selective and Efficient Multiphoton Dissociation of Polyatomic Molecules in Multiple-Frequency IR-Laser Fields . *Appl. Phys. B*, 36:93–103, 1985.
- [44] A. V. Evseev, V. B. Laptev, A. A. Puretskii, E. A. Ryabov, and N. P. Furzikov. Laser Separation of carbon isotopes by two-frequency dissociation of Freons . *Sov. J. Quantum Electron.*, 18(3):385–392, 1988.

Chapter 2

Background information

In this chapter we will give some background information about three topics, information that is needed in order to fully comprehend the work under review:

1. First, section 2.1 will treat the spectroscopy and the intramolecular dynamics of CF_3H molecules.
2. Then, in section 2.2, we will describe the infrared multiple photon dissociation (IRMPD) processes in more detail. In particular, we will introduce a statistical approach to treat IRMPD numerically.
3. Finally we will give a historical overview and some basic theory regarding collisional vibrational energy transfer in section 2.3.

2.1 Spectroscopy and intramolecular dynamics of CF_3H

Here, we will describe the spectroscopy and intramolecular dynamics of CF_3H . For this, the section will be further divided into two subsections. First, we will treat the rovibrational spectroscopy. We will in particular treat Fermi resonances, that can be found in CF_3H due to extensive mixing of vibrational modes. Secondly, we will introduce the notion of intramolecular vibrational energy redistribution (IVR) and show how this is connected to Fermi resonances. We will also treat the subject of IVR induced by collisions with other molecules.

2.1.1 Rovibrational spectroscopy of CF₃H

2.1.1.A Generalities and fundamental frequencies

CF₃H is a symmetric top molecule with a C_{3v} symmetry. As it is a non-linear molecule with 5 atoms, there are $3 \cdot 5 - 6 = 9$ vibrational normal modes. There are three non-degenerate and three doubly degenerate modes. The conventional notation of the 6 modes and their fundamental frequencies are listed in table 2.1, the corresponding normal mode vectors are shown in figure 2.1.

Mode	¹² $\tilde{\nu}$ ^[a]	¹³ $\tilde{\nu}$ ^[a]	Motion	σ / pm ² ^[c]
ν_1 (A ₁ ,)	3035.5 ^[b]	3025.3 ^[b]	symmetric C-H stretch	0.133 ^[c₁]
ν_2 (A ₁ ,)	1141.5	1115.9	symmetric C-F stretch	1.10 ^[c₂,c₃]
ν_3 (A ₁ ,)	700.1	695.3	symmetric C-F ₃ deformation (“umbrella”)	0.69 ^[c₂]
ν_4 (E, ⊥)	1377.8	1368.9	HCF bend	0.91 ^[c₂]
ν_5 (E, ⊥)	1158.3	1132.4	antisymmetric C-F stretch	6.37 ^[c₂,c₃]
ν_6 (E, ⊥)	507.8	506.7	antisymmetric C-F ₃ deformation (“rock”)	0.27 ^[c₄]

Table 2.1: Normal modes and symmetry in ¹²CF₃H and ¹³CF₃H. A parallel/perpendicular (||, ⊥) band has a transition dipole moment parallel/perpendicular to the symmetry axis of the molecule.

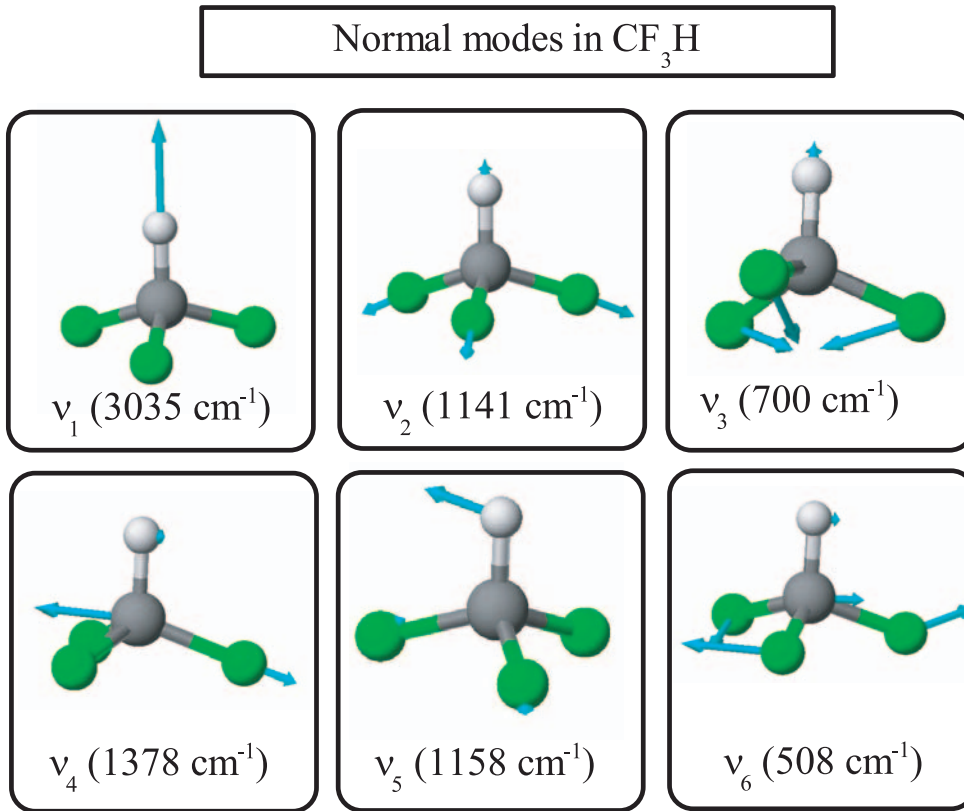
[a] Band origins¹, in cm⁻¹.

[b] ν_1 is strongly mixed by Fermi resonance with $2\nu_4$ and is hence a special case. Without mixing, ν_1 would absorb at 3018.7 cm⁻¹ (¹²CF₃H) and 3008 cm⁻¹ (¹³CF₃H) (see equation 2.9).

[c] Integral absorption cross-section. From (c₁) Lewerenz², (c₂) McPheat³, (c₃) Amrein⁴, (c₄) own measurements (FTIR).

Note that ν_2 and ν_5 are mixed and their relative contributions to the absorption spectrum cannot be determined experimentally; numerical simulations by Amrein⁴ show that their relative contributions are $G(\nu_5) : G(\nu_2) \sim 5.78 : 1$.

The vibrational spectroscopy of CF₃H is rather well studied^{3, 5-18}. Figure 2.2 gives an overview of the IR spectrum of CF₃H. A striking feature of the vibrational spectroscopy of CF₃H is the so-called polyad structure formed by overtones of the C-H stretch vibration (ν_1) strongly anharmonically coupled to overtones of the C-H bending vibration

Figure 2.1: Normal modes in CF₃H (frequencies for ¹²CF₃H).

(ν_4). This will be discussed in section 2.1.1.C.

The permanent dipole moment of CF₃H is $d \approx 1.65$ debye¹⁹. The transition dipole moment $\mu = \langle 0 | d | 1 \rangle$ for a certain transition can be calculated from the integrated band intensity, G , as follows²⁰:

$$G = 41.624 \left(\frac{|\langle 0 | d | 1 \rangle|}{\text{Debye}} \right)^2 \text{ pm}^2 \quad (2.1)$$

These transition dipole moments are given in table 2.2.

	ν_1	ν_2	ν_3	ν_4	ν_5	ν_6
$ \langle 0 d 1 \rangle / \text{Debye}$	$5.65 \cdot 10^{-2}$	$1.62 \cdot 10^{-1}$	$1.28 \cdot 10^{-1}$	$1.47 \cdot 10^{-1}$	$3.91 \cdot 10^{-1}$	$8.05 \cdot 10^{-2}$

Table 2.2: Transition dipole moment between the ground state and the fundamentals.

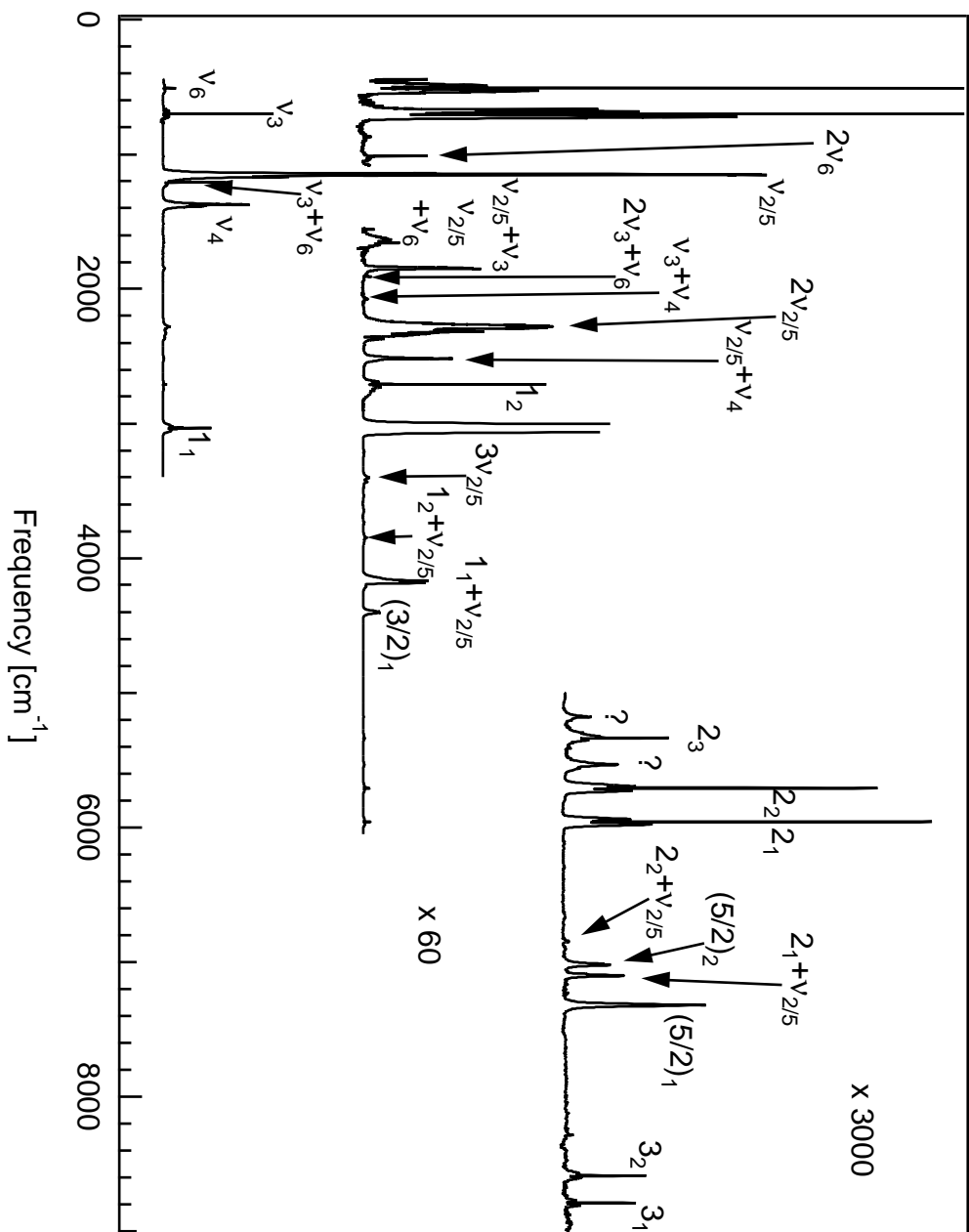


Figure 2.2: FTIR scan of CF_3H at room temperature (own measurement with a Perkin Elmer from Spectrum GX). As the ν_5 and ν_2 vibrations lie close in energy they couple via Coriolis interaction and cannot be completely separated. For this reason the notation $\nu_{2/5}$ is used although the oscillator strength mainly comes from ν_5 . For the bands denoted as N_j (e.g. 3_1) see chapter 2.1.1.C.

2.1.1.B Zeroth-order states in CF₃H

In a first approximation the vibrational modes of a molecule can be viewed as a set of independent oscillators, which means that the vibrational state of a molecule can be described by the number of quanta $v := |v_1, v_2, \dots, v_N\rangle$ in each particular mode. The energy of a state is given by

$$\begin{aligned}
 E(v) &= \sum_s \omega_s \left(v_s + \frac{1}{2}\right) + \sum_t \omega_t (v_t + 1) \\
 &+ \sum_{s \geq s'} x_{ss'} \left(v_s + \frac{1}{2}\right) \left(v_{s'} + \frac{1}{2}\right) \\
 &+ \sum_{t \geq t'} x_{tt'} (v_t + 1) (v_{t'} + 1) \\
 &+ \sum_{s,t} x_{st} \left(v_s + \frac{1}{2}\right) (v_t + 1) \\
 &+ \sum_{t \geq t'} g_{tt'} l_t l_{t'},
 \end{aligned} \tag{2.2}$$

where sums over s are for non-degenerate and sums over t are for doubly degenerate vibrations. l_t are the vibrational angular momentum, where l_t can take the values $-v_t, -v_t + 2, \dots, v_t - 2, v_t$. Equation 2.2 includes harmonic contributions (terms on the first line), shifts due to anharmonic interactions (terms on the second to fourth lines) and splittings of degenerate levels (term on the last line). The values of ω are called the fundamental frequencies, x_{ij} and $g_{tt'}$ are called “spectroscopic anharmonic constants”.

The constants have been measured experimentally²¹ for CF₃H and are given in table 2.3.

The states described by v are called zeroth-order states. They may mix with each other to form higher order states. A rather strong mixing arises through so-called Fermi interactions which are discussed in the next section.

2.1.1.C Fermi resonances

Enrico Fermi observed for the first time strong resonances (later named after him) between ν_1 and $2\nu_2$ in CO₂²². Due to an accidental degeneracy of the two vibrations their interaction (which is proportional to $1/\Delta E$) is large. The states mix strongly and show up as two separate lines in the Raman spectrum, where only one (due to ν_1) should be found. Nowadays “Fermi resonances” refer either to an anharmonic resonance between

ω_1	3077.0	ω_2	1155.1	ω_3	710.3
ω_4	1396.3	ω_5	1184.7	ω_6	520.1
x_{11}	-36.0 (-44.0)	x_{12}	-5.7 (-5.5)	x_{13}	4.8 (1.9)
x_{14}	-5.1 (-54.9)	x_{15}	-7.9 (-1.0)	x_{16}	-0.6 (0.7)
x_{22}	-7.9 (-3.4)	x_{23}	-1.6 (-2.1)	x_{24}	-1.1 (2.5)
x_{25}	-5.6 (-0.9)	x_{26}	1.6 (-2.6)	x_{33}	-2.4 (-0.3)
x_{34}	-0.8 (-0.8)	x_{35}	-5.7 (-3.9)	x_{36}	0.0 (-1.1)
x_{44}	-0.5 (4.5)	x_{45}	-13.7 (-2.5)	x_{46}	-1.0 (-0.7)
x_{55}	0.7 (-3.0)	x_{56}	-7.8 (-3.1)	x_{66}	-0.4 (-0.2)
g_{44}	-2.3	g_{45}	1.0	g_{46}	0.4
g_{55}	1.7	g_{56}	-1.5	g_{66}	0.3

Table 2.3: Anharmonic constants for CF_3H . All values are in cm^{-1} . The values ω_i and x_{ij} are determined experimentally. The bracketed values and the values for g_{ij} are best fit values.

vibrational modes, which have an approximate 1:2 ratio of frequencies²³ or strong anharmonic couplings in general²⁴, depending on the author. In principle, there is nothing special about a 1:2 resonance apart that it occurs quite often.

Let q_i be the vibrational normal coordinate of mode i . The potential part of the molecular Hamiltonian can be written as

$$V = V_0 + \sum_i \left(\frac{\partial^2 V}{\partial q_i^2} \right) q_i q_j + \sum_{i,j,k} \left(\frac{\partial^3 V}{\partial q_i \partial q_j \partial q_k} \right) q_i q_j q_k + \sum_{i,j,k,l} \left(\frac{\partial^4 V}{\partial q_i \partial q_j \partial q_k \partial q_l} \right) q_i q_j q_k q_l + \dots, \quad (2.3)$$

where the sums go from 1 to N (number of modes). In the approximation of independent harmonic oscillators derivatives of V of order higher than 2 are zero. In a real molecule this is not the case and it has to be taken into account for the calculation of the energies of the molecular states. The values of $(\partial^3 V / \partial q_i \partial q_j \partial q_k)$, \dots are called ‘‘anharmonic constants’’.

Sticking to the definition of a 1:2 resonance, a Fermi resonance is formally a third order anharmonic coupling of the type $\langle v_i, v_j, \dots | V_{ijj} | v_i - 1, v_j + 2, \dots \rangle$ where $V_{ijj} =$

$\partial^3 V / \partial q_i \partial q_j^2$ as given in equation 2.3. The value of $V_{ijj} / \Delta E$ is a measure of the mixing of the two states, where ΔE is the difference of the energies of the zeroth order states $|v_i, v_j, \dots\rangle$ and $|v_i - 1, v_j + 2, \dots\rangle$. The larger this ratio is, the more important the Fermi resonance.

Multiple peaks in an absorption spectrum arise from strong mixing of normal modes due to Fermi resonances. To explain this, we begin with a set of $(N + 1)$ so called “zeroth order states” (our normal modes) which we will denote as follows:

$$\begin{array}{ll} |b\rangle & \text{bright state. IR active vibration.} \\ |d_i\rangle & \text{dark states } (i = 1, \dots, N). \text{ IR inactive vibrations.} \end{array} \quad (2.4)$$

$|b\rangle$ and $|d_i\rangle$ couple to give the following eigenstates (called “first order states”):

$$|\psi_j\rangle = c_{0,j}|b\rangle + \sum_{i=1}^N c_{i,j}|d_i\rangle \quad (2.5)$$

If mixing is only weak, these first order states are often labeled the same way as the zeroth order states, which may be confusing but nevertheless useful.

The IR transition strength between the ground state and $|\psi_j\rangle$ is given by

$$\begin{aligned} I_j &\propto |\langle 0 | \vec{d} | \psi_j \rangle|^2 \\ &= |c_{0,j} \underbrace{\langle 0 | \vec{d} | b \rangle}_{\neq 0} + \sum_{i=1}^N c_{i,j} \underbrace{\langle 0 | \vec{d} | d_i \rangle}_{=0}|^2 . \\ &= |c_{0,j} \langle 0 | \vec{d} | b \rangle|^2 \end{aligned} \quad (2.6)$$

Here, \vec{d} is the dipole moment of the molecule. In such a situation, one says that $|\psi_j\rangle$ “borrows” some transition strength from $|b\rangle$. In a spectrum one will see a set of $N + 1$ peaks corresponding to the $|0\rangle \rightarrow |\psi_j\rangle$ transitions. This set of $N + 1$ peaks is called a “polyad” (or “diad” if only two states couple, “triad” if three states couple, and so on). Experimentally one can measure the values of $|c_{0,j}|^2$ by measuring the absorption strengths of the different members of a polyad and using the relation established in equation 2.6, i.e. $I_j \propto |c_{0,j}|^2$. Figure 2.3 shows a schematic example of the effect of state mixing on the spectrum.

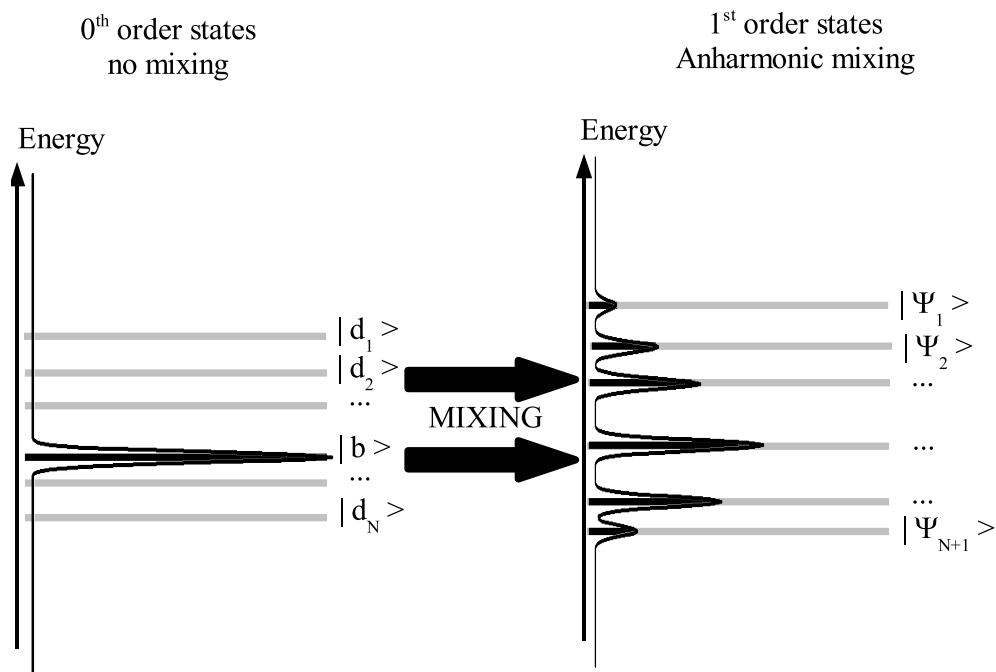


Figure 2.3: Anharmonic coupling between dark and bright states give rise to a polyad structure in the absorption spectra. The figure on the left would apply to a system of one bright state $|b\rangle$ and a set of N dark states $|d_i\rangle$ in the absence of interactions. The horizontal lines represent the states, the dark part of the line represents the brightness of a state (i.e. what can be seen in an absorption spectrum). The figure on the right corresponds to the same system but including anharmonic coupling. The levels are shifted, and the bright part of a state is taken from $|b\rangle$.

2.1.1.D Fermi resonances in CF_3H

The first observation of a Fermi resonance in CF_3H was made in 1948 by Bernstein and Herzberg⁵. They identified a peak at 8792 cm^{-1} to be $3\nu_1$ and a peak at 8589 cm^{-1} to be $2\nu_1 + 2\nu_4$, and the possibility of mixing through Fermi resonances has been correctly suggested by the authors.

We will apply the formalism introduced in the previous section to CF_3H . In this molecule, the ν_1 and $2\nu_4$ vibrations accidentally lie close to each other ($\sim 3,000\text{ cm}^{-1}$). Their cou-

pling is appreciable, which gives rise to polyads discussed above. The ν_1 vibration, $|b\rangle$, is IR active whereas the $2\nu_4$ vibration, $|d\rangle$, is, at least in the harmonic approximation, not.

Using the notation $|x, y\rangle = |n_1 = x, n_4 = y\rangle$, the $|1, 0\rangle$ and the $|0, 2\rangle$ states couple with each other and form first order states:

$$\begin{aligned} |\psi_0\rangle &= c_{0,0}|1, 0\rangle + c_{1,0}|0, 2\rangle \\ |\psi_1\rangle &= c_{0,1}|1, 0\rangle + c_{1,1}|0, 2\rangle \end{aligned} \quad (2.7)$$

Higher overtones couple in a similar manner: e.g. $|3, 0\rangle$, $|2, 2\rangle$, $|1, 4\rangle$ and $|0, 6\rangle$ couple to form following eigenstates:

$$|\psi_j\rangle = c_{0,j}|3, 0\rangle + c_{1,j}|2, 2\rangle + c_{2,j}|1, 4\rangle + c_{3,j}|0, 6\rangle \quad (2.8)$$

One denotes the first order states $|\psi_j\rangle$ per definition as $|N_x\rangle$, where N is the number of quanta in the zeroth order C-H stretch vibration, and x is 1, 2, ... where “1” stands for the state with the highest energy, “2” for the state with the second highest energy, etc²⁰.

Due to the Fermi resonance structure, the C-H stretch vibration and its overtones have received a lot of experimental^{17, 20, 25-33} and theoretical attention. Quack and co-workers have extensively analysed the polyad structure of the CH chromophore in CF₃H^{17, 20, 25}. They propose a tridiagonal structure of the matrix linking the states coupled by Fermi resonances. They define a “chromophore level N ” to be the set of normal modes with a particular $N = v_1 + \frac{1}{2}v_4$. Working in the normal mode basis set, $|N, 0\rangle$, $|N - 1, 2\rangle$, ... $|0, 2N\rangle$, the matrix elements for a given chromophore are given as follows[‡]:

$$\begin{aligned} \langle v_1, v_4 | H | v_1, v_4 \rangle &= \tilde{\nu}'_s v_1 + \tilde{\nu}'_b v_4 + x'_{ss} v_1^2 + x'_{bb} v_4^2 + x'_{sb} v_1 v_4 \\ \langle v_1, v_4 | H | v_1 - 1, v_4 + 2 \rangle &= -\frac{1}{2} k_{sbb} (v_4 + 2) \sqrt{\frac{1}{2} v_1} \end{aligned} \quad (2.9)$$

where H is the molecular Hamiltonian.

All other matrix elements are zero. Least square fits have been performed^{20, 25} to get

[‡]Quack also includes the vibrational angular momentum l_b in the notation. As long as we work with $N = 1, 2, 3, \dots$ this value is $l_b = 0$ and can be left away from the notation. For half-integer values of N we have $l_b = 1$ and the values for off-diagonal matrix elements change, but the fundamental ideas and developments are the same. In our explanations we will omit the angular momentum for simplicity.

the values of $\tilde{\nu}'_s, \dots$. The results are surprisingly good: this simple model predicts both the energies and the intensities of the different members of a polyad very precisely. The values are summarised in table 2.4 (table II of Segall²⁵ and table 2 of Hollenstein²⁶).

	¹² CF ₃ H	¹³ CF ₃ H
$\tilde{\nu}'_s$	3078.67	3068.9
$\tilde{\nu}'_b$	1379.58	1368.1
x'_{ss}	-59.93	-60.8
x'_{sb}	-27.27	-31.5
x'_{bb}	-7.42	-5.9
k_{sbb}	(±) 100.43 ^[a]	(±) 103.5 ^[a]

Table 2.4: Constants for the CH chromophore in CF₃H. All values are in cm⁻¹.

[a] the sign of k_{sbb} is undetermined.

We will often use the commonly used notation “ $\nu_{CH} = N$ ” although the vibrational states are highly mixed, as described previously. This is only done if no ambiguity exists about the state $|N_j\rangle$ we are referring to.

Table 2.5 gives the experimental band origins^{20, 25, 26} of the fundamentals and the overtones of ν_1 and $2\nu_4$.

Band	$^{12}\text{CF}_3\text{H}$	$^{13}\text{CF}_3\text{H}$	Band	$^{12}\text{CF}_3\text{H}$	$^{13}\text{CF}_3\text{H}$
$ (1/2)_1\rangle$	1377.85	1368.9	$ 4_3\rangle$	11,109	11,054
$ 1_2\rangle$	2710.2	2695.1	$ 4_2\rangle$	11,347	11,300.1
$ 1_1\rangle$	3035.5	3024.6	$ 4_1\rangle$	11,563	11,497.3
$ (3/2)_2\rangle$	4044		$ (9/2)_4\rangle$	11,999	
$ (3/2)_1\rangle$	4400		$ (9/2)_3\rangle$	12,351	
$ 2_3\rangle$	5337	5311.2	$ (9/2)_2\rangle$	12,652	
$ 2_2\rangle$	5710.4	5680.9	$ (9/2)_1\rangle$	12,917	
$ 2_1\rangle$	5959.4	5936.6	$ 5_4\rangle$	13,532	
$ (5/2)_3\rangle$	7322		$ 5_3\rangle$	13,800	
$ (5/2)_2\rangle$	7018		$ 5_2\rangle$	14,003	
$ 3_4\rangle$	7890	7855.3	$ 5_1\rangle$	14,289	
$ 3_3\rangle$	8286.0	8244.0	$ (11/2)_4\rangle$	14,735	
$ 3_2\rangle$	8589.3	8548.9	$ (11/2)_3\rangle$	15,025	
$ 3_1\rangle$	8792.7	8753.0	$ (11/2)_2\rangle$	15,302	
$ (7/2)_3\rangle$	9550.0		$ (11/2)_1\rangle$	15,619	
$ (7/2)_2\rangle$	9881.9		$ 6_4\rangle$	16,164	
$ (7/2)_1\rangle$	10,155.9		$ 6_3\rangle$	16,368	
$ 4_4\rangle$	10,777		$ 6_2\rangle$	16,621	

Table 2.5: Band origins of the members of the polyads created by $|N\nu_1\rangle$, $|(N-1)\nu_1 + 2\nu_4\rangle$, \dots , $|2N\nu_4\rangle$. All values are in cm^{-1} .

The individual members of a polyad (with integer N 's) are given by

$$|N_j\rangle = \sum_{i=0}^N c_{i,j}^N |i, 2(N-i)\rangle. \quad (2.10)$$

Table 2.6 gives the values of $c_{i,j}^N$ for $N \leq 4$.

$N = 1$	$ 1, 0\rangle$	$ 0, 2\rangle$			
$ 1_1\rangle$	0.97	-0.23			
$ 1_2\rangle$	0.23	0.97			
$N = 2$	$ 2, 0\rangle$	$ 1, 2\rangle$	$ 0, 4\rangle$		
$ 2_1\rangle$	0.92	-0.39	0.10		
$ 2_2\rangle$	0.40	0.83	-0.40		
$ 2_3\rangle$	0.07	0.41	0.91		
$N = 3$	$ 3, 0\rangle$	$ 2, 2\rangle$	$ 1, 4\rangle$	$ 0, 6\rangle$	
$ 3_1\rangle$	0.77	-0.57	0.27	-0.08	
$ 3_2\rangle$	0.61	0.53	-0.55	0.22	
$ 3_3\rangle$	0.18	0.60	0.58	-0.52	
$ 3_4\rangle$	0.03	0.18	0.54	0.82	
$N = 4$	$ 4, 0\rangle$	$ 3, 2\rangle$	$ 2, 4\rangle$	$ 1, 6\rangle$	$ 0, 8\rangle$
$ 4_1\rangle$	-0.48	0.64	-0.52	0.27	0.09
$ 4_2\rangle$	0.78	0.03	-0.46	0.39	-0.16
$ 4_3\rangle$	0.39	0.66	0.11	-0.55	0.33
$ 4_4\rangle$	0.10	0.38	0.64	0.31	-0.58
$ 4_5\rangle$	0.01	0.09	0.30	0.61	0.72

Table 2.6: Values of $c_{N,j}^i$ defined in equation 2.10 for $^{12}\text{CF}_3\text{H}$ (there are very small differences between the two isotopomers).

The integrated band strengths of the ν_1 fundamental and its overtones are given in table 2.7.

N	$G / (\text{pm}^2)^{[a]}$	$G / (10^{-24} \text{ cm}^2 \text{ cm}^{-1})^{[b]}$
1 ₂	0.0063 ± 0.002	
1 ₁	0.132 ± 0.02	
2 ₂	(1.3 ± 0.3) · 10 ⁻⁴	
2 ₁	(2 ± 0.4) · 10 ⁻⁴	
3 ₃	{0.2 · 10 ⁻⁵ }	
3 ₂	{2.6 · 10 ⁻⁵ }	
3 ₁	(3 ± 1) · 10 ⁻⁵	
4 ₃	{0.6 · 10 ⁻⁶ }	
4 ₂	(2.4 ± 1) · 10 ⁻⁶	
4 ₁	{0.6 · 10 ⁻⁶ }	
5 ₄	[8.8 · 10 ⁻⁹]	1.2
5 ₃	[1.0 · 10 ⁻⁷]	13.9
5 ₂	[7.1 · 10 ⁻⁸]	~10
5 ₁	[8.4 · 10 ⁻⁹]	1.2
6 ₄	[8.6 · 10 ⁻⁹]	1.4
6 ₃	[1.8 · 10 ⁻⁸]	3.0
6 ₂	[4.0 · 10 ⁻⁹]	0.67

Table 2.7: Integrated band strengths G . The values in square brackets are obtained by taking the values from the right column divided by the band origins (see text for explanations). Values in curly brackets have been calculated by knowing the contributions of $|v_{CH} = N\rangle$ to the individual members of a polyad (see table 2.6) and taking the experimental value of one member of the polyad. Bands, which are not mentioned, are weak with respect to other members of the polyad (but not necessarily with respect to higher overtones).

[a] From Dübäl²⁰ (definition 2.11-A)

[b] from Wong³⁴ (definition 2.11-B)

The units for the band strengths G are not the same in the two cited sources. They are

$$G = \begin{cases} \int_{band} \sigma(\tilde{\nu}) \left(\frac{d\tilde{\nu}}{\tilde{\nu}}\right) & \text{(A)} \\ \int_{band} \sigma(\tilde{\nu}) d\tilde{\nu} & \text{(B)} \end{cases} \quad (2.11)$$

The advantage of integrating over $\sigma(\tilde{\nu})/\tilde{\nu}$ is that the values can be linked directly to

basic molecular quantities, such as the transition dipole moment (see equation 2.1). A rough conversion between the two units can be done by multiplying or dividing by the band origin $\tilde{\nu}_0$.

After conversion between the two units the integral band strengths are summed over a polyad to get the transition strengths $|0\rangle \rightarrow |N, 0, \dots\rangle$ which are shown in figure 2.4. If the strength of the $|0\rangle \rightarrow |1\rangle$ absorption is normalised to 1, the strengths for the transitions to $|2\rangle, \dots, |6\rangle$ are well described by the equation

$$G(0 \rightarrow \nu_{CH} = N) = 0.56 \cdot \exp(-1.03 \cdot N) \quad (2.12)$$

using definition (A) of equation 2.11.

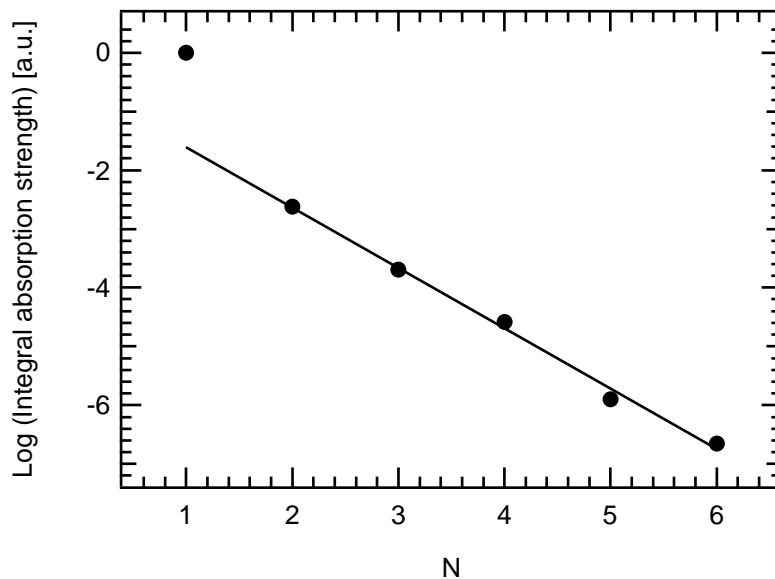


Figure 2.4: Integrated absorption strengths of $0 \rightarrow \nu_{CH} = N$.

2.1.1.E Rotational contours

Analysis of the different rovibrational fundamental bands in CF_3H have been carried out in a number of previous works. Most of the bands exhibit a relatively clean rotational structure. An exception is the ν_5 fundamental, which has received particular

attention^{4, 10, 18, 29, 35} because of Coriolis interaction with ν_2 .

CF₃H is an oblate symmetric top molecule, its rotational contour is hence (mainly) characterised by the rotational constants B and C . The rotational states are well described by the quantum numbers J and K . On a low level of accuracy the rotational levels are given by

$$F(J, K) = \nu_0(v) + B \cdot J \cdot (J + 1) + (C - B) \cdot K^2, \quad (2.13)$$

where $\nu_0(v)$ is the band origin given in equation 2.2. The rotational constants B and C depend on the vibrational excitation v . B and C can be described by

$$B = B_0 - \sum_{i=1}^6 \alpha_i^B \left(v_i + \frac{d_i}{2} \right) \quad (2.14)$$

and similarly for C where d_i is the degeneracy of vibration i (1 for $i = 1-3$, 2 for $i = 4-6$). The values of α_i^B and α_i^C have been measured²⁵ and are given in table 2.8.

	α_1	α_2	α_3	α_4	α_5	α_6
B	1.4	4.116	6.463	4.1	12.457	-1.217
C	0.4	4.7811	1.7	0.8	5.529	3.418

Table 2.8: $\alpha_i \cdot 10^3$ for B and C for CF₃H.

2.1.2 IVR

2.1.2.A Generalities about IVR

IVR^{23, 36-38} is the abbreviation for “Intramolecular Vibrational Energy Redistribution”. In a “classical” (time-resolved) picture, IVR is the process by which vibrational energy deposited in a localised vibration of the molecule redistributes over the whole system. The time-scale for the molecule to redistribute the energy is denoted as τ_{IVR} . The importance of IVR was first noticed in unimolecular reaction studies³⁹. Later, observations in experiments involving IR multiple photon dissociation⁴⁰ (IRMPD) could only be explained using the concept of rapid (\sim ps time-scale) energy redistribution from the pumped mode to the rest of the molecule. Realising the influence of IVR moderated

hopes of mode selective chemistry and opened at the same time a new field of research. The questions are: to what extent (under what conditions) and how fast does IVR take place ?

The explanation of IVR given above is clarified and formalised if one thinks about the problem in frequency space rather than in time. A narrow band laser excites a single eigenstate of the molecule which is by definition stationary. A short broadband laser however excites a coherent superposition of two or more eigenstates, which is not an eigenstate itself. In this case, the state will evolve over time. Bearing in mind that a short laser pulse corresponds to a broadband laser (and a long pulse corresponds to a narrowband laser) one immediately sees that exciting the system with a pulse with $\tau \ll \tau_{IVR}$ corresponds to a spectral width of $\Delta\nu_{laser}/hc \sim h/\tau \gg \Delta\nu/hc$ where $\Delta\nu$ is the spacing between the eigenstates.

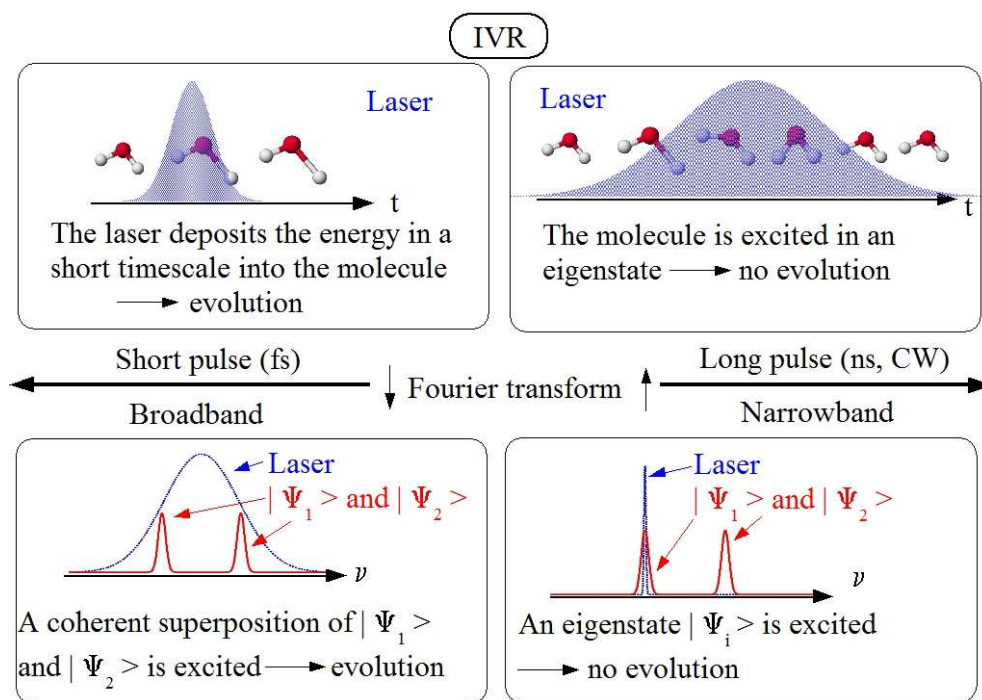


Figure 2.5: IVR

A small example shall illustrate this. Assume two states $|b\rangle$ and $|d\rangle$ where $|b\rangle$ carries

all the oscillator strength and assume them coupled forming the eigenstates

$$\begin{aligned} |\psi_0\rangle &= c_{0,0}|b\rangle + c_{1,0}|d\rangle \\ |\psi_1\rangle &= c_{0,1}|b\rangle + c_{1,1}|d\rangle \quad . \end{aligned} \quad (2.15)$$

Exciting the molecule with a short (and broad) laser pulse excites $|\Psi\rangle$ which can be expressed in terms of the eigenstates

$$|\Psi(t=0)\rangle = |b\rangle = \tilde{c}_0|\psi_0\rangle + \tilde{c}_1|\psi_1\rangle \quad (2.16)$$

and its evolution is described as

$$|\Psi(t)\rangle = \tilde{c}_0 e^{E_0 it/\hbar} |\psi_0\rangle + \tilde{c}_1 e^{E_1 it/\hbar} |\psi_1\rangle \quad (2.17)$$

and the probability of finding the molecule in its initial state is

$$\begin{aligned} P(t) &= |\langle\Psi(t)|\Psi(0)\rangle|^2 \\ &= |\tilde{c}_0|^2 e^{E_0 it/\hbar} + |\tilde{c}_1|^2 e^{E_1 it/\hbar}|^2 \\ &= |\tilde{c}_0|^4 + |\tilde{c}_1|^4 + 2|\tilde{c}_0|^2|\tilde{c}_1|^2 \cos\left(\frac{(E_0-E_1)t}{\hbar}\right) \quad . \end{aligned} \quad (2.18)$$

The state evolves and oscillates between $|b\rangle$ and a certain superposition of $|b\rangle$ and $|d\rangle$. If $|\tilde{c}_0| = |\tilde{c}_1| = 1/\sqrt{2}$ there is a complete oscillation between $|b\rangle$ and $|d\rangle$. In the case of many bath states $|d_i\rangle$ coupled to $|b\rangle$, the population in $|b\rangle$ approximately decays exponentially (the formalism gets slightly more complicated, but the mechanism stays the same).

The generalisation from the case of two coupled states $|\psi_1\rangle$ and $|\psi_2\rangle$ to multiple coupled states $|\psi_1\rangle, |\psi_2\rangle, \dots, |\psi_n\rangle$ is (at least in principle) straightforward. These states are sometimes referred to as “zeroth order states”. They are obtained neglecting the interaction terms amongst each others and only represent an approximation to the real eigenstate. The time-scale for IVR is the time during which this approximation holds well. $|\Psi_1\rangle, |\Psi_2\rangle, \dots$, the states that are obtained without neglecting the interactions between $|\psi_1\rangle, |\psi_2\rangle, \dots$, are sometimes referred to as “first order states”. If these first order states are further (weaker) coupled to other states, this gives in a similar manner rise to second order states (and so on). In this case, the first order states are good approximations to the real eigenstates during the time-scale of this second flow of energy.

This can give rise to multiple time-scales for energy flow within a molecule.

Probing IVR dynamics can be done either in time resolved or in frequency resolved experiments. Both methods should, in principle, yield the same results. In general frequency resolved measurements are preferred^{37, 38} because they contain all necessary information to investigate IVR dynamics. When performing time-resolved experiments one starts with ill-defined states which complicate the analysis considerably.

As a rule of thumb³⁸ IVR becomes important at a density of states ρ of 10-100 states / cm^{-1} . However, whether IVR at a certain energy is important or not depends on the particular experiment in question. We will illustrate this for the example of IR multiple photon excitation (IRMPE - see section 2.2). Here molecules absorb several photons and gain more and more vibrational energy. The vibrational levels at every level of excitation are mixed, but the time-scales for the energy redistribution depend on the vibrational energy; in general one can say that the higher the density of states, the shorter the time-scales on which the energy flows out of a vibrational mode to other close lying levels (although this is not strictly true). The importance of IVR depends on the time-scales of the experiment in question; in the case of IRMPE the molecule goes through energy regions with increasing density of states and will at a given energy reach a region where IVR is faster than the time-scale of the experiment. We will call this energy E_{st} . Experimental measurements with a CO_2 laser by Ryabov and coworkers show that the transition to the regime where IVR is very fast with respect to typical ns experiments is rather abrupt, i.e. E_{st} is, at least in principle, rather well defined. For small polyatomic molecules this value lies around $(5 - 8) \cdot 10^3 \text{ cm}^{-1}$. Thresholds have been determined⁴¹ for SF_6 ($(5000 \pm 500) \text{ cm}^{-1}$), CF_3Br ($(7500 \pm 300) \text{ cm}^{-1}$), CF_3I ($\leq 6000 \text{ cm}^{-1}$), CF_2HCl ($(4-5) \cdot 10^3 \text{ cm}^{-1}$) and CF_2Cl_2 ($\leq 7800 \text{ cm}^{-1}$).

Experimental studies of highly excited small polyatomic molecules over the past decade have resulted in a better comprehension of IVR at high energies. There is a general trend is that the IVR rate Γ goes up as the density of states ρ increases, but there is no monotonic dependence between the two values^{37, 38} although Fermi's Golden Rule, $\Gamma = 2\pi|\langle W \rangle|^2\rho/\hbar$, may suggest this ($|\langle W \rangle|^2$ is the square of the average coupling between the bright state and the bath states it is immersed in). As one goes up in energy

ρ is increased, at the same time $|\langle W \rangle|^2$ decreases as large changes in vibrational quantum numbers must occur between the coupled states. It turns out, that the two effects roughly cancel out.

2.1.2.B IVR in CF₃H

After the fast redistribution of energy within the C-H stretch and bend motions in CF₃H, the energy stays localised for a certain time within these vibrations before it is redistributed over the rest of the molecule. In section 2.1.1.C the fast redistribution has been discussed. The large splitting in the order of several 100's of cm⁻¹ indicates redistribution times of 30-100 fs. In order to investigate the vibrational energy redistribution out of the C-H stretch bend vibrations to the rest of the molecule, higher resolution spectra of single bands are necessary. The widths or splittings of the transition bands give information on vibrational redistribution from the first order states defined previously to second order states. In our case, the states belonging to different tiers of states are given in table 2.9.

Order of tier	States
Zeroth order	$ n_1 = 3\rangle, n_1 = 2, n_4 = 2\rangle, n_1 = 1, n_4 = 4\rangle, n_4 = 6\rangle$
First order	$3_1, 3_2, 3_3, 3_4$
Second (and higher) order	unknown

Table 2.9: Tiers of states in CF₃H

In the case of low state density, the first order state is coupled to one or few other states in its vicinity, and the redistribution occurs on time-scales of $\tau \sim 1/2\pi\Delta\nu c$ (where $\Delta\nu$ is the splitting of single peaks). In the case of coupling to a dense bath of states this time is $\tau \sim 1/2\pi\gamma c$ where γ is the half Lorentzian width of the peak after deconvolution with other broadenings (width of laser, pressure / doppler broadening, ...). This is schematically shown in figure 2.6.

In two papers^{31, 32} such spectra have been reported for some of the overtones of the C-H stretching vibration in CF₃H. Spectral simplifications have been achieved by cooling the molecules down to ~ 8 K in a jet. In some cases double resonance spectra have been

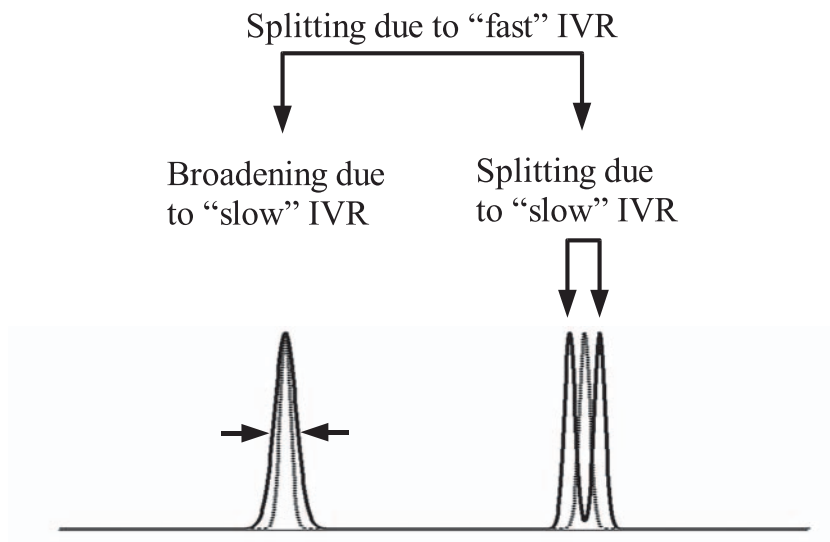


Figure 2.6: Multiple time-scales showing up in an absorption spectrum. Broadening and/or splittings of absorption features are due to IVR and inversely proportional to the time-scale τ_{IVR} . In the presence of multiple time scales there will be multiple splittings and/or broadenings as illustrated schematically.

taken to further eliminate spectral congestion due to a weak but nevertheless present K dependence of the spectral lines. For double resonance experiments, the results presented in table 2.10 have been measured for the lifetime of the stretch-bend first order state (table II from Boyarkin³¹, 5_3 from Boyarkin³²).

Note that because all measured widths are maximum values, which may potentially be a convolution with other (underestimated) broadenings, the calculated lifetimes τ are lower limits. The interesting feature about these values is that the coupling of a certain vibration to the rest of the molecular vibrations does not directly correlate with the density of states, ρ , which becomes clear for the 4_1 and 4_2 bands where ρ is roughly constant - the coupling and hence the energy flow to the rest of the molecule however depends on specific (and accidental) low order resonances.

A theoretical work on IVR in CF_3H has recently been published by Iung⁴² where the energy flow out of the $v_{CH} = 1, 2, 3, 4$ vibrational states has been studied for short time-scales, up to ~ 8 ps. We show in figure 2.7 the computed energy flow out of the

Band	τ_{sr} [ps] ^[a]	τ_{dr} [ps] ^[b]
3 ₂	88	
3 ₁ ^[c]	130	
3 ₁	88	
4 ₂	3.3	15
4 ₁	48 ^[d]	88
5 ₃ ^[e]	2-5	
5 ₂	4.4	13

Table 2.10: “Slow” IVR in CF₃H.

[a] From single resonance experiments.

[b] From double resonance experiments.

[c] in ¹³CF₃H.

[d] by an estimation of the inhomogeneous contribution to the linewidth the authors finally find a value for $\tau_{SR} \sim 90$ ps, which corresponds well to the value measured by double resonance.

[e] there is an oscillation between 5₃ and another (unidentified) zeroth order state with $\tau \sim 4 - 5$ ps and they are coupled to a continuum of bath states with $\tau \sim 1.7 - 2$ ps.

CH stretch vibration to the rest of the molecule for a molecule initially in the $v_1 = 3$ state. The time-scale for IVR lies in the ps region. Note however that this finding is not supported by experiments^{31, 32}.

2.1.2.C Collision-induced IVR

The depopulation of an excited C-H stretch ν_{CH} in CF₃H due to collisions has been studied and presented in several papers by the group of Ryabov^{41, 43-46}. They excite the molecules with a short (ps) laser with a bandwidth of $\Delta \sim 30$ cm⁻¹ to $v_1 = 1$ ($\sim 3,000$ cm⁻¹) and probe the number of molecules still in this state after a time-delay Δt by spontaneous Raman scattering (RS) with a laser beam at 532 nm.

In their first papers^{43, 44} they state that the number of molecules with $\nu_{CH} = 1$ decreases very fast after excitation. The depopulation follows an exponential law and its

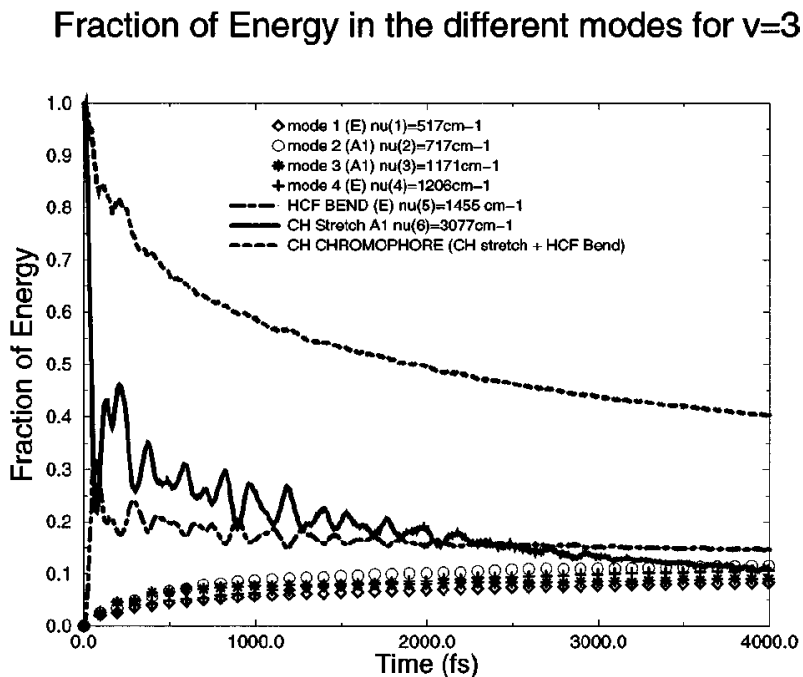


Figure 2.7: Calculated redistribution of vibrational energy in a CF_3H molecule initially in the $v_1 = 3$ state⁴².

— ν_1 , - - - ν_4 , - - - CH chromophore, bullets: other modes.

There is an initial fast energy flow from ν_1 to ν_4 , and from there to the rest of the molecule on the time-scale of $\sim 1\text{ps}$.

Reproduced from Iung⁴² (figure 2).

rate of $1.67 \cdot 10^7 \text{ s}^{-1} \text{ torr}^{-1}$ exceeds the gas kinetic rate by a factor of ~ 1.5 . This means that it necessitates on average 0.7 collisions for the loss of one quantum in ν_{CH} which is unexpectedly low: non-resonant V-V' energy transfer necessitates in general at least 10 collisions, resonant V-V energy transfer typically requires a couple of collisions⁴⁷. Later^{45, 46} the relaxation experiments were performed with buffer gases (He, Kr, Xe, N_2 , SO_2 , H_2S) where any V-V or V-V' energy transfer can be excluded. Neither can the loss of energy in the excited mode ν_{CH} be attributed to IVR of the isolated molecule.

This decrease of the average population of $v_1 = 1$ has been attributed to “Collision-induced IVR” (CI-IVR), i.e. the presence of another molecule or atom perturbs the molecule in such a way that rapid IVR is initiated. Formal considerations can also be

found in the literature^{48, 49}.

2.2 IR multiple photon dissociation (IRMPD)

In this section we discuss IR multiple photon dissociation (IRMPD). First, we give a brief historical overview about IRMPD, then we qualitatively describe different aspects of IRMPD, and finally we give a quantitative description based on a statistical treatment.

2.2.1 Some history

Infrared multiple photon dissociation (IRMPD) is a key feature of the method we employ for the isotope separation process. First observations⁵⁰⁻⁵³ of MPD were carried out in the 1960's on NH_3 , SF_6 , hydrocarbons, Br_2 or BCl_3 in the presence of collisions between the molecules. This was a direct consequence of the development of powerful CW CO_2 lasers in the 9.2 - 10.8 μm (920-1090 cm^{-1}) region. All authors suggested that collisions during IRMPD inducing rotational relaxation were necessary for the whole process to be efficient. The argumentation was that for molecules to be pumped up to the dissociation threshold, each step required a different wavelength if no change in rotational quantum numbers due to collisions occurs between the absorption steps.

Later, in 1974, it was found independently by two research groups that IRMPD can also be efficient under collision-less conditions^{54, 55}. Explanations of why IRMPD is so efficient in collision-less conditions exist⁵⁶ although finer details are still missing up to date.

The first observation of isotopically selective dissociation was made in 1974 on BCl_3 ⁵⁷ and was confirmed later for other molecules such as SF_6 , CCl_4 or OsO_4 . A plethora of studies on IRMPD of small molecules and isotopic selectivity has been published because of the possibility of using this method for molecular laser isotope separation (MLIS) on an industrial scale.

2.2.2 Qualitative description

In general a qualitative image where IRMPD of ground state molecules is composed by two distinct steps is widely accepted^{40, 58}. This image is depicted in figure 2.8.

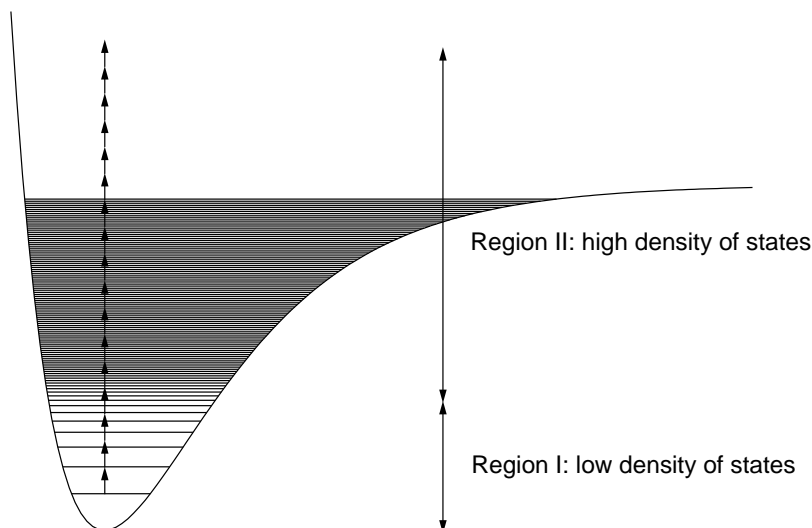


Figure 2.8: While a molecule undergoes IRMPD it is pumped through two qualitatively distinct regions. In region I the density of states (DOS) is low and the absorption has a resonant character, in region II the DOS is high and the absorption is not very wavelength sensitive any more.

The first steps, starting in the ground state of the molecule and leading up to a certain stochastic limit (see comment on page 36), is the natural bottleneck for IRMPD, because the molecule exhibits a relatively low density of states (DOS) in this region, which gives IR absorption a resonant character (region I in figure 2.8). For CF_3H we estimate this limit to be around $E_{st} \sim 7000 \text{ cm}^{-1}$. The individual steps through the energy region with low DOS have different efficiencies because the frequencies with the highest absorption cross-section shift upon excitation of the molecule due to anharmonicity. This bottleneck can be overcome with high power laser pulses which cause substantial power broadening.

The subsequent steps of IRMPD happen in what is called the “vibrational quasi-

continuum” (region II in figure 2.8). It is not a continuum in the strict sense, but the DOS is sufficiently high, that there is always a resonant transition within the bandwidth of the dissociating laser. This is because states that are close in energy mix strongly. Because of this strong mixing there is a broadening of the absorption spectra (see section 5.1.1) which makes pumping through this region relatively easy.

2.2.3 Quantitative description

We have previously described IRMPD on a qualitative level. In this section we will describe it quantitatively. First, we give a brief overview regarding the possibility of finding an exact solution and then describe a simplified approach based on a statistical treatment.

2.2.3.A Exact problem and approximate solutions

We are interested in knowing the evolution of a molecule in the presence of an external electromagnetic field \vec{E} . The wavefunction $|\psi\rangle$ is the solution of the time-dependent Schrödinger equation

$$i\hbar\frac{\partial}{\partial t}|\psi\rangle = H|\psi\rangle, \quad (2.19)$$

where H is the Hamiltonian composed of H_{mol} (Hamiltonian of the isolated molecule) and H_{int} (interaction with the electromagnetic field). The interaction term is given by

$$H_{int} = -\vec{d} \cdot \vec{E}, \quad (2.20)$$

where \vec{d} is the electric dipole moment of the molecule and \vec{E} is the external electric field. It is clear that in general numerical, let alone analytical solutions of the Schrödinger equation are difficult to find.

There are some approximations that can be made to simplify the problem. One can use Floquet’s theorem⁵⁹ with which the problem can be separated to a time-dependent and a time-independent part. A “weak field quasi-resonant approximation” (WFQA) allows further simplification of the problem.

There are, in principle, two problems associated with these approaches. First, the

molecular Hamiltonian is in most cases unknown. Secondly, even if we knew the Hamiltonian, there is a problem of computing power: the number of coupled equations grows enormously with the number of atoms, and an exact solution can be done on reasonable time-scales only for diatomics or at most triatomics.

In our case we will mainly deal with vibrationally hot polyatomic molecules. These molecules have internal energies high enough for them to be well distributed over all molecular vibrations, i.e. IVR is complete. At these energies, the molecules have a statistical behaviour, and we can make some simplifications which we present in the next section.

2.2.3.B Statistical treatment

The molecule we are interested in, CF_3H , has five atoms and cannot be treated by the equations and approximations cited previously, because the number of coupled states gets enormous (CF_3H has $\sim 3 \cdot 10^6$ vibrational states below the dissociation limit which is at $\sim 24,000 \text{ cm}^{-1}$). It is hence unthinkable to treat such a system even with the most powerful computing force on reasonable time-scales.

(I) General ideas

We base our ideas on the following statistical treatment formulated by Martin Quack⁶⁰⁻⁷². A good summary of the development of the theory of a statistical treatment can be found in a review by Letokhov⁷³. In this treatment, vibrational states with similar energies are binned together into “grained” energy states with a certain width Δ . The vibrational states lose their identity and now are simply represented by their bin number I (small letters i, j, \dots refer to the individual vibrational levels and capital letters I, J, \dots refer to the grained levels). In other words, the state of a molecule is not characterised by its wavefunction or by quantum numbers but by the total energy E . All members of bin I are populated with the same probability if the molecule has an energy that falls into this bin. In the presence of absorption or stimulated emission of a photon, the population of the different bins will change due to up- and down-pumping. Formulae, which will be presented below, have been developed^{60, 63} in order to calculate the population and depopulation rates of the bins. Figure 2.9 shows the basic idea of a statistical treatment.

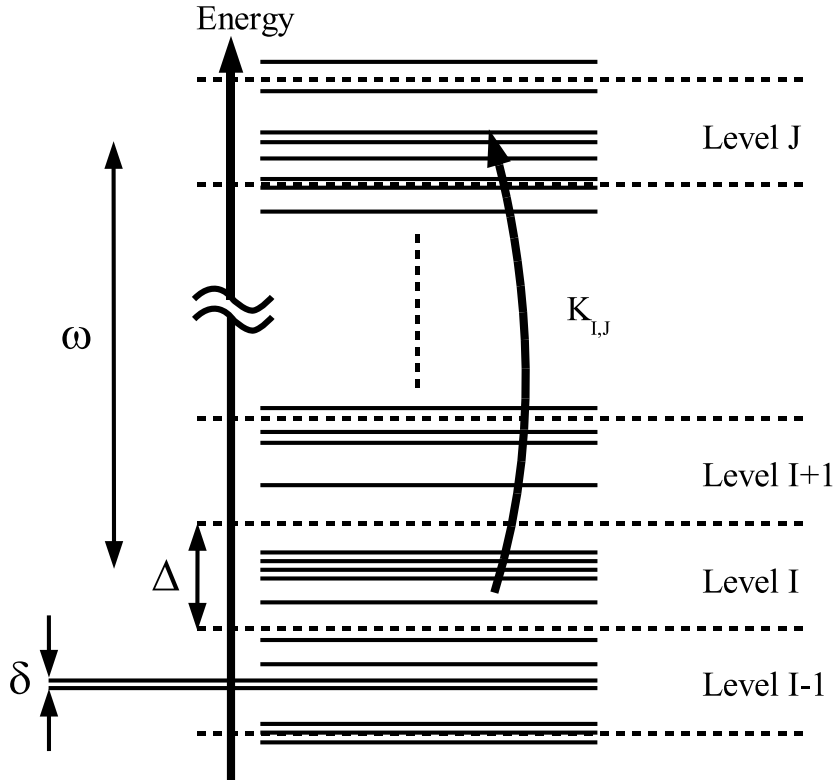


Figure 2.9: Basic idea of the statistical treatment: close lying levels are binned into grained levels $0, 1, \dots, I-1, I, I+1, \dots, J, \dots$. The populations $p_I(t)$ of the grained levels reflect the number of molecules having a certain corresponding energy. $K_{I,J}$ is the transition rate between level I and level J . In general J denotes the upper and I the lower level.

We will not present the entire development of the formulae. For this the reader is referred to the original literature^{60, 63}. Parts will be explained in appendix A. The notations presented in table 2.11 will be used.

Depending on the average density of states $\rho = 1/\delta$ in the bins I and J and the average coupling between them, four different cases can be distinguished in which large simplifications can be done:

Case A: Pumping from a single level to a set of different uncoupled levels.

Notation used		
Δ_I	-	width of a grained level I
δ_I	-	average spacing between vibrational levels in bin I
$ V $	-	average coupling between lower and upper vibrational levels $ V := \sqrt{\langle V_{J,I} ^2 \rangle}$
ω	-	energy of photon
$p_I(t)$	-	population of level I
$K_{X,Y}$	-	transition rate from level X to level Y

Table 2.11: Notation used for the statistical treatment (see also fig 2.9).

Case B: Pumping between sets of levels that are coupled amongst each other through the laser field.

Case C: Pumping between sets of levels that are uncoupled amongst each other (within a bin). The only coupling is due to the radiation field between single states of the upper and the lower bin; this radiation is not strong enough to couple states within a bin.

Case D: Pumping between sets of levels that are coupled amongst each other (within a bin) with a very high power laser.

Table 2.12 summarises the conditions and pumping rates for the four different cases.

	Case A	Case B	Case C	Case D
$K_{I,J}$	$2\pi \frac{ V ^2}{\delta_J}$	$2\pi \frac{ V ^2}{\delta_J}$	$2\pi \frac{ V ^2}{\delta_J}$	$\alpha\pi\sqrt{ V ^2}^{[a]}$
$\frac{K_{I,J}}{K_{J,I}}$	∞	$\frac{\delta_I}{\delta_J}$	$\left(\frac{\delta_I}{\delta_J}\right) \left(\frac{\pi\sqrt{3} V }{2\delta_J}\right)^{[b]}$	$1^{[b]}$
Dependence on the initial distribution of population ?	No	No	Yes	Yes
Conditions ^[c]	$\delta_I > V > \delta_J$	$\Delta > V > \delta$	$ V > \delta > \omega$	$ V > \Delta$
Typical $I^{[d]}$		high	low	ultrahigh
Typical $\rho^{[d]}$		high	low	high
Typical $\Gamma^{[d]}$		large		small

Table 2.12: Pumping rates for the different cases A-D. I refers to the lower level and J refers to the upper level.

[a] Approximate result with $1 \leq \alpha \leq 2$.

[b] These results apply only if the initial population of the upper level is zero ($p_J(0) = 0$).

[c] These conditions are slightly simplified, thus allowing for a better physical understanding of the different regimes.

[d] I = intensity of IR laser; ρ = density of states; Γ = width of absorption feature.

Only cases B and C (and to a certain extent case A) are of a practical importance for use. Case D refers to very high laser intensities, which are in general not reached. We include this case for completeness. The difference between cases B and C concerns the coupling of the vibrational states within one grained level: in case B they are considered to be strongly mixed amongst themselves whereas in case C they are independent levels.

In case B both the up- and down-pumping rates are linear functions of the laser intensity I ($\propto |V|^2$). In case C the down-pumping rate is proportional to the square root of the laser intensity, which introduces non-linearities in IRMPD, which have been well confirmed by experiments⁷⁴⁻⁷⁸. In general case B refers to regions where the DOS is relatively large, whereas case C applies to regions with sparse level distributions. Applied to IRMPD of a ground state molecule this means that in a first step case A has to be applied, then for some steps case C and as soon as the DOS gets high enough case B applies.

The IRMPD process can hence be subdivided into two energy ranges[‡] which have already been illustrated in figure 2.8. In what follows, we will show how to evaluate the pumping rates $K_{I,J}$.

(II) Up-pumping

The given formulae in table 2.12 can be, at least in principle, connected to molecular (spectroscopic) properties or otherwise calculable quantities⁶¹. For our needs, we essentially have to evaluate $2\pi|V|^2/\delta_J$ for the up-pumping rates.

The average coupling $|V|$ is not well characterised. Its square is given by

$$\langle |V_{J,I}|^2 \rangle = \frac{1}{N_I N_J} \sum_{i=1}^{N_I} \sum_{j=1}^{N_J} |V_{i,j}|^2, \quad (2.21)$$

where N_I and N_J are the total number of vibrational states in the respective bins. They are given by

[‡]Sometimes authors include a third regime at very high energies where unimolecular dissociation happens. We consider this to be a separate problem.

$$\begin{aligned} N_I &= \Delta_I \rho_I \\ N_J &= \Delta_J \rho_J \quad . \end{aligned} \quad (2.22)$$

One assumes that only one vibration, ν_p , will absorb quanta of the IR laser. At low energies the bulk transitions are made from states with $\nu_p = 0$. Transitions from $\nu_p > 0$ can be neglected⁶¹ because there are only few of them. There are hence n_I states in bin I that can absorb one quantum in ν_p , with

$$n_I = \Delta_I \rho'_I, \quad (2.23)$$

where ρ'_I is the density of states, where the pumped mode ν_p is not considered, i.e. set to 0. Moreover, the transition strength between two individual states is considered to be constant and equal to the transition for $|0\rangle \rightarrow |\nu_p = 1\rangle$, i.e.

$$|V_{i,j}|^2 = |V_{0,1}|^2 \propto G \cdot I, \quad (2.24)$$

where G is the integral absorption intensity of the pumped mode (which can be measured experimentally) and I is the intensity of the laser. Using equations 2.21-2.24 and with $\Delta = \Delta_I = \Delta_J$ we get

$$\begin{aligned} \langle |V_{I,J}|^2 \rangle &= \frac{n_I}{N_I N_J} |V_{0,1}|^2 \\ &\propto \frac{G \cdot I}{\Delta} \frac{\rho'_I}{\rho_I \rho_J} \quad . \end{aligned} \quad (2.25)$$

With the values given for the pumping constant $K_{I,J}$ given in table 2.12 and given that per definition $\rho = 1/\delta$ we finally get

$$K_{I,J} = \tilde{C} \cdot 2\pi \left(\frac{G \cdot I}{\Delta} \right) \left(\frac{\rho'_I}{\rho_I} \right) \quad (2.26)$$

for the cases A, B and C. The multiplicative constant \tilde{C} has been evaluated and the final relation reads⁷⁴:

$$K_{I,J} = 1.511 \cdot \frac{(G/pm^2) (I/MW cm^{-2}) \rho'_I}{(\Delta/cm^{-1}) \rho_I}, \quad (2.27)$$

where G and I are experimentally accessible values, and ρ and ρ' are easily estimated with a simple computer programme. Δ is a fitting parameter⁷⁴.

(III) Down-pumping

For the numerical simulations the up-pumping rate constants $K_{I,J}$ are calculated as described above. The down-pumping rate constants $K_{J,I}^B$ and $K_{J,I}^C$ are evaluated for cases B and C using the ratio $K_{I,J}/K_{J,I}$ given in table 2.12, and the larger of the two values is taken:

$$K_{J,I} = \max\{K_{J,I}^B, K_{J,I}^C\} \quad (2.28)$$

It is clear that the transition between the two regimes should in principle take place in a slightly smoother way. However, as the evaluation of $K_{J,I}^B$ and $K_{J,I}^C$ involves some approximations which include errors just as large as this one, any smoother connection between cases B and C is not a real improvement⁶³.

We can now draw a clearer image of how the up and down-pumping behaves as a function of the energy stored in the molecule and the laser intensity. At higher energies (case B) the up- and down-pumping rates are roughly the same (up-pumping is slightly faster), at lower energies (case C) the down-pumping gets faster than up-pumping which makes it difficult for molecules to be pumped through that region (molecules having absorbed a photon have a large probability to re-emit it again through stimulated emission, but there is a small, but finite probability that it re-absorbs a next photon before that, and so on). The energy separating the two regimes B and C decreases as the laser intensity is increased. This is shown in figure 2.10.

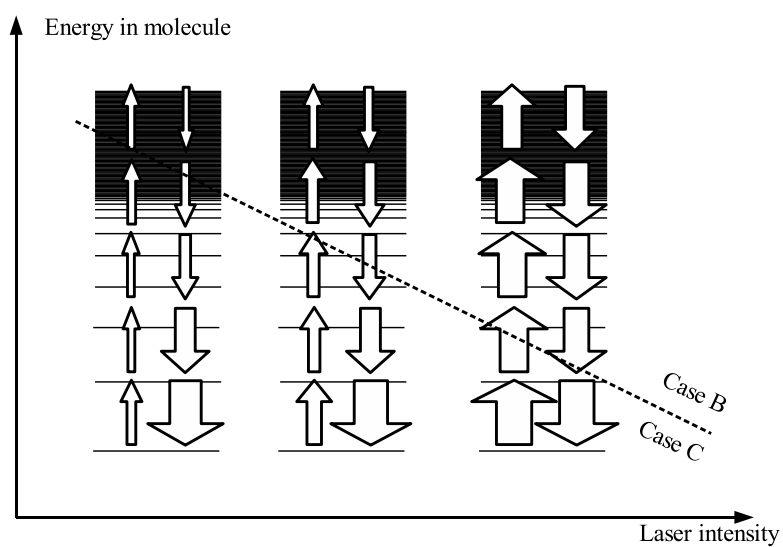


Figure 2.10: Behaviour of up- and down-pumping rates between different bins. The width of the arrows indicates the strength of the pumping. As the laser intensity goes up the limit between the case B and the case C regions drops.

2.3 Collisional vibrational relaxation

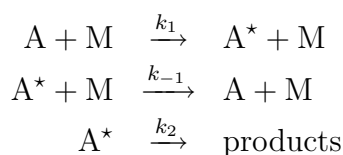
In this section we present some background information on collisional vibrational energy transfer (CVET). This subject was extensively studied in the past and the main ideas are outlined in a few excellent reviews^{47, 79–89}.

The interest in VET is ultimately driven by the fact that such events have an influence on the chemical or unimolecular reactivity of (excited) molecular species. An encounter of two molecules with a successful transfer of energy will most probably (but not necessarily) decrease this reactivity of the molecule. Furthermore, as far as chemical and unimolecular reactions are concerned, the vibrational energy is more important than rotational, electronic or translational energy, because the breaking and making of chemical bonds is also controlled by the relative motions of the atoms. As a lot of these chemical or unimolecular reactivities happen in the electronic ground state, most of the experiments over the past 100 years were concentrated on this electronic state.

We first give a brief overview of the history of collisional energy transfer (CET, see section 2.3.1). Then we describe two fundamentally different mechanisms for CET, called “hard” and “soft” collisions, where different interaction forces intervene (section 2.3.2). We continue in section 2.3.3 by giving some current views on CET. We finish by describing isotopic influences on CET in section 2.3.4.

2.3.1 A historical overview of collisional energy transfer

The very first experimental observations related to collisional energy transfer (CET) go back to the 1920’s. Information on CET was obtained mainly from studies on unimolecular dissociation processes. In 1922 Lindemann⁹⁰ pointed out for the first time that CET may play an important role in unimolecular dissociation processes. He proposed a simple three-step mechanism:



where A is the reactant molecule and M is a collision partner. Using the predicted

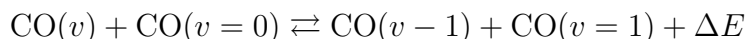
pressure dependent expression for the unimolecular dissociation k_{uni} , he could estimate the values for k_1 , k_{-1} and k_2 . Later, in 1926, Hinshelwood⁹¹⁻⁹³ introduced an energy dependence into k_1 and in 1927/28 Rice, Ramsperger and Kassel introduced an energy dependence in k_2 (which gave rise to the RRK theory⁹⁴⁻⁹⁶, see also section 5.3.3.C).

First experiments directly related to V-V energy transfer (i.e. not related to unimolecular dissociation) were performed in the 1960's. Callear showed that the rate of vibrational relaxation of nitric oxide (NO) by other molecules (N₂, CO) is sensitively dependent on the energy mismatch ΔE , where, for example⁹⁷,



In the period between 1967-1970 a number of shock tube experiments were performed in order to examine V-V energy processes in simple molecules (e.g. CO + NO, N/N₂ + CO, CO + O₂, N₂ + O₂), in particular their temperature dependence.

Smith^{98, 99} carried out experiments where they produced CO in a O + CS → CO($v = 4-13$) + S reaction and measured relaxation rates of



All of these experiments were interpreted in terms of an earlier developed theory by Schwartz, Slawsky and Herzfeld (the SSH-theory¹⁰⁰, see section 2.3.2). In particular, this theory predicted an increase of the vibrational energy transfer (VET) probability as the temperature increases. In a lot of the experiments, SSH theory could describe the results reasonably well. However, some experiments yielded contradictory results. One of the first examples involved VET from excited CO₂ to N₂. An inverse dependence has been measured by Rosser¹⁰¹ in these experiments for temperatures below 1000 K. At the same time new theories based on dipole-dipole interactions mediating VET were developed by Mahan¹⁰² which explained the observed discrepancies between experiment and theory (see section 2.3.2).

Experimentally, the bulk of the work before the mid 1960's was done by the use of ultrasonic (sound propagation and loss) and shock tube experiments or on unimolecular

dissociation experiments. When powerful lasers were invented and introduced into the field in 1966, the impact on research on VET was at least remarkable. By using lasers as experimental tools, researchers were for the first time able to evaluate the V-V energy transfer mechanisms more directly, and the respective roles of long-range and short-range interaction forces (see section 2.3.2) could be evaluated for a number of physical systems (see for example references 26-66 of Flynn, Parmenter and Wodtke⁸⁵).

In the mid 1970's the study on vibrational energy transfer became an increasingly growing research area. In particular, infrared fluorescence (IRF) and ultraviolet absorption (UVA) techniques contributed largely to progress. Vibrational relaxation rates have been measured by different techniques for small and low vibrationally excited molecules, such as for example CH₃F, C₆H₆, SF₆, HF, CO, CD₃H, CH₄, ONF, NO, C₁₀H₈, O₂, N₂, C₆H₆, CF₃I, N₂. Later, vibrational relaxation of highly excited molecules were measured for different molecules and relaxation partners. Multiquantum energy transfer¹⁰³ ($\Delta v > 1$) has also been investigated. The role of vibration to rotation (V-R) energy transfer has been studied closer, such as the respective influences of short and long-range interactions and the temperature on VET. Finally, a lot of energy has been put into the calculation of VET rates using trajectory calculations.

2.3.2 Soft and hard collisions: theoretical models

As we pointed out in the previous section, some theoretical models for V-V energy transfer had been suggested in the 1950's and 1960's. Basically two theories have been developed based on two different mechanisms, each one being able to explain certain experimental results. In the first case, the repulsive part of the interaction potential V between two molecules mediates VET, in the second case it is the interaction of the dipole moments of two molecules that mediates VET. In the first case, there must be a close encounter of two molecules so that the two molecules feel the repulsive part of V . The trajectory of the molecules change because they cannot occupy the same place in space and at the same time vibrational energy is exchanged. For this reason such collisions are called "hard" collisions and VET is mediated by short-range interactions. VET due to dipole-dipole interactions does not necessitate such close encounters, and, in general, their trajectories can be considered to be straight lines. For this reason, these

collisions are called “soft” collisions and VET is mediated by long-range interactions.

In the following two subsections we will give some background about the development of the two theories.

2.3.2.A Hard collisions

Here we present some simple theory related to VET, which is due to the repulsive part of the interaction potential of two colliding molecules⁴⁷. First theories were formulated in 1952 by Schwartz, Slawsky and Herzfeld¹⁰⁰ for the case of relatively large energy mismatches (SSH-theory). Later the case of small energy mismatches and the resonant case have been solved by Rapp¹⁰⁴.

The model used is very simple and it is depicted in figure 2.11. A linear encounter of two diatomic molecules A-B and C-D is considered.

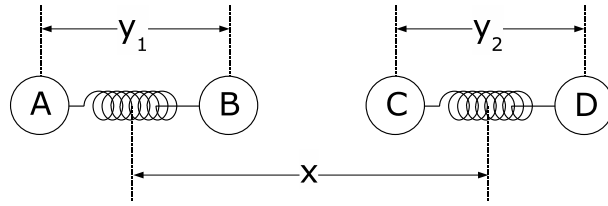


Figure 2.11: Model for hard collisions.

Considering only the repulsive part of the interaction potential of the two molecules, and further considering only the interaction between the closest atoms (B and C in figure 2.11), the interaction potential can be written as

$$\begin{aligned}
 V &= V_0 \cdot \exp\left(-\frac{x - \gamma_1 y_1 - \gamma_2 y_2}{L}\right) \\
 &= V_0 \cdot \underbrace{\exp\left(-\frac{x - \gamma_1 y_{10} - \gamma_2 y_{20}}{L}\right)}_{(I)} \cdot \underbrace{\exp\left(-\frac{\gamma_1 (y_{10} - y_1)}{L}\right) \cdot \exp\left(-\frac{\gamma_2 (y_{20} - y_2)}{L}\right)}_{(II)},
 \end{aligned} \tag{2.29}$$

where $\gamma_i = \partial \Delta x_i / \partial y_i$ ($i = 1, 2$), L is a parameter describing the steepness of the interaction and y_{i0} ($i = 1, 2$) are the equilibrium values for y_i . Part (I) is then treated in a

classical way. The expressions $(y_{i0} - y_i)$ in part (II) are described by quantum states between which transitions may take place. This can be solved to yield⁴⁷ the transition probability P_{if}

$$P_{if} = \frac{1}{\hbar^2} |U_{if}|^2 \mu^2 4\Delta\omega^2 \pi^2 L^4 \cosh(\pi\Delta\omega L/v), \quad (2.30)$$

where μ is the reduced mass, $\Delta\omega$ is the energy mismatch in the energy transfer process, v is the relative velocity between the two molecules and

$$U_{if} = \langle f_1 | \exp(\gamma_1 L^{-1}(y_1 - y_{10})) | i_1 \rangle \langle f_2 | \exp(\gamma_2 L^{-1}(y_2 - y_{20})) | i_2 \rangle, \quad (2.31)$$

where $|i_j\rangle$ and $|f_j\rangle$ ($j = 1, 2$) are the initial and final states of the two molecules. Equation 2.31 can be solved exactly, and for equation 2.30 approximate solutions can be found for large¹⁰⁰ and small¹⁰⁴ values of $\Delta\omega$. The case of large energy mismatches (typically $\gtrsim 40 \text{ cm}^{-1}$) is known as the SSH theory (Schwartz, Slawsky and Herzfeld).

The theory we presented here applies to colliding diatomic molecules. The SSH theory was generalised to polyatomic molecules by Tanczos¹⁰⁵ in 1956.

2.3.2.B Soft collisions

Long-range interactions can also mediate vibrational energy transfer. The general expression for the transition probability P_{if} in the first-order perturbation theory gives¹⁰⁶

$$P_{if} = \frac{1}{\hbar^2} \left| \int_{-\infty}^{\infty} V_{if}(t) \exp(i\Delta\omega t) dt \right|^2, \quad (2.32)$$

where

$$V_{if}(t) = \langle i | V(t) | f \rangle. \quad (2.33)$$

Let us have a look at the interaction between the two dipoles d_1 and d_2 :

$$V(t) = -\frac{d_1 d_2}{r(t)^3} \cdot \underbrace{(-2 \cos \theta_1 \cos \theta_2 + \sin \theta_1 \sin \theta_2 \cos(\phi_2 - \phi_1))}_{\star}, \quad (2.34)$$

where d_1 and d_2 are the dipole moments of the two colliding molecules, r is the distance between the two molecules and θ_i and ϕ_i ($i = 1, 2$) describe the orientation of the

dipoles in space. If the dipole moments d_1 and d_2 are constants with respect to the vibrational coordinates, then the transition probability P_{if} is clearly zero. However, it is well known that the charge distribution within the molecule changes with the normal vibrational coordinates Q_i :

$$d \approx d_0 + \sum_i \left(\frac{\partial d}{\partial Q_i} \right)_0 Q_i + \dots \quad (2.35)$$

This way

$$\langle i | d_1 d_2 | f \rangle \approx \langle i_1 | Q_1 | f_1 \rangle \left(\frac{\partial d_1}{\partial Q_1} \right)_0 \langle i_2 | Q_2 | f_2 \rangle \left(\frac{\partial d_2}{\partial Q_2} \right)_0, \quad (2.36)$$

where $|i_j\rangle$ and $|f_j\rangle$ ($j = 1, 2$) are the initial and final states of the two colliding molecules, d_1 and d_2 their dipole moments and Q_1 and Q_2 the vibrational coordinates involved in the energy transfer process. The values $\langle 0 | Q_i | 1 \rangle (\partial d_i / \partial Q_i)_0$ can be linked to the integrated absorption intensity of the concerned particular band in the IR spectrum (see equation 2.1) and $\langle i | Q_i | f \rangle$ can be related¹⁰⁷ to $\langle 0 | Q_i | 1 \rangle$ (see also equation 5.4 on page 156).

For the moment we can omit the angular dependence of V and replace the starred expression in equation 2.34 by a scaling factor. Different authors suggest different values for this factor: Mahan¹⁰² first proposed $\frac{1}{\sqrt{6}}$, later Stephenson and Moore¹⁰⁸ used $\frac{1}{3}$. We write

$$V_{if}(t) = \frac{C}{r(t)^3}, \quad (2.37)$$

where C includes the angular dependence and $\langle i | d_1 d_2 | f \rangle$.

In a next step, a straight line trajectory of the relative motion of the molecules is assumed:

$$r(t) = \sqrt{r_0^2 + (vt)^2}, \quad (2.38)$$

where r_0 is the minimum distance of the two molecules (the so-called ‘‘impact parameter’’) and v the relative velocity. It can be shown⁴⁷, that with such a trajectory and with

the interaction potential described in equation 2.37, the transition probability defined in equation 2.32 is evaluated as follows:

$$P(r_0, v) = \left(\frac{C|(2\Delta\omega/r_0v^2)K_1(r_0\Delta\omega/v)|}{\hbar} \right)^2, \quad (2.39)$$

where K_1 is a modified Bessel function. For small values of $\Delta\omega$, this Bessel function can be readily approximated by

$$K_1\left(\frac{r_0\Delta\omega}{v}\right) \approx \frac{v}{r_0\Delta\omega}, \quad (2.40)$$

which simplifies equation 2.39 to

$$P(r_0, v) \approx \frac{4C^2}{\hbar^2 r_0^4 v^2}, \quad (2.41)$$

which needs to be adequately averaged over r_0 and v .

A problem arises through the fact that $P(r_0, v)$ diverges for small values of r_0 and v . Different authors have proposed different approaches to deal with this difficulty, which we present below. For this, we define the parameters r_c and r_{hs} as follows:

$$\begin{aligned} P(r_c, v) &= \frac{1}{2} \\ r_{hs} &= \text{hard sphere radius} \end{aligned} \quad (2.42)$$

Note that r_c depends on v . Table 2.13 summarises the different approaches to deal with the problem of divergence.

With these expressions for $P(r_0, v)$ the cross-section $\sigma(v)$ for two colliding molecules with a relative velocity v can be evaluated by averaging over r_0 , and the average transition probability $\langle\langle P \rangle\rangle$ can also be evaluated by averaging $\sigma(v)$ over v with a Boltzmann speed distribution.

$$\begin{aligned} \sigma(v) &:= 2\pi \int_0^\infty r_0 P(r_0, v) dr_0 = 2\pi\sqrt{2}C/\hbar v \\ \langle\langle P \rangle\rangle &:= \langle\sigma v\rangle/\pi d^2\langle v \rangle \end{aligned} \quad (2.43)$$

The functional dependencies of $\sigma(v)$ and $\langle\langle P \rangle\rangle(T)$ where T is the temperature are given in table 2.14.

Author	$P(r_0, v)$
(A) Mahan ¹⁰² (1967)	$P(r_0, v) = \begin{cases} 4C^2/\hbar^2 r_0^4 v^2 & (r_0 \geq r_c) \\ 1/2 & (r_0 < r_c) \end{cases}$
(B) Sharma and Brau ^{109–111} (1967)	$P(r_0, v) = \begin{cases} 4C^2/\hbar^2 r_0^4 v^2 & (r_0 \geq r_{hs}) \\ 4C^2/\hbar^2 r_{hs}^4 v^2 & (r_0 < r_{hs}) \end{cases}$
(C) Stephenson, Wood and Moore ^{108, 112} (1968)	$P(r_0, v) = \begin{cases} 1/2 & (r_c \geq r_{hs}, r_0) \\ 4C^2/\hbar^2 r_0^4 v^2 & (r_0 \geq r_c, r_{hs}) \\ 4C^2/\hbar^2 r_{hs}^4 v^2 & (r_{hs} \geq r_0, r_c) \end{cases}$

Table 2.13: Three approaches how to deal with the problem of the divergence of $P(r_0, v)$. The model proposed in (C) is a combination of (A) and (B).

Model	$\sigma(v)$	$\langle\langle P \rangle\rangle$
(A)	$\sigma(v) \propto 1/v$	$\langle\langle P \rangle\rangle \propto 1/\sqrt{T}$
(B)	$\sigma(v) \propto 1/v^2$	$\langle\langle P \rangle\rangle \propto 1/T$
(C)	$\sigma(v) \propto \begin{cases} 1/v & (v < 2\sqrt{2}C/\hbar d^2) \\ 1/v^2 & (v \geq 2\sqrt{2}C/\hbar d^2) \end{cases}$	$\langle\langle P \rangle\rangle \propto \text{erf}\left(2C\sqrt{\mu}/\hbar d^2\sqrt{kT}\right)$

Table 2.14: Dependence of σ on the relative velocity of the two molecules and of $\langle\langle P \rangle\rangle$ on the temperature T , for the different models.

These formulae can be generalised to non-resonant cases ($\Delta\omega \neq 0$). The modified Bessel function in equation 2.39 can be approximated by

$$K_1\left(\frac{r_0\Delta\omega}{v}\right) \approx \sqrt{\frac{\pi v}{2r_0\Delta\omega}} \exp\left(-\frac{r_0\Delta\omega}{v}\right) \quad (2.44)$$

for large values of $\Delta\omega$. Going through similar reasoning as previously for the resonant case, one can calculate⁴⁷, using the Sharma-Brau cut-off criteria:

$$\begin{aligned} \sigma(v) &\propto v^{-3} \exp(-2d\Delta\omega/v) \\ \ln\langle\langle P \rangle\rangle &\propto \Delta\omega^{2/3} \\ \ln\langle\langle P \rangle\rangle &\propto T^{-1/3} \end{aligned} \quad (2.45)$$

Note, in particular, that for low velocities $\sigma(v)$ first increases with increasing velocity, and drops only later.

All these theories have been developed in the absence of any rotational contributions.

These contributions have also been included later^{108, 113–115}, but will not be presented in detail here.

This theory applies only to weakly excited small molecules, where the vibrational spectrum is discrete and the calculations of the transition probabilities reduce to the problem of the excitation of an oscillator, or the problem of transitions in a two-level system or in a system of two weakly interacting oscillators. In highly excited polyatomic molecules however, the density of states of the vibrational spectrum becomes very large and the time-scale of IVR can become smaller than the one of the collisional process. Vibrational energy transfer mediated by long-range dipole-dipole interactions becomes very important in such cases. The theory for vibrational energy transfer mediated by dipole-dipole interactions has been generalised to strongly excited polyatomic molecules^{116–118}. The transition rate W in the case of two molecules A and B with respective transition dipole moments $\mu_A := \langle f_A | d_A | i_A \rangle$ and $\mu_B := \langle f_B | d_B | i_B \rangle$ (where d_X is the dipole moment and $|i_X\rangle$ and $|f_X\rangle$ are the initial and final states of the molecule X) and a distance R_{AB} is proportional to:

$$W \propto R_{AB}^{-3} \int_0^{\infty} F_A(\omega) F_B(\omega) \frac{d\omega}{\omega} \mu_A^2 \mu_B^2, \quad (2.46)$$

where F_A and F_B are the absorption spectra of the two molecules in the region of interest (the vibrational band mediating vibrational energy transfer) normalised to unity, i.e. $\int_{band} F_x(\omega) d\omega = 1$.

More complete information on VET probabilities can be gained in trajectory calculations, although they do not necessarily permit a lot of physical insight into the process. In such calculations the Schrödinger or Hamilton equation has to be integrated. For diatomic, at best triatomic molecules, such calculations are readily done, for larger molecules they become more difficult. In particular, the results depend very much on the potential energy surface (PES) chosen, so basically any experimental result can be reproduced by adequately tweaking the PES.

2.3.2.C Joint action of soft and hard collisions

There is a qualitative difference between soft and hard collisions as far as the temperature dependence of the transition rate is concerned. Soft collisions get less efficient as the temperature rises (table 2.14) as opposed to hard collisions which get more efficient with increasing temperature (equation 2.30). This is physically reasonable. Increasing the relative velocity v in the case of head-on collisions results in the two molecules coming closer in the repulsive part of the interaction potential, which increases their interaction and the transition probability. In the case of soft collisions, higher relative velocities decrease the time the two molecules are interacting and hence decreases the transition probability.

Although the exact temperature dependence cannot be evaluated (as it depends on the applied model), it helps to evaluate the nature of VET in particular cases. If the vibrational relaxation rates increase with temperature, VET through short-range interactions prevail and vice versa. In general one would expect that at lower temperatures long-range interactions are more important than short-range interactions, at higher temperatures the opposite is the case. One of the first examples of such a behaviour was published in 1969 by Taylor¹¹⁹ which we reproduce in figure 2.12.

2.3.3 Current views on collisional energy transfer

In this section we will give some information on vibrational energy transfer of excited molecules. In the first subsection, we will focus on large and medium-sized molecules, and the second subsection is devoted to small molecules.

2.3.3.A Vibrational energy transfer of medium-sized or large, highly excited molecules

(I) Energy loss probability $P(E, E')$

Here, we will concentrate on a function $P(E, E')$ which describes the probability that an excited molecule at an energy E' will find itself at an energy E after a collision. This function $P(E, E')$ is nowadays often used to describe how efficient bath molecules or

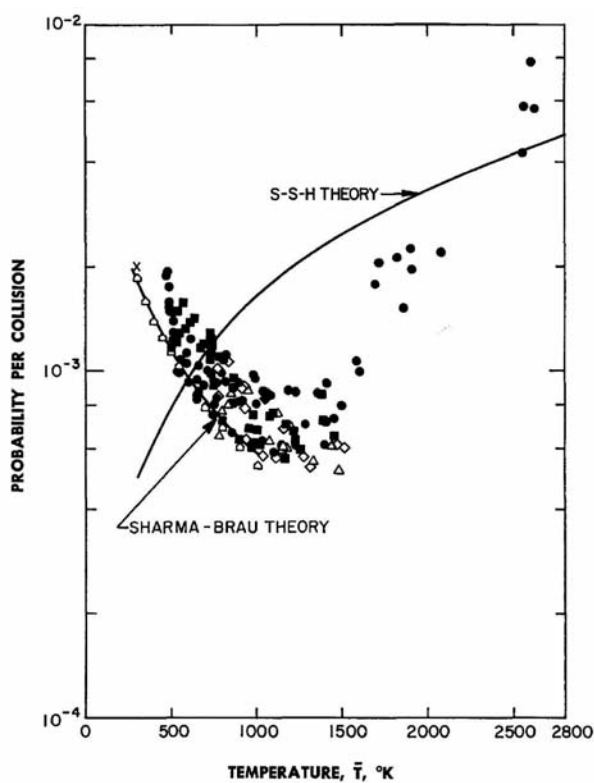


Figure 2.12: Experimental data (bullets) demonstrating the dependency of the probability of energy transfer between an excited CO_2 molecule and an N_2 molecule in the ground state under the effects of long-range ($T \lesssim 1000$ K) and short-range ($T \gtrsim 1000$ K) interaction forces. The solid lines show the values calculated with the SSH and the Sharma-Brau theories.

Reproduced from Taylor¹¹⁹ (figure 6).

atoms can relax an excited parent molecule. Note that here vibrational relaxation can imply not only V-V relaxation, but also V-T,R relaxation.

Strictly speaking, $P(E, E')$ cannot be defined the way we have done it here, as it implies a strict definition of what a collision means and when it occurs (molecules encountering each other at a large relative distance can still exchange energy via long-range dipole-dipole interactions). One sometimes *defines* the collision number⁸⁴ Z_{hs} :

$$Z_{hs} := \sqrt{\frac{8k_B T}{\pi\mu}} \pi d_{hs}^2, \quad (2.47)$$

where k_B is the Boltzmann constant, T is the temperature of the sample, μ is the reduced mass of the pair of colliding molecules and d_{hs} is a reasonably chosen hard sphere (geometrical) diameter of the molecule. This way, $P(E, E')$ will be defined as

$$P(E, E') := \frac{R(E, E')}{Z_{hs}}, \quad (2.48)$$

where $R(E, E')$ is the number of occurrences per unit time where a molecule at an energy E' loses $E' - E$ of energy (the dimension of R is 1/time).

However, for convenience, $P(E, E')$ is often defined such that

$$\int_0^{\infty} P(E, E') dE = 1. \quad (2.49)$$

If we denote the population density of molecules at an energy E' as $y(E', t)$ (in the vibrational quasicontinuum), then the evolution of y is defined by

$$\frac{dy(E', t)}{dt} dE' = \int_0^{\infty} dE (R(E', E) dE' y(E, t) - R(E, E') dE' y(E', t)) + \dots, \quad (2.50)$$

where the dots “...” denote any further terms which may change the population distribution such as a source term (initial excitation), pumping due to IR absorption or emission, dissociation, etc.

For practical purposes, in general one *assumes* a certain functional dependence of R on E and E' and fits any parameters of this function so that the net results coincide with experimental data.

Often the following “exponential step-size distribution” is chosen to model such VET. It turns out that this model can be often used for the description of VET on monoatomic bath gases:

$$P(E, E') = \frac{1}{N(E')} \exp\left(-\frac{E' - E}{\alpha}\right), \quad (2.51)$$

where $N(E')$ is a normalisation constant and α is a fitting parameter. Sometimes collisions in which the excited molecule gains energy (i.e. $E > E'$) are taken into account with the same expression, but a different value of α .

Other distributions for $P(E, E')$ exist but are either much more complicated without necessarily giving additional physical insight (e.g. “biased random walk”, BRW¹²⁰ or an “impulsive ergodic collision theory”) or are physically unreasonable (e.g. “strong collision model”, $P(E, E') = f(E)$). We do not present these models in further depth; they can be found in the literature⁸⁴.

An important value characterising $P(E, E')$ is the average energy transfer for a molecule at an energy E' :

$$\langle \Delta E(E') \rangle = \frac{\int_0^{E'} (E' - E) P(E, E') dE}{\int_0^{E'} P(E, E') dE} \quad (2.52)$$

Some experimental findings regarding $\langle \Delta E(E') \rangle$ are listed below:

- $\langle \Delta E(E') \rangle$ increases as the number of atoms in bath gas increase^{82, 83, 121, 122}
- In general $\langle \Delta E(E') \rangle$ is a linear function of E' (with a factor of proportionality b)^{85, 86, 122}. It might have an offset a which may be positive or negative:

$$\langle \Delta E(E') \rangle = a + b \cdot E' \quad (2.53)$$

We show in figure 2.13 a figure by Hold¹²³ to illustrate this point.

(II) Quantum state resolved energy loss probabilities

There is an increasing interest in measuring not only the total energy transferred in a

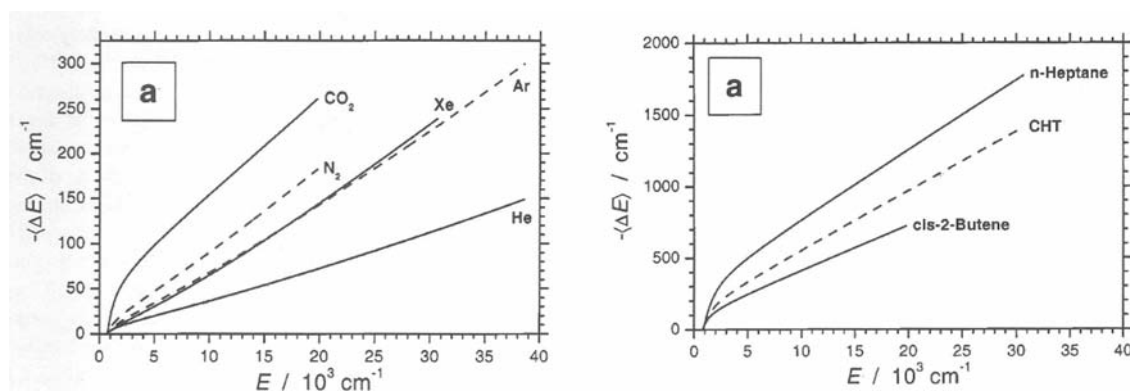


Figure 2.13: Average energy transferred $\langle \Delta E \rangle$ in a collision of excited azulene at an energy E , for different bath gas molecules.

Reproduced from Hold¹²³ (figures 18(a) and 19(a)).

collision, but also more detailed information on the final states of the excited molecules after a collision. However, the high density of states of the excited molecule makes such studies rather difficult. Some experimental tools exist with the ability to separate the energy transfer processes into vibrational, rotational and translation degrees of freedom.

Basically, these techniques comprise following steps: vibrational excitation of molecules of an arbitrary complexity, their relaxation in a bath gas B, and finally probing the quantum state of the bath gas produced by the interaction with the excited molecules. The mechanism of energy transfer can be “seen through the eyes of the acceptor molecule B”. For example, VET studies of C_6F_6 excited up to $\sim 40,000 \text{ cm}^{-1}$ relaxing on ground state CO_2 have been performed using this approach¹²⁴. Approximately 2300 cm^{-1} of ro-vibrational energy is transferred in each collision. The CO_2 molecule makes changes of its quantum state from $(00^0_0, J', V')$ to $(00^0_1, J, V)$ where the first v_1, v_2^x, v_3 are vibrational and J and V are rotational quantum numbers which can be probed individually. Also the translational energies could be measured. In this particular experiment, it was found that the rotational and translational energies were near thermal, which indicates that there is little V-T,R energy transfer. This shows that here VET is mainly mediated by long-range interactions.

Alternatively, large molecules can be only weakly excited (one or two quanta of vi-

brational excitation) up to energies where the vibrational states can be described by a set of quantum numbers, and adequately probing the final states^{48, 125}. The drawback of such experiments is that the molecules are not at chemically significant energies, but physical insight can still be gained.

(III) Supercollisions

Supercollisions¹²⁶ are a curiosity amongst collisional relaxation. They are encounters of two molecules, where an astonishingly large amount of vibrational energy, say, for example 10^4 cm^{-1} , is transferred. In general, only a negligible number of collisions (typically less than one per cent) result in a supercollision. A lot of experimental and theoretical work has been directed towards studying supercollisions.

2.3.3.B Vibrational energy transfer of small molecules

Small molecules (diatomics, triatomics) can be well described by quantum numbers up to high energies. The preparation of the excited states is either done by direct overtone pumping¹²⁷ or stimulated emission pumping (SEP)¹²⁸. The detection of the excited states can be done by different methods, for example by photoacoustics, overtone fluorescence, infrared double-resonant absorption, optothermal methods or IRLAPS. The study of vibrational relaxation of very small molecules is interesting because it can be compared with calculations, which is difficult, if not impossible, in the case of large molecules.

Early experiments on small molecules^{47, 100, 129} revealed some general trends of *low* excited small molecules:

1. Light collision partners quench molecules faster than heavier molecules.
2. The temperature dependence of V-T,R energy transfer (hard collisions) was found to be positive, i.e. the higher the temperature, the larger is the energy transfer probability. For V-V energy transfer (soft collisions), the inverse is observed.
3. Theory predicted that for vibrationally excited molecules single quantum energy transfer ($\Delta v = 1$) prevails.

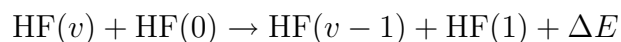
4. Furthermore, theory predicted that V-T,R energy transfer scales with the vibrational quantum number v of the donor molecule.

As experiments on highly excited small molecules became possible, a lot of similarities, but also some differences could be observed:

1. In some experiments performed on I_2 molecules excited up to $v = 42$ and on NO molecules excited up to $v = 23$, it was found that lighter collision partners relax the excited molecules more efficiently than heavier relaxation partners.
2. Not a lot of temperature dependency measurements have been performed for highly excited molecules, but the few of them point in the same direction as for low excited molecules. For example, V-T,R self-relaxation of O_2 molecules excited up to $v = 26$ has found to have a positive temperature dependence¹³⁰, and near resonant V-V energy transfer between excited O_2 ($v = 17$) and CO_2 and N_2O shows an inverse temperature dependence¹³¹.
3. Experiments on highly excited I_2 and NO molecules¹³² showed that single quantum energy transfer was the preferred relaxation channel.
4. In some experiments on NO ¹³³ a linear dependence of the V-T,R relaxation has been measured as predicted ($k(v) = v \cdot k(1)$).

There are some fundamental differences between the relaxation of low excited and highly excited small molecules.

Whereas in low excited molecules the V-T,R energy transfer is the dominating vibrational relaxation pathway, it was found that for highly excited molecules V-V self-relaxation due to long range dipole-dipole interaction can become more important. First experiments on this were performed on highly excited HF where the following collisional process was studied:



It was found that the relaxation rate goes through a maximum at $v = 2$ and decreases for higher overtones because ΔE grows larger due to anharmonicity, which shifts the

absorption spectra. Similar results were obtained for other molecules, for example in the case of self-relaxation of NO. The relaxation of low energy molecules on surrounding bath molecules is in general not resonant, and if so, only by accident. For example N_2 ($v = 1 \rightarrow 0$) is accidentally in resonance with CO_2 ($v_3 = 0 \rightarrow 1$). As the energy lost by giving away one quantum in a vibrational mode moves smoothly due to anharmonicity as the initial quantum number increases, there will be a certain vibrational excitation where this energy loss corresponds to the energy gained by the bath gas molecules by absorbing a vibrational quantum.

This will be explained using the example of O_2 relaxing on CO_2 . O_2 has received a particular attention due to its importance in atmospheric physics. We show in figure 2.14 a measurement of the relaxation rate of excited O_2 on ground state N_2 .

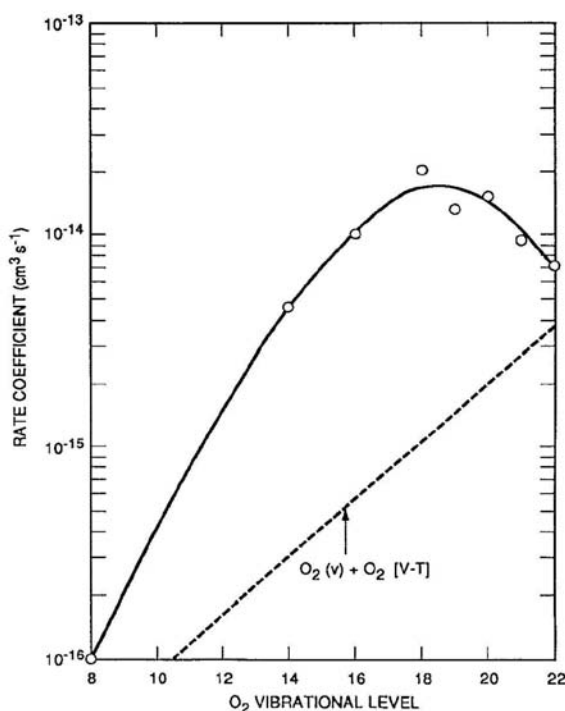
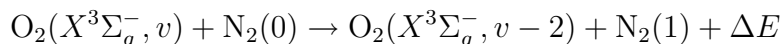


Figure 2.14: Example of the dependence of the vibrational relaxation rate on the vibrational excitation, for the case of excited O_2 relaxing on N_2 (\circ). The relaxation rate goes through a maximum at $v \approx 18 - 19$.

Reproduced from Park and Slanger¹³⁴ (figure 9).

Figure 2.14 shows a clear peak for $v \approx 18 - 19$. This is because the energy mismatch ΔE for the process



goes through a minimum for this excitation level. This is an example of a 2-1 resonance, but the principle is the same as for 1-1 resonances. Different functional dependencies of the relaxation rates on the energy mismatch have been proposed and measured. For example, in the case of relaxation of excited CO on ground state CO, a roughly gaussian dependence has been observed¹³⁵.

Other differences between low and highly excited molecules can be observed, for example vibration to electronic (V-E) energy transfer or collision-induced dissociation (for example $\text{NO}_2(v) + \text{CO} \rightarrow \text{NO} + \text{O} + \text{CO}$).

2.3.4 Isotopic influences on collisional relaxation

As we have pointed out in the previous section, the efficiency of vibrational energy transfer depends largely on the energy mismatch of the emission and absorption of a quantum in the two colliding molecules. We demonstrated this by the example of O_2 relaxing on N_2 (see figure 2.14). If the energy mismatch plays an important role for the relaxation rates, one can expect that there should be some influences upon isotopic substitution of an atom in one of the two colliding molecules, as this changes the vibrational frequencies and hence the energy mismatch.

Isotopic influences on collisional relaxation rates have been observed as early as the late 1960's. For example, Stephenson, Wood and Moore¹¹² reported isotopically selective relaxation rates for excited $^{12}\text{C}^{16}\text{O}_2(00^01)$ on ground state $^{12}\text{C}^{16}\text{O}^{18}\text{O}$ and $^{13}\text{C}^{16}\text{O}_2$ (with roughly a factor of 2 between the relaxation rates) and on ground state $^{14}\text{N}_2\text{O}$ and $^{15}\text{N}_2\text{O}$ (with roughly a factor of 10 between the relaxation rates), which could be explained by the different energy mismatches. Similarly, isotopically selective relaxation of N_2O on N_2O^{136} , CO on CO^{137} and CO on $\text{N}_2^{138-141}$ has been found. We show in figure 2.15 a graph indicating different relaxation rates and their temperature dependence for different isotopic partners for $\text{CO}^*\text{-CO}$ and $\text{CO}^*\text{-N}_2$ collisions (where the starred

molecule is the excited one).

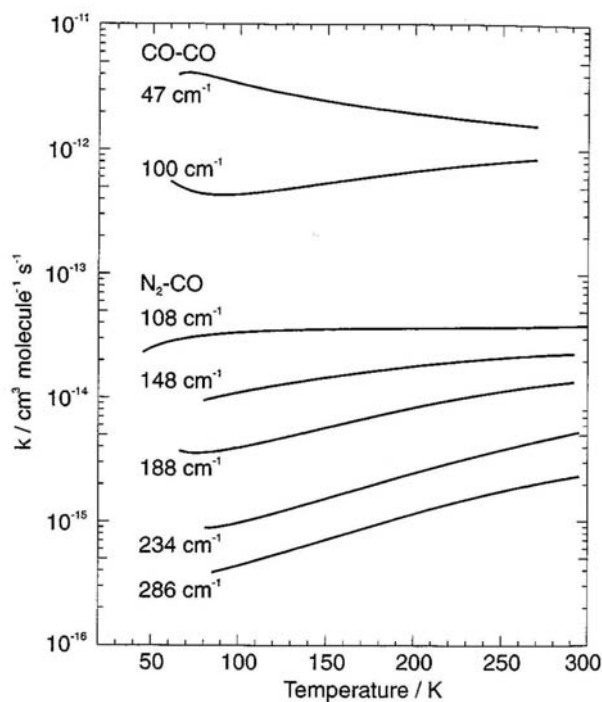


Figure 2.15: Temperature dependency for $\text{CO}(00^01)+\text{CO}(00^00) \rightarrow \text{CO}(00^00)+\text{CO}(00^01)$ and for $\text{CO}(00^01)+\text{N}_2(v=0) \rightarrow \text{CO}(00^00)+\text{N}_2(v=1)$ collisions. The values in the figure indicate the energy mismatch for the particular collision. From top to bottom:

- ▶ $^{12}\text{C}^{16}\text{O}-^{13}\text{C}^{16}\text{O}$, $^{12}\text{C}^{16}\text{O}-^{13}\text{C}^{18}\text{O}$.
- ▶ $^{12}\text{C}^{16}\text{O}-^{15}\text{N}_2$, $^{12}\text{C}^{16}\text{O}-^{14}\text{N}^{15}\text{N}$, $^{12}\text{C}^{16}\text{O}-^{14}\text{N}_2$, $^{13}\text{C}^{16}\text{O}-^{14}\text{N}_2$, $^{12}\text{C}^{18}\text{O}-^{14}\text{N}_2$.

Reproduced from Turnidge¹³⁷ (figure (3)).

On the figure different qualitative behaviours can be observed for the temperature dependence, especially for the CO-CO relaxation. For the pair of CO molecules with $\Delta E = 47 \text{ cm}^{-1}$ ($^{12}\text{C}^{16}\text{O}-^{13}\text{C}^{16}\text{O}$), the relaxation rate decreases as the temperature increases, for the other pair with $\Delta E = 100 \text{ cm}^{-1}$ ($^{12}\text{C}^{16}\text{O}-^{13}\text{C}^{18}\text{O}$) the dependence on the temperature is the other way round. This shows that for the first case resonant V-V relaxation is prevailing, whereas for the second case non-resonant V-T,R relaxation is more important. For the case of $\text{CO}^*\text{-N}_2$ collisions, all dependencies are positive, so V-T,R is always the fastest energy transfer channel. Good qualitative agreements between the

experimental data and calculations for CO-CO collisions have been found by Coletti¹⁴².

Information about the influence of isotopic substitution on the relaxation rates of medium-sized or large molecules is rather sparse^{143, 144} and it is concentrated on effects of deuteration of molecules. In a set of calculations it has been found that the relaxation of excited azulene ($C_{10}H_8$) on Xenon and Helium does not exhibit an appreciable difference upon isotopic substitutions of the hydrogen atoms in the excited azulene¹⁴⁴. Experiments with excited toluene and excited benzene show that the relaxation on buffer gas is roughly the same for the different isotopic species¹⁴³. In two out of twenty cases, excited toluene relaxing on ground state D_2 and on ground state D_2O , there seems to be a difference of up to 25% in the relaxation rates upon deuteration of the excited species. However no uncertainties are given for the measured values, so we are not sure whether this difference is significant.

The only observation of a relatively strong influence of the isotopic composition on the relaxation rate is given in a paper by Toselli¹⁴³. They report that the average energy $\langle\langle\Delta E\rangle\rangle$ transferred per collision between an excited and a ground state regular benzene molecule is twice as high as in the case of deuterated benzene relaxing on deuterated benzene. The same applies to normal and deuterated toluene. Figure 2.16 shows their results.

We are very astonished about their finding, because it seems to us that there is no reason why self-relaxation should be significantly different for normal and deuterated molecules. The authors themselves write that these differences may be artifacts and have to be further investigated. As we have not found any other papers confirming these measurements, we may assume that it finally indeed turned out to be errors in their measurements.

Any other publications we found on the collisional relaxation of excited medium-sized molecules such as CH_3F ¹⁴⁵ or CF_3I ¹⁴⁶ do not reveal any isotopic selectivity in the collisional relaxation rates neither.

To sum up, it can be said that clear evidence of isotopically selective relaxation rates

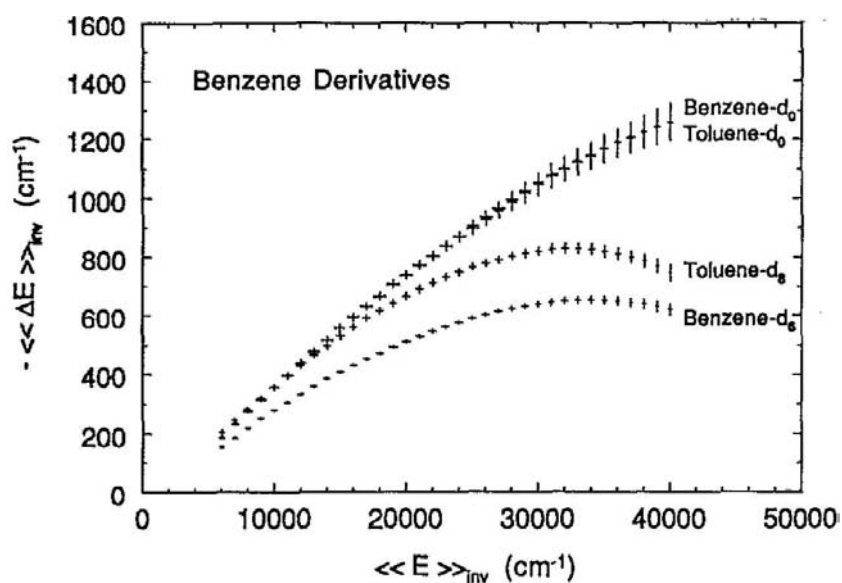


Figure 2.16: Average energy $\langle\langle\Delta E\rangle\rangle$ transferred between an excited molecule and the same unexcited species.

Reproduced from Toselli¹⁴³ (figure 1).

exists for small molecules (diatomics and triatomics), but from the literature it is not at all clear that larger molecules should exhibit the same phenomenon. One would expect little, if at all, isotopic influence on vibrational relaxation, because the density of vibrational states of larger polyatomic molecules is very large and hence mixed. Because of this extensive mixing, the donor and the acceptor molecules can always find a resonant pathway for collisional vibrational energy transfer. We have not found any other works on isotopically selective collisional relaxation of polyatomics since that publication in 1992.

Bibliography

- [1] O. V. Boyarkin, M. Kowalczyk, and T. R. Rizzo. Collisionally Enhanced Isotopic Selectivity in Multiphoton Dissociation of vibrationally excited CF_3H . *J. Chem. Phys.*, 118(1):93–103, 2003.
- [2] M. Lewerenz and M. Quack. Vibrational Overtone Intensities of the Isolated CH and CD Chromophores in Fluoroform and Chloroform. *Chem. Phys. Lett.*,

- 123(3):197–202, 1986.
- [3] Robert McPheat and Geoffrey Duxbury. Infrared absorption cross-sections and integrated absorption intensities of chloroform and fluoroform vapour . *J. Quant. Spectrosc. Rad. transf.*, 66:153–167, 2000.
- [4] Andreas Amrein, Martin Quack, and Ulrich Schmitt. High resolution interferometric Fourier transform infrared absorption spectroscopy in a supersonic free jet expansion - The interacting states ν_2 , ν_5 and $\nu_3 + \nu_6$ of trifluoromethane . *Molec. Phys.*, 60(1):237–248, 1987.
- [5] H. J. Bernstein and G. Herzberg. Rotation-Vibration spectra of diatomic and simple polyatomic molecules with long absorption paths. 1. The spectrum of Fluoroform (CHF_3) from 2.5μ to 0.7μ . *J. Chem. Phys.*, 16(1):30–39, 1948.
- [6] R. A. Ashby. The infrared spectrum in the regions of the fundamentals of fluoroform . *J. Molec. Spectrosc.*, 28(2):265–266, 1968.
- [7] A. Ruoff, H. Bürger, and S. Biedermann. Schwingungsspektren und Kraftkonstanten symmetrischer Kreisel - III Die IR-Spektren von HCF_3 und DCF_3 . *Spectrochimica Acta*, 27A:1359–1376, 1971.
- [8] T. E. Sullivan and L. Frenkel. Measurement of fourth order distortion constants in symmetric top molecules . *J. Molec. Spectrosc.*, 39(2):185–201, 1971.
- [9] P. Lockett and P. M. Wilt. Rotational Analysis of ν_6 of DCF_3 and $\nu_3 + \nu_6$ of HCF_3 . *J. Chem. Phys.*, 60(8):3203–3207, 1974.
- [10] N. J. Fyke, P. Lockett, J. K. Thompson, and P. M. Wilt. The Infrared Spectra of HCF_3 and DCF_3 . *J. Molec. Spectrosc.*, 58:87–101, 1975.
- [11] H. F. Chambers, R. W. Kirk, J. K. Thompson, M. J. Warner, and P. M. Wilt. The Infrared Spectrum of HC^{13}F_3 . *J. Molec. Spectrosc.*, 58:76–86, 1975.
- [12] R. W. Kirk and P. M. Wilt. General harmonic force-field of fluoroform . *J. Molec. Spectrosc.*, 58(1):102–110, 1975.
- [13] C. E. Blom and A. Müller. A study on the GVFF of CHF_3 , CH_2F_2 , and CH_3F . *J. Molec. Spectrosc.*, 70(3):449–458, 1978.

- [14] G. Graner, R. Anttila, and J. Kauppinen. High-resolution infrared spectrum of the ν_3 and ν_6 bands of HCF_3 and of their hot bands . *Mol. Phys.*, 38(1):103–128, 1979.
- [15] Shigeo Kondo and Shinnosuke Saeki. Coriolis interactions and infrared intensities in fluoroform . *J. Chem. Phys.*, 74(12):6603–6611, 1981.
- [16] Susumu Sofue, Kentarou Kawaguchi, Eizi Hirota, and Tsunetake Fujiyama. Absolute Intensity Measurements of the ν_4 Band of Fluoroform by the Use of a Tunable Diode-laser Source . *Bull. Chem. Soc. Jpn.*, 54:3546–3550, 1981.
- [17] Hans-Rolf Dübal and Martin Quack. High-Resolution IR spectrum of Fluoroform: A close Resonance . *Chem. Phys. Lett.*, 80(3):439–444, 1981.
- [18] G. Graner and G. Guelachvili. Fluoroform: the Polyad at 8-9 μm . *J. Molec. Spectrosc.*, 107:215–228, 1984.
- [19] Robert C. Weast and Melvin J. Astle, editors. *CRC Handbook of Chemistry and Physics*. CRC Press Inc., Florida, 59th edition, 1978.
- [20] Hans-Rolf Dübal and Martin Quack. Tridiagonal Fermi resonance structure in the IR spectrum of the excited CH chromophore in CF_3H . *J. Chem. Phys.*, 81(9):3779–3791, 1984.
- [21] Günter Klatt, Andrew Willetts, Nicholas C. Handy, Riccardo Tarroni, and Paolo Palmieri. An Improved Anharmonic Potential for CHF_3 . *J. Molec. Spectrosc.*, 176:64–74, 1996.
- [22] Enrico Fermi. Über den Ramaneffekt des Kohlendioxyds . *Z Phys*, 71:250–259, 1931.
- [23] Martin Quack. Spectra and Dynamics of coupled vibrations in polyatomic molecules . *Annu. Rev. Phys. Chem.*, 41:839–874, 1990.
- [24] Gerhard Herzberg. *Molecular Spectra and Molecular Structure. II. Infrared and Raman Spectra of Polyatomic Molecules*. Krieger Publishing Company: Malabar, Florida, 1991.

- [25] J. Segall, R. N. Zare, H. R. Dübal, M. Lewerenz, and M. Quack. Tridiagonal Fermi resonance structure in the IR spectrum of the excited CH chromophore in CF_3H . *J. Chem. Phys.*, 86(2):634–646, 1987.
- [26] Hans Hollenstein, Marius Lewerenz, and Martin Quack. Isotope effects in the Fermi resonance of the CH Chromophore in CHX_3 Molecules. *Chem. Phys. Lett.*, 165(2,3):175–183, 1990.
- [27] A. S. Pine, G. T. Fraser, and J. M. Pliva. Molecular beam spectrum of the highly perturbed C-H stretching region of fluoroform. *J. Chem. Phys.*, 89(5):2720–2728, 1988.
- [28] A. S. Pine and J. M. Pliva. Doppler-Limited Spectra of the C-H Bending Overtone of Fluoroform. *J. Molec. Spectrosc.*, 130:431–444, 1988.
- [29] A. Amrein, M. Quack, and U. Schmitt. High-Resolution Interferometric Fourier-Transform Infrared- Absorption Spectroscopy in Supersonic Free Jet Expansions - Carbon-Monoxide, Nitric-Oxide, Methane, Ethyne, Propyne, and Trifluoromethane. *J. Phys. Chem.*, 92(19):5455–5466, 1988.
- [30] Zhen Lin, Kirk Boraas, and James P. Reilly. The vibrational overtone spectrum of fluoroform in the $\Delta v=4$ C-H stretching region. *Chem. Phys. Lett.*, 217(3):239–244, 1994.
- [31] O. V. Boyarkin and T. R. Rizzo. Secondary time scales of intramolecular vibrational energy redistribution in CF_3H studied by vibrational overtone spectroscopy. *J. Chem. Phys.*, 105(15):6285–6292, 1996.
- [32] O. V. Boyarkin, R. D. F. Settle, and T. R. Rizzo. Vibrational Overtone Spectra of Jet-Cooled CF_3H by Infrared Laser Assisted Photofragment Spectroscopy. *Ber. Bunsenges. Phys. Chem.*, 99(3):504–513, 1995.
- [33] D. Romanini and A. Campargue. Vibrational overtone spectroscopy of the 4_1 band of CHF_3 . *Chem. Phys. Lett.*, 254:52–58, 1996.
- [34] James S. Wong, William H. Green, Chi ke Cheng, and C. Bradley Moore. Coupling of CH stretching and bending vibrations in trihalomethanes. *J. Chem. Phys.*, 86(11):5994–5999, 1987.

- [35] J. P. Champion and G. Graner. Fluoroform - A new analysis of the polyad at 8-9 μm . *Molec. Phys.*, 58(3):475–484, 1986.
- [36] David J. Nesbitt and Robert W. Field. Vibrational Energy Flow in Highly Excited Molecules: Role of Intramolecular Vibrational Redistribution . *J. Phys. Chem.*, 100:12735–12756, 1996.
- [37] K. K. Lehman, G. Scoles, and B. H. Pate. Intramolecular dynamics from eigenstate-resolved infrared spectra . *Annu. Rev. Phys. Chem.*, 45:241–274, 1994.
- [38] John Keske and Brooks H. Pate. Decoding the Dynamical Information Embedded in Highly Mixed Quantum States . *Annu. Rev. Phys. Chem.*, 51:323–353, 2000.
- [39] Izhack Oref and B. Seymour Rabinovitch. Do Highly Excited Reactive Polyatomic Molecules Behave Ergodically ? . *Acc. Chem. Res.*, 12:166–175, 1979.
- [40] C. D. Cantrell. *Multiple-Photon Excitation and Dissociation of Polyatomic Molecules*. Springer Verlag: Berlin Heidelberg New York, 1986.
- [41] A. L. Malinovsky, E. A. Ryabov, and V. S. Letokhov. Laser time-resolved Raman Spectroscopy of Mode Selectivity and Vibrational Energy Distribution for IR MP Excited Polyatomic Molecules . *Chem. Phys.*, 139:1989, 229-238.
- [42] Christophe Iung, Fabien Gatti, and Hans-Dieter Meyer. Intramolecular vibrational energy redistribution in the highly excited fluoroform molecule: A quantum mechanical study using the multiconfiguration time-dependent Hartree algorithm . *J. Chem. Phys.*, 120(15):6992–6998, 2004.
- [43] A. A. Kosterev, A. L. Malinovskii, and E. A. Ryabov. Fast vibrational relaxation of valence vibrations of the C-H bond in halogenated methane . *JETP Lett.*, 54(1):14–17, 1991.
- [44] A. A. Kosterev, A. L. Malinovsky, and E. A. Ryabov. Vibrational relaxation of C-H stretching modes in methane and its halogenated derivatives . *Chem. Phys. Lett.*, 199(3,4):349–354, 1992.
- [45] A. A. Kosterev, A. L. Malinovsky, and E. A. Ryabov. Ultrafast collisional redistribution of vibrational energy in small polyatomic molecules . *J. Molec. Struct.*, 349:231–234, 1995.

- [46] A. A. Kosterev, A. L. Malinovsky, S. A. Tretyak, and E. A. Ryabov. Ultrafast Collisional Redistribution of Vibrational Energy in Highly Excited Polyatomic Molecules. The Role of Intramolecular Interactions . *Ber. Bunsenges. Phys. Chem.*, 99:378–380, 1995.
- [47] J. T. Yardley. *Introduction to Molecular Energy Transfer*. Academic Press: New York, 1980.
- [48] Brian J. Orr. Collision-induced state-to-state energy transfer in perturbed rovibrational manifolds of small polyatomic molecules: mechanistic insights and observations. . *Chem. Phys.*, 190:261–278, 1995.
- [49] A. A. Kosterev, A. A. Makarov, A. L. Malinovsky, and E. A. Ryabov. Fast collision-induced redistribution of vibrational energy in halogenated methanes . *Chem. Phys.*, 219:305–316, 1997.
- [50] M. C. Bordé, A. Henry, and M. L. Henry. Emission du gaz ammoniac excité par le rayonnement d'un laser à gaz Carbonique . *CR Acad. Sci. B Phys.*, 262(21):1389, 1966.
- [51] M. C. Bordé, A. Henry, and M. L. Henry. Comportement de différents gaz soumis au rayonnement d'un laser à gaz Carbonique . *CR Acad. Sci. B Phys.*, 263(9):619, 1967.
- [52] N. V. Karlov, Y. N. Petrov, A. M. Prokhorov, and O. M. Atel'makh. Dissociation of Boron Trichloride Molecules by CO₂ Laser Radiation . *JETP Lett.*, 11(4):135, 1970.
- [53] W. B. Tiffany, H. W. Moos, and A. L. Schawlow. Selective Laser Photocatalysis of Bromine Reactions . *Science*, 157:40–43, 1967.
- [54] N. R. Isenor, V. Merchant, R. S. Hallsworth, and M. C. Richardson. CO₂ laser induced Dissociation of SiF₄ Molecules into electronically excited fragments . *Can. J. Phys.*, 51(12):1281–1287, 1973.
- [55] R. V. Ambartzumian, N. V. Chekalin, V. S. Doljikov, V. S. Letokhov, and E. A. Ryabov. The Visible Luminescence Kinetics of BCl₃ in the Field of a High-Power CO₂ Laser . *Chem. Phys. Lett.*, 25(4):515–518, 1974.

- [56] V. S. Letokhov and A. A. Makarov. “Leakage” effect as an Exciting Mechanism of High Vibrational Levels of Polyatomic Molecules by a Strong Quasi-Resonant Laser IR Field . *Optics Comm.*, 17(3):250–253, 1976.
- [57] R. V. Ambartzumyan, V. S. Letokhov, E. A. Ryabov, and N. V. Chekalin. Isotopic selective chemical reaction of BCl_3 molecules in a strong infrared laser field . *JETP Lett.*, 20(9):273–274, 1974.
- [58] Vladilen Stepanovic Letokhov. *Laser spectroscopy of highly vibrationally excited molecules*. Adam Hilger, Bristol and Boston, 1989.
- [59] M. G. Floquet. Sur les équations différentielles linéaires à coefficients périodiques . *Ann. Scient. Ecole Norm. Ser. 2*, 12:47–XX, 1883.
- [60] Martin Quack. Theory of unimolecular reactions induced by monochromatic infrared radiation . *J. Chem. Phys.*, 69(3):1282–1307, 1978.
- [61] Martin Quack. Master Equations for Photochemistry with Intense Infrared Light . *Ber. Bunsenges. Phys. Chem.*, 83:757–775, 1979.
- [62] Martin Quack. Master Equations for Photochemistry with Intense Infrared Light (III) The Influence of Molecular Parameters in URIMIR . *Ber. Bunsenges. Phys. Chem.*, 83:1287–1293, 1979.
- [63] Martin Quack. Master Equations for Photochemistry with Intense Infrared Light (IV). A Unified Treatment of Case B and Case C Including Nonlinear Effects . *Ber. Bunsenges. Phys. Chem.*, 85:318–330, 1981.
- [64] Martin Quack. Theory of Multiphoton Excitation . In Schleyer P. v. R.; Allinger N. L.; Clark T.; Gasteiger J.; Kollman P. A.; Schaefer III H. F.; Schreiner P. R., editor, *The Encyclopedia of Computational Chemistry*. John Wiley & Sons, Chichester, 1998.
- [65] Martin Quack. Reaction Dynamics and statistical Mechanics of the preparation of highly excited states by intense infrared Radiation . *Adv. Chem. Phys.*, 50:396–473, 1982.
- [66] Martin Quack. Infrared laser Chemistry and the dynamics of molecular multiphoton excitation . *Infrared Phys.*, 29(2-4):441–466, 1989.

- [67] Martin Quack, Emile Sutcliffe, Peter A. Hackett, and David M. Rayner. Molecular Photofragmentation with Many Infrared Photons . *Faraday Discuss. Chem. Soc.*, 82:229–240, 1986.
- [68] M. Quack and E. Sutcliffe. On the validity of the quasiresonant approximation for molecular infrared-multiphoton excitation . *J. Chem. Phys.*, 83(8):3805–3812, 1985.
- [69] Martin Quack. IR Laser Chemistry . *Infrared Phys. and Technol.*, 36:365–380, 1995.
- [70] Katharina von Puttkamer, Hans-Rolf Dübal, and Martin Quack. Time-dependent Processes in Polyatomic Molecules During and After Intense Infrared Irradiation . *Faraday Discuss. Chem. Soc.*, 75:197–210, 1983.
- [71] Donald W. Lupo and Martin Quack. IR-Laser Photochemistry . *Chem. Rev.*, 87:181–216, 1987.
- [72] Martin Quack. Photochemistry with Infrared Radiation . *Chimia*, 35(12):463–475, 1981.
- [73] Vladilen Stepanovic Letokhov. *Laser spectroscopy of highly vibrationally excited molecules*, chapter Chapter 1. Introduction to the Physics of Multiple-Photon Excitation of Vibrations in Polyatomic molecules. Adam Hilger, Bristol and Boston; ed. by V. S. Letokhov, 1989.
- [74] O. V. Boyarkin, T. R. Rizzo, D. S. Rueda, M. Quack, and G. Seyfang. Nonlinear intensity dependence in the infrared multiphoton excitation and dissociation of methanol preexcited to different energies . *J. Chem. Phys.*, 117(21):9793–9805, 2002.
- [75] E. M. Alonso, J. A. O’Neill, and L. Pateopol. Non-linear processes in the IR multiple-photon absorption of CF_3H . *J. Phys. B: At. Mol. Opt. Phys.*, 27:2217–2227, 1994.
- [76] J. A. O’Neill, L. Pateopol, and B. Pogue. Multiphoton absorption measurements in CF_3H . *J. Phys. B: At. Mol. Opt. Phys.*, 25:3335–3344, 1992.

- [77] M. Quack and G. Seyfang. Frequency-dependent non-linear intensity dependence in the IR Photochemistry of CF_3I . *Chem. Phys. Lett.*, 93(5):442–447, 1982.
- [78] R. V. Ambartzumian, N. P. Furzikov, Y. A. Gorokhov, V. S. Lethokov, G. N. Makarov, and A. A. Poretzky. Selective dissociation of SF_6 molecules in a two-frequency infrared laser field. *Optics Commun.*, 18(4):517–521, 1976.
- [79] J. D. Lambert. *Vibrational and Rotational Relaxation in Gases*. Oxford Clarendon Press, 1977.
- [80] A. B. Callear. Molecular Energy Transfer. *Annu. Rep. Prog. Chem.*, 61:48–60, 1964.
- [81] W. H. Flygare. Molecular Relaxation. *Accounts Chem. Res.*, 1(4):121–127, 1968.
- [82] D. C. Tardy and B. S. Rabinovitch. Intermolecular Vibrational Energy Transfer in Thermal Unimolecular Systems. *Chem. Rev.*, 77(3):369–408, 1977.
- [83] I. Oref and D. C. Tardy. Energy Transfer in Highly Excited Large Polyatomic Molecules. *Chem. Rev.*, 90:1407–1445, 1990.
- [84] Robert G. Gilbert. Theory of collisional energy transfer of highly excited molecules. *Int. Rev. Phys. Chem.*, 10(3):319–347, 1991.
- [85] George W. Flynn, Charles S. Parmenter, and Alec M. Wodtke. Vibrational Energy Transfer. *J. Phys. Chem.*, 100:12817–12838, 1996.
- [86] John R. Barker, Laurie M. Yoder, and Keith D. King. Vibrational Energy Transfer Modeling of Nonequilibrium Polyatomic Reaction Systems. *J. Phys. Chem. A*, 105(5):796–809, 2001.
- [87] Hai-Lung Dai. *Highly Excited Molecules*, chapter Collisional Energy Transfer of Highly Vibrationally Excited Molecules: The Role of Long-Range Interaction and Intramolecular Vibronic Coupling. ACS Symposium Series. American Chemical Society, 1996.
- [88] Ralph E. Weston and George W. Flynn. Relaxation of Molecules with Chemically Significant Amounts of Vibrational Energy: The Dawn of the Quantum State Resolved Era. *Annu. Rev. Phys. Chem.*, 43:559–589, 1992.

- [89] Robert J. Gordon. Recent Trends in Experimental Studies of Vibrational Energy Transfer . *Comments At. Mol. Phys.*, 21(3):123–151, 1988.
- [90] F. A. Lindemann, Svante Arrhenius, Irving Langmuir, N. R. Dhar, J. Perrin, and W. C. McC. Lewis. Discussion on “the radiation theory of chemical action” . *Trans. Faraday Soc.*, 17:598–606, 1922.
- [91] C. N. Hinshelwood. Quasi-Unimolecular Reactions. The Decomposition of Diethyl Ether in the Gaseous State . *Proc. Roy. Soc. London A*, 114(766):84–97, 1927.
- [92] C. N. Hinshelwood and P. J. Askey. Homogeneous Reactions Involving Complex Molecules. The Kinetics of the Decomposition of Gaseous Dimethyl Ether . *Proc. Roy. Soc. London A*, 114(770):215–226, 1927.
- [93] C. N. Hinshelwood and P. J. Askey. The Influence of Hydrogen on Two Homogeneous Reactions . *Proc. Roy. Soc. London A*, 114(773):163–170, 1927.
- [94] Oscar Knefler Rice and Herman C. Ramsperger. Theories of unimolecular gas reactions at low Pressures . *J. Am. Chem. Soc.*, 49(7):1617–1629, 1927.
- [95] Oscar Knefler Rice. The Quantum Theory of Quasi-Unimolecular Gas Reactions . *Proc. Natl. Acad. Sci. U.S.A.*, 14(2):113–118, 1928.
- [96] L. S. Kassel. Studies in Homogeneous Gas Reactions. II. Introduction of Quantum Theory . *J. Phys. Chem.*, 32(7):1065–1079, 1928.
- [97] A. B. Callear. Vibrational relaxation of Nitric Oxide . *Discuss. Faraday Soc.*, 33:33–36, 1962.
- [98] G. Hancock and I. W. M. Smith. Quenching of infrared chemiluminescence. 1. Rates of de-excitation of CO($4 \leq v \leq 13$) by He, CO, NO, N₂, O₂, OCS, N₂O, and CO₂ . *Appl. Opt.*, 10(8):1827–1842, 1971.
- [99] C. Wittig and I. W. M. Smith. Vibrational energy transfer in carbon monoxide at low temperatures . *J. Chem. Soc. - Faraday Trans. 2*, 69:939–951, 1973.
- [100] R. N. Schwartz, Z. I. Slawsky, and K. F. Herzfeld. Calculation of Vibrational Relaxation Times in Gases . *J. Chem. Phys.*, 20(10):1591–1599, 1952.

- [101] W. A. Rosser, A. D. Wood, and E. T. Gerry. Deactivation of Vibrationally Excited Carbon Dioxide (ν_3) by Collisions with Carbon Dioxide or with Nitrogen . *J. Chem. Phys.*, 50(11):4996–5008, 1969.
- [102] Bruce H. Mahan. Resonant Transfer of Vibrational Energy in Molecular Collisions . *J. Chem. Phys.*, 46(1):98–101, 1967.
- [103] T. A. Dillon and J. C. Stephenson. Multiquantum Vibrational-Energy Exchange . *Phys. Rev. A*, 6(4):1460–1468, 1972.
- [104] Donald Rapp and Thomas Kassal. The theory of vibrational energy transfer between simple molecules in nonreactive collisions . *Chem. Rev.*, 69:61–102, 1968.
- [105] Frank I. Tanczos. Calculation of Vibrational Relaxation Times of the Chloromethanes . *J. Chem. Phys.*, 25(3):439–447, 1956.
- [106] L. D. Landau and E. M. Lifschitz. *Quantum mechanics: non-relativistic theory*. London; Pergamon Press, 1958.
- [107] S. Califano. *Vibrational States*. John Wiley and Sons, 1976.
- [108] John C. Stephenson and C. Bradley Moore. Near-Resonant Vibration \rightarrow Vibration Energy Transfer: CO_2 ($\nu_3=1$) + M \rightarrow CO_2 ($\nu_1 = 1$) + M* + ΔE . *J. Chem. Phys.*, 52(5):2333–2340, 1970.
- [109] R. D. Sharma and C. A. Brau. Near-Resonant vibrational energy transfer in N_2 - CO_2 Mixtures . *Phys. Rev. Lett.*, 19(22):1273–1275, 1967.
- [110] R. D. Sharma and C. A. Brau. Energy Transfer in Near-Resonant Molecular Collisions due to Long-Range Forces with Application to Transfer of Vibrational Energy from ν_3 Mode of CO_2 to N_2 . *J. Chem. Phys.*, 50(2):924–930, 1969.
- [111] R. D. Sharma. Vibration-to-Vibration energy transfer in CO-CO collisions . *Chem. Phys. Lett.*, 30(2):261–266, 1975.
- [112] John C. Stephenson, Robert E. Wood, and C. Bradley Moore. Near-Resonant Energy Transfer between Infrared-Active Vibrations . *J. Chem. Phys.*, 48:4790–4791, 1968.

- [113] R. D. Sharma. Near-Resonant Vibrational Energy Transfer Among Isotopes of CO_2 . *Phys. Rev.*, 177(1):102–107, 1969.
- [114] T. A. Dillon and J. C. Stephenson. Effect of the straight path approximation and exchange forces on vibrational energy transfer. *J. Chem. Phys.*, 58(9):3849–3854, 1973.
- [115] T. A. Dillon and J. C. Stephenson. Calculation of vibrational and rotational energy transfer between HF, DF, HCl, and CO_2 . *J. Chem. Phys.*, 58(5):2056–2064, 1973.
- [116] V. T. Platonenko and N. A. Sukhareva. On vibrational energy exchange between strongly excited polyatomic molecules. *Sov. Phys. JETP*, 51(6):1065–1071, 1980.
- [117] V. T. Platonenko and N. A. Sukhareva. Vibrational relaxation of strongly excited polyatomic molecules. *Sov. Phys. JETP*, 54(3):454–459, 1981.
- [118] V. M. Akulin. Singularities of collisional vibrational relaxation processes in strongly excited spectrally complex polyatomic molecules. *Sov. Phys. JETP*, 57(4):774–780, 1983.
- [119] Raymond L. Taylor and Steven Bitterman. Experimental Measurements of the Resonant Vibrational Energy Transfer between Mode ν_3 of CO_2 and N_2 . *J. Chem. Phys.*, 50(4):1720–1726, 1969.
- [120] R. G. Gilbert. Collisional Energy Transfer Exchange in Highly Vibrationally Excited Molecules - the Biased Random Walk Model. *J. Chem. Phys.*, 80(11):5501–5509, 1984.
- [121] M. Quack and J. Troe. Unimolecular reactions and energy transfer of highly excited molecules. In P.G. Ashmore and R.J. Donovan, editors, *Gas Kinetics and Energy Transfer 2*. The Chemical Society London, 1977.
- [122] B. Abel, B. Herzog, H. Hippler, and J. Troe. Infrared multiphoton excitation of CF_3I . II. Collisional energy transfer of vibrationally highly excited CF_3I . *J. Chem. Phys.*, 91(2):900–905, 1989.
- [123] Uwe Hold, Thomas Lenzer, Klaus Luther, and Andrew C. Symonds. Collisional energy transfer probabilities of highly excited molecules from KCSI. III. Azulene:

- $P(E', E)$ and moments of energy transfer for energies up to 40 000 cm^{-1} via self-calibrating experiments . *J. Chem. Phys.*, 119(21):11192–11211, 2003.
- [124] Arthur J. Sedlacek, Ralph E. Weston, and George W. Flynn. Interrogating the vibrational-relaxation of highly excited polyatomics with time-resolved diode-laser spectroscopy - C_6H_6 , C_6D_6 and $\text{C}_6\text{F}_6 + \text{CO}_2$. *J. Chem. Phys.*, 94(10):6483–6490, 1991.
- [125] C. P. Bewick, J. F. Martins, and B. J. Orr. Rotationally specific mode-to-mode vibrational energy transfer in $\text{D}_2\text{CO}/\text{D}_2\text{CO}$ collisions. II. Kinetics and modelling . *J. Chem. Phys.*, 93(2):8643–8657, 1990.
- [126] S. Hassoon, I. Oref, and C. Steel. Collisional activation of quadricyclane by azulene - an example of very strong Collisions . *J. Chem. Phys.*, 89(3):1743–1744, 1988.
- [127] F. F. Crim. Selective Excitation Studies of Unimolecular Reaction Dynamics . *Annu. Rev. Phys. Chem.*, 35:657–691, 1984.
- [128] C. E. Hamilton, J. L. Kinsey, and R. W. Field. Stimulated Emission Pumping: New Methods in Spectroscopy and Molecular Dynamics . *Annu. Rev. Phys. Chem.*, 37:493–524, 1986.
- [129] R. N. Schwartz and K. F. Herzfeld. Vibrational relaxation times in gases (3-dimensional treatment) . *J. Chem. Phys.*, 22(5):767–773, 1954.
- [130] C. A. Rogaski, J. A. Mack, and A. M. Wodtke. State-to-state Rate Constants for Relaxation of Highly Vibrationally Excited O_2 and Implications for its Atmospheric Fate . *Faraday Discuss.*, 100:229–251, 1995.
- [131] J. A. Mack, K. Mikulecky, and A. M. Wodtke. Resonant vibration-vibration energy transfer between highly vibrationally excited $\text{O}_2(X^3\Sigma_g^-, v = 15 - 26)$ and CO_2 , N_2 , N_2 and O_3 . *J. Chem. Phys.*, 105(10):4105–4116, 1996.
- [132] M. L. Nowlin and M. C. Heaven. Energy transfer rate constants for highly excited rovibrational levels of $\text{I}_2(X)$. *J. Chem. Phys.*, 99(8):5654–5660, 1993.
- [133] X. Yang, J. M. Price, J. A. Mack, C. G. Morgan, C. A. Rogaski, D. McGuire, E. H. Kim, , and A. M. Wodtke. Stimulated emission pumping studies of energy

- transfer in highly vibrationally excited molecules . *J. Phys. Chem.*, 97(16):3944–3955, 1993.
- [134] H. Park and T. G. Slanger. $O_2(X, v = 8 - 22)$ 300 K quenching rate coefficients of O_2 and N_2 , and $O_2(x)$ vibrational distribution from 248 nm O_3 photodissociation . *J. Chem. Phys.*, 100(1):287–300, 1994.
- [135] H. T. Powell. Vibrational relaxation of carbon monoxide using a pulse discharge. II. $T = 100, 300, 500$ K . *J. Chem. Phys.*, 63(6):2635–2645, 1975.
- [136] L. Doyennette, M. Margottin-Maclou, A. Chakroun, H. Gueguen, , and L. Henry. Vibrational energy transfer from the (00^0_1) level of $^{14}N_2O$ and $^{12}CO_2$ to the $(m, n^l, 1)$ levels of these molecules and of their isotopic species . *J. Chem. Phys.*, 62(2):440–447, 1975.
- [137] M. L. Turnidge, J. P. Reid, P. W. Barnes, and C. J. S. M. Simpson. Vibrational energy transfer between the isotopomers of carbon monoxide at low temperatures . *J. Chem. Phys.*, 108(2):485–491, 1998.
- [138] D. C. Allen and C. J. S. M. Simpson. Vibrational energy exchange between CO and the isotopes of N_2 between 300 K and 80 K . *Chem. Phys.*, 45(2):171–334, 1980.
- [139] E. T. Chandler, E. A. Gregory, R. M. Siddles, and C. J. S. M. Simpson. Vibrational energy exchange between $CO(v=1)$ and $^{14}N_2$ and $CO(v=1)$ and $^{15}N_2$ measured to 60 K in the gas phase . *Chem. Phys. Lett.*, 78(2):236–240, 1981.
- [140] H. T. Williams, S. V. Gwynne, and C. J. S. M. Simpson. Non-and near-resonant (VV) energy transfer between the isotopes of N_2 and of CO in liquid Ar and in the gas phase at 85 K . *Chem. Phys. Lett.*, 138(1):95–98, 1987.
- [141] G. J. Wilson, M. L. Turnidge, and C. J. S. M. Simpson. Vibrational energy transfer between $^{12}C^{16}O$ and $^{15}N_2$ in the gas phase down to 45 K and in liquid Ne solution . *Chem. Phys. Lett.*, 227(3):299–304, 1994.
- [142] Cecilia Coletti and Gert D. Billing. Isotopic effects on vibrational energy transfer in CO . *J. Chem. Phys.*, 111(9):3891–3897, 1999.

- [143] Beatriz M. Toselli and John R. Barker. Isotope effects in the vibrational deactivation of large molecules . *J. Chem. Phys.*, 97(3):1809–1817, 1992.
- [144] David L. Clarke and Robert G. Gilbert. Collisional Energy Transfer in Highly Excited Molecules: Deuteration effects . *J. Phys. Chem.*, 96:8450–8453, 1992.
- [145] Jack M. Preses and George W. Flynn. Infrared laser double resonance study of vibrational energy exchange between $^{12}\text{CH}_3\text{F}$ and $^{13}\text{CH}_3\text{F}^*$. *J. Chem. Phys.*, 66(7):3112–3116, 1977.
- [146] Martin Quack, René Schwarz, and Georg Seyfang. Time-resolved infrared-spectroscopic observation of relaxation and reaction processes during and after infrared-multiphoton excitation of $^{12}\text{CF}_3\text{I}$ and $^{13}\text{CF}_3\text{I}$ with shaped nanosecond pulses . *J. Chem. Phys.*, 96(12):8727–8740, 1992.

Chapter 3

Experimental setup

In this chapter we present our experimental setup. In the first part, in section 3.1, we present the optical setup, in section 3.2 we discuss the ideal sample pressure for our experiments, and in section 3.3 we present the chemical synthesis of isotopically enriched CF_3H used in our experiments.

3.1 Optical setup of our experiments

In this section we present the optical setup of our experiments. First, in the sub-section 3.1.1, we recall the general energy level diagram followed in our experiments. Then, the sub-section 3.1.2 describes optical setup in details. After that, the sub-sections 3.1.3-3.1.5 describe how the laser radiation is generated for pre-excitation of the CF_3H molecules via the different overtones of the CH stretching bending vibration. Finally, the sub-section 3.1.6 describes how we determine the fluence of the second laser, which is a critical value in our experimental investigations.

3.1.1 General energy level diagram

We have previously described the proposed setup for the new laser isotope separation process which consists of selectively dissociating vibrationally pre-excited molecules (section 1.1). For the investigation of the mechanisms leading to an increase of isotopic selectivity upon increasing the sample pressure or the time-delay between the two lasers, we need to *detect* the photofragments. This can be done, for example, by

mass-spectrometric detection of the products of the MLIS procedure after recombination via $\text{CF}_2 + \text{CF}_2 \rightarrow \text{C}_2\text{F}_4$. An alternative way is to detect the CF_2 fragments in situ via LIF before recombination. In this work we chose this latter detection method, as this allows us to monitor the number of dissociated CF_3H molecules in real time. Because we use LIF for the detection of the fragments, our experimental procedure resembles very much to the one we would use to record absorption spectra using the IR-LAPS method. We show in figure 3.1 a general energy level diagram of our experiments.

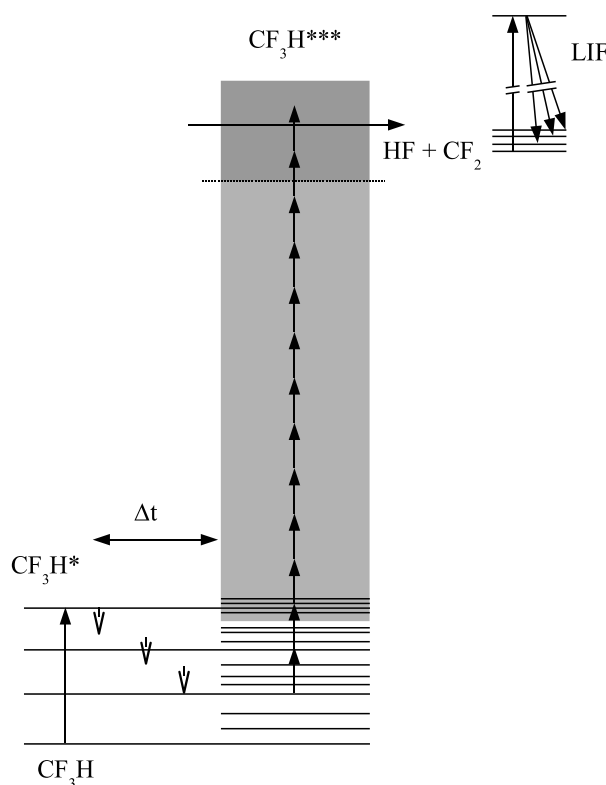


Figure 3.1: General energy level diagram used in our experiments.

First, a laser pulse pre-excites room temperature CF_3H molecules through a vibrational overtone transition of the CH stretching-bending vibration. Following this, a pulse from a tunable TEA CO_2 laser promotes some fraction of the vibrationally excited molecules to energies above their dissociation limit by infrared multiple photon excitation (IRMPE). We monitor CF_2 fragments by a third laser pulse via laser induced fluorescence (LIF).

Although LIF is, at least in principle, isotopically selective, in the case of CF_2 the electronic transitions are broadened and substantially overlapped, such that, in practice, isotopically selective LIF is impossible (for the CF_2 fragments we estimate a shift of $\sim 1 \text{ cm}^{-1}$ between the transitions of the two isotopic species¹, which has to be compared with a typical width of $\sim 50 \text{ cm}^{-1}$ of a single absorption feature²). Our measured LIF signals are both due to dissociated $^{12}\text{CF}_3\text{H}$ and $^{13}\text{CF}_3\text{H}$, and we correct them adequately in our data analysis[‡].

Excited CF_2 can also relax via non-radiative energy transfer in collisions, so the measured LIF signal is not necessarily proportional to the number of dissociated CF_3H molecules. This effect, collisional quenching, is also taken into account in our data analysis. We show in appendix B the effect of collisional quenching of excited CF_2 and how the results are corrected.

3.1.2 General optical setup

Figure 3.2 shows the main features of the optical layout in our experimental setup.

The generation of the light for the pre-excitation of the molecules depends on the pre-excitation level. We will describe the different methods in the following sections.

For the IRMPD step, we use a $10 \mu\text{m}$ pulse from a line tunable TEA CO_2 laser (Lumonics, TEA-840, bandwidth $\sim 0.1\text{-}0.15 \text{ cm}^{-1}$) that consists of an intense 250 ns (FWHM) spike and a $5\text{-}10 \mu\text{s}$ low intensity tail. The first spike contains $\sim 30\text{-}40 \%$ of the total pulse energy. A TEM_{00} laser beam is produced by inserting a 10 mm iris into the CO_2 laser cavity. The total energy of a typical laser pulse is up to 300 mJ . The laser light is focussed by a 70 cm ZnS lens into the cell. Before entering the cell, the CO_2 laser light can be attenuated by a set of teflon sheets.

[‡]In the case of natural abundant gas ($\sim 99\% \text{ }^{12}\text{CF}_3\text{H}$), we first measure the decay rate for pre-excited $^{12}\text{CF}_3\text{H}$; the signal contains no contribution of pre-excited $^{13}\text{CF}_3\text{H}$. By taking an IRLAPS excitation spectrum around the Q-branch of $^{13}\text{CF}_3\text{H}$, we determine the dissociation selectivity at a zero time-delay (see for example section 4.3.3). With these pieces of information the contributions due to excited $^{12}\text{CF}_3\text{H}$ and due to excited $^{13}\text{CF}_3\text{H}$ for the case of pre-excitation at the Q-branch of $^{13}\text{CF}_3\text{H}$ is easily calculated. Similar considerations apply to carbon-13 enriched samples.

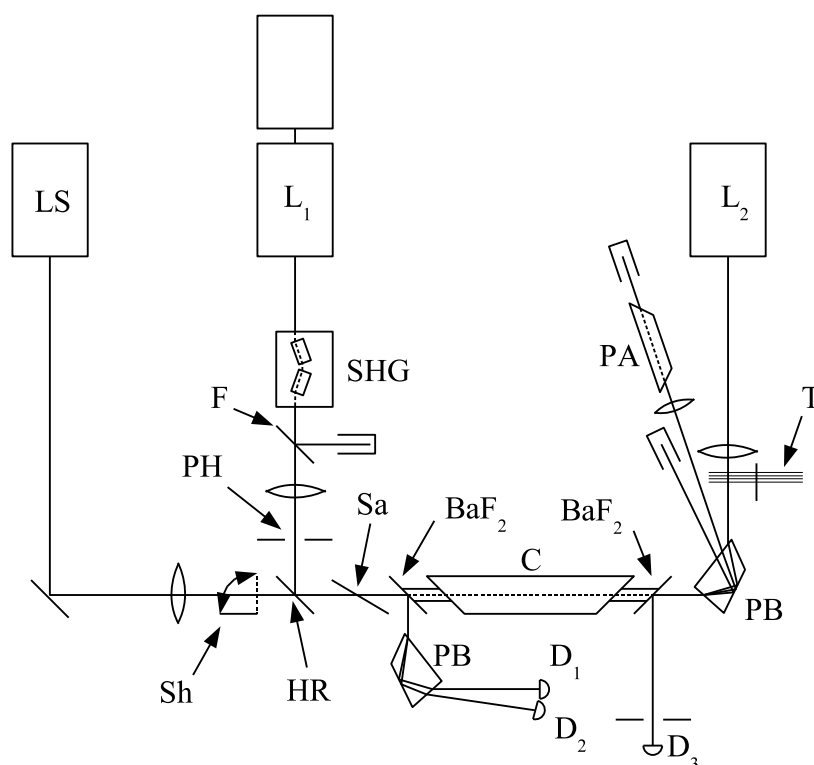


Figure 3.2: Optical setup of the experiments.

LS = laser for the pre-excitation of the molecules. L_1 : Nd:YAG pumped dye laser, L_2 : TEA CO_2 laser. PB = Pellin-Broca prism. SHG = autotracker for second harmonic generation. $\text{Det}_{1\dots 3}$ = detectors. HR = highly reflective mirror for UV light. F: filter for visible light. Sh = mechanical shutter. PH = pinhole. Sa = Sapphire plate. BaF_2 = windows. C = cell. PA = photoacoustic cell. T = teflon sheets.

The experiments are performed at a rate of 10 Hz.

For LIF detection of CF_2 we use the 5-10 mJ output of a Nd:YAG pumped (Lumonics, YM 600) dye laser (Continuum, ND60, linewidth $\sim 0.08 \text{ cm}^{-1}$, Coumarin-500 dye) that has been frequency-doubled in a BBO crystal. The remaining green light after frequency doubling is separated out by a UG-5 filter (Schott). Some green light is reflected on the front surface of the filter and directed into a beamstopper. The laser wavelength is tuned to the $A(0, 2, 0)^1B_1 \leftarrow X(0, 1, 0)^1A_1$ electronic transition³ in CF_2 at ~ 266.08

nm. The UV beam is focussed by a 100 cm fused silica lens into the centre of the cell. A pinhole clips the beam to make it clean.

Beams from the pre-excitation laser and 266 nm LIF detection laser are combined by a dichroic mirror prior to entering the cell. Upon exiting the cell, the residual pre-excitation and LIF detection beams are decoupled from the incoming dissociation beam by a BaF₂ Pellin-Broca prism, and the residual of the latter is absorbed upon exiting by a sapphire Brewster plate. After the decoupling from the dissociation and the LIF detection lasers, the pre-excitation laser beam is directed through a photoacoustic cell filled with CF₃H prior to being directed into a beam dump. All lasers enter the cell through BaF₂ Brewster windows.

The total undispersed LIF signal is collected by a 5.6 cm diameter 1:1 condenser lens (focal length 50 mm) and imaged onto a 1 x 11 mm slit in front of a UV sensitive photomultiplier tube (PMT) (Thorn EMI). The slit limits the LIF detection of CF₂ to the volume near the focal point. We, therefore, monitor the dissociation yield only from this volume, where the dissociation fluence along the CO₂ laser beam is almost constant. A U-340 (Schott) filter in front of the PMT cuts most of the scattered light at 266 nm while it lets pass the light due to fluorescence.

The reaction cell is a home-built, 20 cm long anodised aluminium vessel with a volume of ~ 0.5 ℓ and two 15 cm long stainless steel side-arms. The two BaF₂ windows are at the Brewster angle. To avoid unwanted scattered light several baffles are inserted into the side-arms.

A standard rotary pump (Pfeiffer Vacuum, Duo 5, 5 m³/h) pumps the cell through a LN₂ trap typically to $2 \cdot 10^{-3}$ mbar background pressure as measured by a capacitance manometer (MKS, Baratron).

The timing of the pre-excitation and LIF pulses is continuously monitored by a photodiode, and that of the CO₂ dissociation laser is verified using a fast Ge photon-drag detector. The frequency and linewidth of the pre-excitation and probe lasers are continuously monitored by a pulsed wavemeter (Burleigh, WA-4500).

To ensure stable experimental conditions and correct the LIF signal, we continuously monitor the relative power of the lasers during the course of an experiment by photodiodes that detect reflections from the entrance windows. As the CO₂ laser displays in general a rather stable intensity (after some warming up time), normally only the LIF and the pre-excitation laser beams are monitored.

Our measurements are not background free, since some dissociated ground state molecules and scattered light can also contribute to the measured signal. Every measured value is obtained by first measuring the collected LIF signal as described above and then by measuring the same signal by blocking the pre-excitation laser with a mechanical shutter. The difference of the two signals is proportional to the amount of dissociated pre-excited molecules.

The lasers and the signals are timed as follows: $\Delta t_{PE-IRMPD}$ is the time-delay between the pre-excitation (PE) laser pulse and the onset of the CO₂ (IRMPD) laser pulse (see figure 3.3). $\Delta t_{IRMPD-LIF}$ is the time-delay between the CO₂ and the LIF (UV) laser pulses. It is typically kept to 800 ns.

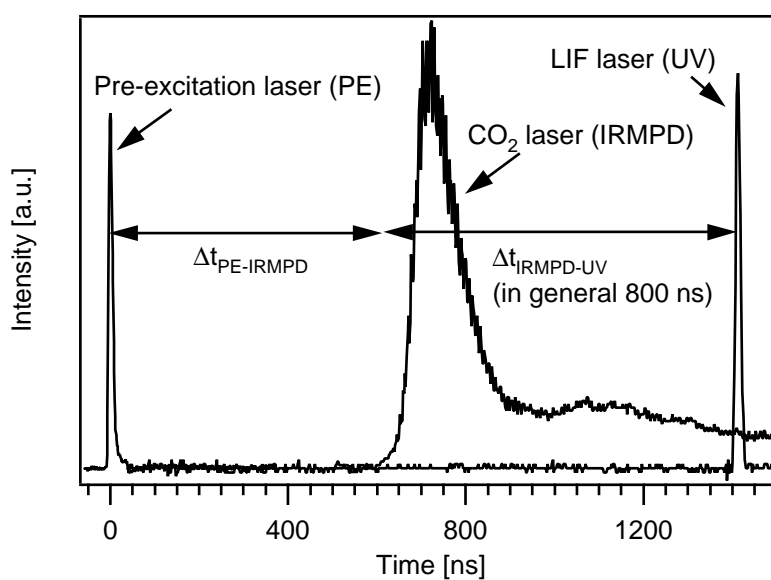


Figure 3.3: Timing of pre-excitation, dissociation and LIF lasers. Here an example for a time-delay of 600 ns between pre-excitation and dissociation lasers.

3.1.3 Pre-excitation via the 2_1 band

For the generation of laser radiation at $\sim 5900\text{ cm}^{-1}$ for the excitation to the first overtone region (2_1 band) we use the system shown in figure 3.4 and described below.

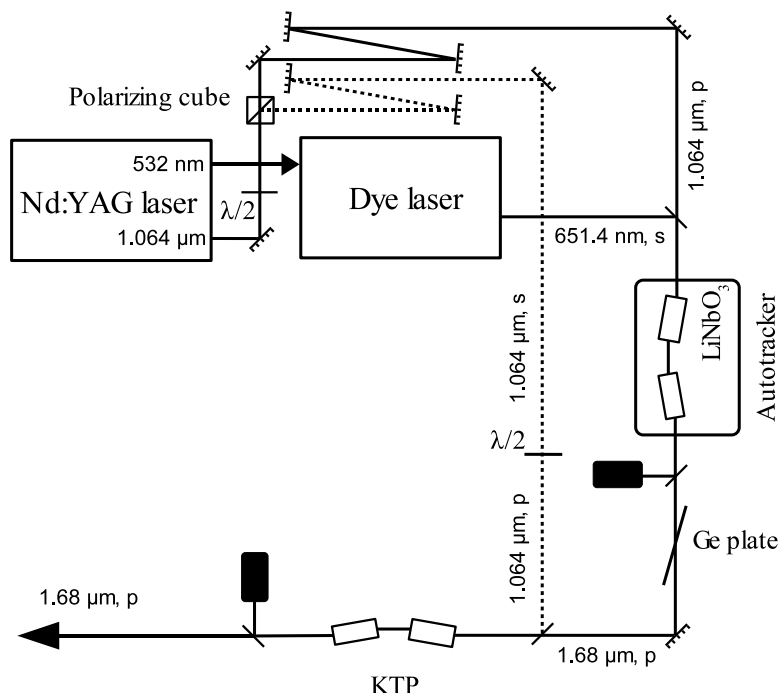


Figure 3.4: Generation of the laser beam for pre-excitation of CF_3H molecules via the 2_1 band. The image is reproduced from the thesis of Mikhail Polianski⁴.

The central piece of this system is a powerful, single-mode Nd:YAG laser (Spectra-Physics GCR-250). A fraction of the 1064 nm output of this laser is frequency doubled to pump a dye laser (Lambda Physik Scanmate 2E). The 30-40 mJ output of the dye is mixed with 150 mJ of the Nd:YAG laser fundamental in a LiNbO_3 crystal to generate 2-4 mJ of tunable IR radiation through a difference frequency mixing (DFM) process. The phase match angle of the crystal is adjusted automatically by a commercial autotracking unit (INRAD-II) as the laser wavelength is scanned. This unit also compensates for changes in phase match angle arising from temperature variations. The output of the DFM is further amplified in a two stage optical parametric amplifier (OPA) pumped by 200 mJ of the infrared fundamental of the same Nd:YAG laser. This gives narrow

bandwidth, tunable radiation up to 130 mJ per pulse at $1.68 \mu\text{m}$. The amplification stage is however not used in our experiments, as the resulting power of the beam is relatively high and pre-excites a too large fraction of molecules for our experiments.

3.1.4 Pre-excitation via the 3_1 and 3_2 bands

For the generation of laser radiation at $\sim 8800 \text{ cm}^{-1}$ for the excitation to the second overtone region (3_1 and 3_2 bands) we use the system shown in figure 3.5 and described below.

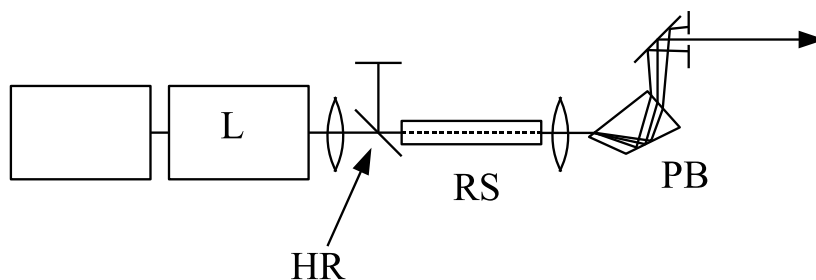


Figure 3.5: Generation of the laser beam for pre-excitation of CF_3H molecules via the 2_1 band.

L = Laser system. HR = highly reflective @ $1.14 \mu\text{m}$. RS = Raman shifter. PB = Pellin-Broca prism.

The 5-6 ns pre-excitation pulse of up to 20 mJ is generated by stimulated Raman scattering the 40 mJ output of a Nd:YAG pumped (Spectra Physics, GCR 250) dye laser (Lumonics, HD-500, bandwidth $\sim 0.04 \text{ cm}^{-1}$, LDS 765 dye) in a cell (home-made⁵, length 60 cm) filled to ~ 40 bar with H_2 . An internal gas circulator displaces the pumped H_2 between laser pulses. The backward first Stokes beam first is separated from the incoming beam by a 45° dichroic, retroreflected by a mirror and finally re-injected back to the Raman-shifter along with the forward first Stokes beam. This allows an improved overall efficiency of the Raman-shifter ($\sim 20\%$). The exiting beams of different wavelengths are separated by a fused silica Pellin-Broca prism. The first Stokes beam at $\sim 8800 \text{ cm}^{-1}$ is singled out and focused with a 70 cm lens into the centre of the cell.

3.1.5 Pre-excitation via the 4_1 and 5_2 bands

For the pre-excitation of the molecules in the 11,600 and in the 14,000 cm^{-1} regions (pre-excitation via the 4_1 and 5_2 bands), we directly use the output of a Nd:YAG pumped dye laser.

3.1.6 Control of the fluence of the dissociation laser

The dissociation process with the second laser depends non-linearly on the fluence of this laser beam. Unfortunately, the power of the CO_2 laser beam can only be adjusted over a small range without changing the focal properties of the laser beam. We chose to attenuate the beam with a set of 0.1 mm thick teflon sheets. The fluence is calculated as follows:

$$\Phi = \frac{E \cdot f_1 \cdot f_2 \cdot \exp(-\varepsilon n)}{\pi r_0^2}, \quad (3.1)$$

where E is the energy in the whole pulse, f_1 is the fraction of transmitted light from where we measure the power at the centre of the cell, f_2 is the temporal fraction of the pulse used, ε is an absorption parameter of teflon, n is the number of sheets used for the attenuation and r_0 is the radius of the laser beam in the centre of the cell. With this system, the fluence can be adjusted over a large range of energies (however not continuously) without changing the focussing properties of the laser beam. We give some details in appendix C.

3.2 Working pressure

In some experiments we wish to work at low pressures in order to avoid collisional relaxation during IRMPD. This way, an increase of isotopic selectivity can be well separated into isotopically selective collisional relaxation and different IRMPD rates. However, two effects limit the pressure towards the bottom:

1. **Molecules flying out of the reaction volume:** If we pre-excite a certain amount of molecules at $t = 0$, we want to be sure that the molecules are still in the reaction volume after a time-delay of Δt on the time-scales of our experiments

(typically hundreds of ns to a couple of μs). By measuring some pressure dependent decay rates we determine that for a pressure of $\gtrsim 1$ mbar it is safe to assume no losses of molecules this way. Figure 3.6 shows the decay rate k (the loss of dissociated molecules as the time-delay between the laser pulses is increased) as a function of the pressure p . The measurements are taken for $^{13}\text{CF}_3\text{H}$ molecules pre-excited via the 3_1 band at a moderate CO_2 laser fluence.

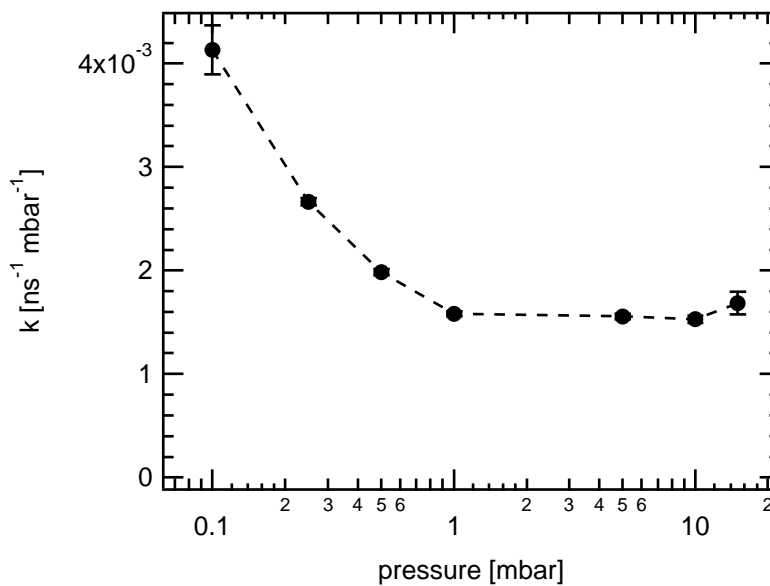
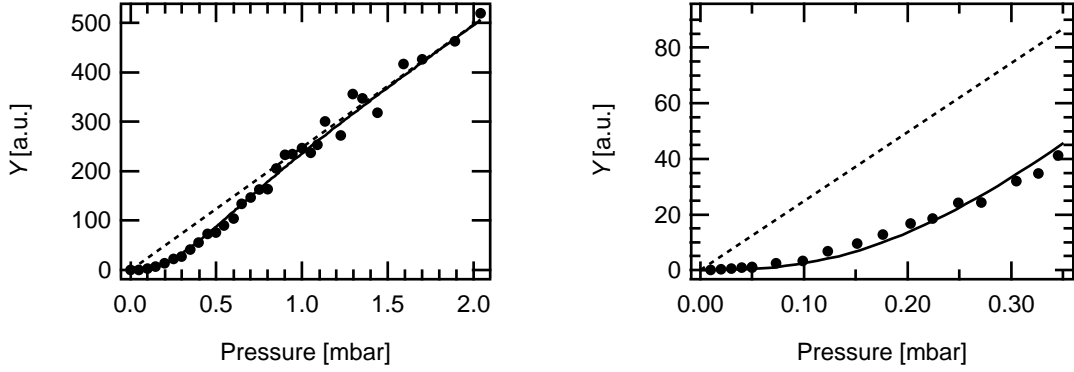


Figure 3.6: The decay rate k goes up as p goes down, indicating that molecules flying out of the reaction volume falsify the experimental measurement.

For pressures $\lesssim 1$ mbar the fly-out gets important.

2. **Rotational relaxation:** The data analysis is highly facilitated if we can always assume complete rotational relaxation of the molecules, thus avoiding a rotational bottleneck in IRMPD. In order to investigate on this, we measure the IRMPD yield as a function of the pressure for molecules pre-excited via the 2_1 band. In figure 3.7-a the dissociation yield Y is plotted for pressures between 0 and 2 mbar.

The measured data can be fitted by an empirical function



(a) Dissociation yield Y as a function of the pressure p .

(b) Blowup of figure (a).

Figure 3.7: Measurements for rotational relaxation. At low pressures the relative dissociation yield goes down. The solid curve represents a phenomenological fit and the dotted line would be the yield if rotational relaxation were complete. All measurements are for $^{12}\text{CF}_3\text{H}$. The results are corrected for quenching.

$$Y(p) = \eta \cdot p \cdot \left(1 - \exp\left(-\frac{p}{\varrho}\right)\right)^2, \quad (3.2)$$

where η and ϱ are fitting constants, η incorporates all transmission efficiencies and conversion constants and p is the sample pressure. ϱ has been found to be ~ 0.27 mbar. The value of ϱ depends on the exact experimental conditions such as e.g. dissociation laser fluence, but it can be used as indicative value. We define the value ϵ to be the “completeness of rotational relaxation”, where

$$\epsilon = \left(1 - \exp\left(-\frac{p}{\varrho}\right)\right)^2. \quad (3.3)$$

It is plotted in figure 3.8. It can be seen that for pressures of $p \gtrsim 1$ mbar rotational relaxation can be considered to be complete for pre-excitation via the 2_1 band.

For these reasons, the measurements with time-delayed laser pulses are performed at a pressure of 1 mbar.

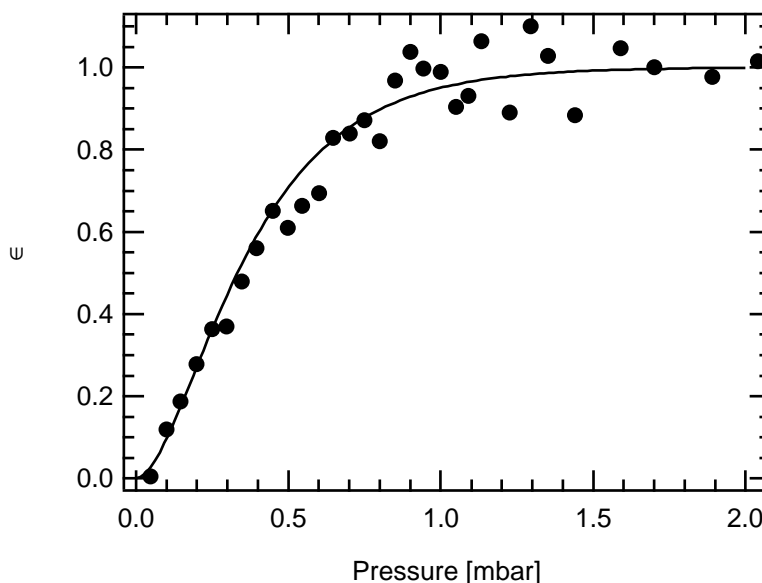
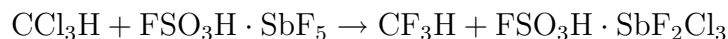


Figure 3.8: Completeness of rotational relaxation (see equation 3.3). For pressures below ~ 1 mbar rotational relaxation is not complete and IRMPD through the low density of states is a natural bottleneck.

3.3 Synthesis of $^{13}\text{CF}_3\text{H}$

Some of our experiments are performed with carbon-13 enriched CF_3H . As the price for commercially available $^{13}\text{CF}_3\text{H}$ is very high (\$10,500 for 1g at Cambridge Isotope Laboratories), we produce it in our laboratory. This section describes how we produce isotopically enriched CF_3H .

Enriched $^{13}\text{CF}_3\text{H}$ is made by mixing 1g enriched chloroform $^{13}\text{CCl}_3\text{H}$ (Cambridge Isotope Laboratories, enrichment $\geq 99\%$) with 100 g of magic acid (fluorosulfuric acid-antimony pentafluoride, $\text{FSO}_3\text{H} \cdot \text{SbF}_5$, Aldrich, 100 %) ⁶. The chlorine atoms of chloroform are substituted by fluorine atoms from the magic acid. The overall multistep reaction is described by the following equation:



The production is done in glass vessels, which are hooked up to a vacuum line. In the first step (fig 3.9) the magic acid is poured into a spherical vessel with a volume of

$\sim 0.6 \ell$ and pumped out to $\leq 10^{-2}$ mbar. At 300 K chloroform is a liquid, but with a vapour pressure of ~ 0.27 bar it, is very volatile⁷. The isotopically enriched chloroform is carefully poured into a smaller vessel at room temperature which has previously been filled with N_2 . The valve to the vessel is immediately closed to prevent any chloroform from escaping. The vessel is then immersed into LN_2 to freeze the chloroform. Finally it is degassed by a few dew-freeze cycles.

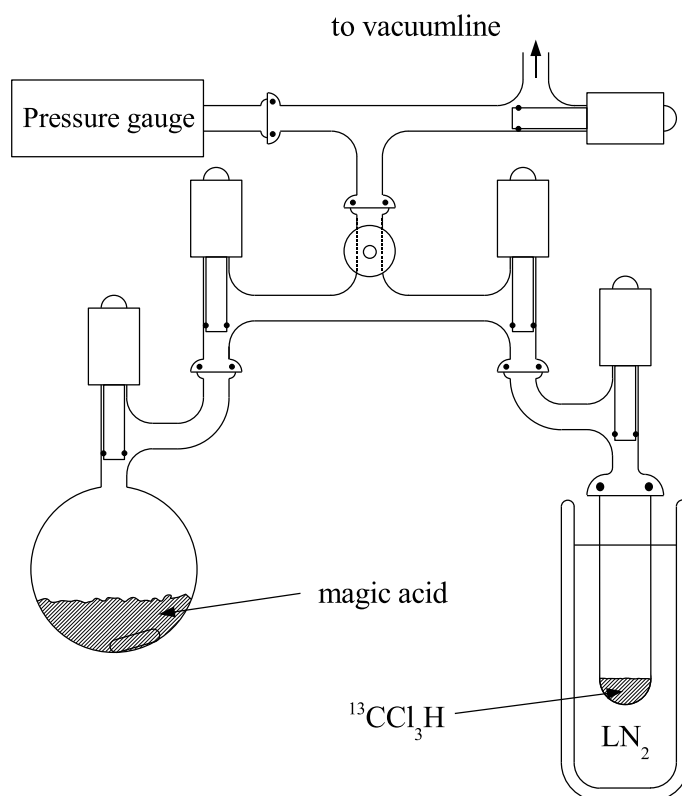


Figure 3.9: Initial setup for the production of ^{13}C enriched CF_3H .

Once the system is under vacuum, the chloroform is transferred by vacuum distillation into the large vessel containing magic acid cooled by LN_2 (fig 3.10-a). This reaction vessel is disconnected from the vacuum system and warmed up to room temperature. The mixture of magic acid and chloroform is stirred over night (fig 3.10-b). After stirring we are left over with a mixture of magic acid, some remaining chloroform and fluoroform. To separate the fluoroform, the vessel is immersed into a mixture of isopropanol and solid CO_2 (dry ice) which is at $-78^\circ C$, which traps chloroform. A new vessel ($V \sim$

0.15 ℓ) is hooked up and the fluoroform, which is still in the vapour phase at -78°C , is trapped with LN_2 in the new vessel (fig 3.10-c).

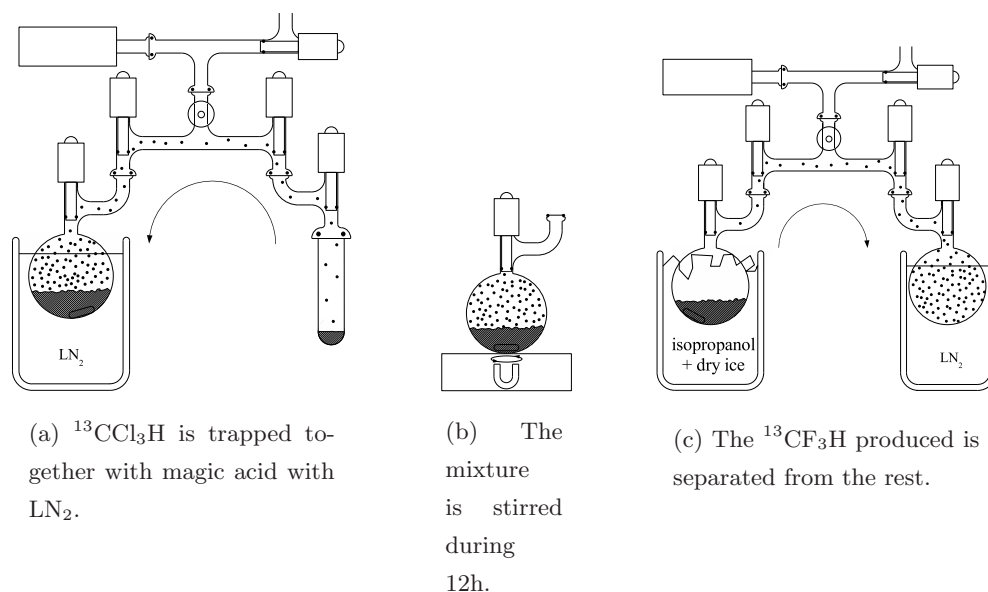
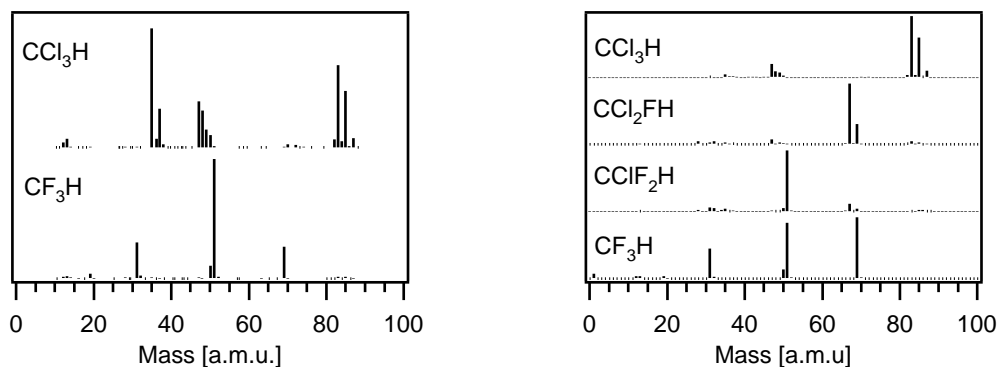


Figure 3.10: Procedure for the synthesis of $^{13}\text{CF}_3\text{H}$.

Before performing the actual synthesis, two test runs are performed with ordinary chloroform (i.e. with $\sim 99\%$ $^{12}\text{CCl}_3\text{H}$) to ensure that the synthesis works with a large conversion efficiency to avoid loss of isotopically enriched chloroform, which is quite expensive. We take mass spectra of the final mixture of chloroform, fluoroform and magic acid. By comparing the mass spectra with fragmentation data from literature⁸, the composition of the gas can be evaluated. It turns out that stirring long enough ensures a very high percentage of converted chloroform (at least 99.5%). This is verified by measuring a mass spectrum of the resulting gas before the separation of the produced fluoroform from the initial chloroform.

Figure 3.11-a shows two mass spectra, one of the initial $^{13}\text{CCl}_3\text{H}$ and one of what we expect to be isotopically enriched CF_3H . Figure 3.11-b shows literature fragmentation patterns of CCl_3H , CCl_2FH , CClF_2H and CF_3H , which serve as a basis for the identification of the final mixture.



(a) Mass spectra of initial gas (chloroform) and product (essentially fluoroform).

(b) Literature mass spectra⁸ for different hydrofluorochlorocarbons.

Figure 3.11: Comparison of measured and literature mass-spectra for the identification of the gas.

The identification of the fragments is straightforward[‡]: the initial chloroform is readily identified and the product is for our purposes very pure CF_3H . We estimate the purity to be $\gtrsim 99.5\%$, the transformation is quantitative.

Figure 3.12 shows a mass spectrum of the isotopically enriched $^{13}\text{CF}_3\text{H}$ produced. The peaks are shifted by one mass with respect to the peaks for the test synthesis of $^{12}\text{CF}_3\text{H}$. The sample is isotopically very clean, and $^{12}\text{CF}_3\text{H}$ created from residual $^{12}\text{CCl}_3\text{H}$ is not detectable. Recording action spectra with IRLAPS confirm this as well, as no $^{12}\text{CF}_3\text{H}$ is detected. An additional peak at 85 amu is probably SiF_4 created by the traces of H_2O forming H_2F_2 which in turn reacts on the glass surface to form SiF_4 ⁹. Its absence in the mass spectrum for the synthesised $^{12}\text{CF}_3\text{H}$ is not very clear but probably due to the fact that we stirred the reactive mixture for a shorter time.

This way we estimate to have produced $\sim 0.2 \ell$ of isotopically enriched $^{13}\text{CF}_3\text{H}$ at 1 bar.

[‡]The relative intensities of the peaks are not the same. This is likely because of different characteristics (detection efficiencies, ioniser, ...) of our QMS and the ones used to obtain the published mass-spectra⁸.

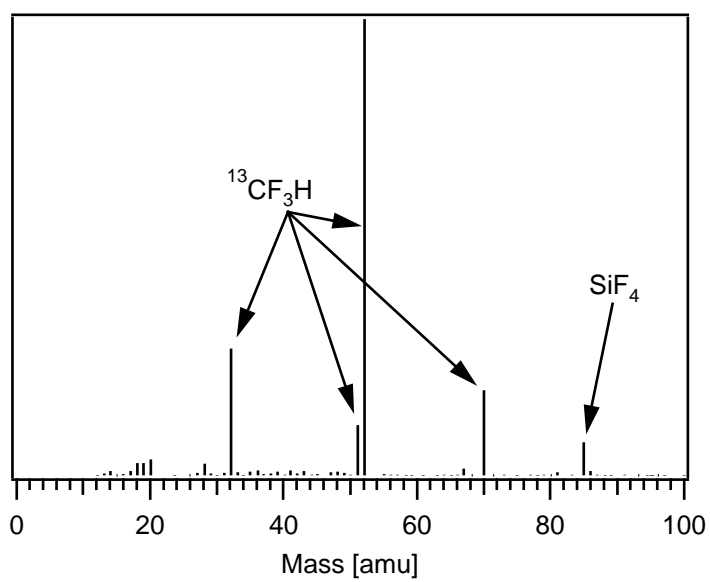


Figure 3.12: Mass spectrum of the final products of the $^{13}\text{CF}_3\text{H}$ synthesis.

Bibliography

- [1] M. Polianski, O. V. Boyarkin, and T.R. Rizzo. Collisionally-assisted, highly-selective laser isotope separation of carbon-13 . *J. Chem. Phys.*, 121(23):11771–11779, 2004.
- [2] L. Rubio, M. Santos, and J. A. Torresano. Laser induced fluorescence detection of CF, CF₂ and CF₃ in the infrared multiphoton dissociation of C₃F₆ . *J. Photochem. Photobiol. A: Chem.*, 146:1–8, 2001.
- [3] David S. King, Peter K. Schenck, and John C. Stephenson. Spectroscopy and Photophysics of the CF₂ \tilde{A}^1B_1 - \tilde{X}^1A_1 System . *J. Molec. Spectrosc.*, 78:1–15, 1979.
- [4] Mikhail N. Polianski. *Overtone pre-excitation - Infrared Multiple Photon Dissociation Under Collisional Conditions. New Potential for Laser Isotope Separation* . PhD thesis, Ecole polytechnique fédérale de Lausanne, Switzerland, 2004.
- [5] Julien Pitteloud. Construction d'un Ramanshifter . Projet d'ingénieur. EPFL, 2002. The report can be obtained upon request from the author of this thesis.
- [6] Lester Andrews, Helge Willner, and Frank T. Prochaska. A Simple Synthesis for Carbon-13 Enriched Fluorochloromethanes and Fluoromethanes . *J. Fluorine Chem.*, 13:273–278, 1979.
- [7] Robert C. Weast and Melvin J. Astle, editors. *CRC Handbook of Chemistry and Physics*. CRC Press Inc., Florida, 59th edition, 1978.
- [8] E. Stenhagen, S. Abrahamsson, and F. W. McLafferty. *Atlas of Mass Spectral Data. Volume I*. New York: Interscience, 1969.
- [9] Amanz Ruf (LCPM EPFL Switzerland). Private communication .

Chapter 4

Experimental investigations

This chapter deals with our experimental investigations. In the recently developed method of molecular laser isotope separation (MLIS) by selectively dissociating pre-excited CF_3H molecules, we have observed an increase of isotopic selectivity upon an increase of the sample pressure and/or the time-delay between the two lasers involved (see section 1.2). We propose two possible mechanisms for this observation: isotopically selective collisional relaxation of vibrationally excited molecules and different absorption rates of IR photons for the two different isotopomers. Our goal is to determine the relative contributions of these mechanisms. Here we present the experimental methods and ideas employed for this study.

4.1 Introduction

4.1.1 General idea

In figure 4.1 we show the general energy level diagram used in our MLIS process and the main parameters that can be varied for the investigation of the mechanisms leading to an increase of isotopic selectivity due to collisions.

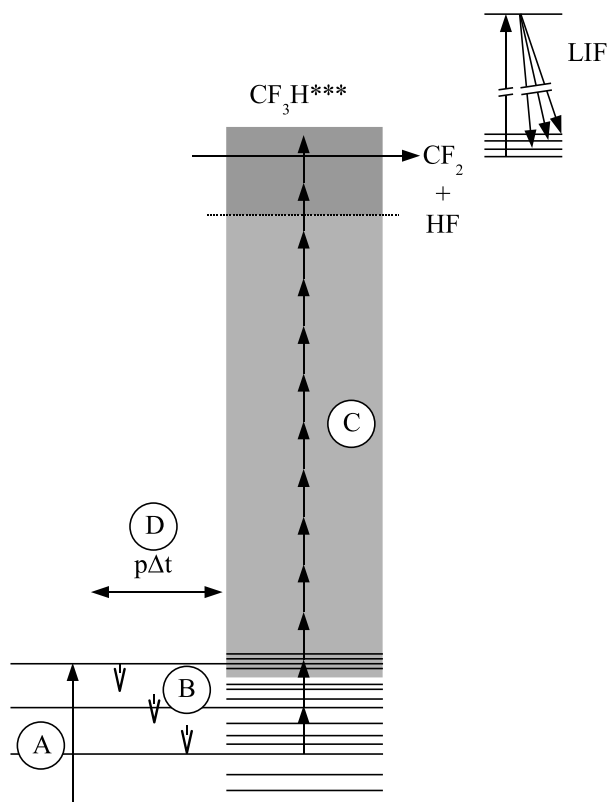


Figure 4.1: General experimental procedure. In our experiments we can vary A - the pre-excitation level, B - the relaxation partners, C - the dissociation laser wavelength and fluence, D - the time-delay between the pre-excitation and the dissociation lasers and/or the sample pressure. The time-delay between the dissociation laser and the UV laser for LIF detection is kept fix at 800 ns.

We wish to keep the IRMPD step free from collisions and hence fix a low pressure of typically 1 mbar (see section 3.2). We show in table 4.1 four schemes that can be used for the investigation, based on varying or fixing the parameters A-D shown in figure 4.1.

Scheme	A	B	C	D	Comment
#1			×		This way, we investigate only the IRMPD step, eliminating collisional effects.
#2	×			×	Measure the dissociation yield as a function of the time-delay between the lasers, for different... ... pre-excitation energies
#3		×		×	... collision partners
#4			×	×	... dissociation laser fluence and wavelength

Table 4.1: Four schemes for the investigation of the mechanisms of the enhancement of isotopic selectivity varying different parameters (× A-D).

Based upon these different schemes, we propose the following experiments:

- Experiments described in section 4.2 follow scheme #2: here we scan the time-delay between the pre-excitation and the dissociation lasers for different pre-excitation energies. This way, we get information about the influence of the initial rovibrational state of the molecule on the relaxation and IRMPD processes. This helps to determine the state specificity of the increase of isotopic selectivity upon an increase of the time-delay between the two lasers.
- Experiments described in section 4.3 follow scheme #1: here we measure the dissociation probability of vibrationally excited $^{12}\text{CF}_3\text{H}$ and $^{13}\text{CF}_3\text{H}$ molecules as a function of the CO_2 dissociation laser fluence and wavelength. By measuring such photofragment excitation spectra of CF_3H molecules excited via the 3_1 band we are able to get information about the dissociation process.
- Experiments described in section 4.4 follow scheme #4: by adequately changing the dissociation laser wavelength we can compare the disappearance of the molecules upon a time-delay between the pre-excitation and the dissociation laser under conditions, where IRMPD is the same for the two isotopomers. This way, we eliminate any effects of isotopically selective IRMPD.

- Experiments described in section 4.5 follow scheme #3: by replacing the $^{12}\text{CF}_3\text{H}$ by $^{13}\text{CF}_3\text{H}$ molecules as relaxation partners, we can directly compare relaxation rates between the different isotopomers.

4.1.2 Definitions

For the characterisation of the influence of the different mechanisms to the enhancement of isotopic selectivity upon an increase of the pressure and/or time-delay between the pre-excitation and the dissociation lasers, we define the following values:

1. The dissociation yield Y .
2. The dissociation probability D , which is $D = Y/Y_0$, where Y_0 is the amount of pre-excited molecules.
3. The dissociation selectivity S , which is $S = {}^{13}D/{}^{12}D$ where ${}^x D$ is the dissociation probability of the ${}^x\text{CF}_3\text{H}$ molecule.
4. The decay rate k for measurements where the time-delay is scanned between the pre-excitation and dissociation lasers. k is the rate at which molecules relax and disappear from the region where they can be effectively dissociated by the CO_2 laser. In general, the dissociation yield as a function of time-delay can be well described by an exponential $Y(\Delta t) = \eta \cdot \exp(-k \cdot p \cdot \Delta t)$ where η is the transmission of the LIF signal through the detection system, p is the sample pressure and k is the “decay rate”. k is not a constant, but rather a parameter, which depends on the level of pre-excitation and the low energy cut-off below which dissociation is inefficient which depends on the conditions of IRMPD (frequency, fluence and intensity of dissociation laser) and the isotopic species of the pre-excited molecule.
5. The decay selectivity \mathbb{S} , which is $\mathbb{S} = {}^{12}k/{}^{13}k$.

4.1.3 Uncertainties on the decay rates k

As in all physical measurements, we have a certain spread of the experimentally measured values due to random errors. As the experiments are time consuming, we are not able to evaluate this uncertainty for every data point. For this we determine it for one case and use the measured relative error for all experimental values of the decay rate k .

Figure 4.2-a shows the evaluation of the statistical error by successive measurements of k under equal experimental conditions, and figure 4.2-b the distribution of the measured data. The relative error $\delta k/k_0$ is $0.098 \approx 10\%$, where k_0 the centre of a Gaussian curve fitted to the distribution of the values of k and $\delta k = 1.15 \times$ width of the same Gaussian which corresponds to a confidence interval of 90%.

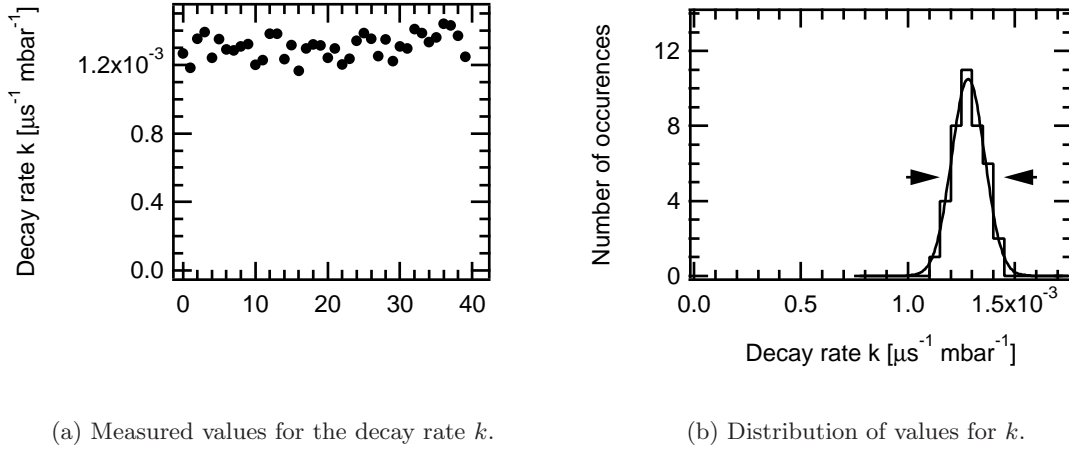


Figure 4.2: Successive measurements of the decay rate k .

There is an additional error due to the fitting procedure. k is determined by fitting a function $Y(\Delta t) = A \cdot \exp(-k \cdot p \cdot \Delta t)$ to the measured data. As the measured data will in general not be able to be perfectly fitted by the exponential function, the fitted parameters have a certain uncertainty given by the programme we use for the data analysis (Igor Pro 4.0) for a 90% confidence interval.

In this sense, our quoted data will have the form $k = {}^0k_{\pm\delta k_1(stat)}^{\pm\delta k_2(fit)}$, where 0k is the fitted value and δk_1 and δk_2 are the uncertainties discussed above.

In what follows (sections 4.2-4.5), we present our experiments varying the parameters discussed above. Section 4.6 discusses and concludes this chapter.

4.2 State specificity of the increase of isotopic selectivity upon leaving a time-delay between the pre-excitation and the dissociation lasers

4.2.1 Introduction

Our molecular laser isotope separation (MLIS) scheme consists of pre-exciting $^{13}\text{CF}_3\text{H}$ molecules via the 3_1 band with a subsequent selective dissociation of pre-excited molecules by a CO_2 laser (called “dissociation laser”). The pre-excitation laser excites a small fraction of $^{12}\text{CF}_3\text{H}$ too which results in the dissociation products not being isotopically pure. Experimentally it has been observed that by increasing the time-delay between the two lasers and/or by increasing the sample pressure, the isotopic selectivity increases. In other words, the rates ^{12}k and ^{13}k at which the molecules lose enough vibrational energy due to collisions such that they are not effectively dissociation by the CO_2 laser any more, are different. The question arises as to whether these different rates are due to the fact the the rovibrational identities of the excited $^{12}\text{CF}_3\text{H}$ and $^{13}\text{CF}_3\text{H}$ are not the same (with the chosen wavelength of the pre-excitation laser $^{13}\text{CF}_3\text{H}$ is excited via the Q-branch, $^{12}\text{CF}_3\text{H}$ via a P-branch) or whether the energy can be considered to be randomly distributed over the molecule and no state specific vibrational relaxation and/or multiple photon dissociation (MPD) occurs.

In order to study this question, the pre-excitation laser is set to a particular rovibrational transition of $^{12}\text{CF}_3\text{H}$ or $^{13}\text{CF}_3\text{H}$, the dissociation laser wavelength and fluence is kept fixed and the rates k are determined by scanning the time-delay between the pre-excitation and the dissociation lasers. These rates (called “decay rates”) are measured for different pre-excitation wavelengths (resulting in different rovibrational identities of the pre-excited molecules). The energy level diagram followed in these experiments is shown in figure 4.3.

4.2.2 Results

We perform measurements of the decay rate k by scanning the time-delay between the pre-excitation and the dissociation lasers for different pre-excited rovibrational states.

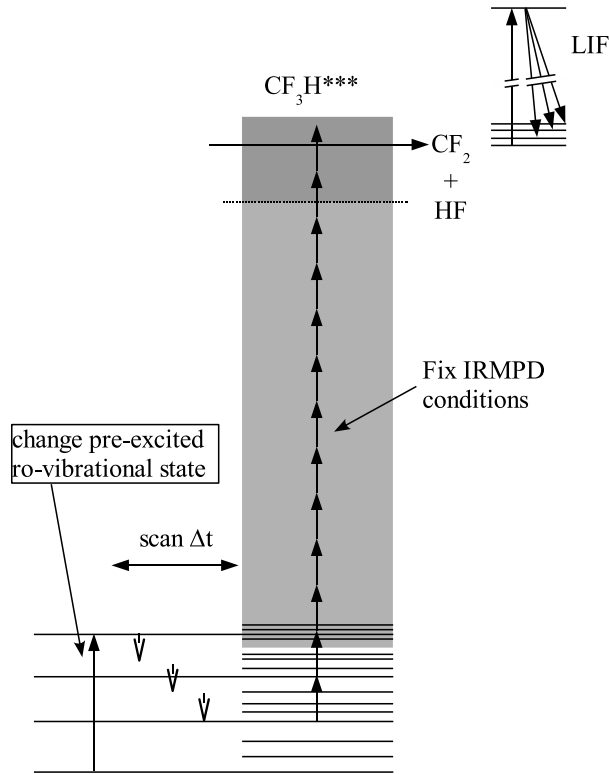


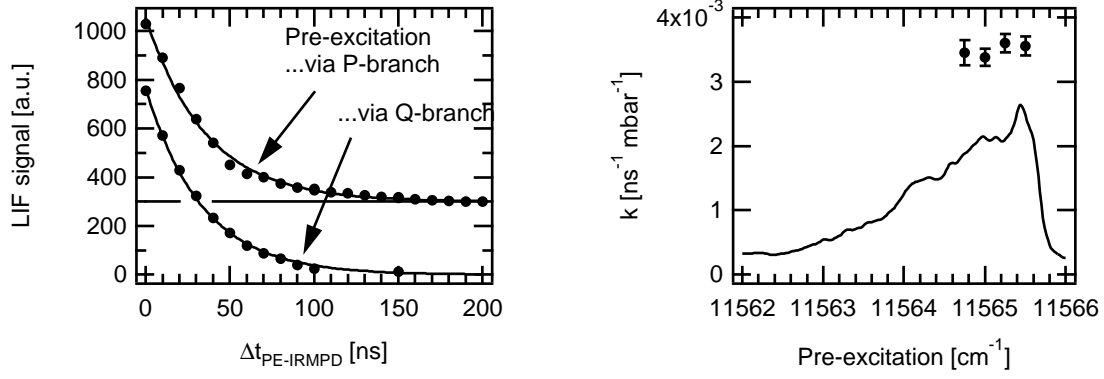
Figure 4.3: Energy scheme used in the experiments for the determination state specificity of relaxation rates.

In a first step, we change the rotational identity of the pre-excited state, and in a second step we change the vibrational identity too.

(I) Rotational identity

First, we compare the decay rate k for the P(32) transition of the 3_1 band at $12,927.78 \text{ cm}^{-1}$ with k for molecules pre-excited via the Q-branch of the 3_1 band (for $^{12}\text{CF}_3\text{H}$). We measure decay rates of $2.92_{\pm 0.29}^{\pm 0.13(\text{fit})} \cdot 10^{-3}$ and $2.89_{\pm 0.29}^{\pm 0.07(\text{fit})} \cdot 10^{-3} \text{ ns}^{-1} \text{ mbar}^{-1}$ for pre-excitation via the P-branch and via the Q-branch. A measurable influence of the rotational identity of the pre-excited state is not observed. We show in figure 4.4-a the measured LIF signals as a function of the time-delay between the pre-excitation and dissociation lasers for $^{12}\text{CF}_3\text{H}$ molecules pre-excited via the Q-branch and via a P-branch of the 3_1 band. In a second step, we scan the wavelength of the pre-excitation laser

across the Q-branch of the 4_1 pre-excitation level for the $^{12}\text{CF}_3\text{H}$ molecule, and measure decay rates k for different pre-excitation wavelengths. Within the Q-branch of the 4_1 pre-excitation level, we measure decay rates of $3.45^{\pm 0.19(\text{fit})}_{\pm 0.35(\text{stat})} \cdot 10^{-3}$, $3.37^{\pm 0.13(\text{fit})}_{\pm 0.34(\text{stat})} \cdot 10^{-3}$, $3.60^{\pm 0.14(\text{fit})}_{\pm 0.36(\text{stat})} \cdot 10^{-3}$ and $3.55^{\pm 0.14(\text{fit})}_{\pm 0.36(\text{stat})} \cdot 10^{-3} \text{ ns}^{-1} \text{ mbar}^{-1}$ for pre-excitation frequencies of 11,564.75, 11,565.00, 11,565.25 and 11,565.50 cm^{-1} . We show in figure 4.4-b the measured decay rates as a function of the pre-excitation energy.



(a) Relaxation of vibrationally excited $^{12}\text{CF}_3\text{H}$ molecules pre-excited via the Q-branch and a P-branch (the curves are offset with respect to each other for clarity).

(b) Action spectrum around the 4_1 peak of $^{12}\text{CF}_3\text{H}$ such as the decay rates measured at the respective wavelengths. The four different measurements are separated by 0.25 cm^{-1} .

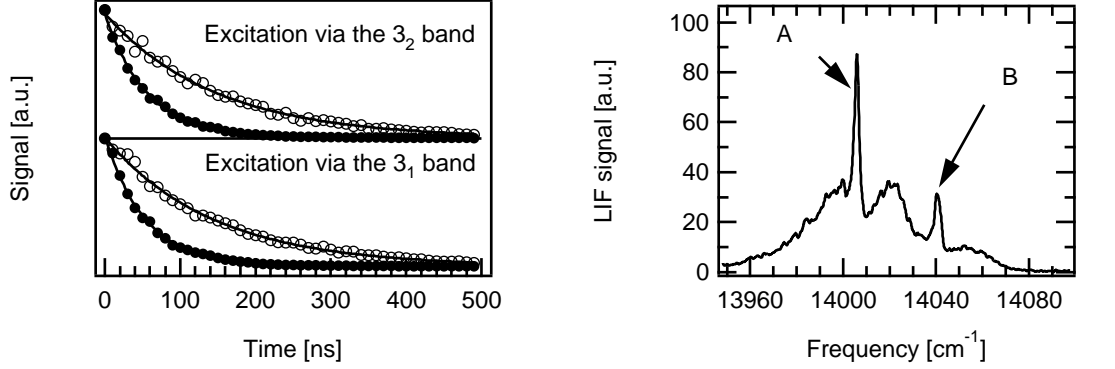
Figure 4.4: Experiments to test the influence of the rotational identity of the pre-excited state on the decay rates.

We conclude that the rotational identity of the pre-excited state does not influence the decay rates.

(II) Vibrational identity

In a second step, we compare different pre-excited vibrational states. We measure decay rates of molecules of both isotopic species pre-excited via the 3_1 and via the 3_2 bands. For $^{12}\text{CF}_3\text{H}$, we measure decay rates of $4.70^{\pm 0.05(\text{fit})}_{\pm 0.47(\text{stat})} \cdot 10^{-3}$ and $4.50^{\pm 0.04(\text{fit})}_{\pm 0.45(\text{stat})} \cdot 10^{-3} \text{ ns}^{-1} \text{ mbar}^{-1}$ and for $^{13}\text{CF}_3\text{H}$, we measure decay rates of $1.75^{\pm 0.02(\text{fit})}_{\pm 0.18(\text{stat})} \cdot 10^{-3}$ and $1.71^{\pm 0.025(\text{fit})}_{\pm 0.17(\text{stat})} \cdot 10^{-3} \text{ ns}^{-1} \text{ mbar}^{-1}$. The decay rates are independent on the pre-excitation

level. This is shown in figure 4.5-a.



(a) Relaxation curves for \bullet $^{12}\text{CF}_3\text{H}$ and \circ $^{13}\text{CF}_3\text{H}$ molecules pre-excited via the 3_1 and 3_2 bands.

(b) IRLAPS action spectrum of the 5_2 band of $^{12}\text{CF}_3\text{H}$. (A): Q-branch of 5_2 band at $14,006.00\text{ cm}^{-1}$ (B): unidentified band at $14,040.09\text{ cm}^{-1}$.

Figure 4.5: Experiments to test the influence of the vibrational identity of the pre-excited state on the decay rates.

We also measure decay rates of molecules pre-excited via the 5_2 ($\sim 14,006\text{ cm}^{-1}$) band with the decay rates of molecules excited at $14,040.09\text{ cm}^{-1}$. This last frequency corresponds to a transition to a so far unidentified sub-band which couples via Fermi resonance to the 5_2 level¹. The decay rates we measure are given in table 4.2. We show in figure 4.5-b an IRLAPS action spectrum around the 5_1 band of $^{12}\text{CF}_3\text{H}$ which shows the unidentified band too.

Pre-excitation level	Fluence		
	$\Phi = 0.94\text{ J cm}^{-2}$	$\Phi = 2.35\text{ J cm}^{-2}$	$\Phi = 14.7\text{ J cm}^{-2}$
5_2 band	$3.66_{\pm 0.37}^{\pm 0.29(\text{fit})}$ $\cdot 10^{-3}$	$3.00_{\pm 0.30}^{\pm 0.19(\text{fit})}$ $\cdot 10^{-3}$	$2.64_{\pm 0.26}^{\pm 0.22(\text{fit})}$ $\cdot 10^{-3}$
peak at $11,565.5\text{ cm}^{-1}$	$3.68_{\pm 0.37}^{\pm 0.38(\text{fit})}$ $\cdot 10^{-3}$	$3.00_{\pm 0.30}^{\pm 0.24(\text{fit})}$ $\cdot 10^{-3}$	$2.63_{\pm 0.26}^{\pm 0.38(\text{fit})}$ $\cdot 10^{-3}$

Table 4.2: Decay rates (in $\text{ns}^{-1}\text{mbar}^{-1}$) for molecules excited via the 5_2 vibrational mode with molecules excited via another (unidentified) band

Here we do not detect any influence of the vibrational state on the decay rate either.

4.2.3 Discussion

From these experiments we conclude that the exact rovibrational identity of the pre-excited molecules does not influence the decay rates. We can hence treat the vibrational energy as randomly distributed over all vibrational modes of the molecule although the experiments do not include fast collisionally induced IVR prior to vibrational energy transfer and IRMPD. This means that we can study the behaviour of the $^{12}\text{CF}_3\text{H}$ molecule by pre-exciting it via the Q-branch of a transition as its behaviour is the same as when we excite it via a P-branch.

4.3 Properties of collision-free IRMPD of excited molecules: photofragment excitation spectrum and dissociation selectivity of vibrationally excited CF_3H

In this section we present some experiments in which we study the IRMPD step of our MLIS scheme in the absence of vibrational relaxation, which is avoided by using low working pressures and a zero time-delay between the two laser.

4.3.1 Introduction

First, we present measurements of photofragment spectra of CF_3H molecules pre-excited to the 3_1 level. For this, the pre-excitation laser is tuned to the Q-branch of $^{12}\text{CF}_3\text{H}$ or $^{13}\text{CF}_3\text{H}$, the timing between the pre-excitation, dissociation and LIF lasers is kept fixed, and the wavelength of the CO_2 dissociation laser is changed. The dissociation yield as a function of the dissociation laser wavelength (at a given fluence) results in a photofragment excitation spectrum. This set of experiments aims at verifying to what extent the MPD step is selective. The energy level diagram followed in these experiments is shown in figure 4.6. In order to get good signal, we use a pulsed alexandrite laser (PAL) instead of a Nd:YAG pumped dye laser for the pre-excitation step.

In a second step we present some complementary information, where we directly compare the dissociation probabilities of $^{12}\text{CF}_3\text{H}$ and $^{13}\text{CF}_3\text{H}$ as a function of the CO_2 laser fluence and wavelength using a Nd:YAG pumped dye laser for the pre-excitation of the molecules. In principle this information can be deduced from the data obtained using

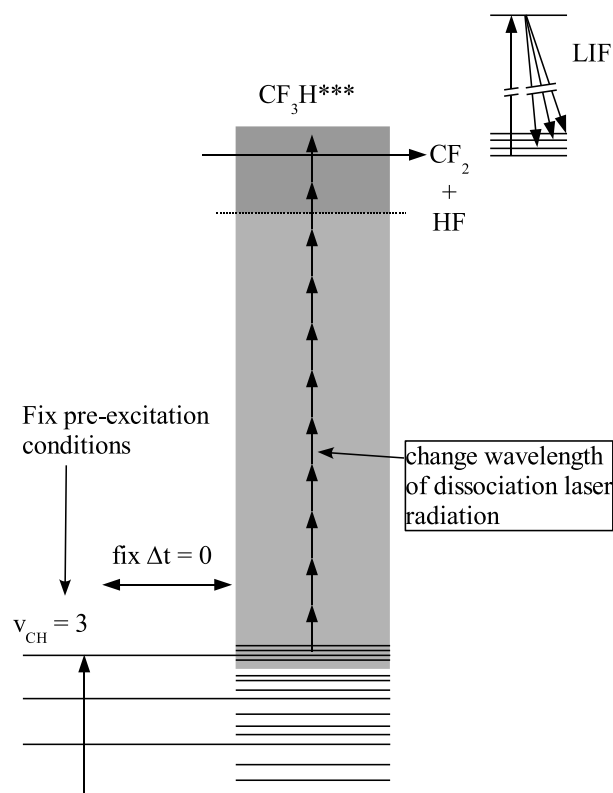


Figure 4.6: Energy scheme used in the experiments for the determination of photofragment excitation spectra of excited molecules.

the PAL, but as we are able to measure the dissociation yields for pre-excited $^{12}\text{CF}_3\text{H}$ and pre-excited $^{13}\text{CF}_3\text{H}$ in a same experiment, it is clear that a direct comparison of the dissociation probabilities of $^{13}\text{CF}_3\text{H}$ and $^{12}\text{CF}_3\text{H}$ is more precise than comparing data that has been acquired independently. The energy level diagram followed in these experiments is the same as for the measurement of photofragment excitation spectra shown in figure 4.6.

We present in sections 4.3.2 and 4.3.3 the results for these two experiments, in section 4.3.4 we discuss the results and we finally make some conclusive remarks in section 4.3.5.

4.3.2 Results: photofragment excitation spectra

The goal is to measure the dissociation yield at a fixed fluence of the dissociation laser as a function of the dissociation laser wavelength. However, we cannot choose or attenuate this fluence continuously, because both the maximum fluence (figure C.5 on page 251) and the attenuation of the laser beam by the teflon sheets (figure C.1 on page 248) varies from line to line. For this reason we measure at a given dissociation wavelength the dissociation yield at different fluences such that we can adequately interpolate the data for any fluence in the measured range. From this data we can construct a dissociation yield spectrum.

Figure 4.7 shows two examples of measured dissociation yield as a function of fluence for two different fixed values of ν . In order to do an interpolation of the dissociation yield for any fluence Φ a fitting function is used ($Y(\Phi) = \exp(C_1 \cdot \exp(-D_1 \cdot \Phi) + C_2 \cdot \exp(-D_2 \cdot \Phi))$).

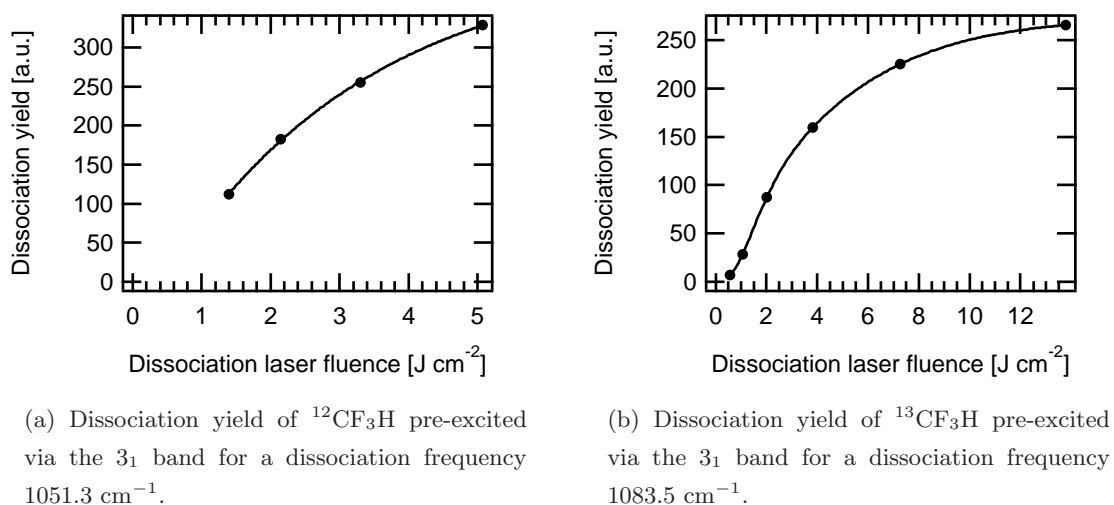
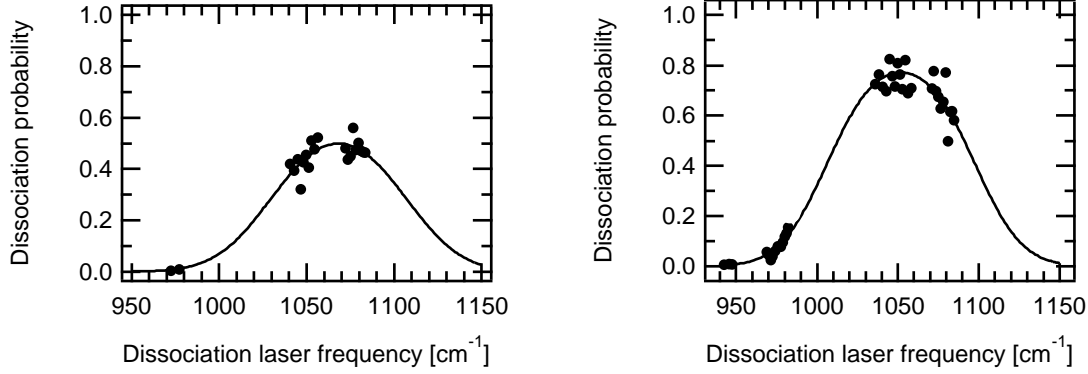


Figure 4.7: Sample curves of measured dissociation yields.

Figure 4.8 shows two sample cuts of $Y(\Phi, \nu)$ in the other dimension, i.e. keeping the dissociation laser fluence Φ fixed and varying ν . Assuming that in the limit of high fluence the dissociation step is saturated (i.e. the dissociation probability is unity), we can convert the dissociation yields Y into dissociation probabilities D by normalising the signals with the value of Y at saturation. This way, we construct the photofragment

spectrum $D(\nu)$ which is the dissociation probability as a function of the dissociation laser frequency.



(a) Dissociation yield of $^{12}\text{CF}_3\text{H}$ pre-excited via the 3_1 band for a fluence of the CO_2 laser of $\Phi = 2 \text{ J cm}^{-2}$.

(b) Dissociation yield of $^{13}\text{CF}_3\text{H}$ pre-excited via the 3_1 band for a fluence of the CO_2 laser of $\Phi = 4 \text{ J cm}^{-2}$.

Figure 4.8: Sample curves of measured dissociation probability.

For convenience, we describe the dissociation yield curves with the following function[‡]:

$$D_{sat}(\nu) = 1 - \exp\left(-B \cdot \exp\left(-\left(\frac{\nu - \nu_0}{\omega}\right)^2\right)\right) \quad (4.1)$$

B , ν_0 and ω are fitting constants and depend on the fluence Φ of the CO_2 laser: ν_0 is the centre of the band, ω the width and B is a measure of saturation. For $B \ll 1$, which corresponds to the unsaturated case, we have

$$D_{sat}(\nu) \approx B \cdot \exp\left(-\left(\frac{\nu - \nu_0}{\omega}\right)^2\right), \quad (4.2)$$

which is a gaussian curve centred at ν_0 and with a width ω . Curves obeying equation 4.1

[‡]The overall dissociation step is the result of multiple absorption steps. We assume that the absorption spectrum $\sigma_i(\nu)$ for every single absorption step i to have a Gaussian dependence on laser wavelength, so the photofragment spectrum $D(\nu) = \prod_i \sigma_i(\nu)$ is also Gaussian. In order to take into account saturation effects, the amount of dissociated molecules is given by² $D_{sat}(\nu) = 1 - \exp(-c \cdot \Phi \cdot D(\nu))$ where Φ is the fluence of the dissociation laser and c is an adequate scaling parameter. This relation can be easily identified with equation 4.1.

are fitted to the experimental data for different fluences of the CO₂ laser. Unfortunately we only have parts of the photofragment spectra due to the limited tuning range of the CO₂ laser, which makes the uncertainties on the fitted constants relatively large (see figure 4.8). Figure 4.9 shows the values of ν_0 , ω and B obtained for the ¹²CF₃H and the ¹³CF₃H isotopomers for different fluences.

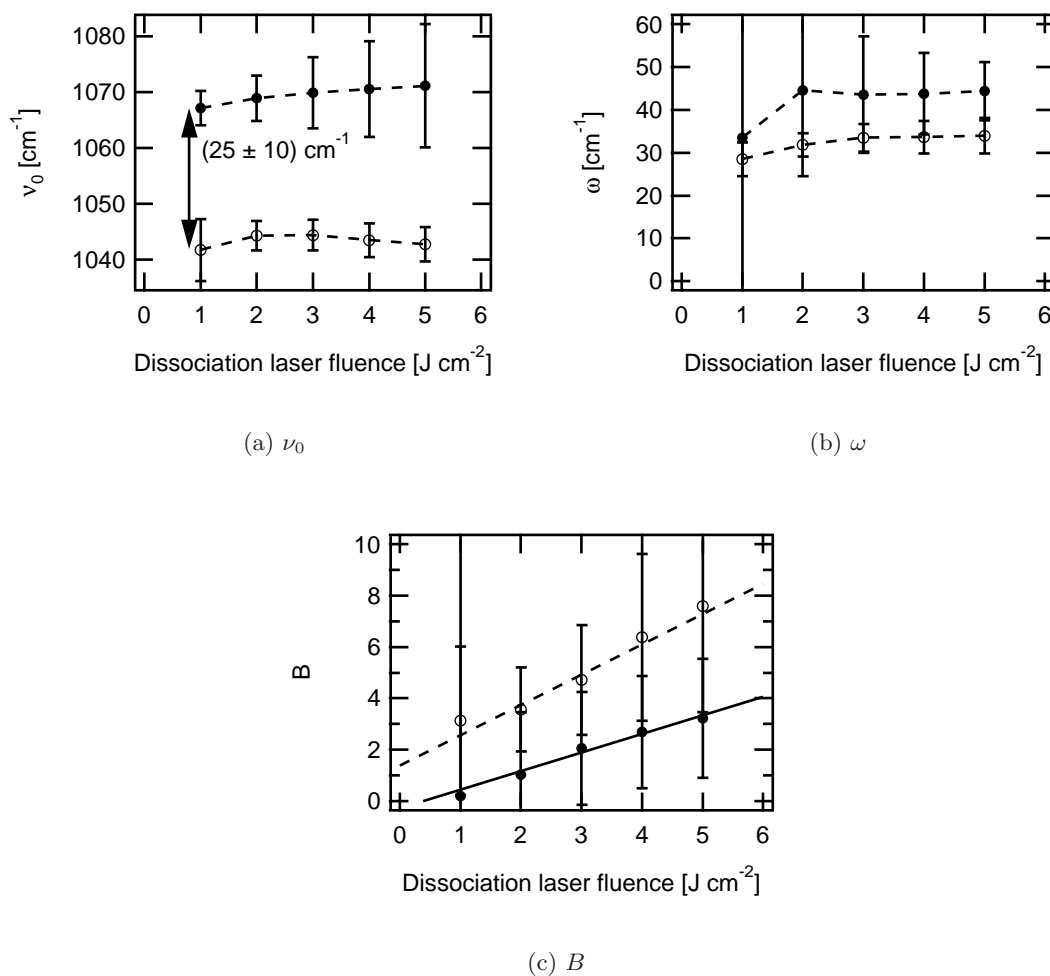


Figure 4.9: ν_0 , ω and B found for the photofragment spectra of excited ¹²CF₃H and ¹³CF₃H for different fluences of the CO₂ laser.

● ¹²CF₃H, ○ ¹³CF₃H

The following statements can be made about the dependence of fitted values ν_0 , ω and

B on the dissociation laser fluence Φ :

- The centre ν_0 does not change significantly upon increasing the Φ . The difference between the centres for $^{12}\text{CF}_3\text{H}$ and $^{13}\text{CF}_3\text{H}$ lies around $\sim 25 \text{ cm}^{-1}$, which corresponds to the isotopic shift of the absorption spectrum of the ν_5 band in the vibrational ground state.
- The width ω for $^{13}\text{CF}_3\text{H}$ seems to increase slightly upon an increase of Φ , for $^{12}\text{CF}_3\text{H}$ the uncertainties are too large to make any statements. The origin of this broadening may either be unreal, or, if it is real, due to power broadening: we estimate a typical broadening[‡] of $\sim 1 \text{ cm}^{-1}$ for a fluence of 3 J cm^{-2} .
- B , which is a measure of the saturation, is a linear function of Φ , which is also expected considering the footnote on page 117. For $^{12}\text{CF}_3\text{H}$ there is a slight offset: B is 0 for $\Phi \approx 0.4 \text{ J cm}^{-2}$, which demonstrates the non-linearity of MPD. This value is coherent with a previously measured³ IRMPD threshold of $0.2\text{-}0.3 \text{ J cm}^{-2}$. For $^{13}\text{CF}_3\text{H}$ this “threshold” seems to be negative, but the uncertainties on the values of B are relatively large.

The measured photofragment spectra demonstrate the red shift of the absorption spectra as the molecules gain vibrational energy. The centre at $\sim 1070 \text{ cm}^{-1}$ (for $^{12}\text{CF}_3\text{H}$) lies well to the red with respect to the centre of the absorption spectra of CF_3H in the vibrational ground state, which lies at 1158 cm^{-1} . It is also shifted to lower frequencies with respect to the photofragment spectra of CF_3H molecules in the ground state, where appreciable dissociation is measured⁴ only for frequencies higher than $\sim 1080 \text{ cm}^{-1}$.

4.3.3 Results: dissociation selectivity

Here we compare the dissociation probabilities of $^{12}\text{CF}_3\text{H}$ and $^{13}\text{CF}_3\text{H}$ pre-excited via the 3_1 band under collision-free conditions. The dissociation probability does not depend on the rotational state of the pre-excited molecule⁵. We measure the dissociation selectivity S , which is defined as follows:

[‡]At higher laser radiation fields, absorption features are broadened by a Lorentzian of a width of δE . This power broadening is $\delta E = \mu \cdot E$ where μ is the transition dipole moment of the pumped mode, ν_5 , and E is the electric field from the laser radiation. The electric field can be calculated from the relation $S = \epsilon_0 c E^2$ where S is the energy flux, c is the speed of light and ϵ_0 is the electric constant.

$$S := \frac{{}^{13}D}{{}^{12}D} = \frac{{}^{13}Y / {}^{13}P}{{}^{12}Y / {}^{12}P}, \quad (4.3)$$

where ${}^x D$ is the dissociation probability, ${}^x Y$ the number of dissociated and ${}^x P$ the number of pre-excited molecules. For this we measure IRLAPS action spectra around the Q-branch of the 3_1 band of ${}^{13}\text{CF}_3\text{H}$ and separate the measured spectrum into a part due to the ${}^{12}\text{CF}_3\text{H}$ (P-branches) and a part due to the ${}^{13}\text{CF}_3\text{H}$ isotopomer (Q-branch) (see figure 4.10). We can take any of the P-branches for the ${}^{12}\text{CF}_3\text{H}$ isotopomer for the evaluation of S . The ratio ${}^{13}Y / {}^{12}Y$ is evaluated from the IRLAPS action spectrum taken, the ratio ${}^{12}P / {}^{13}P$ can be evaluated from a photoacoustic spectrum which reflects the pre-excitation probability.

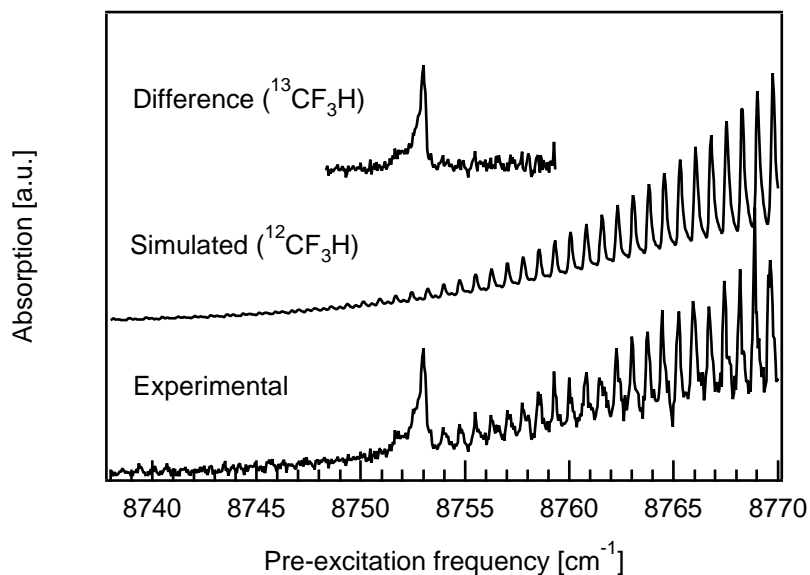


Figure 4.10: An IRLAPS action spectrum around the Q-branch of the 3_1 band in ${}^{13}\text{CF}_3\text{H}$ is split into two parts due to the two different isotopomers.

This selectivity S is only due to different IRMPD efficiencies of the two isotopomers, any effects due to isotopically selective collisional relaxation are excluded because the experiments are done in a collision-free environment (low pressure) at a zero time-delay between the lasers. For this, we identify $S_{IRMPD} = S$.

We measure dissociation selectivities S_{IRMPD} for different dissociation laser frequencies

and fluences. We show in figure 4.11 an example of a measurement of S_{IRMPD} for two different dissociation laser frequencies (978 and 1052 cm^{-1}). Measured data is interpolated by an adequate empirical fitting function ($S_{IRMPD}(\Phi) = 1 + A \cdot \left(\frac{\Phi}{\text{J cm}^{-2}}\right)^\alpha \cdot \exp\left(-\frac{\Phi}{\Phi_0}\right)$, where A , α and Φ_0 are fitting constants).

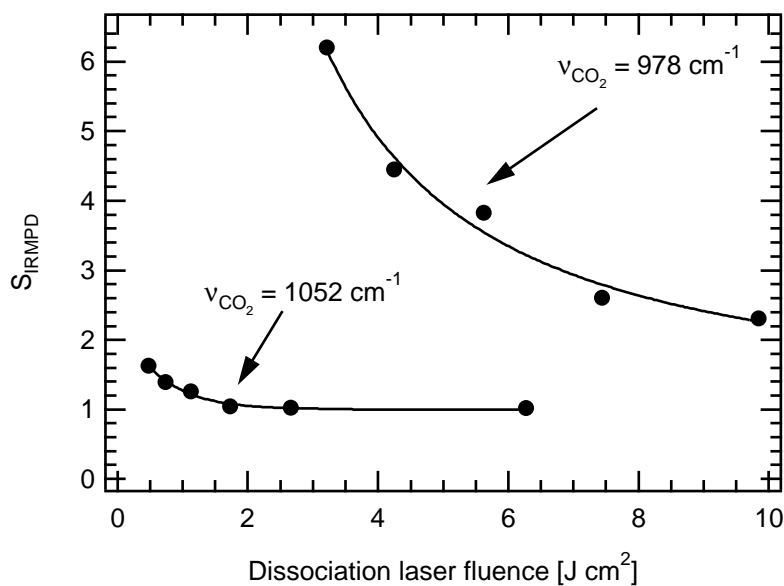


Figure 4.11: Example of a measurement of the dissociation selectivity S_{IRMPD} . The sample pressure is 0.4 mbar.

We show in figure 4.12 the dissociation selectivities S_{IRMPD} for two laser fluences (2 and 9 J cm⁻²) for pre-excitation via the 3₁ band. There is a very clear dependence of S_{IRMPD} on the wavelength of the CO₂ laser. The ratio of the dissociation probabilities S_{IRMPD} increases significantly to $S_{IRMPD} \gg 1$ as we tune the dissociation laser wavelength out of resonance. As we have shown in section 4.3 the absolute yield however decreases considerably at the same time.

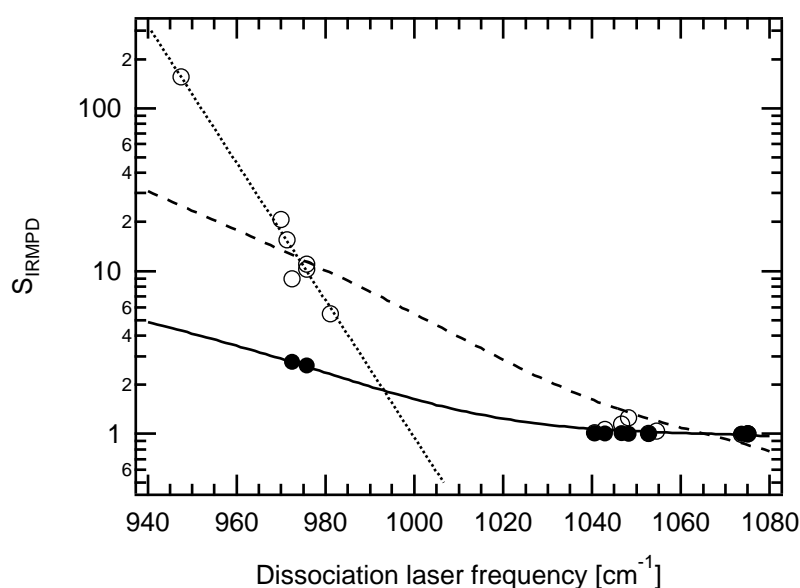


Figure 4.12: Dissociation selectivity S_{IRMPD} for \circ 3 J cm⁻² and \bullet 9 J cm⁻².

► The — full and - - dashed lines are obtained by dividing the fitted curves (equation 4.1) to the photofragment spectra for ¹²CF₃H and ¹³CF₃H presented in section 4.3 by each other (for a fluence of 9 J cm⁻² the fitting parameters in equation 4.1 are extrapolated from the data for 1-5 J cm⁻²). For a fluence of 3 J cm⁻² the curves do not fit the datapoints very well which shows the limits of our fitting function.

► For the \cdots dotted line, see text in section 4.3.4.

We also measure S_{IRMPD} for molecules pre-excited through the 2₁ band, i.e. they are promoted up to ~ 5950 cm⁻¹ before dissociation. For this pre-excitation energy, we measure S_{IRMPD} for a dissociation laser frequency of 1047 cm⁻¹. Figure 4.13 shows the measurements such as the equivalent data for molecules pre-excited through the 3₁ band.

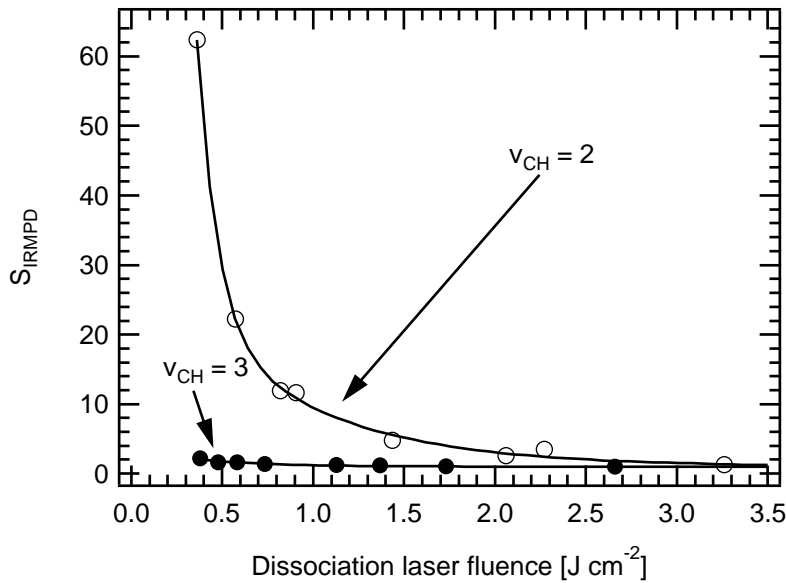


Figure 4.13: Dissociation selectivity S_{IRMPD} for molecules pre-excited via the \bullet 3_1 and via the \circ 2_1 bands for a dissociation laser frequency of 1047 cm^{-1} .

For the region between 0.4 and 3 J cm^{-2} an enhancement of isotopic selectivity of up to 30 is measured (for $\Phi \approx 0.4 \text{ J cm}^{-2}$) as the pre-excitation energy is lowered from 8800 to 5950 cm^{-1} . This increase is measured under collision-free conditions and is only due to different IRMPD efficiencies.

4.3.4 Discussion

We can tentatively try to explain the measured photofragment spectra and the dissociation selectivities by a simple model as follows. The photofragment spectrum is, in principle, a product of single absorption steps

$$D(\nu) = \sigma_1(\nu) \cdot \sigma_2(\nu) \cdot \dots \cdot \sigma_n(\nu), \quad (4.4)$$

where $\sigma_i(\nu)$ is the absorption probability of step i . With the knowledge of fundamental frequencies and the spectroscopic anharmonic constants of a molecule, it is possible to evaluate the absorption spectrum of a molecule with a vibrational energy E . As will be shown later (see section 5.1), we estimate this spectrum $\sigma_E(\nu)$ to be:

$$\sigma_E(\nu) \simeq \frac{A(E)}{\omega(E)\sqrt{\pi}} \cdot \exp\left(-\left(\frac{\nu - \nu_0(E)}{\omega(E)}\right)^2\right), \quad (4.5)$$

where

$$\begin{aligned} A(E) &= 1 + 2.08 \cdot 10^{-4} \cdot \left(\frac{E}{\text{cm}^{-1}}\right) \\ \omega(E) &= \sqrt{(15.9\text{cm}^{-1})^2 + (3.05 \cdot 10^{-3} \cdot E)^2} \\ \nu_0(E) &= 1158\text{cm}^{-1} - 6.35 \cdot 10^{-3} \cdot E \end{aligned} \quad (4.6)$$

The photofragment spectrum of a molecule pre-excited to 8800 cm^{-1} ($\nu_{CH} = 3$) is given by equation 4.4 where the product goes over all intermediate steps between 8800 and $24,000 \text{ cm}^{-1}$ which is the dissociation limit.

If we try to calculate the photofragment spectrum using this Ansatz, we see that there is a large discrepancy between the simulated and measured photofragment spectra: although the centre of the photofragment spectrum of, for example, vibrationally excited $^{13}\text{CF}_3\text{H}$ is correctly predicted at $\sim 1045 \text{ cm}^{-1}$, the width is well underestimated (12 cm^{-1} compared to $35\text{-}45 \text{ cm}^{-1}$ measured experimentally). We show in figure 4.14 data measured for a dissociation laser fluence of 2 J cm^{-2} and the corresponding dissociation yields predicted with equation 4.4.

This figure demonstrates that our model for the calculation of dissociation yields is too simple. For the numerical reproduction of the measured data, we need to use more sophisticated simulations. For the explanation of the dissociation yields, a simple model consisting of a multiplication of the subsequent absorption steps, is not enough. This is because we do not take into account any non-linearity effects of the single absorption steps, and stimulated emission of photons is neglected too. Furthermore, we should adapt a dynamical picture of the subsequent absorption steps rather than simply multiply absorption spectra. We present in section 5.3 master equation calculations including all these effects.

Concerning the dissociation selectivity the following can be stated:

- For molecules pre-excited via the 3_1 band, substantial isotopic selectivity is gained

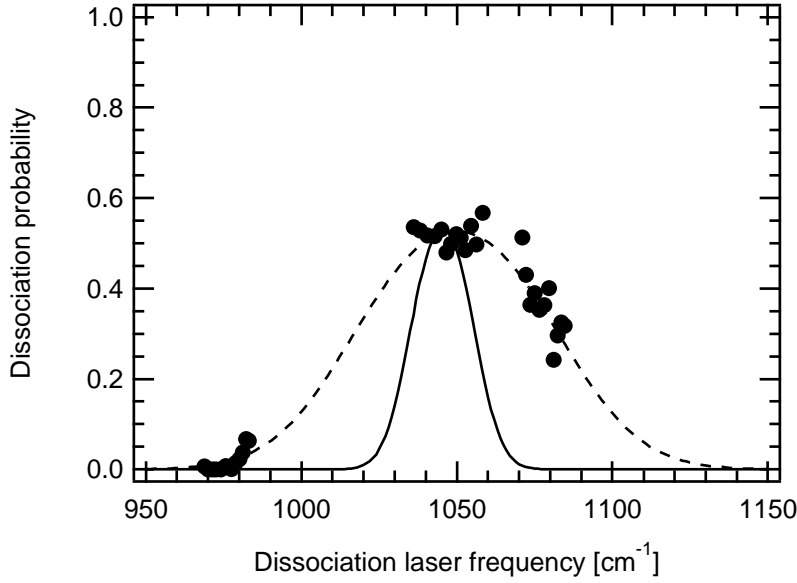


Figure 4.14: Comparison of • - - experimental and — predicted dissociation yields for vibrationally excited $^{13}\text{CF}_3\text{H}$.

for off-resonant dissociation laser frequencies ($\lesssim 1000 \text{ cm}^{-1}$). For typical wavelengths used for laser isotope separation, selectivity is only gained for moderate and low fluences of the dissociation laser radiation.

- The behaviour of S_{IRMPD} as a function of the frequency of the dissociation laser frequency can be understood as follows (see figure 4.12 on page 122). The dissociation yield Y of excited molecules has roughly a Gaussian dependence on the frequency ν of the CO_2 laser (see section 4.3.2). Within this approximation, the dissociation selectivity is

$$\begin{aligned}
 S_{IRMPD}(\nu) &= \frac{{}^{13}Y(\nu)}{{}^{12}Y(\nu)} \\
 &= \frac{\exp\left(-\left(\frac{\nu-\nu_{13}}{\omega}\right)^2\right)}{\exp\left(-\left(\frac{\nu-\nu_{12}}{\omega}\right)^2\right)} \\
 &\propto \exp\left(-\frac{2\cdot\nu\cdot(\nu_{12}-\nu_{13})}{\omega^2}\right) ,
 \end{aligned} \tag{4.7}$$

where ν_{12} and ν_{13} are the centres of the Gaussians describing the dissociation probabilities and ω is the width. An exponential dependence of S_{IRMPD} on ν is predicted (equation 4.7). The data on figure 4.12 does not suggest such an

exponential behaviour. However, at central frequencies around 1040-1060 cm^{-1} the dissociation yields are partly saturated and the dissociation probability is hence not well described by a Gaussian in that region. Fitting an exponential to the dissociation selectivity for frequencies below 1000 cm^{-1} where the dissociation is far from saturation (see figure 4.8 on page 117) yields a slope of ~ 0.097 (dotted line in figure 4.12) which gives, using $\nu_{12} - \nu_{13} = 25 \text{ cm}^{-1}$, a value of 23 cm^{-1} for ω which compares well with the values obtained by the direct measurements of the photofragment excitation spectra ($\omega \approx 30\text{-}40 \text{ cm}^{-1}$, see figure 4.9-b).

- For a dissociation laser frequency of 1047 cm^{-1} , the dissociation yield selectivity is greatly enhanced using vibrational pre-excitation up to $v_{CH} = 2$ instead of $v_{CH} = 3$, especially for moderate and low dissociation laser fluences. In particular, we cannot make any statements concerning the increase of isotopic selectivity of a factor of 16 upon an adequate increase of pressure and time-delay between the lasers previously observed for CF_3H molecules pre-excited via the 3_1 band⁶, as the experimental conditions are not exactly the same. This 16 fold increase may or may not be explained only by different IRMPD rates.

4.3.5 Conclusions

We have measured photofragment excitation spectra and dissociation selectivities of vibrationally pre-excited ($v_{CH} = 3$) CF_3H molecules. The experimental conditions (in particular the zero time-delay between the pre-excitation and dissociation lasers and the low pressures) are such that any effects of vibrational relaxation are excluded and any dissociation selectivities are only due to different IRMPD rates. We have measured a typical shift of $\sim 25 \text{ cm}^{-1}$ between the photofragment excitation spectra of excited $^{12}\text{CF}_3\text{H}$ and excited $^{13}\text{CF}_3\text{H}$, which demonstrates that the shift of the ground state absorption spectra (25 cm^{-1}) is maintained upon excitation. We have determined the width of the photofragment excitation spectrum of molecules pre-excited to the second overtone of the C-H stretch vibration: first, by a direct measurement of this spectrum (section 4.3.2) and then by comparison of the dissociation yield for excited $^{12}\text{CF}_3\text{H}$ and $^{13}\text{CF}_3\text{H}$ (section 4.3.3). The values compare well: $\omega \approx 20 - 30 \text{ cm}^{-1}$ determined by direct measurement and $\omega \approx 23 \text{ cm}^{-1}$ determined by comparison of the dissociation yields of the two different isotopomers.

Further we have determined strong dependencies of the photofragment excitation spectra on the dissociation laser fluence which complicates the data analysis strongly, and we showed that for a better understanding of our results we need to perform master equation calculations.

4.4 Separation of different mechanisms changing the wavelength of the dissociation laser

4.4.1 Introduction

In this section we present experiments where we investigate the influence of different vibrational relaxation rates on the increase of isotopic selectivity upon an increase of the time-delay between the pre-excitation and the dissociation lasers. For this, we use the result obtained previously in section 4.3: the properties of the IRMPD step are the same for $^{12}\text{CF}_3\text{H}$ and $^{13}\text{CF}_3\text{H}$ if the wavelength of the dissociation laser is shifted by 25 cm^{-1} to the red for excited $^{13}\text{CF}_3\text{H}$ with respect to the wavelength used to dissociate excited $^{12}\text{CF}_3\text{H}$.

In these experiments the pre-excitation laser is first set to the Q-branch of an overtone of the CH stretching-bending vibration of $^{12}\text{CF}_3\text{H}$, the fluence of the dissociation laser is kept fixed and its frequency is set to a certain value ν . The time-delay between the pre-excitation and the dissociation lasers is scanned and the decay rate ^{12}k is determined from this. This value is compared to ^{13}k measured the same way, pre-exciting $^{13}\text{CF}_3\text{H}$ at its Q-branch and using a dissociation laser frequency of $\nu - 25\text{ cm}^{-1}$. The energy level diagram followed in these experiments is shown in figure 4.15.

4.4.2 Results

Experiments are performed for molecules pre-excited via the 3_1 ($\sim 8800\text{ cm}^{-1}$) and via the 4_1 ($\sim 11,500\text{ cm}^{-1}$) bands. We present the results we obtain for molecules pre-excited to $\sim 8800\text{ cm}^{-1}$ in some detail, the procedures for molecules pre-excited to $\sim 11,500\text{ cm}^{-1}$ are in principle exactly the same. The final results are presented for both cases at the

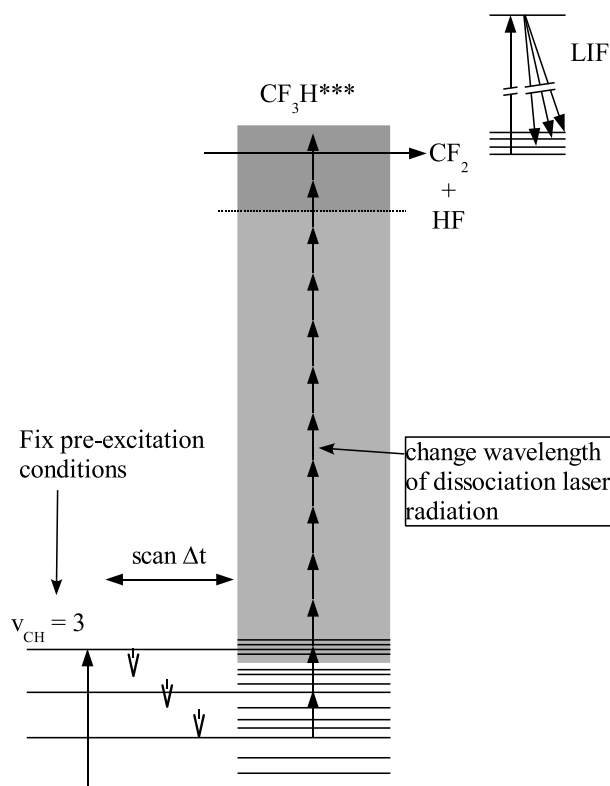
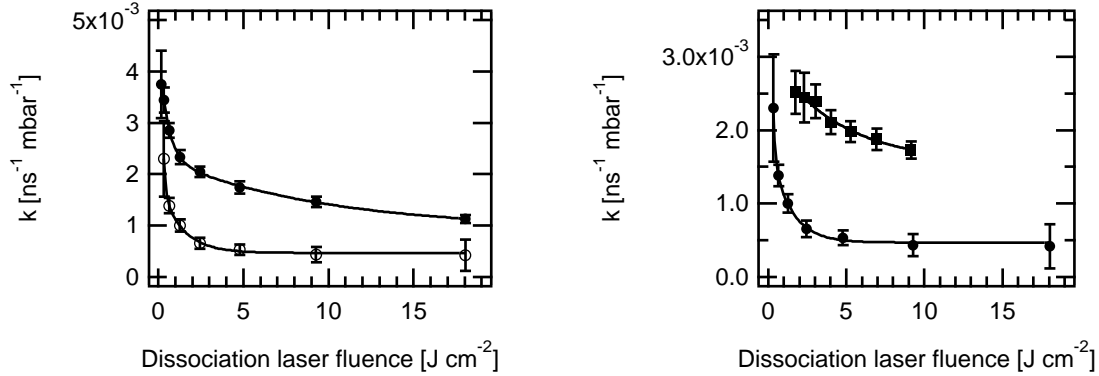


Figure 4.15: Energy scheme used in the experiments for the relaxation experiments changing the wavelength of the dissociation laser.

end.

The measurements for CF_3H molecules pre-excited via the 3_1 band are carried out for a set of different frequencies of the dissociation laser, namely 981, 1036, 1042, 1047, 1051, 1054 and 1078 cm^{-1} . Figure 4.16 shows two examples of measured decay rates k . In one graph we compare the measurements done for $^{12}\text{CF}_3\text{H}$ with those done for $^{13}\text{CF}_3\text{H}$, in the second graph measurements done with two different dissociation laser frequencies are compared for $^{13}\text{CF}_3\text{H}$.

We find that a double exponential function fits the data very well: $k(\Phi) = A + B_1 \cdot \exp(-C_1 \cdot \Phi) + B_2 \cdot \exp(-C_2 \cdot \Phi)$, where Φ is the fluence of the dissociation laser radiation. The fitting parameters A , B_1 , C_1 , B_2 and C_2 depend on the CO_2 dissociation laser fluence and wavelength and, of course, the isotopic species of the molecule. The



(a) Decay rate k for the \bullet $^{12}\text{CF}_3\text{H}$ and the \circ $^{13}\text{CF}_3\text{H}$ isotopomers at a frequency of 1078 cm^{-1} of the CO_2 laser.

(b) Decay rate k for the $^{13}\text{CF}_3\text{H}$ isotopomer, for a frequency of \bullet 1078 and \blacksquare 981 cm^{-1} of the CO_2 laser.

Figure 4.16: Sample measurements of the decay rate k . The errorbars are fitting errors (see section 4.1.3).

function is purely empirical.

With this information, we can evaluate k at a fix fluence for different dissociation laser frequencies used in our experiments. Figure 4.17 shows an example of interpolated values of k obtained this way, for a fluence of 3 J cm^{-2} .

A linear function, $k(\nu) = A + B \cdot \nu$ seems to be a reasonable fit for the data points on figure 4.17, where A and B are fitting parameters and depend on the fluence of the dissociation laser and the isotopic species.

4.4.3 Discussion

For the data analysis, the effect of different IRMPD rates can be eliminated if we compare measurements using a CO_2 laser frequency ν for $^{13}\text{CF}_3\text{H}$ and $\nu + 25\text{ cm}^{-1}$ for $^{12}\text{CF}_3\text{H}$. Thus, we define the ratio

$$\mathbb{S}_{VET}(\nu, \Phi) := \frac{k_{12}(\nu, \Phi)}{k_{13}(\nu - 25\text{cm}^{-1}, \Phi)}, \quad (4.8)$$

where $k_x(\nu, \Phi)$ is the decay rate of $^x\text{CF}_3\text{H}$ at a dissociation laser frequency ν and fluence

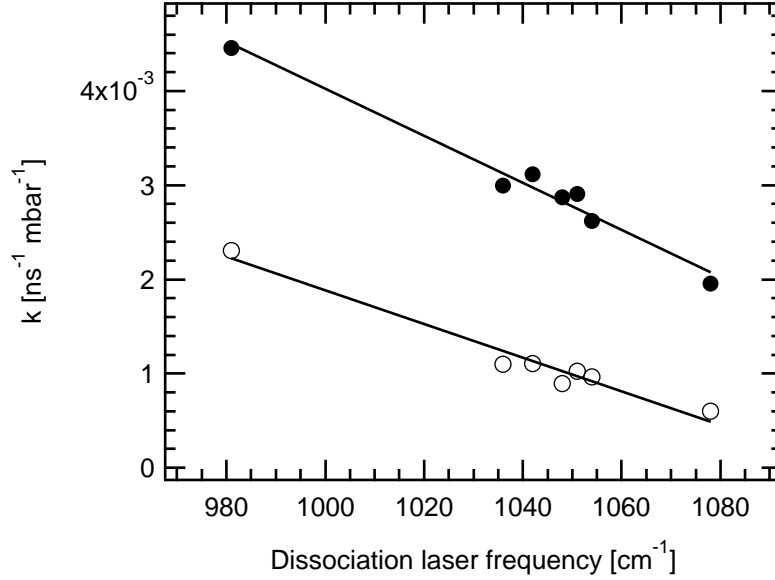


Figure 4.17: Decay rate k for \bullet $^{12}\text{CF}_3\text{H}$ and \circ $^{13}\text{CF}_3\text{H}$ at a fluence of $\Phi = 3 \text{ J cm}^{-2}$ as a function of the dissociation laser frequency.

Φ . It can be calculated for dissociation laser frequencies between ~ 980 and $\sim 1080 \text{ cm}^{-1}$ using the linear fit we did for $k(\nu)$. \mathbb{S}_{VET} is the decay selectivity due to isotopically selective collisional relaxation. Analogous to this value, we can define the decay selectivity due to different IRMPD rates:

$$\mathbb{S}_{IRMPD}(\nu, \Phi) := \frac{\mathbb{S}_{tot}}{\mathbb{S}_{VET}} = \frac{k_{13}(\nu - 25\text{cm}^{-1}, \Phi)}{k_{13}(\nu, \Phi)}, \quad (4.9)$$

where $\mathbb{S}_{tot} = k_{12}(\nu, \Phi)/k_{13}(\nu, \Phi)$ is the total decay selectivity (ratio of decay rates).

We show in figure 4.18 the values of \mathbb{S}_{IRMPD} and \mathbb{S}_{VET} as a function of the fluence of the dissociation laser, for a dissociation laser wavelength $\nu = 1047 \text{ cm}^{-1}$.

It can be seen, that in general isotopically selective collisional relaxation contributes more to the decay selectivity \mathbb{S}_{tot} than the different IRMPD rates.

We define the ‘‘importance’’ (or contribution) of a mechanism for a gain in selectivity to be

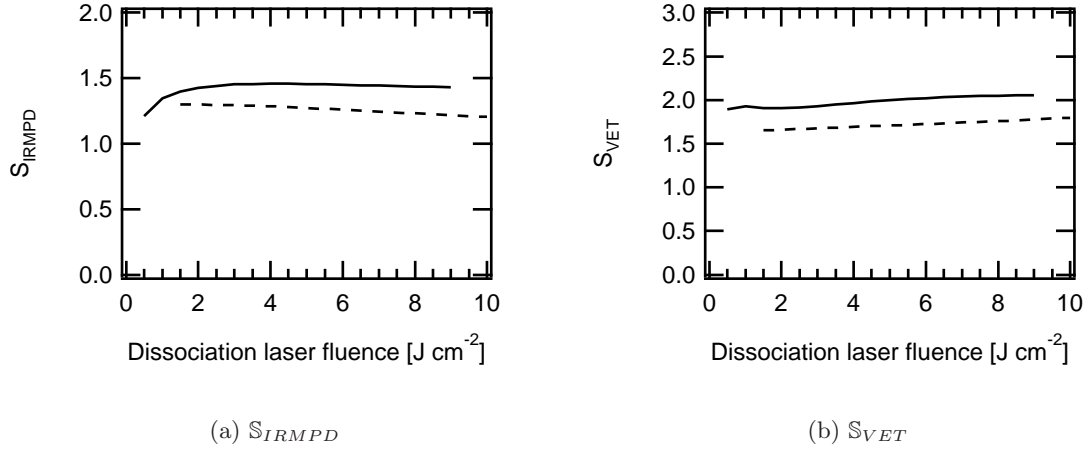


Figure 4.18: S_{IRMPD} and S_{VET} determined by changing the wavelength of the CO₂ dissociation laser for pre-excitation via the — 3₁ and the - - 4₁ bands.

$$\mathcal{I}_x := \frac{S_x - 1}{\sum_i (S_i - 1)}, \quad (4.10)$$

where $x = \text{IRMPD}$ and VET (this way $\mathcal{I}_{IRMPD} + \mathcal{I}_{VET} = 1$).

Following equation 4.10 for the evaluation of the relative importance of a mechanism to the increase of isotopic selectivity, we evaluate the relative contributions shown in table 4.3 to the enhancement of the isotopic selectivity upon leaving a time-delay between the pre-excitation and dissociation lasers.

	\mathcal{I}_{VET}	\mathcal{I}_{IRMPD}
3 ₁	0.67	0.33
4 ₁	0.70	0.30

Table 4.3: Relative contributions of isotopically selective collisional relaxation and isotopically selective IRMPD to the enhancement of isotopic selectivity, for a dissociation laser fluence of 3 J cm⁻² and frequency of 1047 cm⁻¹.

We show in figure 4.19 the importance of the isotopically selective collisional relaxation and isotopically selective IRMPD rates for a dissociation laser wavelength 1047 cm⁻¹

as a function of the dissociation laser fluence.

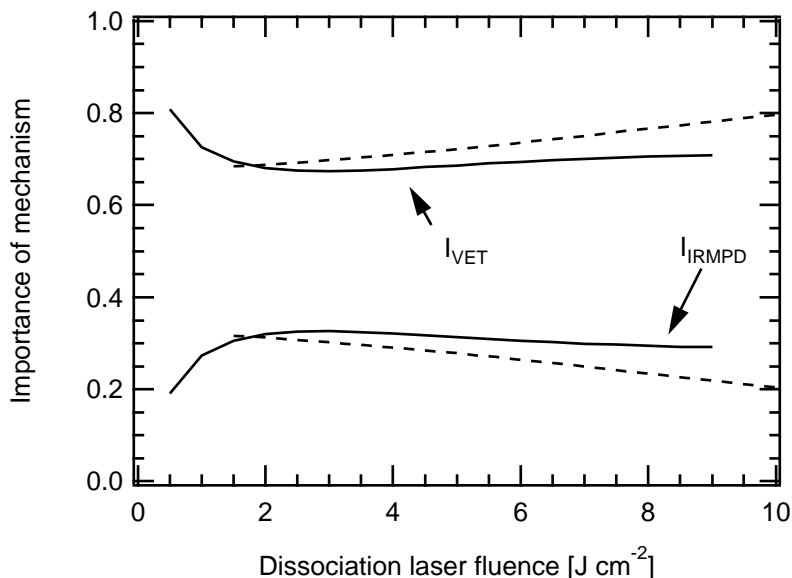


Figure 4.19: Importance \mathcal{I} of a mechanism for the enhancement of isotopic selectivity upon leaving a time-delay between the pre-excitation and the dissociation lasers, for a dissociation laser frequency of 1047 cm^{-1} , for pre-excitation via the — 3_1 and via the - - 4_1 bands.

Finally, from the values of S_{VET} we can make certain conclusions concerning the relative vibrational relaxation rates. With our detection system, the CO_2 laser selectively dissociates pre-excited molecules and subsequently detects the photofragments via LIF. We do not exclusively detect molecules that still have all their initial rovibrational energy at the onset of the dissociation laser, but also some molecules having lost a part of it. Because they lose vibrational energy, their dissociation probability drops. This drop of the dissociation probability depends on the fluence of the dissociation laser. In the limit of high fluences and in the limit of low fluences the *drop* of dissociation probability as a function of the vibrational energy in the molecule is small and goes through a maximum somewhere in between. This can be found by determining the fluence at which the decay rate is maximum: this value lies in general around $1\text{-}2\text{ J cm}^{-2}$. We give some details in appendix D. The value of S_{VET} around $1\text{-}2\text{ J cm}^{-2}$ is hence close to the ratio of absolute relaxation rates $^{12}\kappa$ and $^{13}\kappa$:

$$S_{VET} \approx \frac{{}^{13}\kappa}{{}^{12}\kappa} \quad (4.11)$$

With this, we determine the ratio of relaxation rates of 1.91 for molecules pre-excited through the 3_1 band and 1.65 for molecules pre-excited through the 4_1 band, that is ${}^{12}\text{CF}_3\text{H}$ relaxes 1.91 (1.65) times faster on itself than ${}^{13}\text{CF}_3\text{H}$ on ${}^{12}\text{CF}_3\text{H}$.

Note that the ratio of relaxation rates ${}^{12}\kappa/{}^{13}\kappa$ depends on the internal energy. The selectivity in collisional relaxation decreases upon an increase of the level of vibrational pre-excitation (here, from 8800 up to 11,500 cm^{-1}).

4.4.4 Conclusion

By measuring decay rates k as a function of the frequency of the dissociation laser, we can eliminate the influence of a difference in IRMPD efficiencies of the two isotopomers on the observed isotopic selectivity. First, this allows us to quantify the relative contributions of isotopically selective collisional relaxation and isotopically selective IRMPD to the increase of isotopic selectivity upon leaving a time-delay between the pre-excitation and dissociation lasers. At the same time, we have determined the relative relaxation rates of excited ${}^{12}\text{CF}_3\text{H}$ and excited ${}^{13}\text{CF}_3\text{H}$ on ${}^{12}\text{CF}_3\text{H}$ molecules in the ground state: we have determined that for molecules pre-excited via the 3_1 band ${}^{12}\text{CF}_3\text{H}$ relaxes ~ 1.91 times faster than ${}^{13}\text{CF}_3\text{H}$, and for molecules pre-excited via the 4_1 band they relax ~ 1.65 times faster.

4.5 Separation of different mechanisms using a carbon-13 enriched sample

4.5.1 Introduction

In this section we present experiments where we investigate the influence of different IRMPD rates and different vibrational relaxation rates on the increase of isotopic selectivity upon an increase of the time-delay between the pre-excitation and dissociation lasers. By using ${}^{13}\text{CF}_3\text{H}$ as relaxation partner for excited ${}^x\text{CF}_3\text{H}$ molecules instead of ${}^{12}\text{CF}_3\text{H}$ (which is the main relaxation partner in a normal isotopic abundant gas) we are able to directly separate the mechanisms of isotopically selective VET and isotopically

selective IRMPD to the different decay rates. The production of $^{13}\text{CF}_3\text{H}$ is described in section 3.3.

In these experiments the pre-excitation laser is set to the Q-branch of an overtone of the CH stretching-bending vibration of $^{13}\text{CF}_3\text{H}$, the dissociation laser fluence and wavelength are kept fixed and the time-delay between the two lasers is scanned. This way we measure the decay rates $k(x^* - y)$ where $x, y = 12, 13$ which is the rate at which the $^x\text{CF}_3\text{H}$ molecules disappear from the dissociation window when relaxing on $^y\text{CF}_3\text{H}$ in the ground state. For practical reasons, we measure this decay rates for different mixtures of $^{12}\text{CF}_3\text{H}$ and $^{13}\text{CF}_3\text{H}$ (always keeping the total pressure at 1 mbar), fit a linear dependence to k as a function of the isotopic composition of the sample and extrapolate to 0 and 100% of $^{13}\text{CF}_3\text{H}$. The energy level diagram followed in these experiments is shown in figure 4.20.

4.5.2 Results

We present experiments where the decay rate k is measured for different pre-excitation energies (pre-excitation via 2_1 , 3_1 , 4_1 and 5_2 bands) and dissociation laser fluences as a function of the isotopic mixture of the sample.

As for experiments presented previously we measure the decay rates as a function of the CO_2 laser fluence because k depends on this fluence. By measuring such data for different isotopic mixtures of the sample gas (keeping the total pressure always at 1 mbar), we measure the decay rate k as a function of the fraction f of $^{13}\text{CF}_3\text{H}$ in the sample. Figure 4.21 shows an example of such a measurement.

Several points are observed:

1. The decay rate k depends on the isotopic composition of the sample.
2. The decay rates are larger when the collision partners are $^{13}\text{CF}_3\text{H}$ molecules.

The first statement is not trivial and it indicates that collisional vibrational relaxation of CF_3H is isotopically selective.

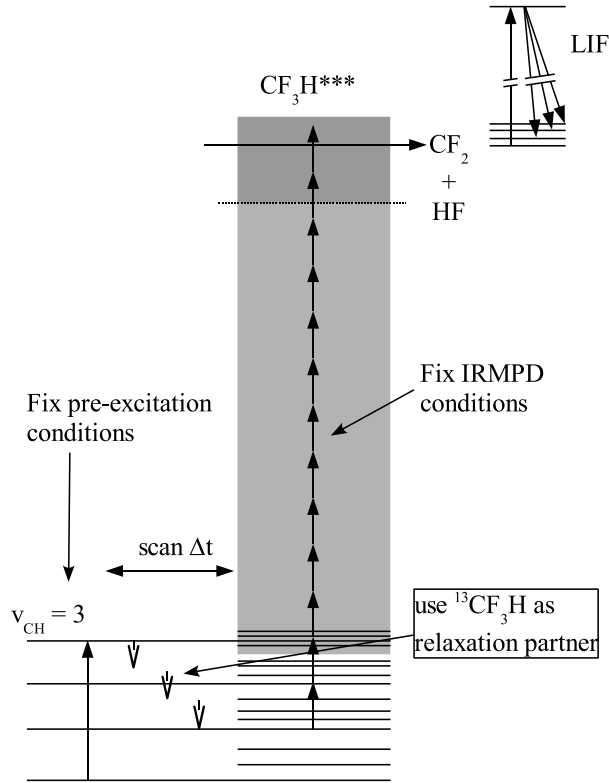


Figure 4.20: Energy scheme used in the experiments for the relaxation experiments using $^{13}\text{CF}_3\text{H}$ as relaxation partner of excited CF_3H .

We believe that this is the first direct experimental observation of isotopically selective collisional relaxation of polyatomics in the vibrational quasi-continuum.

The second statement is at first view not obvious to understand. Whereas it is intuitively understandable that excited $^{13}\text{CF}_3\text{H}$ relaxes faster on ground state $^{13}\text{CF}_3\text{H}$ than on ground state $^{12}\text{CF}_3\text{H}$ (because of stronger resonances between the same isotopic species), it may appear confusing that excited $^{12}\text{CF}_3\text{H}$ also relaxes faster on ground state $^{13}\text{CF}_3\text{H}$ than on ground state $^{12}\text{CF}_3\text{H}$. We will discuss this point in the next section.

We measure k for a set of experimental conditions (pre-excitation energy, CO_2 laser wavelength and fluence) for different isotopic compositions of the sample. We give in figures 4.22 and 4.23 the values for $k(x^* - y)$ we measure.

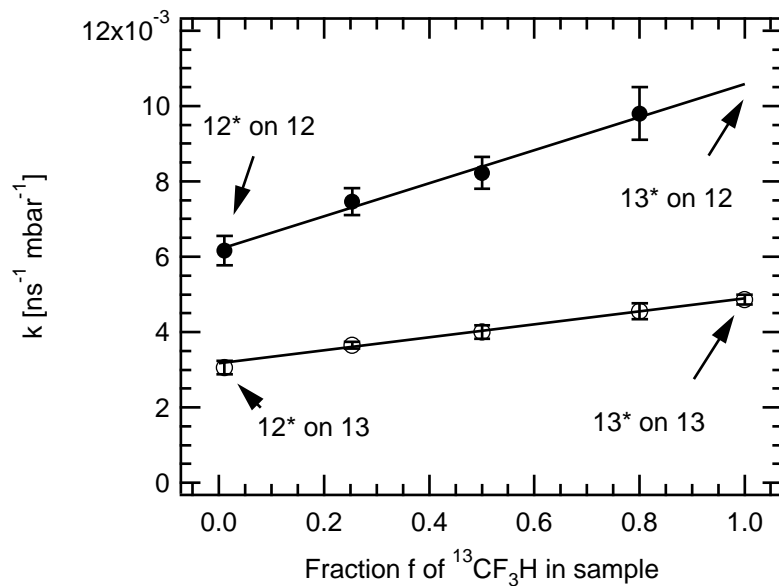


Figure 4.21: Example of measurement of the decay rate k for different isotopic composition of the sample for \bullet $^{12}\text{CF}_3\text{H}$ and \circ $^{13}\text{CF}_3\text{H}$. This example is obtained for CF_3H molecules pre-excited via the 4_1 band, for a dissociation laser fluence of 0.4 J cm^{-2} and a dissociation laser frequency of 1047 cm^{-1} . The errorbars are fitting errors (see section 4.1.3).

In the next two sections we propose an interpretation of the data presented in figures 4.22 and 4.23. We start with a qualitative interpretation (section 4.5.3) and later analyse the data on a quantitative level (section 4.5.4).

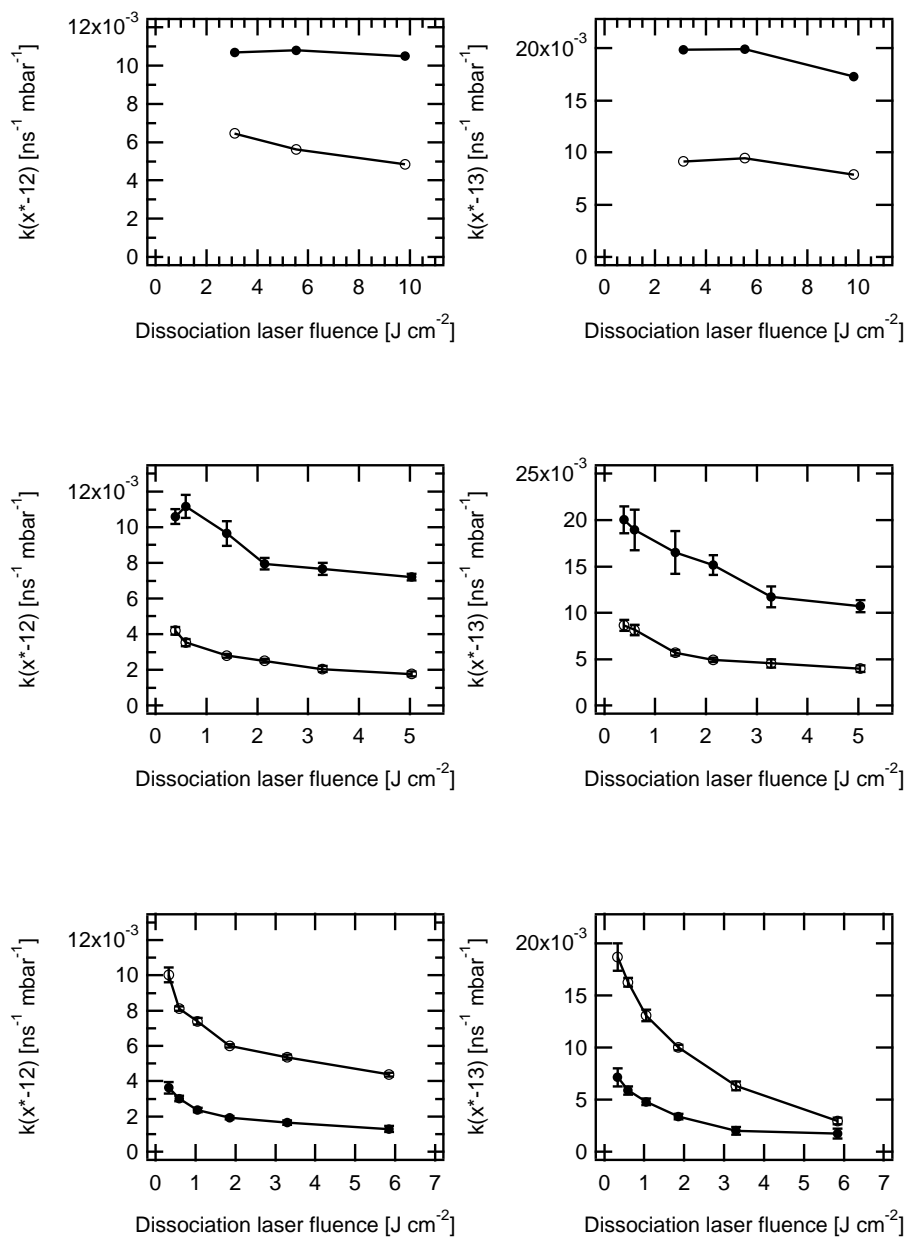


Figure 4.22: Values for $k(12^*-12)$ and $k(13^*-12)$ (left column) and $k(12^*-13)$ and $k(13^*-13)$ (right column) for molecules pre-excited via the 3_1 band. The three sets of graphs are for three different dissociation laser frequencies: 977 (top), 1047 (middle) and 1076 (bottom) cm⁻¹.

● ¹²CF₃H ○ ¹³CF₃H

The errorbars are fitting errors (see section 4.1.3).

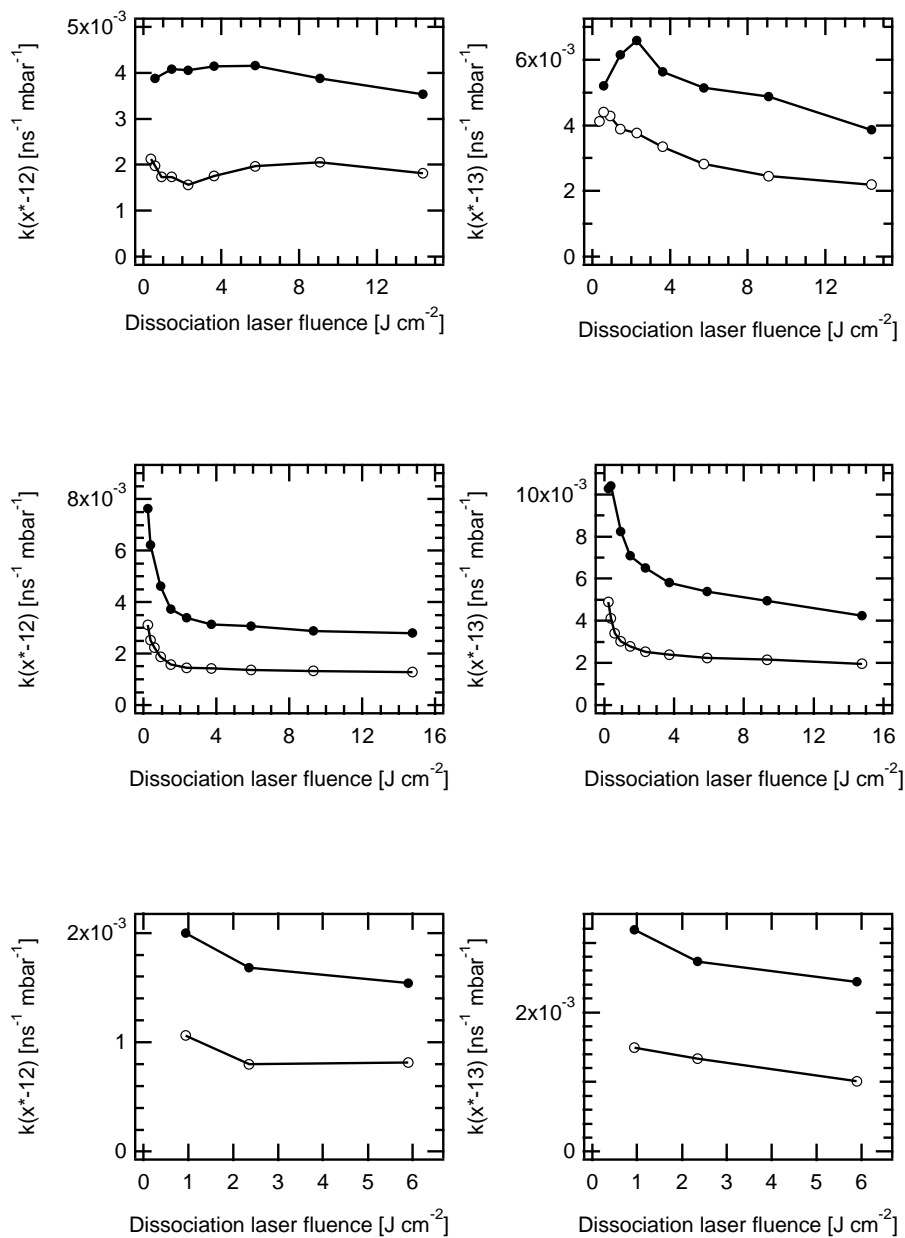


Figure 4.23: Values for $k(12^* - 12)$ and $k(13^* - 12)$ (left column) and $k(12^* - 13)$ and $k(13^* - 13)$ (right column) for molecules pre-excited via the 2₁ (top), 4₁ (middle) and 5₂ (bottom) bands. For all measurements a dissociation laser frequency of 1047 cm⁻¹ is used.

● ¹²CF₃H ○ ¹³CF₃H

4.5.3 Qualitative discussion

It is important to note that excited $^{12}\text{CF}_3\text{H}$ relaxes faster on the other isotopic species, $^{13}\text{CF}_3\text{H}$, than on itself. We explain this as follows. Vibrational energy transfer (VET) is largely mediated by dipole-dipole interactions between the two molecules. As the efficiency of VET depends strongly on the transition dipole moment between the ground state and the fundamental of the corresponding vibration, the main mediator of VET is the ν_5 mode, as it has the strongest transition dipole moment. The efficiency of this process has a reciprocal dependence on the energy mismatch between a vibrational quantum of the donor and the acceptor molecules. This energy mismatch is, in our case, determined by two values (see figure 4.24).

1. **Anharmonic shift.** Upon vibrational excitation the band origins shift to the red.
2. **Isotopic shift.** There is a shift of $\sim 25\text{ cm}^{-1}$ between the ν_5 frequencies of $^{12}\text{CF}_3\text{H}$ and $^{13}\text{CF}_3\text{H}$ (see section 4.3).

Thus, for excited $^{13}\text{CF}_3\text{H}$ molecules relaxing on ground state $^{13}\text{CF}_3\text{H}$ molecules the energy mismatch is only due to anharmonicity, while if they relax on $^{12}\text{CF}_3\text{H}$ there is an additional 25 cm^{-1} shift which makes relaxation on $^{12}\text{CF}_3\text{H}$ slower than on $^{13}\text{CF}_3\text{H}$. In the case of excited $^{12}\text{CF}_3\text{H}$ molecules relaxing on ground state $^{12}\text{CF}_3\text{H}$ molecules, there is also an energy mismatch due to the anharmonic shift. For excited $^{12}\text{CF}_3\text{H}$ molecules relaxing on ground state $^{13}\text{CF}_3\text{H}$ molecule the isotopic and the anharmonic shifts, however, have opposite signs and cancel themselves partially, which makes relaxation of excited $^{12}\text{CF}_3\text{H}$ on cold $^{13}\text{CF}_3\text{H}$ faster than on cold $^{12}\text{CF}_3\text{H}$ molecules. This idea is illustrated in figure 4.24.

In the following section we will explain how we interpretate the experimental data quantitatively.

4.5.4 Quantitative discussion

In this section we describe how to interpretate our results quantitatively. We describe how to link the measured value k (the “decay rate”) with the physically relevant value κ (the “relaxation rate”) for vibrationally excited molecules and what information we can gain from this.

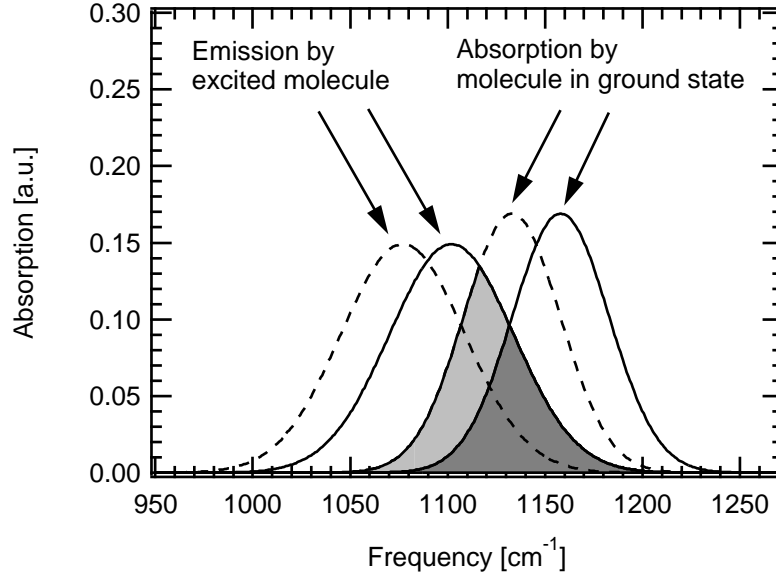


Figure 4.24: Schematic absorption and emission spectra of — $^{12}\text{CF}_3\text{H}$ and - - $^{13}\text{CF}_3\text{H}$ for molecules in the ground state (on the right) and with 8800 cm^{-1} vibrational energy (on the left). The overlap of the spectra for excited $^{12}\text{CF}_3\text{H}$ and ground state $^{12}\text{CF}_3\text{H}$ is shaded in dark grey. The overlap of the spectra for excited $^{12}\text{CF}_3\text{H}$ and ground state $^{13}\text{CF}_3\text{H}$ is the same and in addition the light grey shaded area.

For a fix pre-excitation energy and dissociation laser fluence and wavelength we have

$$\begin{aligned} \frac{k(12^*-13)}{k(12^*-12)} &= \frac{\kappa(12^*-13)}{\kappa(12^*-12)} \\ \frac{k(13^*-13)}{k(13^*-12)} &= \frac{\kappa(13^*-13)}{\kappa(13^*-12)} \end{aligned} \quad (4.12)$$

where $k(x^* - y)$ is the decay rate measured in our experiments where excited $^x\text{CF}_3\text{H}$ relaxes on $^y\text{CF}_3\text{H}$ in the ground state. In other words, the ratio of decay rates of the same pre-excited isotopic species on different relaxation partners entirely reflects the ratio of relaxation rates, as the effect of the IRMPD step is the same. We define, for convenience, the following two values:

$$\begin{aligned} \mathcal{R}_{12} &= \frac{\kappa(12^*-13)}{\kappa(12^*-12)} \\ \mathcal{R}_{13} &= \frac{\kappa(13^*-13)}{\kappa(13^*-12)} \end{aligned} \quad (4.13)$$

Equation 4.13 links relaxation rates of one isotopomer relaxing on different collisional partners. We make the very important assumption that the self-relaxation rates for the two isotopomers are the same:

$$\kappa(12^* - 12) = \kappa(13^* - 13) \quad (4.14)$$

Indeed, these rates are mainly determined by the anharmonic shift of vibrations in excited molecules, which depends very little on the isotopic composition of the molecule.

Finally, we also define:

$$\mathcal{R}_E := \frac{k(12^* - 12)}{k(13^* - 13)} \quad (4.15)$$

With the definitions of \mathcal{R}_{12} , \mathcal{R}_{13} and \mathcal{R}_E we can analyse our data presented in section 4.5.2. We analyse and interpretate the results from two points of view:

1. From a fundamental point of view, what are the relative relaxation rates of the different isotopomers relaxing on each other ?
2. What can we deduce concerning the laser isotope separation process ? When leaving a time-delay Δt between the pre-excitation and dissociation lasers, how much selectivity is gained by isotopically selective collisional relaxation and how much is gained due to the different IRMPD efficiencies of the two different isotopomers ?

(I) Fundamental considerations

Concerning fundamental considerations on vibrational relaxation, we plot \mathcal{R}_{12} and \mathcal{R}_{13} defined in equation 4.13 for different experimental conditions. This is shown in figure 4.25.

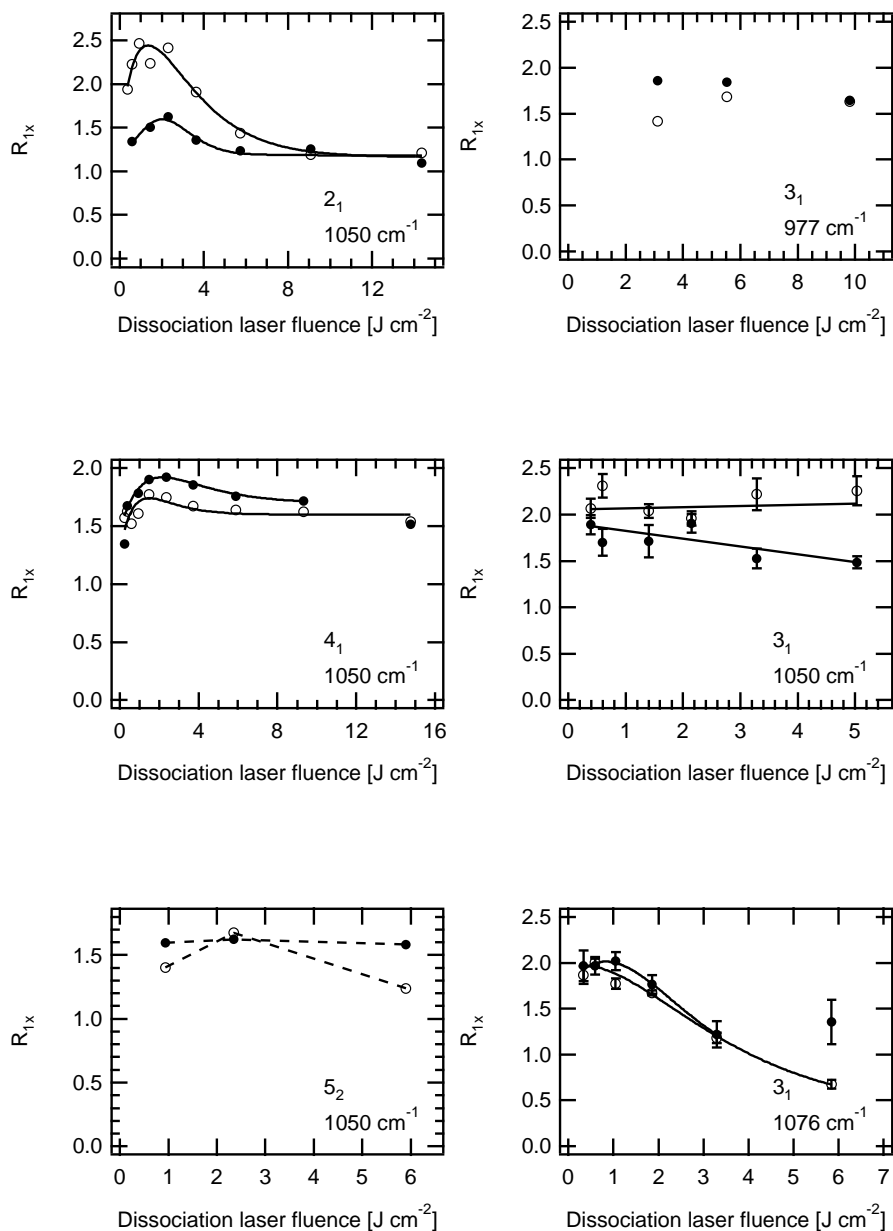


Figure 4.25: Values for $\bullet R_{12}$ and $\circ R_{13}$ for different pre-excitation energies and dissociation laser conditions shown on the individual graphs. The errorbars are fitting errors (see section 4.1.3).

First we have to notice that the values of \mathcal{R}_{12} and \mathcal{R}_{13} depend on the dissociation laser fluence. As a consequence we have to take the value for \mathcal{R}_{12} and \mathcal{R}_{13} at a fluence where the dissociation yield drops off as fast as possible as the molecules relax and lose energy. As we explained earlier, this fluence lies around 1-2 J cm⁻² for standard dissociation laser wavelengths. This way we extract the values presented in table 4.4 for \mathcal{R}_{12} and \mathcal{R}_{13} .

Pre-excitation band	Pre-excitation energy [cm ⁻¹]	\mathcal{R}_{12}	\mathcal{R}_{13}
2 ₁	5950	1.6	2.45
3 ₁	8800	1.94	1.98
4 ₁	11,530	1.9	1.75
5 ₂	14,000	1.65	1.7

Table 4.4: Experimentally measured ratio of relaxation rates. $\mathcal{R}_x = \kappa(x^* - 13)/\kappa(x^* - 12)$.

For the 3₁ pre-excitation band we have two measurements yielding slightly different values for \mathcal{R}_{12} and \mathcal{R}_{13} . We take the average between the two measurements yielding $\mathcal{R}_{12} = 1.94$ and $\mathcal{R}_{13} = 1.98$. The values of \mathcal{R}_{12} and \mathcal{R}_{13} as a function of the vibrational energy of the CF₃H molecule are plotted in figure 4.26.

It is very interesting to notice the general trends we see on figure 4.26. For excited ¹³CF₃H, the ratio of relaxation rates on ¹²CF₃H and on ¹³CF₃H decreases as the pre-excitation energy is increased from 6000 up to 14,000 cm⁻¹. For pre-excited ¹²CF₃H molecules, it goes through a maximum lying at $\sim 10,000$ cm⁻¹.

(II) Consequences for laser isotope separation

We now analyse our data from the point of view of laser isotope separation. Remember, our initial problem was to understand how much of the selectivity gained due to collisions is due to isotopically selective collisional relaxation and how much is due to different IRMPD efficiencies of the two different isotopomers. The influence of the two effects can be quantified as follows:

1. First, we want to compare the relaxation rates of excited ¹²CF₃H on itself with

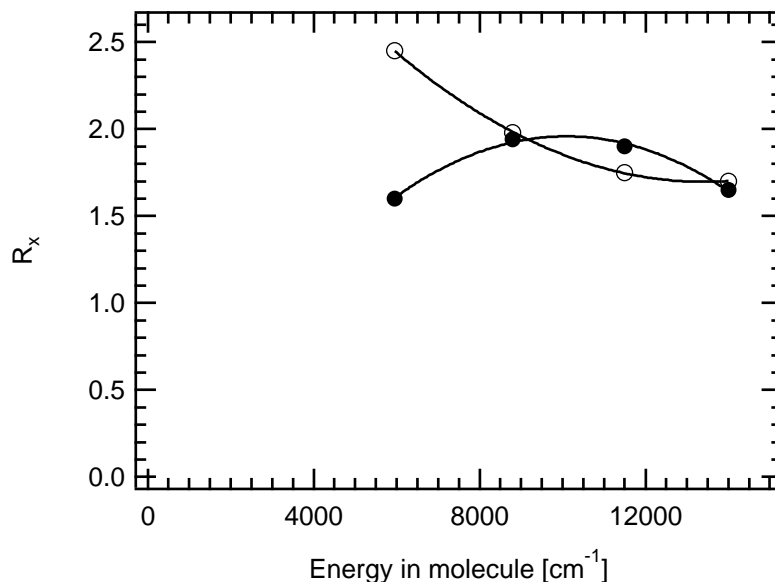


Figure 4.26: Relative relaxation rates ● \mathcal{R}_{12} and ○ \mathcal{R}_{13} .

the relaxation rate of excited $^{13}\text{CF}_3\text{H}$ on $^{12}\text{CF}_3\text{H}$. This is given by the value \mathcal{R}_{13} which we defined earlier:

$$\frac{\kappa(13^* - 13)}{\kappa(13^* - 12)} = \frac{\kappa(12^* - 12)}{\kappa(13^* - 12)} = \mathcal{R}_{13} \quad (4.16)$$

2. The influence of different IRMPD efficiencies can be expressed in a similar manner, by using the value \mathcal{R}_E defined in equation 4.15. This is because self-relaxation, i.e. excited $^{12}\text{CF}_3\text{H}$ on ground state $^{12}\text{CF}_3\text{H}$ and excited $^{13}\text{CF}_3\text{H}$ on ground state $^{13}\text{CF}_3\text{H}$, is independent of the isotopic species (see equation 4.14).

We identify

$$\begin{aligned} \mathcal{S}_{VET} &= \mathcal{R}_{13} = \frac{k(13^* - 13)}{k(13^* - 12)} \\ \mathcal{S}_{IRMPD} &= \mathcal{R}_E = \frac{k(12^* - 12)}{k(13^* - 13)} \end{aligned} \quad (4.17)$$

The total decay selectivity is, as expected, $\mathcal{S}_{tot} = \mathcal{S}_{VET} \cdot \mathcal{S}_{IRMPD}$. This can be graphically illustrated in figure 4.27.

In the laser isotope separation process where we work with a sample containing 1% of $^{13}\text{CF}_3\text{H}$ the selectivity increases because the decay rate for $^{12}\text{CF}_3\text{H}$ (point 1 in fig-

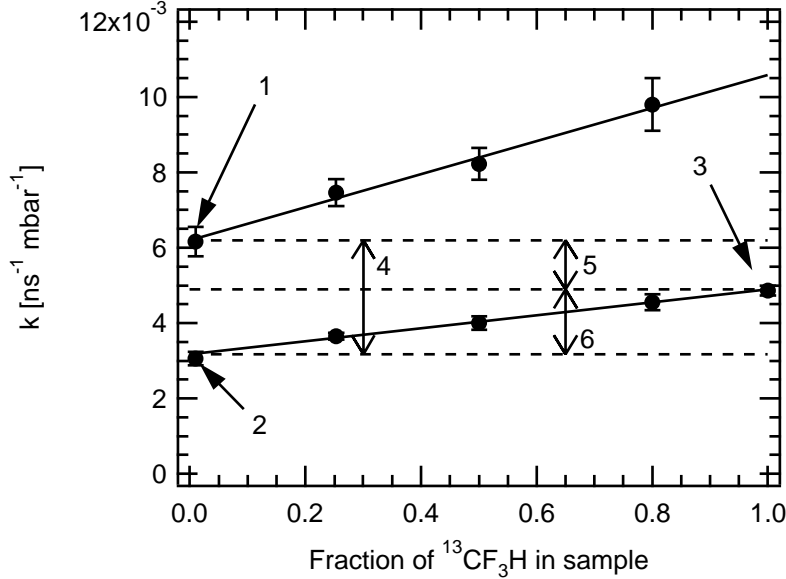


Figure 4.27: Interpretation of our results obtained with isotopically enriched samples. The two solid lines on this graphs show k as a function of the isotopic composition of the sample (upper line for $^{12}\text{CF}_3\text{H}$, lower line for $^{13}\text{CF}_3\text{H}$, see also figure 4.21). Refer to the text for explanations.

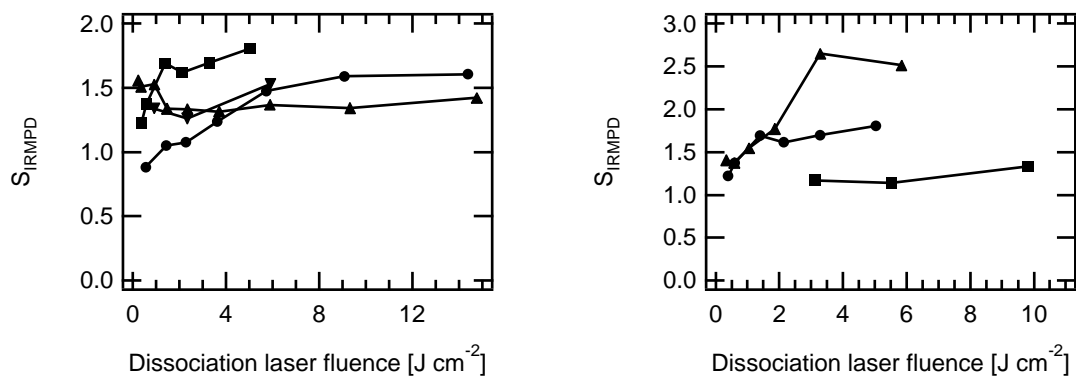
ure 4.27) is faster than the decay rate for $^{13}\text{CF}_3\text{H}$ (point 2). The differences between decay rates in points 1 and 3 are only due to IRMPD effects and differences between decay rates in points 3 and 2 are only due to isotopically selective collisional relaxation.

The values of \mathcal{S}_{VET} ($=\mathcal{R}_{13}$) are shown in figure 4.26. In figure 4.28 we plot the values for \mathcal{S}_{IRMPD} , as a function of the dissociation laser fluence.

The ‘‘importance’’ (or ‘‘contribution’’) \mathcal{I} of the two mechanisms has been defined in equation 4.10 as follows

$$\begin{aligned} \mathcal{I}_{IRMPD} &= \frac{\mathcal{S}_{IRMPD}-1}{(\mathcal{S}_{IRMPD}-1)+(\mathcal{S}_{VET}-1)} \\ \mathcal{I}_{VET} &= \frac{\mathcal{S}_{VET}-1}{(\mathcal{S}_{IRMPD}-1)+(\mathcal{S}_{VET}-1)} \end{aligned} \quad (4.18)$$

with $\mathcal{I}_{IRMPD} + \mathcal{I}_{VET} = 1$. With this, we now can evaluate the relative contributions to the enhancement of selectivity as a function of the different pre-excitation energies. This is shown in figure 4.29.



(a) S_{IRMPD} for molecules pre-excited through the • 2₁, ■ 3₁, ▲ 4₁, ▼ 5₂ bands, for a dissociation laser frequency of 1047 cm⁻¹.

(b) S_{IRMPD} for molecules pre-excited through the 3₁ band, for a dissociation laser frequency of ■ 977, • 1047 and ▲ 1076 cm⁻¹.

Figure 4.28: Measured values of S_{IRMPD} .

From these measurements we conclude:

In general isotopically selective collisional relaxation and different IRMPD efficiencies equally contribute to the enhancement of isotopic selectivity of the dissociation yield.

The exact contribution depends on the exact experimental conditions, in particular the pre-excitation energy of the molecules, the dissociation laser fluence and wavelength. *For our standard conditions for our MLIS process, pre-excitation via the 3₁ band and with a CO₂ dissociation laser frequency of 1047 cm⁻¹ and fluence of 3 J cm⁻², roughly 60% of the selectivity is gained through isotopically selective collisional relaxation and roughly 40% by isotopically selective IRMPD.*

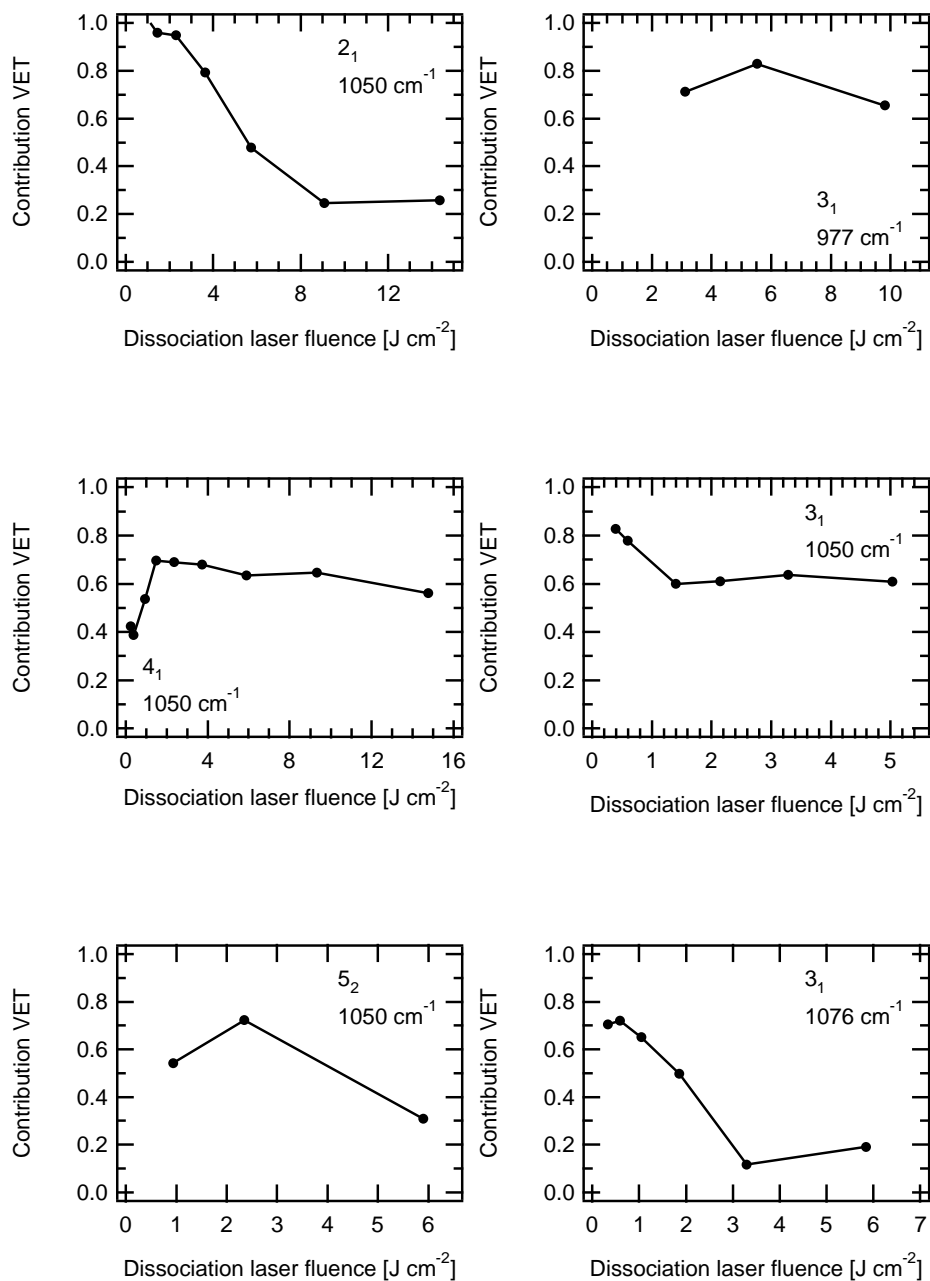


Figure 4.29: Contributions of isotopically selective collisional relaxation (\mathcal{I}_{VET} , below curve) and different IRMPD efficiencies (\mathcal{I}_{IRMPD} , above curve) to the increase of isotopic selectivity, for different pre-excitation levels and fluences.

4.6 Discussion and conclusion

The goal of this work is to explain the increase of isotopic selectivity of our MLIS procedure upon an increase of the sample pressure or of the time-delay between the pre-excitation and dissociation lasers. We proposed two mechanisms: (a) isotopically selective collisional relaxation and (b) different IRMPD efficiencies of the two isotopomers, and the experiments proposed here targeted a disentanglement of the two mechanisms for time delayed laser pulses. An additional question was whether the observed properties are general properties which can, in principle, also be found in other molecules with similar qualitative properties as CF_3H , or whether the observed increase in isotopic selectivity is very specific to the pre-excitation through the 3_1 band of CF_3H . In other words: can we treat the energy distribution in the molecule as statistical or is it localised in a specific vibrational mode? In a set of experiments we have addressed these questions.

1. In section 4.2 we showed that the decay rates are not state specific. This finding is supported by the fact that the same observation has been done for the CF_2HCl molecule⁷.
2. In a second step we determined the intrinsic isotopic selectivity due to the IRMPD step only (section 4.3), at low pressures and with a zero time-delay between the pre-excitation and dissociation lasers. We showed (see figures 4.11 and 4.12 on pages 121 and 122) that under such conditions this selectivity is 1 for fluences of $\gtrsim 2 \text{ J cm}^{-2}$ if the dissociation laser is not too off-resonant (i.e. $\gtrsim 1000 \text{ cm}^{-1}$). We also showed that a simple model describing IRMPD as a set of multiple absorption steps is not adequate for the description of our results, and that more sophisticated modeling needs to be done.
3. In two different experiments (sections 4.4 and 4.5) we have studied the influence of vibrational relaxation and the different IRMPD efficiencies on the enhancement of isotopic selectivity due to collisions. By changing different parameters in our experimental setup (the wavelength of the dissociation laser in the experiments presented in section 4.4 and the relaxation partner in the experiments presented in section 4.5), we determined the relative contributions of isotopically selective collisional relaxation and isotopically selective IRMPD. Some of these results can

be directly compared: our experiments yield the results shown in table 4.5 for the relative importance of different IRMPD efficiencies \mathcal{I}_{IRMPD} and isotopically selective collisional relaxation \mathcal{I}_{VET} for a dissociation laser frequency of 1047 cm^{-1} and fluence of 3 J cm^{-2} .

Experiment	$v = 3$		$v = 4$	
	\mathcal{I}_{IRMPD}	\mathcal{I}_{VET}	\mathcal{I}_{IRMPD}	\mathcal{I}_{VET}
• Change of dissociation laser frequency	$\sim 30\%$	$\sim 70\%$	$\sim 33\%$	$\sim 67\%$
• Isotopically enriched sample	$\sim 37\%$	$\sim 63\%$	$\sim 31\%$	$\sim 69\%$

Table 4.5: Results obtained for the separation of IRMPD and vibrational relaxation for a dissociation laser frequency of 1047 cm^{-1} and fluence of 3 J cm^{-2} .

Furthermore, we have determined the ratio of the relaxation rate of excited $^{13}\text{CF}_3\text{H}$ and the relaxation rate of excited $^{12}\text{CF}_3\text{H}$ on ground state $^{12}\text{CF}_3\text{H}$. The findings are shown in figure 4.30.

Although small differences exist between the results of the two experiments are similar, which makes us believe that the experiments, where we changed the dissociation laser frequency and where we worked with isotopically enriched fluoroform, are reliable. Thus, we may conclude:

- (a) Collisional relaxation is isotopically selective. The selectivity depends on the level of excitation (figure 4.26). For molecules with a vibrational energy between 6000 and $14,000\text{ cm}^{-1}$, relaxation on $^{13}\text{CF}_3\text{H}$ is 1.5-2.5 faster than on $^{12}\text{CF}_3\text{H}$.
- (b) The mechanism of the increase of isotopic selectivity upon leaving a time-delay between the overtone and dissociation lasers consists of a joint contribution of isotopically selective collisional relaxation and different IRMPD efficiencies of the two isotopomers. The exact contributions depend on the fluence of the dissociation laser and on the pre-excitation energy (figure 4.29). As one tunes the dissociation laser frequency to the red, vibrational relaxation becomes more and more important with respect to the IRMPD efficiencies. For typical frequencies used for the laser isotope separation process ($\sim 1047\text{ cm}^{-1}$), both effects contribute roughly equally to the enhancement of isotopic selectivity.

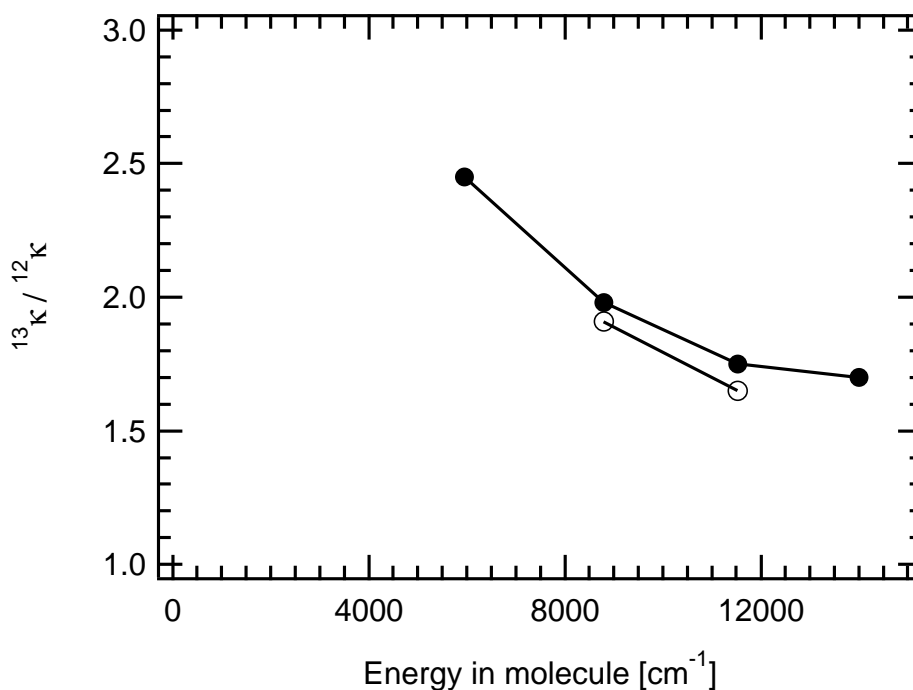


Figure 4.30: Experimentally determined ratio of relaxation rates, measures
 ○ by changing the wavelength of the dissociation laser.
 ● by letting the molecules relax on $^{13}\text{CF}_3\text{H}$ instead of $^{12}\text{CF}_3\text{H}$.

Furthermore, at these conditions and pre-excitation levels of up to $v_{CH} = 2$ and $v_{CH} = 3$, vibrational relaxation becomes more and more important as the fluence of the dissociation laser is lowered.

Summarising, we were able to:

- ★ Directly observe isotopic selective relaxation of highly excited polyatomic molecules.
- ★ Determine their relative relaxation rates as a function of the pre-excitation energy summarised in figure 4.26 on page 144.
- ★ Quantify the relative contributions of the mechanisms of isotopically selective collisional relaxation and of different IRMPD rates to the enhancement of isotopic selectivity upon leaving a time-delay between the pre-excitation and the dissociation lasers.

Bibliography

- [1] O. V. Boyarkin, R. D. F. Settle, and T. R. Rizzo. Vibrational Overtone Spectra of Jet-Cooled CF_3H by Infrared Laser Assisted Photofragment Spectroscopy . *Ber. Bunsenges. Phys. Chem.*, 99(3):504–513, 1995.
- [2] Richard Barry Bernstein. *Chemical dynamics via molecular beam and laser techniques*. Oxford: Clarendon Press; New York: Oxford University Press, 1982.
- [3] M. Polianski, O. V. Boyarkin, and T.R. Rizzo. Collisionally-assisted, highly-selective laser isotope separation of carbon-13 . *J. Chem. Phys.*, 121(23):11771–11779, 2004.
- [4] J. A. O'Neill, L. Pateopol, and B. Pogue. Multiphoton absorption measurements in CF_3H . *J. Phys. B: At. Mol. Opt. Phys.*, 25:3335–3344, 1992.
- [5] R. D. F. Settle and T. R. Rizzo. CO_2 laser assisted vibrational overtone spectroscopy . *J. Chem. Phys.*, 97(4):2823–2825, 1992.
- [6] O. V. Boyarkin, M. Kowalczyk, and T. R. Rizzo. Collisionally Enhanced Isotopic Selectivity in Multiphoton Dissociation of vibrationally excited CF_3H . *J. Chem. Phys.*, 118(1):93–103, 2003.
- [7] Thierry Krombach. Spectroscopy of CF_2HCl and study of the collisional deactivation taking place in laser induced isotopic separation . Master's thesis, Ecole polytechnique fédérale de Lausanne, Switzerland, 2000. The report can be obtained upon request from the author of this thesis.

Chapter 5

Numerical simulations of V-V energy transfer and IRMPD of CF_3H

In this section we present numerical simulations of two different parts involved in our experiments.

1. First we have directly observed isotopically selective collisional relaxation and we could determine the relative relaxation rates of the different isotopic species as a function of the vibrational energy of a molecule (see section 4.5). Here, we present a model involving vibrational relaxation both due to long-range dipole-dipole interactions and due to short-range head-on collisions, and we show that we can reproduce our experimental results very well.
2. Secondly, we present simulations of the laser isotope separation process involving IRMPD of vibrationally pre-excited molecules (OP-IRMPD). In this part, we first present simulations, in which we reproduce some of our experimental findings described in chapter 4 thus demonstrating the validity of our calculations. From this, we then present calculations that aim to determine the relative influences of isotopically selective collisional relaxation and selective IRMPD to the enhancement of isotopic selectivity at high pressures. We also present some predictions of the dissociation yield of vibrationally excited CF_3H molecules for different experimental conditions, such as the pre-excitation energy, the sample pressure and

the dissociation laser fluence and wavelength and some practical predictions for a possible industrial application of the laser isotope separation process.

For both of these parts, we need to be able to calculate the absorption and the emission spectra of highly excited molecules. For this reason, this topic is singled out and presented as an independent section.

This chapter of numerical simulations is hence built up as follows: in section 5.1 we present the calculation of absorption and emission spectra of excited molecules, in section 5.2 we present simulations concerning collisional vibrational relaxation and finally in section 5.3 we present our calculations of the MLIS process.

5.1 Absorption and emission spectra of an excited molecule

Both for simulations of IRMPD and V-V energy transfer, we need to know the IR absorption and emission spectra of an excited CF_3H molecule. In this section we explain how this is done.

5.1.1 Statistical “inhomogeneous” broadening

In this section the absorption and emission spectra[‡] of excited molecules will be described neglecting rotational effects (i.e. with $\Delta J = \Delta K = 0$). Rotational contributions will be added in section 5.1.3. The absorption feature of excited molecules differs in two points from ground state molecules: it *shifts* and it *broadens*.

Above a certain level of vibrational energy, this energy is no longer localised in a particular vibrational mode of the molecule, but distributed over all vibrational modes due to IVR. The state of a molecule can be represented by

$$|\Psi\rangle \simeq \sum_{i=1}^N c_i |v_1^i, v_2^i, \dots, v_n^i\rangle, \quad (5.1)$$

[‡]The concepts for the absorption and emission spectra are very similar. Here we mainly present the results for absorption spectra, but they can be directly transposed to emission spectra.

where the sum goes over all zeroth order states $|v_1^i, v_2^i, \dots, v_n^i\rangle$ which have energies close to each other. For simplicity we will assume in our calculations that the values of $|c_i|^2$ are the same ($= 1/N$). It has to be clearly stated that an explicit assumption is intensive mixing of the vibrational states, which is not the case for vibrationally low excited molecules.

Statistically the molecule can be in any of these zeroth order states. For the absorption of a photon, the oscillator strength can originate from any of these zeroth order states and is only given by the concerned matrix element.

Recall formula 2.2 giving the energy of a state with vibrational quantum numbers $v = (v_1, v_2, \dots, v_N, l_k, l_{k+1}, \dots, l_N)$:

$$\begin{aligned}
 E(v) &= \sum_s \omega_s (v_s + \frac{1}{2}) + \sum_t \omega_t (v_t + 1) \\
 &+ \sum_{s \geq s'} x_{ss'} (v_s + \frac{1}{2}) (v_{s'} + \frac{1}{2}) \\
 &+ \sum_{t \geq t'} x_{tt'} (v_t + 1) (v_{t'} + 1) \\
 &+ \sum_{s,t} x_{st} (v_s + \frac{1}{2}) (v_t + 1) \\
 &+ \sum_{t \geq t'} g_{tt'} l_t l_{t'} \quad ,
 \end{aligned} \tag{5.2}$$

where v_s, v_t are the vibrational quantum numbers, l_i are the vibrational angular momentum quantum number for doubly degenerate modes, ω_s, ω_t are the harmonic frequencies, and x_{ij} and g_{ij} are the spectroscopic anharmonic constants. Sums over s are for non-degenerate modes, sums over t relate to doubly degenerate modes. This expression neglects higher order terms which are, at least at lower vibrational energies, negligible. At higher energies these higher order terms may grow more important, but the effect will be at least partially washed out by the broadening described here.

When the number of quanta in a mode ν_p is increased by one the energy changes by

$$\begin{aligned}
 \Delta E &= E(v_1, v_2, \dots, v_p + 1, \dots, v_N, l_k, l_{k+1}, \dots, l_i \pm 1, \dots, l_N) \\
 &- E(v_1, v_2, \dots, v_p, \dots, v_N, l_k, l_{k+1}, \dots, l_i, \dots, l_N)
 \end{aligned} \tag{5.3}$$

with the selection rule $\Delta l = \pm 1$ (in the case of a doubly degenerate mode). The set of all possible ΔE constitutes the possible vibrational bands. As the number of coupled states increases as the vibrational energy in the molecule goes up, the number of possible band origins ΔE increases as well. This explains why the spectrum broadens as the molecule gains energy¹⁻⁵. In addition to the broadening, there is a shift of the absorption spectrum; in general this shift is towards lower energies (i.e. $x_{ij} < 0$) which gives the shift the name of a “red-shift”.

The broadening is often called “statistical inhomogeneous broadening” (SIB)[‡]. For the calculation of vibrational spectra one has to determine all states $|v_1, v_2, \dots, v_N\rangle$ lying within an energy region $E \pm \Delta E$ and determine the band origin of the transition $|v_1, v_2, \dots, v_p, \dots, v_N\rangle \rightarrow |v_1, v_2, \dots, v_p \pm 1, \dots, v_N\rangle$ where ν_p is the mode accepting or emitting a photon in the harmonic approximation with a linear dipole function. The matrix elements scale as⁶

$$\begin{aligned}\langle v_p | q | v_p + 1 \rangle &= \sqrt{v_p + 1} \cdot \langle 0 | q | 1 \rangle \\ \langle v_p | q | v_p - 1 \rangle &= \sqrt{v_p} \cdot \langle 1 | q | 0 \rangle\end{aligned}\tag{5.4}$$

and hence, in the case of a non-degenerate vibration,

$$\begin{aligned}\sigma(v_p \rightarrow v_p - 1) &= v_p \cdot \sigma(1 \rightarrow 0) \\ \sigma(v_p \rightarrow v_p + 1) &= (v_p + 1) \cdot \sigma(0 \rightarrow 1) \\ \sigma(0 \rightarrow 1) &= \sigma(1 \rightarrow 0)\end{aligned},\tag{5.5}$$

where σ is the absorption (emission) cross-section. Similarly, for a doubly degenerate vibration the strength scales as⁷

$$\sigma(v_p, k \rightarrow v_p - 1) = \frac{v_p + k}{v_p + 1} \cdot \sigma(1 \rightarrow 0),\tag{5.6}$$

where k is the vibrational angular momentum. Note that a summation over k gives a total absorption strength for the $v_p \rightarrow v_p - 1$ transition which is $\sum_k \sigma(v_p, k \rightarrow v_p - 1) = v_p \cdot \sigma(1 \rightarrow 0)$, which is coherent with equation 5.5.

[‡]In general the term “inhomogeneous” refers to a system, where the broadening is caused by an ensemble of different molecules absorbing at different wavelengths. This is not the case for this kind of broadening. We will, in what follows, nevertheless adopt the term “inhomogeneous” broadening because it is widely accepted in parts of the scientific community.

We call the set of band origins $\Delta\nu_0$ disregarding rotational contributions as a ‘‘SIB spectrum’’ (SIB = statistical inhomogeneous broadening). With these considerations and the spectroscopic anharmonic constants of a particular molecule, such SIB spectra of excited molecules can be calculated. This is done in the next section for CF_3H .

5.1.2 Vibrational absorption and emission spectra of vibrationally excited CF_3H

In this section we present calculated SIB spectra of vibrationally excited CF_3H molecules.

Anharmonic constants listed previously⁸ (table 2.3 on page 24) are used to calculate the shift and broadening of the absorption and emission spectra using the considerations presented in the previous section. We calculate these spectra for excited CF_3H molecules assuming that levels over a width of 400 cm^{-1} mix (this is quite large, the results are however not very sensitive to this width). The calculations of the SIB absorption and emission spectra are done for CF_3H molecules over a wide range of internal energies. The spectra for the absorption of one quantum in ν_5 are shown in figure 5.1 for the internal energies $E = 0, 2500, 5000, \dots, 20,000\text{ cm}^{-1}$. Note however, that the spectra for low excited molecules have to be taken with care, as the mixing of the states is not large enough for complete redistribution of energy in the molecule on the time-scales of our experiments. The curves are included for completeness.

In figure 5.2 the same graphs for ν_2 , ν_3 and ν_6 are shown. We leave out ν_1 and ν_4 because they mix strongly via Fermi Resonances. This mixing is not accounted for in equation 5.2.

The SIB spectra approach roughly a Gaussian curve as the molecules gain energy and can be described as:

$$\sigma_E(\nu) \simeq \frac{A_p(E)}{\delta\nu_p\sqrt{\pi}} \cdot \exp\left(-\left(\frac{\nu - (\nu_0 + \Delta\nu_p)}{\delta\nu_p}\right)^2\right) \quad (5.7)$$

The width $\delta\nu_p$ and the shift $\Delta\nu_p$ of these Gaussians, as well as the integral intensity

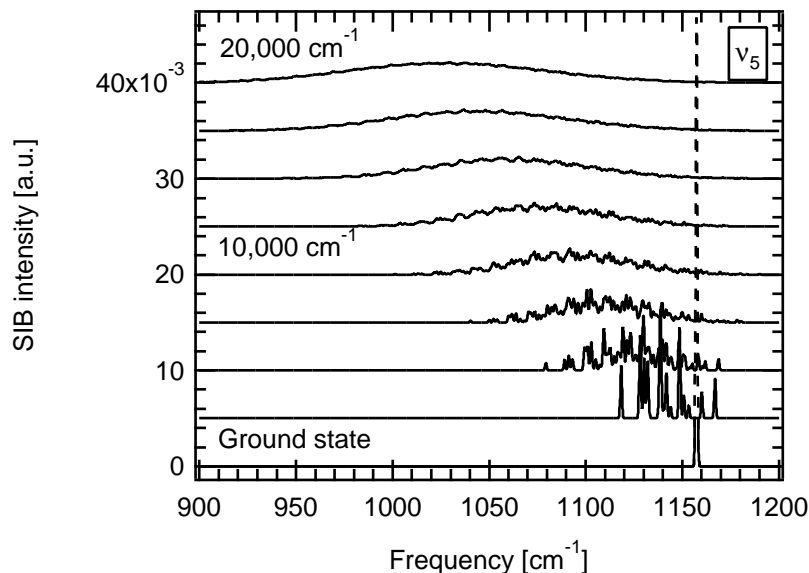


Figure 5.1: Absorption spectra for CF_3H molecules at 0, 2500, 5000, 7500, \dots , 20,000 cm^{-1} .

$A_p = \int_{\text{band}} \sigma(\nu) d\nu$, can be estimated in a simple way with the following expressions⁹

$$\begin{aligned}
 \Delta\nu_p &\approx \sum_{i=1}^{s'} (1 + \delta_i^p) \cdot g_i \cdot x_{i,p} \cdot \langle n_i \rangle \\
 \delta\nu_p &\approx \frac{\Delta\nu_p}{\sqrt{s}} \\
 A_p &\approx A_0 \cdot (\langle n_i \rangle + 1)
 \end{aligned} \tag{5.8}$$

where p designates the mode which undergoes a change, s the number of modes disregarding degeneracy, s' the number of independent modes, g_i is the degeneracy of a mode, $x_{i,p}$ are the spectroscopic anharmonic constants, δ_i^p is the Kronecker symbol and $\langle n_i \rangle$ is the average occupation number of a mode. In our case $s = 9$, $s' = 6$, $g_{1,\dots,6} = (1, 1, 1, 2, 2, 2)$ and $x_{i,j}$ is taken from literature⁸. The average occupation number can be estimated as

$$\langle n_i \rangle \approx g_i \cdot \frac{E}{s} \cdot \frac{1}{\omega_i}, \tag{5.9}$$

where E is the energy in the molecule and ω_i is the harmonic frequency of the mode.

The values for $\Delta\nu$, $\delta\nu$ and A obtained by fitting gaussian curves to our calculated SIB spectra are shown in graphs 5.3-(a-c).

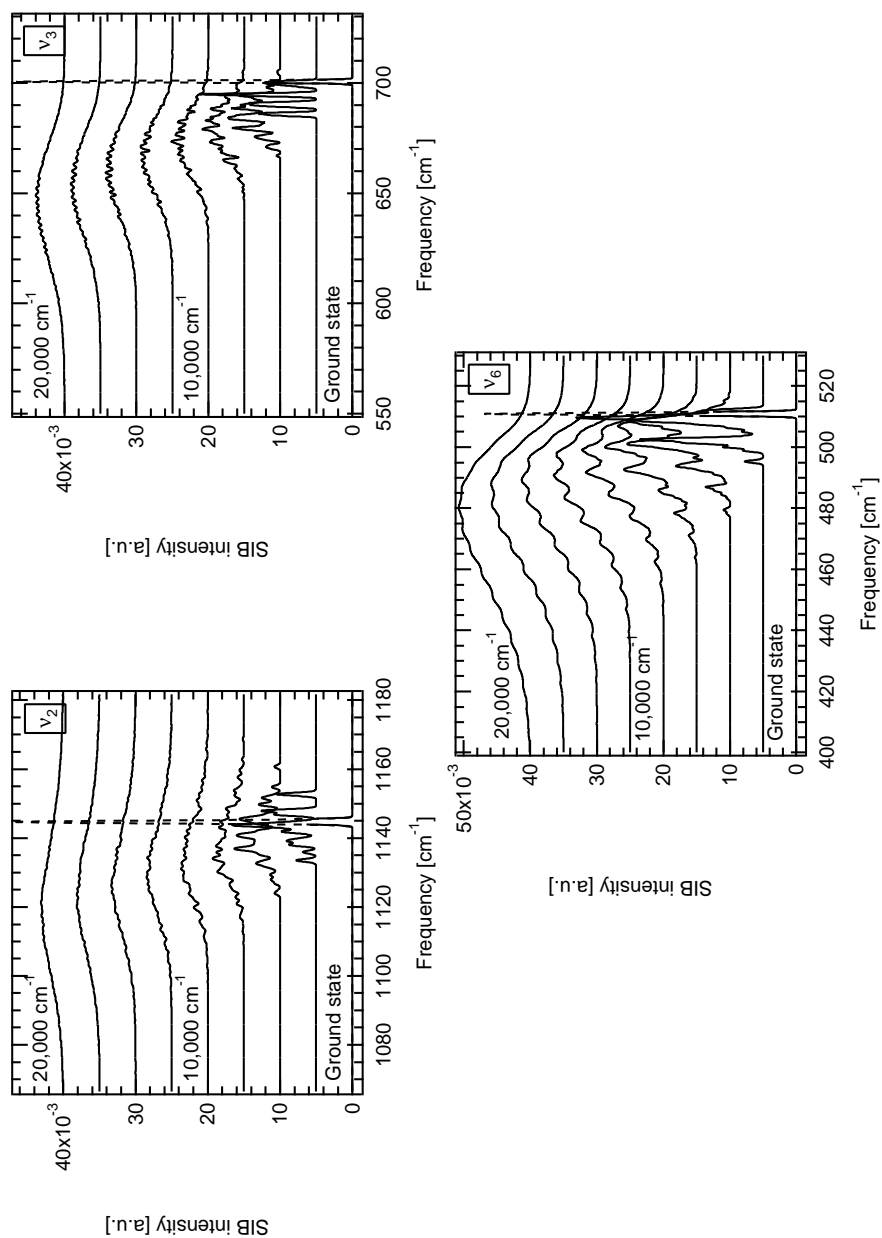
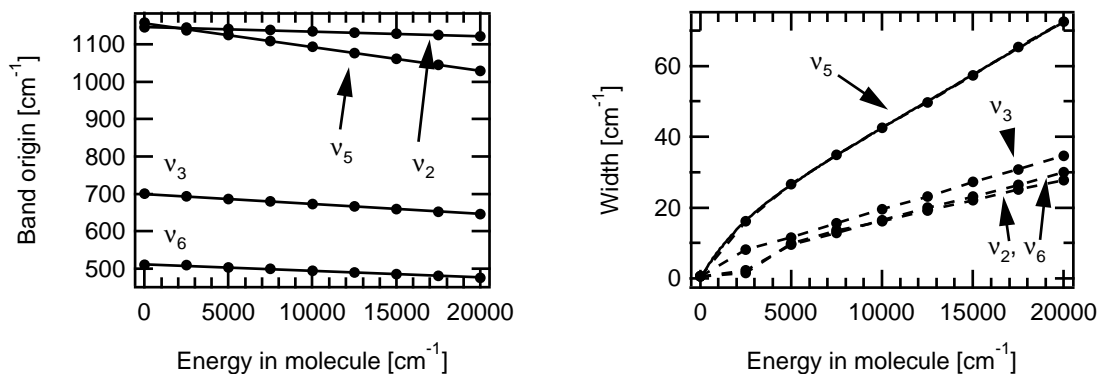
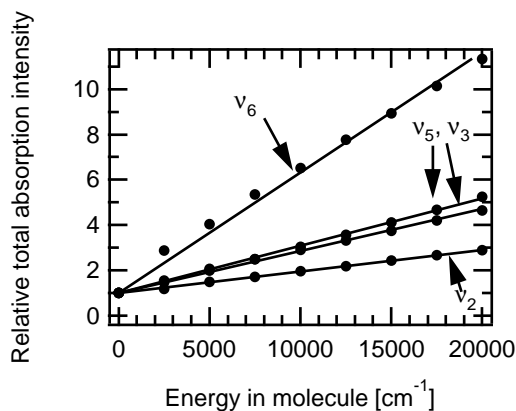


Figure 5.2: SIB absorption spectra for ν_2 , ν_3 and ν_6 . The curves are for vibrational energies of the molecules which are multiple integers of 2500 cm⁻¹.



(a) Centre of SIB spectra. The slopes are given in the first column of table 5.1.

(b) Width of SIB spectra. The functional dependence on the internal energy are of the (empirical) form of $w = A \cdot (E/\text{cm}^2) + B \cdot \exp(-k \cdot (E/\text{cm}^2))$. The slopes for energies larger than 5000 cm^{-1} are given in the second column of table 5.1.



(c) Integral intensity of SIB spectra. The slopes are given in the third column of table 5.1. The value for the lowest frequency vibration, ν_6 , increases the fastest, the value for the highest frequency vibration, ν_2 , increases the slowest.

Figure 5.3: The transition spectra of excited molecules shift, broaden and get more intense as the energy of the molecules increase.

In table 5.1 the shifts, widths and intensities are given both for the estimations using equations 5.8 and for fitted values to the calculated SIB spectra.

	$\Delta\nu(E)/E$	$\delta\nu(E)/E$	$(A(E)/A(0)E) - 1$	
ν_2	$-1.16 \cdot 10^{-3}$	$0.39 \cdot 10^{-3}$	$9.65 \cdot 10^{-5}$	(eq)
	$-1.25 \cdot 10^{-3}$	$1.18 \cdot 10^{-3}$	$9.51 \cdot 10^{-5}$	(calc)
ν_3	$-1.96 \cdot 10^{-3}$	$0.65 \cdot 10^{-3}$	$1.58 \cdot 10^{-4}$	(eq)
	$-2.72 \cdot 10^{-3}$	$1.53 \cdot 10^{-3}$	$1.85 \cdot 10^{-4}$	(calc)
ν_5	$-7.09 \cdot 10^{-3}$	$2.36 \cdot 10^{-3}$	$1.91 \cdot 10^{-4}$	(eq)
	$-6.35 \cdot 10^{-3}$	$3.05 \cdot 10^{-3}$	$2.08 \cdot 10^{-4}$	(calc)
ν_6	$-1.87 \cdot 10^{-3}$	$0.63 \cdot 10^{-3}$	$4.38 \cdot 10^{-4}$	(eq)
	$-1.82 \cdot 10^{-3}$	$1.36 \cdot 10^{-3}$	$5.32 \cdot 10^{-4}$	(calc)

Table 5.1: Shifts, widths and intensity of the SIB spectra.

(eq) equations 5.8

(calc) Fits to calculated SIB spectra.

There are some inconsistencies between the estimations and the simulations, in particular as far as the widths are concerned. However, the estimations do not take into account splittings due to the vibrational angular momentum.

We have shown how to calculate the SIB absorption / emission spectrum of an excited CF_3H molecule disregarding rotational contributions. The next section deals with this problem.

5.1.3 Rotational contribution to the absorption spectrum

For the total absorption spectra the rotational contributions have to be considered in addition to SIB. For this, the SIB spectra are convoluted with a clean rotational contour.

The rotational energy which has already been noted in equation 2.13 are taken:

$$F(J, K) = B \cdot J \cdot (J + 1) + (C - B) \cdot K^2, \quad (5.10)$$

where B and C are rotational constants of the molecule in the ground state. Using this rotational contour is an approximation:

- First, the values of B and C depend on the vibrational excitation. Their values are well given by equation 2.14 on page 33. Using excitation dependent values for B and C shifts the overall absorption spectrum by $\sim 1 \text{ cm}^{-1}$ to the red.
- The rotational levels of $|v_5 = 1\rangle$ interact via Coriolis interaction with rotational levels of $|v_2 = 1\rangle$ and, in a smaller extent, via Fermi interactions with rotational levels of $|v_3 = 1, v_6 = 1\rangle$. The corresponding matrix elements are given as follows¹⁰⁻¹⁴:

$$\begin{aligned} \langle \nu_5, J, K \pm 1, l = \pm 1 | H | \nu_3 + \nu_6, J, K \pm 1, l = \pm 1 \rangle &= W_f \\ \langle \nu_5, J, K \pm 1, l = \pm 1 | H | \nu_2, J, K, l = 0 \rangle &= \pm \xi \cdot F_{\pm}(J, K) \\ \langle \nu_3 + \nu_6, J, K - 1, l = -1 | H | \nu_3 + \nu_6, J, K + 1, l = +1 \rangle &= -\frac{1}{2} \cdot q_6 \cdot F_+(J, K) \cdot F_-(J, K) \end{aligned} \quad (5.11)$$

where J and K are the rotational quantum numbers, l is the vibrational quantum number associated with the ν_5 vibration,

$$F_{\pm}(J, K) = \sqrt{J \cdot (J + 1) - K \cdot (K \pm 1)} \quad (5.12)$$

and $W_f = 6.5 \text{ cm}^{-1}$, $\xi = 0.341985 \text{ cm}^{-1}$ and $q_6 = 11.91 \cdot 10^{-4} \text{ cm}^{-1}$. These interactions lead to a distorted rotational contour of the $0 \rightarrow n_5 = 1$ vibrational band.

It should be expected the higher excited states interact similarly. If one wanted to calculate the rotational structure of a state $|v_1, v_2, v_3, v_4, v_5, \bar{v}_6\rangle$ one would have

to let it interact through Coriolis interaction with $|v_1, v_2 + 1, v_3, v_4, v_5 - 1, v_6\rangle$ but also with $|v_1, v_2 - 1, v_3, v_4, v_5 + 1, v_6\rangle$ which themselves are again coupled to $|v_1, v_2 + 2, v_3, v_4, v_5 - 2, v_6\rangle$ and $|v_1, v_2 - 2, v_3, v_4, v_5 + 2, v_6\rangle$ and so on. This gets a rather difficult task, and the uncertainties on the results will become increasingly important (nothing is known on the interaction constants W_f , ξ and q_6 upon excitation, and further interactions may further distort the rotational levels). In this sense there is no real improvement if we try to include any Coriolis interactions.

The shift of the rotational contour of the $0 \rightarrow n_5 = 1$ transition due to Coriolis interactions ($\sim 2\text{-}3 \text{ cm}^{-1}$) is more important than the $\sim 1 \text{ cm}^{-1}$ due to the vibrational excitation dependence of the rotational constants B and C . For this reason we neglect changes in the values of B and C upon vibrational excitation as it is smaller than the influence of Coriolis interactions. These will also be left away because of the associated difficulties.

The selection rules for a transition are $\Delta J = 0, \pm 1$ and $\Delta K = 0$ for a \parallel transition (ν_1, ν_2 and ν_3) and $\Delta J = 0, \pm 1$ and $\Delta K = \pm 1$ for a \perp transition (ν_4, ν_5 and ν_6). The intensity of the transition is given by¹⁵

$$I \propto A_{KJ} \cdot (2J + 1) \cdot e^{-F(J,K)/k_B T}, \quad (5.13)$$

where A_{KJ} is proportional to the square of the transition moment summed over all orientations of J , $(2J + 1)$ is the degeneracy of the state due to different M quantum numbers (projection of J onto the laboratory z-axis) and the exponential is the Boltzmann population of the state. The values A_{KJ} are known as the ‘‘Hönl-London factors’’.

The values of A_{KJ} for a \parallel band are given by¹⁵

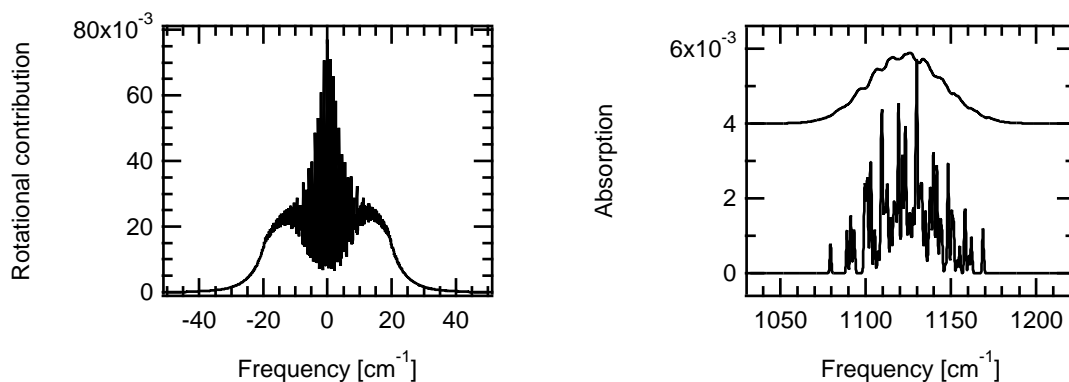
$$A_{KJ} = \begin{cases} \frac{(J+1)^2 - K^2}{(J+1) \cdot (2J+1)} & (\Delta J = +1) \\ \frac{K^2}{J \cdot (J+1)} & (\Delta J = 0) \\ \frac{J^2 - K^2}{J \cdot (2J+1)} & (\Delta J = -1) \end{cases} \quad (5.14)$$

and for a \perp band by

$$A_{KJ} = \begin{cases} \frac{(J+2\pm K)\cdot(J+1\pm K)}{(J+1)\cdot(2J+1)} & (\Delta J = +1) \\ \frac{(J+1\pm K)\cdot(J\mp K)}{(J+1)\cdot J} & (\Delta J = 0) \\ \frac{(J-1\mp K)\cdot(J\mp K)}{J\cdot(2J+1)} & (\Delta J = -1) \end{cases}, \quad (5.15)$$

where the upper and lower signs of \pm and \mp refer to $\Delta K = +1$ and to $\Delta K = -1$ respectively.

With these considerations the total absorption / emission spectrum can be easily evaluated by the convolution of the rotational spectrum and the SIB spectrum. This rotational contour is shown in figure 5.4-a for a transition in ν_5 . We show in figure 5.4-b the SIB spectrum and its convolution with the rotational structure for a CF_3H molecule at a vibrational energy of 5000 cm^{-1} for the absorption of one quantum in ν_5 .



(a) Rotational contour used for the convolution with the SIB spectra.

(b) SIB spectrum (bottom) and its convolution with the rotational contour (top) for a molecule with 5000 cm^{-1} of vibrational energy.

Figure 5.4: For the calculation of the whole absorption spectrum the SIB spectrum is convoluted with a rotational contour.

Because of this convolution, the width of the gaussian approximation of the spectra (equation 5.7) shifts. For the additional broadening consider that the convolution of two gaussians of width δ_{SIB} and δ_{rot} is again a gaussian of width $\delta_{tot} = \sqrt{\delta_{SIB}^2 + \delta_{rot}^2}$. Although both the rotational contour and the SIB spectra are not gaussians at all, it turns out that the formula holds very well if we use a rotational width of $\delta_{rot} \approx 15.9$

cm^{-1} .

We have shown how to take into account the rotational structure for the calculation of the complete absorption (and emission) spectra. In summary, in the case of an absorption of one quantum in ν_5 , the gaussian fits to the SIB spectra have to be broadened by a second gaussian of a width of 15.9 cm^{-1} . Although a gaussian curve does not describe the pure SIB spectra in an adequate manner, they are adequate for the total absorption spectrum (including rotations) for molecules with a vibrational energy of $\gtrsim 3000\text{-}4000 \text{ cm}^{-1}$.

5.2 Numerical simulations of vibrational energy transfer between excited and ground state molecules

In this section we present calculations concerning vibrational relaxation rates of excited CF_3H molecules on CF_3H molecules in the ground state. The calculations shall be compared with the experimental measurements presented in figure 4.26 on page 144. First, we state the basic assumptions for these calculations, then we present our model based on the Fermi Golden Rule (FGR). We then present the actual results and discuss them.

5.2.1 Assumptions

For our calculations we have to make a certain number of assumptions:

1. **Complete rotational relaxation.** The rotational thermalisation is always complete, i.e. the time between two collisions with vibrational energy transfer (VET) is enough for the rotational relaxation to be complete (i.e. rotational relaxation rates \gg vibrational relaxation rates). This condition is in general well met in molecular systems.
2. **IVR is complete.** We initially pre-excite molecules through a N_j band, so the initial vibrational state is well defined. Collision-free IVR occurs on typical time-scales of $\gtrsim 100 \text{ ps}$ (pre-excitation via 3_1 and 4_1 bands) and $\gtrsim 5 \text{ ps}$ (pre-excitation via 5_2 band) (see section 2.1.2.B). Furthermore, collision-induced IVR occurs with

an estimated rate of 4.3 times the hard sphere collision rate[‡]. For these reasons IVR can be assumed to be complete on the time-scale of our experiment.

5.2.2 V-V energy transfer mediated by dipole-dipole interactions

This section describes the calculation of rates of V-V energy transfer mediated by dipole-dipole interactions between an excited and a ground state molecule. When two molecules collide[§] there is a certain probability that one molecule (called the *donor*) loses one quantum in a certain mode ν_i and another molecule (called the *acceptor*) gains one quantum in ν_i . In what follows, all values referring to the donor molecule will have a superscript (D) , and those referring to the acceptor molecule are denoted by a (A) .

The potential energy $V(R, \Theta, q_i^{(D)}, q_i^{(A)})$ due to two interacting molecules depends on the distance R between the centres of mass, the mutual orientation in space, defined by the set of angle variables Θ and the vibrational coordinates q of the two molecules. V can be expressed as a series in q :

$$\begin{aligned} V = & V_0(R, \Theta) + \sum_i V_i^{(D)}(R, \Theta) q_i^{(D)} + \sum_i V_i^{(A)}(R, \Theta) q_i^{(A)} \\ & + \sum_{ij} V_{ij}^{(DD)}(R, \Theta) q_i^{(D)} q_j^{(D)} + \sum_{ij} V_{ij}^{(AA)}(R, \Theta) q_i^{(A)} q_j^{(A)} + \sum_{ij} V_{ij}^{(AD)}(R, \Theta) q_i^{(A)} q_j^{(D)} \\ & + \dots \text{(higher order terms)} \end{aligned} \tag{5.16}$$

At relatively large distances it is the $V_{ii}^{(AD)}(R, \Theta) q_i^{(A)} q_i^{(D)}$ terms that are responsible for the exchange of one quantum in the mode ν_i . These terms represent the dipole-dipole interaction of the two molecules. Higher order terms, represented by $V_{ijkl}^{(AADD)}(R, \Theta) q_i^{(A)} q_j^{(A)} q_k^{(D)} q_l^{(D)}$ etc are for higher order pole interactions.

[‡]Experimentally it has been shown that for molecules pre-excited via the fundamental of the C-H stretch vibration collision-induced IVR occurs at a rate of $1.67 \cdot 10^7 \text{ s}^{-1} \text{ torr}^{-1}$ which is 1.4 times faster than the hard sphere collision rate (see section 2.1.2.C). CI-IVR scales roughly with the vibrational energy of the molecule¹⁶, so molecules excited via the 3_1 band undergo CI-IVR at a rate of $\sim 3 \cdot 1.67 \cdot 10^7 \text{ s}^{-1} \text{ torr}^{-1}$.

[§]One has to be careful when using the term ‘‘collision’’ as this is not well defined. Using the term ‘‘collision’’ implicitly includes that there is a relatively sharp cut-off in the distance where V-V energy transfer takes place and where it does not. This may be applicable to a certain extent to hard collisions (see section 2.3), but for soft collisions where the interaction potential between the colliding molecules goes as $1/r^n$ where r is the distance between the molecules there is no sharp cut-off. Nevertheless we use the term ‘‘collision’’ but we have to bear in mind the problem associated with the expression.

In general, i.e. for large distances between two molecules (say $R \gtrsim 5 - 10 \text{ \AA}$), the prevailing terms in equation 5.16 for V-V energy transfer are the terms representing the dipole-dipole interactions, $V_{ij}^{(AD)}$. Because of this, we formulate the following, additional simplification:

- In our calculations we consider only dipole-dipole interactions. To avoid the region where higher order poles can interfere, we assume a minimum distance R_0 between two encountering molecules.

A collision between an excited molecule and a ground state molecule with internal energies $E^{(D)}$ and $E^{(A)}$ and rotational quantum numbers $|J^{(D)}, K^{(D)}, M^{(D)}\rangle$ and $|J^{(A)}, K^{(A)}, M^{(A)}\rangle$ may result in the transfer of one quantum in the mode p of the excited molecule to the ground state molecule. This change in vibrational quantum numbers is accompanied by a change in rotational quantum numbers such as the energy defect caused through the mismatch of vibrational frequencies is compensated by rotations[‡].

The following selection rules apply: $\Delta J^{(D)} = 0, \pm 1$, $\Delta J^{(A)} = 0, \pm 1$, $\Delta K^{(D)} = \pm 1$ (for a \perp transition) or $\Delta K^{(D)} = 0$ (for a \parallel transition), and similarly $\Delta K^{(A)} = \pm 1$ or $\Delta K^{(A)} = 0$. In addition to this the total M , i.e. $M^{(D)} + M^{(A)}$, has to be conserved. These selection rules apply to dipole-dipole interactions and are direct consequences of the angular dependence of $V_{ii}^{(AD)}$. For higher order interactions, which become important at close distances, the selection rules are different (they scale with the order of the pole).

For the calculation of the transition rate we use the Fermi Golden Rule:

$$W = \frac{2\pi}{\hbar} |\langle i | V | f \rangle|^2 \mathcal{C}(E), \quad (5.17)$$

where $\mathcal{C}(E)$ is the density of states (DOS) which depends on the vibrational energy E of the excited molecule, $|i\rangle$ and $|f\rangle$ are the initial and final states of the pair of molecules and V is the considered interaction. In the frame of the model outlined above the following expression for the density of states has been derived elsewhere¹⁷⁻¹⁹:

[‡]Here we neglect translational degrees of freedom

$$\mathcal{C}(E) = \int_{band} \mathcal{A}_r(\nu) \mathcal{E}_r(\nu) d\nu, \quad (5.18)$$

where \mathcal{A}_r is the absorption spectrum of the acceptor molecule and \mathcal{E}_r is the emission spectrum of the donor molecule (see also equation 2.46 on page 60).

In principle we should perform the calculations using trajectory calculations (“dynamical image”). We choose to adopt a “static image” for our calculations, which is slightly easier to calculate. In this model, given the large number of molecules interacting pairwise, any mutual position between two molecules can be found somewhere in the sample, and all mutual positions are equally probable. In this case we do not integrate over time following the trajectory of two molecules, but we integrate over the whole space at a given time. In principle the two models are equivalent, although there is one point that has to be verified. If, for a given situation in the dynamical image, the transition gets saturated (i.e. the probability of vibrational energy transfer in a collision is close to 1), the static model will overestimate the transition rate for this situation. We show in section 5.2.3 that in our case it is justified to use the “static model” for collisions with closest distance of $\sim 5-8 \text{ \AA}$.

At the first step we consider a single rotational state $|J^{(D)}, K^{(D)}\rangle$ of the excited molecule and calculate its relaxation rate. Then we average this rate over all possible $J^{(D)}$ and $K^{(D)}$ quantum numbers with their respective Boltzmann weights. This allows a better control over the calculation procedure and an easier verification of the results.

The V-V energy transfer rate of a molecule with rotational quantum numbers J and K relaxing on a molecule in the ground state in the static picture is given by the Fermi Golden Rule as follows¹⁶:

$$W_{JK} = 2\pi N \cdot \left(\int_{R_0}^{\infty} \langle | \langle i | V_d(R) | f \rangle |^2 \rangle (4\pi R^2) dR \right) \cdot \sum_{J'K'} \mathcal{Q}(\Delta\omega_{J'K'JK}) A_{J'K'JK}, \quad (5.19)$$

where N is the density of molecules, $\langle | \langle i | V_d(R) | f \rangle |^2 \rangle$ is $| \langle i | V_d(R) | f \rangle |^2$ averaged over their mutual orientations, the integral over the distances between the two molecules,

$A_{J'K'JK}$ are the Hönl-London factors cited previously in equations 5.14 and 5.15 and \mathcal{Q} is the correlation of the vibrational SIB spectrum $\mathcal{E}(\nu)$ of the excited molecule calculated previously in section 5.1.2 and the observed ground state absorption spectrum, $\mathcal{A}_r(\nu)$:

$$\mathcal{Q}(\Delta\omega) = \int_{\text{band}} \mathcal{E}(\nu') \mathcal{A}_r(\nu' + \Delta\omega) d\nu' \quad (5.20)$$

$\Delta\omega$ is the energy mismatch created by the rotational transition of the excited molecule and reads

$$\begin{aligned} \Delta\omega_{JKJ'K'} = & \langle B \rangle_E \cdot J \cdot (J + 1) - \langle B \rangle_{E-\nu_5} \cdot J' \cdot (J' + 1) \\ & + \langle C - B \rangle_E \cdot K^2 - \langle C - B \rangle_{E-\nu_5} \cdot K'^2, \end{aligned} \quad (5.21)$$

where unprimed quantum numbers refer to the initial state and the primed numbers to the final state of the donor molecule, and $\langle B \rangle$ and $\langle C \rangle$ are average rotational constants at the energy E . The values of $\langle B \rangle$ and $\langle C \rangle$ can be calculated with equation 2.14. Equations 5.17 and 5.19 are equivalent.

The interaction energy V_d between two dipole moments \vec{d}_1 and \vec{d}_2 at a certain respective distance \vec{R} and orientation is given by

$$V_d = \frac{1}{4\pi\epsilon_0} \cdot \left(\frac{(\vec{d}_1 \vec{d}_2)}{R^3} - 3 \cdot \frac{(\vec{d}_1 \vec{R})(\vec{d}_2 \vec{R})}{R^5} \right). \quad (5.22)$$

Thus, using the initial and final states $|i\rangle = |i_1\rangle |i_2\rangle$ and $|f\rangle = |f_1\rangle |f_2\rangle$, we get

$$\begin{aligned} (4\pi\epsilon_0) \cdot \langle i | V_d | f \rangle &= (\langle i_1 | \langle i_2 |) \left(\frac{(\vec{d}_1 \vec{d}_2)}{R^3} - 3 \cdot \frac{(\vec{d}_1 \vec{R})(\vec{d}_2 \vec{R})}{R^5} \right) (| f_1 \rangle | f_2 \rangle) \\ &= \frac{(\langle i_1 | \vec{d}_1 | f_1 \rangle \langle i_2 | \vec{d}_2 | f_2 \rangle)}{R^3} - 3 \cdot \frac{(\langle i_1 | \vec{d}_1 | f_1 \rangle \vec{R})(\langle i_2 | \vec{d}_2 | f_2 \rangle \vec{R})}{R^5} \\ &= \frac{(\vec{\mu}_1 \vec{\mu}_2)}{R^3} - 3 \cdot \frac{(\vec{\mu}_1 \vec{R})(\vec{\mu}_2 \vec{R})}{R^5}, \end{aligned} \quad (5.23)$$

where we defined $\vec{\mu} := \langle i | \vec{d} | f \rangle$, which is called the ‘‘transition dipole moment’’. The average of $|\langle i | V_d | f \rangle|^2$ can be calculated. We set $\vec{\mu}_i = (\mu_i \sin \phi_i \sin \theta_i, \mu_i \sin \phi_i \cos \theta_i, \mu_i \cos \phi_i)$ (for $i = 1, 2$) and $\vec{R} = (0, 0, R)$. The z axis is chosen to be parallel to \vec{R} . Then equation 5.23 becomes (with $\mu_1 = \mu_2 = \mu$):

$$(4\pi\epsilon_0) \cdot \langle i | V_d | f \rangle = \frac{\mu^2}{R^3} (\sin \phi_1 \sin \theta_1 \sin \phi_2 \sin \theta_2 + \sin \phi_1 \cos \theta_1 \sin \phi_2 \cos \theta_2 - 2 \cos \phi_1 \cos \phi_2) \quad (5.24)$$

To calculate the average value $\langle |\langle i | V_d | f \rangle|^2 \rangle$ the following integrations have to be performed:

$$(4\pi\varepsilon_0)^2 \cdot \langle |\langle i | V_d | f \rangle|^2 \rangle = \frac{\int_0^\pi d\phi_1 \int_0^{2\pi} d\theta_1 \int_0^\pi d\phi_2 \int_0^{2\pi} d\theta_2 (|\langle i | V_d | f \rangle|^2 \sin \phi_1 \sin \phi_2)}{\int_0^\pi d\phi_1 \int_0^{2\pi} d\theta_1 \int_0^\pi d\phi_2 \int_0^{2\pi} d\theta_2 (\sin \phi_1 \sin \phi_2)} \quad (5.25)$$

This integration has been done with the programme *mathematica*. The result is given as follows:

$$(4\pi\varepsilon_0) \cdot \langle |\langle i | V_d | f \rangle|^2 \rangle = \frac{2\mu^4}{3R^6} \quad (5.26)$$

For convenience we define

$$\mathcal{C}_{JK}(E) = \sum_{J'K'} \mathcal{Q}(\Delta\omega_{J'K'JK}) A_{J'K'JK}, \quad (5.27)$$

where the subscripts “ JK ” reflects the fact that we are treating excited molecules with the rotational quantum numbers J and K .

Equation 5.19 may now be rewritten. It reads, after integration:

$$W_{JK} = \frac{16\pi^2\mu^4 N \mathcal{C}_{JK}(E)}{9R_0^3 (4\pi\varepsilon_0)^2} \quad (5.28)$$

The calculation of W , i.e. the overall relaxation rate, is done by averaging the individual W_{JK} over all J and K rotational states with the weights $(2J+1) \cdot \exp(-F(v, J, K)/k_B T)$, where $F(v, J, K)$ is the energy of the initial level given in equation 5.10.

We have shown how to calculate energy transfer rates using the static picture presented here. As we have pointed out, we have to show that the energy transfer probability for a collision is smaller than 1 in order to avoid the static model overestimating the transfer rates. This will be done in the next section.

5.2.3 Justification of the “static model”

In this section we want to get an estimate of the conditions under which the static model can be used. For this, we have to ensure ourselves that the vibrational energy

transfer in an encounter between two molecules is not in saturation, otherwise the static model cannot be applied. We do this estimation by doing an approximate trajectory calculation the way described in what follows.

Figure 5.5 shows the relevant parameters for the calculation.

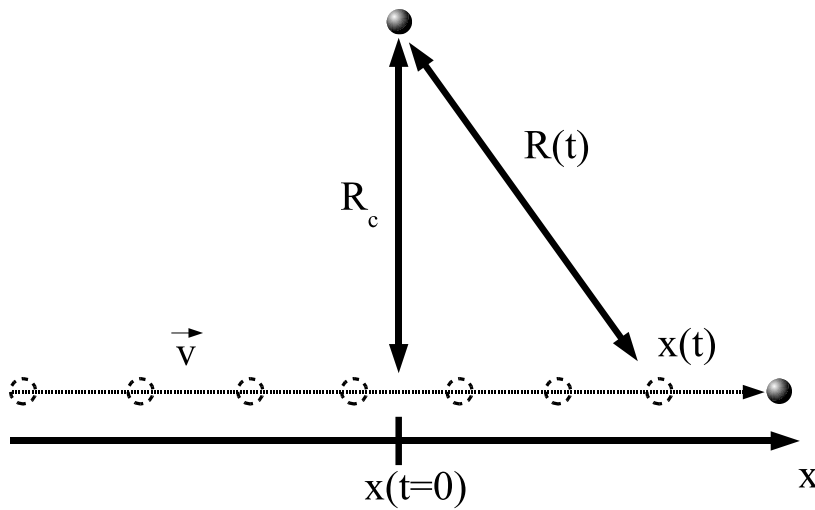


Figure 5.5: The calculation of the transition rate is done by integrating over the trajectory.

As the value of R_c is decreased, the overall probability of successful energy transfer is increased and will at a given moment approach saturation. We are interested in knowing at what value of R_c this happens. For that we will perform a simplified trajectory calculation of two molecules encountering each other. We define the moment when the molecules are the closest as $t=0$ and we wish to know what the probability of successful energy transfer integrated over the trajectory, from $t = -\infty$ to $t = +\infty$.

The probability that the excited molecule has successfully transferred a quantum of energy is given by $N_{success}(t) = 1 - \mathcal{P}(t)$ where \mathcal{P} is defined as follows:

$$\begin{aligned} \frac{d\mathcal{P}(t)}{dt} &= -W(t) \cdot \mathcal{P}(t) \\ \mathcal{P}(-\infty) &= 1 \end{aligned} \quad (5.29)$$

where W is given by the Fermi Golden Rule given in equation 5.17. We average over the mutual orientations (equation 5.26) and get:

$$\begin{aligned}
W(t) &= \frac{2\pi}{\hbar} \mathcal{C} \frac{2\mu^4}{3R(t)^6 (4\pi\epsilon_0)^2} \\
&= \frac{2\pi}{\hbar} \mathcal{C} \frac{2\mu^4}{3(R_c^2 + (v \cdot t)^2)^3 (4\pi\epsilon_0)^2}
\end{aligned} \tag{5.30}$$

where v is the relative velocity of the two molecules. The solution of equation 5.29 is

$$\mathcal{P}(t) = \exp\left(-\frac{A}{B} \cdot \frac{3\pi}{16}\right) \cdot \exp\left(-\frac{A}{8} \cdot \left(\frac{t(5 + 3B^2t^2)}{(1 + B^2t^2)^2} + \frac{3 \arctan(Bt)}{B}\right)\right), \tag{5.31}$$

where we defined

$$\begin{aligned}
A &= \frac{4\pi\mathcal{C}\mu^4}{3\hbar R_c^6 (4\pi\epsilon_0)^2} \\
B &= \frac{v}{R_c},
\end{aligned} \tag{5.32}$$

and hence

$$\mathcal{P}(t \rightarrow \infty) = \exp\left(-\frac{4\pi^2\mathcal{C}\mu^4}{8\hbar R_c^5 (4\pi\epsilon_0)^2 v}\right). \tag{5.33}$$

or, in a more convenient form:

$$\mathcal{P}(t \rightarrow \infty) = \exp\left(-2.2 \cdot 10^{-2} \cdot \left(\frac{\mathcal{C}}{0.01(\text{cm}^{-1})^{-1}}\right) \cdot \left(\frac{\mu}{0.391\text{D}}\right)^4 \cdot \left(\frac{10\text{\AA}}{R_c}\right)^5 \cdot \left(\frac{250\text{ms}^{-1}}{v}\right)\right), \tag{5.34}$$

where $0.01 (\text{cm}^{-1})^{-1}$ is a typical value for \mathcal{C} , 0.391 D is the strongest transition dipole moment in CF_3H (for the ν_5 mode) and 250 ms^{-1} is the average speed of a CF_3H molecule at room temperature.

If we choose to define a transition to be in saturation as soon as $N_{\text{success}}(t \rightarrow \infty) > 0.5$, we get for the minimum closest distance (using $\mu = 0.391 \text{ D}$ and $v = 250 \text{ ms}^{-1}$):

$$R_c^{\text{min}} = 5.0 \text{ \AA} \cdot \left(\frac{\mathcal{C}}{0.01 (\text{cm}^{-1})^{-1}}\right)^{\frac{1}{5}} \tag{5.35}$$

For a typical value of $\mathcal{C} = 0.01 (\text{cm}^{-1})^{-1}$, we get $R_c^{\text{min}} \approx 5 \text{ \AA}$, and even for exceptionally large values of $\mathcal{C} = 0.1 (\text{cm}^{-1})^{-1}$, the distance down to which our simulations can be done with the static image is $\sim 8 \text{ \AA}$.

These values are relatively low and we should be able to use our approach without any problems. However, we can only judge once we have calculated the value of R_0 and compare it with R_c^{min} .

5.2.4 Results

The expression 5.26 suggests a quartic power dependence of the probability of vibrational energy transfer on the transition dipole moment. In CF_3H , the ν_5 fundamental transition has the strongest change in dipole moment. For this reason, resonant V-V energy will be dominated by changes of quantum numbers in the ν_5 mode. For completeness, we include also the ν_2 , ν_3 and ν_6 modes. The ν_1 and ν_4 modes are excluded from the calculations since their polyad structure of the interacting modes ν_1 and ν_4 make it impossible to evaluate the relaxation rates of these modes. As their transition dipole moments are relatively small, excluding them will not influence the results noticeably.

Figure 5.6 shows the computed deactivation rates involving the ν_5 vibration as a function of the vibrational energy in the CF_3H molecule, obtained for different combinations of CF_3H isotopic species in a donor-acceptor pair. The calculations have been performed taking a value of $R_0 = 7.5 \text{ \AA}$. For the calculation of *relative* relaxation rates the choice of R_0 is unimportant. “Reasonable” values lie between¹⁶ ~ 6 and $\sim 9 \text{ \AA}$.

The corresponding plots for the ν_2 , ν_3 and ν_6 vibrations are shown in figure 5.7. The cases of ν_1 and ν_4 are left away, because the calculation of the SIB emission spectrum \mathcal{E} is not easy due to the strong Fermi Resonances between the two modes. We can leave away these modes: in the case of ν_4 , the transition dipole moment is 0.15 debye as opposed to 0.39 debye for ν_5 (see table 2.2) and the frequency ($\sim 1380 \text{ cm}^{-1}$) is comparable to that of ν_5 ($\sim 1158 \text{ cm}^{-1}$). Taking into account the strong dependence of the V-V energy transfer probability on the dipole moment ($W \propto d^4$) the contribution of ν_4 should be relatively small. ν_1 has a very high frequency ($\sim 3035 \text{ cm}^{-1}$) and a very small transition dipole moment (0.06 debye) so it will have a negligible influence on the relaxation rates.

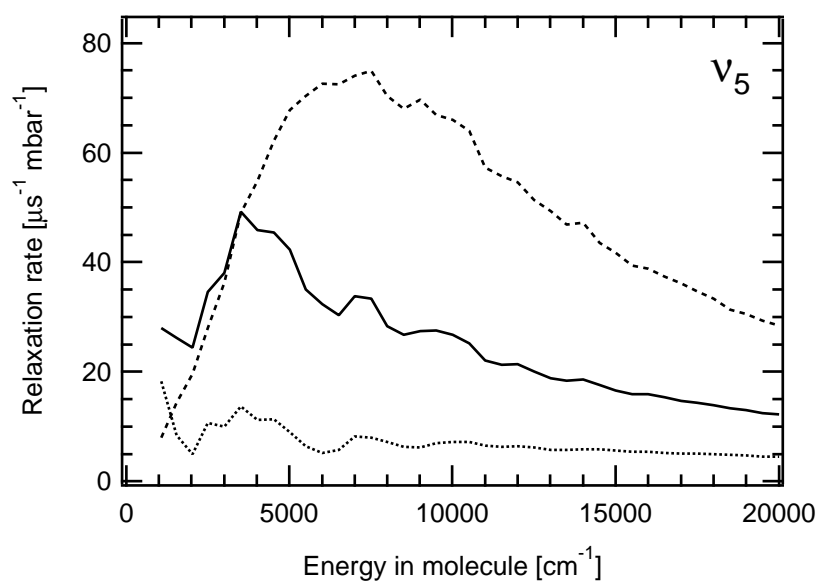


Figure 5.6: Absolute vibrational energy transfer rates for V-V relaxation mediated by the ν_5 mode.

— Self-relaxation ($^{12}\text{CF}_3\text{H}^* - ^{12}\text{CF}_3\text{H}$ and $^{13}\text{CF}_3\text{H}^* - ^{13}\text{CF}_3\text{H}$)

... $^{13}\text{CF}_3\text{H}^* - ^{12}\text{CF}_3\text{H}$

- - $^{12}\text{CF}_3\text{H}^* - ^{13}\text{CF}_3\text{H}$

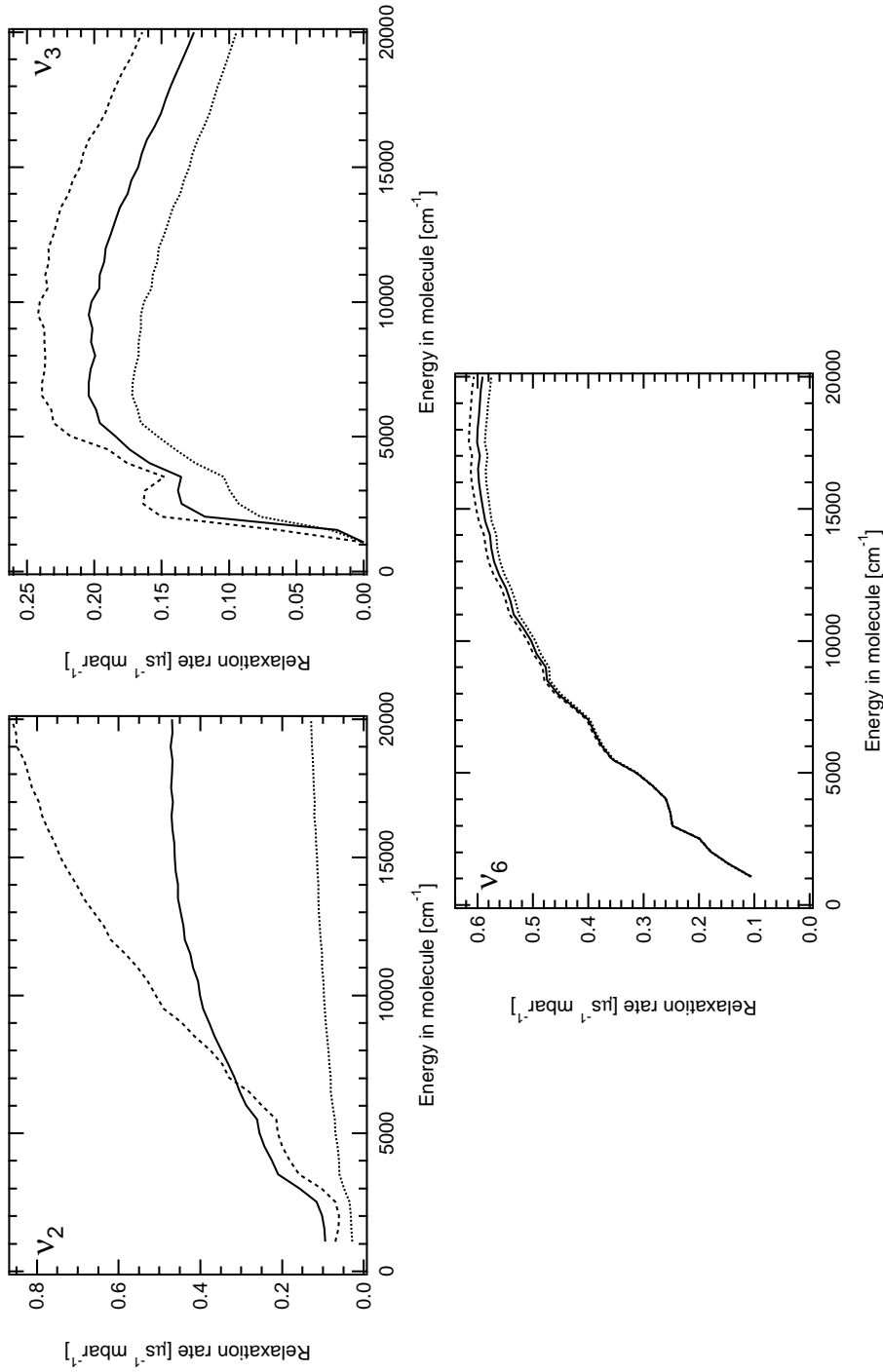


Figure 5.7: Relaxation rates associated with a particular mode.
 — Self-relaxation ($^{12}\text{CF}_3\text{H}^*_{12}\text{CF}_3\text{H}$ and $^{13}\text{CF}_3\text{H}^*_{13}\text{CF}_3\text{H}$), \cdots $^{13}\text{CF}_3\text{H}^*_{12}\text{CF}_3\text{H}$, $-\ -$ $^{12}\text{CF}_3\text{H}^*_{13}\text{CF}_3\text{H}$.

The figures 5.6 and 5.7 show different behaviours of the relaxation rates as a function of the vibrational energy in the donor molecule. However, a general feature is that the relaxation rate increases first, goes through a maximum and falls afterwards. This can be understood as follows. The relaxation rate is defined by the overlap of the absorption and the emission spectra of the donor and acceptor molecules, i.e. the shift between the two spectra and their intensities (integral absorption/emission strength). The behaviour of the shift is illustrated in figure 5.8 for the example of an excited $^{12}\text{CF}_3\text{H}$ molecule relaxing on a $^{13}\text{CF}_3\text{H}$ molecule in the ground state.

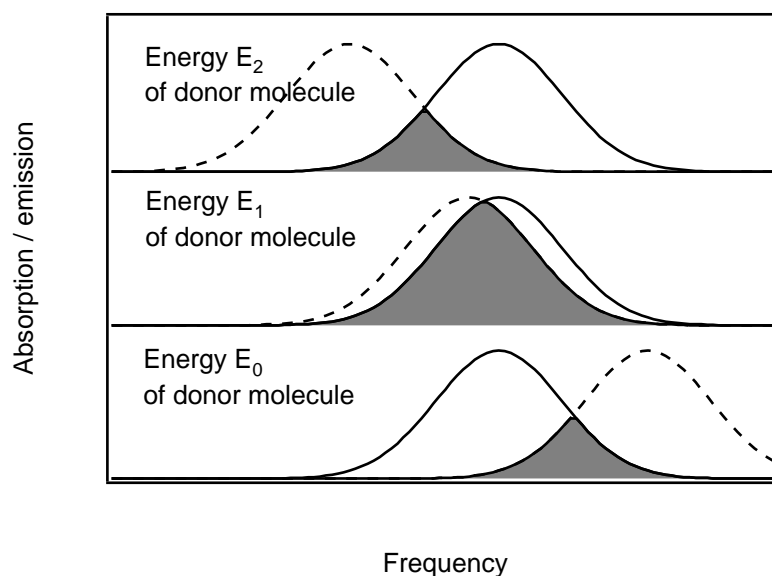


Figure 5.8: The shift between — absorption and - - emission spectra as a function of the energy of the donor molecule ($E_0 < E_1 < E_2$), using the example of $^{13}\text{CF}_3\text{H}$ as acceptor molecule and $^{12}\text{CF}_3\text{H}$ as donor molecule.

In order to get a feeling for the behaviour of the relaxation rate as a function of the vibrational energy E of the excited molecule we use the following approximate Gaussian absorption spectrum \mathcal{A}_r and emission spectrum \mathcal{E}_r (see section 5.1, using constant widths ω of the absorption/emission spectra):

$$\begin{aligned}\mathcal{A}_r &\approx \exp\left(-\left(\frac{\nu-\nu_a}{\omega}\right)^2\right) \\ \mathcal{E}_r &\approx (1 + A \cdot E) \cdot \exp\left(-\left(\frac{\nu-(\nu_d-E\cdot\Delta\nu)}{\omega}\right)^2\right),\end{aligned}\quad (5.36)$$

where A and $\Delta\nu$ are constants which depend on the vibrational modes we are considering (see table 5.1 on page 161) and ν_a and ν_d are the concerned band origins in the vibrational ground state of the acceptor and donor molecules. In this case, the vibrational relaxation rate W is given by

$$\begin{aligned}W &\propto \int_{\text{band}} \mathcal{A}_r(\nu)\mathcal{E}_r(\nu)d\nu \\ &\propto \underbrace{(1 + A \cdot E)}_{(I)} \cdot \underbrace{\exp\left(-\frac{1}{2} \cdot \left(\frac{(\nu_d - \nu_a) - E \cdot \Delta\nu}{\omega}\right)^2\right)}_{(II)},\end{aligned}\quad (5.37)$$

The figure 5.9 shows this function using again the example of excited $^{12}\text{CF}_3\text{H}$ relaxing on ground state $^{13}\text{CF}_3\text{H}$, using the ν_5 vibration as mediating vibration ($A = 2.08 \cdot 10^{-4}(\text{cm}^{-1})^{-1}$, $\Delta\nu = -7.09 \cdot 10^{-3}(\text{cm}^{-1})^{-1}$ (table 5.1), $\nu_d - \nu_a = 25 \text{ cm}^{-1}$ and $\omega \approx 25 \text{ cm}^{-1}$).

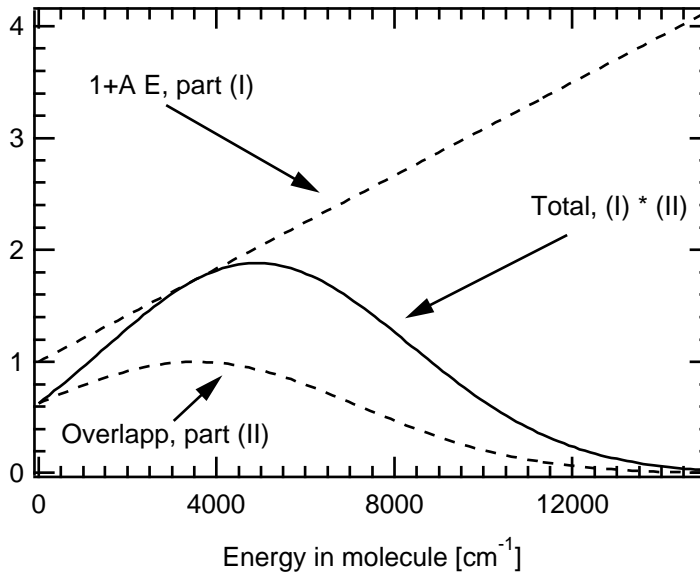


Figure 5.9: Parts (I) and (II) of equation 5.37 and the total relaxation rate W .

The solid curve in figure 5.9 can be compared with the dashed curve in figure 5.6 on page 174. The differences are due to the fact that here we have only done an approximate calculation in order to get an intuitive understanding of the processes.

In this spirit the following observations can be done and understood regarding the calculated relaxation rates given in figures 5.6 and 5.7.

1. In general the cross-relaxation of vibrationally excited $^{12}\text{CF}_3\text{H}$ on $^{13}\text{CF}_3\text{H}$ is faster than self-relaxation, which itself is faster than the relaxation of excited $^{13}\text{CF}_3\text{H}$ on $^{12}\text{CF}_3\text{H}$ in the ground state. For two molecules of the same isotopic species, the absorption and emission spectra are shifted by the anharmonic shift due to the vibrational excitation of the donor molecule ($E \cdot \Delta\nu \neq 0$, $\nu_d = \nu_a$ in equation 5.37). In the case of relaxation between molecules of different isotopic species, there is an additional isotopic shift ($\nu_d \neq \nu_a$). For excited $^{13}\text{CF}_3\text{H}$ relaxing on $^{12}\text{CF}_3\text{H}$ in the ground state, these shifts have the same sign ($\nu_d - \nu_a < 0$, $-E \cdot \Delta\nu < 0$), thus decreasing the energy transfer rate. In the case of excited $^{12}\text{CF}_3\text{H}$ relaxing on $^{13}\text{CF}_3\text{H}$ in the ground state, these shifts have opposite signs ($\nu_d - \nu_a > 0$, $-E \cdot \Delta\nu < 0$) canceling each other and this way increasing the energy transfer rates.
2. The anharmonic red-shift of the absorption spectrum grows upon increasing the level of vibrational excitation. In the case of self-relaxation and the relaxation of excited $^{13}\text{CF}_3\text{H}$ on ground state $^{12}\text{CF}_3\text{H}$ this effect tends to decrease the overall relaxation rate because the overlap of the emission spectrum with the ground state absorption spectrum decreases. In the case of excited $^{12}\text{CF}_3\text{H}$ relaxing on ground state $^{13}\text{CF}_3\text{H}$ this effect first tends to increase the relaxation rates because the isotopic and the anharmonic shifts have opposite signs, such as the overall shift reduces upon excitation. At some point the anharmonic shift prevails and the overall shift begins to increase, resulting in a decrease of the relaxation rates (ν_3 and ν_5 are good examples).
3. In the case of the ν_6 mode the isotopic shift is small ($\sim 1 \text{ cm}^{-1}$) compared with the anharmonic one ($\nu_d \approx \nu_a$ in equation 5.37), such as the computed relaxation rates are almost the same for all three pairs of isotopic species.

4. For strong anharmonic modes, the drop in V-V energy transfer rate at high energies is faster because the overlap of the emission spectrum and the ground state absorption spectrum decreases faster (ν_5 is very anharmonic whereas ν_2 and ν_6 are only slightly anharmonic).

The resulting relaxation rates for the ν_2, ν_3, ν_5 and ν_6 modes can be added together to get the total relaxation rate. It turns out that in most cases ν_5 is by far the most important mediating mode for V-V energy transfer, which is due to the very large transition dipole moment. This shows a posteriori that leaving away ν_1 and ν_4 does not alter the results significantly. In general, in the dipole-dipole model of collisional vibrational energy transfer the most important contribution is to be expected from the vibrations with a large transition dipole moment (ν_5) and/or a low frequency[‡] (ν_6).

Figure 5.10 shows the contribution of the ν_5 mode to the V-V energy transfer for self-relaxation ($^{12}\text{CF}_3\text{H}^* - ^{12}\text{CF}_3\text{H}$ and $^{13}\text{CF}_3\text{H}^* - ^{13}\text{CF}_3\text{H}$) and for cross-relaxation ($^{12}\text{CF}_3\text{H}^* - ^{13}\text{CF}_3\text{H}$ and vice versa). For example, at $v_{CH} = 3$, the contribution of ν_5 lies between 90% ($^{13}\text{CF}_3\text{H}^* - ^{12}\text{CF}_3\text{H}$) and 98% ($^{12}\text{CF}_3\text{H}^* - ^{13}\text{CF}_3\text{H}$).

The resulting relaxation rates will be dominated by ν_5 and closely resemble the curves for this mode which is presented in figure 5.6. We defined in equation 4.13 the following values:

$$\begin{aligned}\mathcal{R}_{12} &:= \kappa(12^* - 13)/\kappa(12^* - 12) \\ \mathcal{R}_{13} &:= \kappa(13^* - 13)/\kappa(13^* - 12) \quad ,\end{aligned}\tag{5.38}$$

where $\kappa(x^* - y)$ is the relaxation rate of excited $^x\text{CF}_3\text{H}$ on ground state $^y\text{CF}_3\text{H}$. We were able to measure \mathcal{R}_{12} and \mathcal{R}_{13} experimentally. Figure 5.11 shows the calculated and the measured values for \mathcal{R}_{12} and \mathcal{R}_{13} as a function of the vibrational energy in the excited molecule.

[‡]The transition strength between two states $|v_1, v_2, \dots, v_p, \dots, v_6\rangle \rightarrow |v_1, v_2, \dots, v_p - 1, \dots, v_6\rangle$ scales as $\sigma(v_p \rightarrow v_p - 1) = v_p \cdot \sigma(1 \rightarrow 0)$. This means that upon an increase of vibrational quantum numbers (i.e. with increasing level of vibrational excitation) the transition strengths go up. In general, ν_6 ($\omega_6 \sim 507 \text{ cm}^{-1}$) has the highest average occupation number, making this mode increasingly important for relaxation at high vibrational levels.

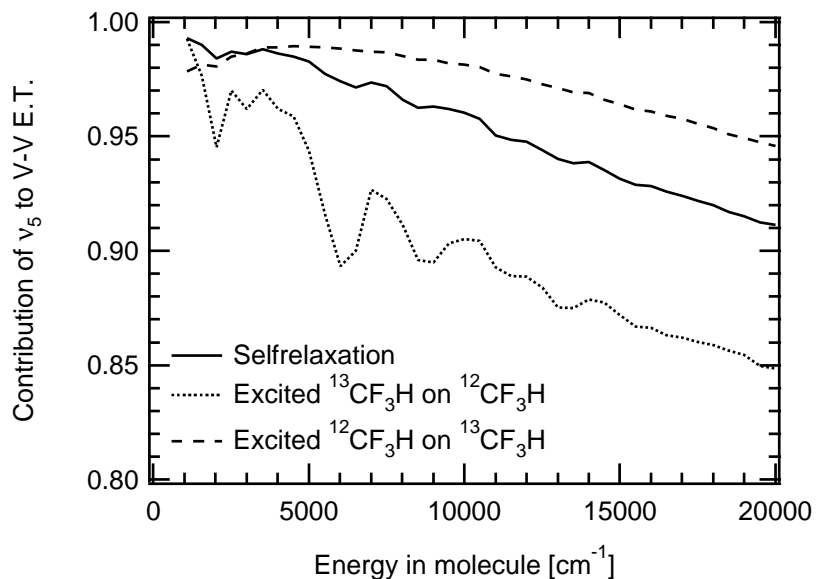


Figure 5.10: Contribution of ν_5 to the V-V energy transfer process.

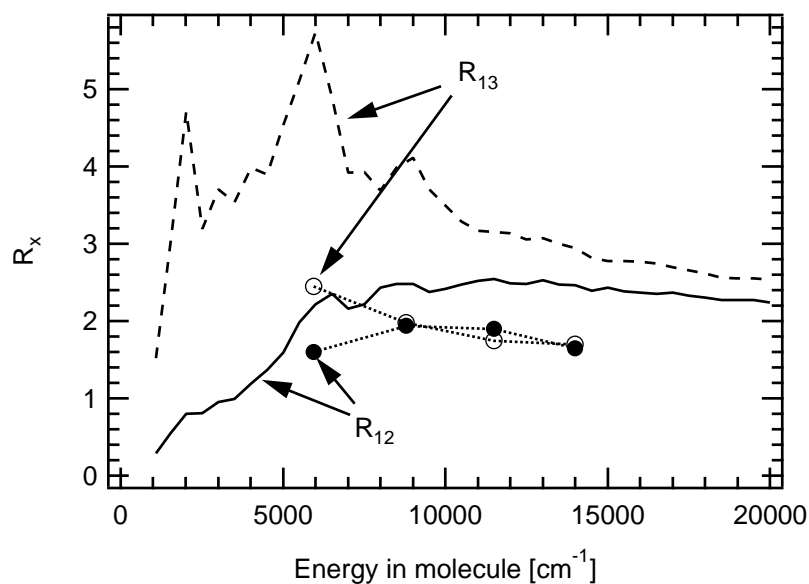


Figure 5.11: Results for \bullet — \mathcal{R}_{12} and \circ - - \mathcal{R}_{13} where only vibrational energy transfer via long range dipole-dipole interactions are considered (\bullet and \circ : experimental data, — and - -: numerical simulations).

The calculated values of \mathcal{R}_{13} are nearly twice as high as the experimental values, overes-

timating the observed isotopic selectivity. Also the calculated values for \mathcal{R}_{12} are slightly overestimated. Apparently our simple model does not account for all details of the process to make the results accurate. Although we do not attempt to elaborate a suitable accurate model here, we discuss in the following section the most sensitive simplifications of our model and possible physical mechanisms, which are likely to be considered in the initial stages of improving accuracy.

5.2.5 Discussion

Perhaps the most important result of our performed calculations in the framework of a relatively simple model based only on dipole-dipole interactions is that there has to be, indeed, a significant isotopic selectivity in collisional vibrational deactivation of CF_3H . The qualitative behaviour of this selectivity corresponds well to our experimental observations. Nevertheless there is still a considerable quantitative discrepancy between the calculations and the experiments (figure 5.11). Below we analyse in more detail the assumptions of the model that we used in the previous section. The following assumptions were used:

1. Rotational relaxation is complete.
2. IVR is complete.
3. Higher order poles do not contribute to V-V energy transfer. All encounters of two molecules with a distance $R < R_0$ are excluded. R_0 is a cut-off distance where higher order interaction terms prevail with respect to dipole-dipole interactions.

Assumption 1 is well met, since we do not detect any rotational dependence of isotopic selectivity (see the experimental data in section 3.2), so this point will not be investigated further.

Concerning the problem of IVR (assumption 2), we made the assumption IVR is complete in the molecule undergoing vibrational energy transfer[‡]. Intrinsic IVR such as collisionally induced IVR can occur. We have discussed this issue earlier: in CF_3H

[‡]Vibrational energy transfer *prior* to IVR is possible, but very slow, because the emission spectrum of a molecule in the 3_1 state overlaps very little with the absorption spectrum of a CF_3H molecule in the ground state.

excited via the 3_1 mode the time-scale for collision-free IVR is on the 100 ps time-scale (section 2.1.2.B) and for collision-induced IVR roughly 10-20 ns for a sample pressure of 1 mbar (section 2.1.2.C and using the relation the CI-IVR scales with the pre-excitation energy¹⁶). Furthermore a single encounter of two molecules can potentially induce IVR and then mediate V-V energy transfer in the same collision. It is hence reasonable to assume that our second assumption is well met.

Assumption 3 is a rather strong simplification. In the last section we described our calculations of vibrational energy transfer rates for CF_3H assuming exclusively the dipole-dipole interaction mechanism of the transfer. In reality, higher order interactions, like quadrupole, may also be significant, especially at short intermolecular distances. It is reasonable to expect that the isotopic selectivity of the energy transfer caused by these short distance interactions is negligible. The rotational selection rules $\Delta J, \Delta K = (0, \pm 1)$ are broken and scale with the order of the pole broadening the emission and absorption spectra. For very high order interactions this broadening scrambles any isotopic selectivity. This non-selective transfer via multipole interactions would offset the isotopically selective transfer rates, calculated for dipole-dipole interactions, approaching the overall calculated isotopic selectivity to the experimentally measured values.

In what follows we take into account these higher order poles in such “head-on” collisions. Although in principle we could treat the process in a similar manner as we did for dipole-dipole interactions, it is practically not feasible, as no information on quadrupole, let alone higher order poles exist for this molecule. We hence empirically summarise the set of higher order poles into one single parameter: the number of collisions \aleph with a mutual distance $\leq R_0$ it takes for a molecule to lose the same amount of energy as by resonant energy transfer (via the ν_5 vibration, i.e. $\sim 1000 \text{ cm}^{-1}$). We are now left with two parameters: R_0 and \aleph , which have to be varied to adequately fit our experimental data. For the vibrational energy transfer rate for large distance encounters $R \geq R_0$ we use the transition rates calculated previously. We use two fitting parameters, R_0 and \aleph , because we want to reproduce both the isotopic selectivity for the relaxation rates and their absolute values. Note that we have two values, $\mathcal{R}_{12} = \kappa(12^* - 12)/\kappa(12^* - 13)$ and $\mathcal{R}_{13} = \kappa(13^* - 12)/\kappa(13^* - 13)$, for four different pre-excitation levels we would like to reproduce with only two fitting parameters.

From physical considerations the values of our fit parameters can be limited:

- R_0 typically¹⁶ lies between ~ 6 and ~ 9 Å. At smaller distances and very close encounters repulsive forces of the intermolecular interaction are much more important than the attractive, dipole-dipole interactions.
- \aleph is difficult to evaluate. For close encounters it is reasonable to assume that some energy will be transferred, but we have only little information on the quantity of energy transferred. However, the amount of energy transferred should scale with the internal energy of the molecule, what has been explained in a previous section (see e.g. equation 2.53 on page 64). Thus, we set $\aleph(E) = \aleph'/E$, and we wish to determine the constant \aleph' .

This model we present here resembles to the ones presented earlier by Mahan²⁰ and Sharma and Brau²¹⁻²³ (the theories have been presented earlier in this text, in section 2.3.2.B). The essential difference is that these authors *defined* a certain value for R_0 and \aleph . In our case, we *fit* these parameters, because we have the possibility to do so because we have a set of measurements involving different isotopic species which allows us to separate the influence of resonant vibrational energy transfer due to long-range, attractive interactions and non-resonant vibrational energy transfer due to short-range, repulsive interactions.

In order to sum the two contributions, we use the following relaxation rate that can be calculated with the hard sphere model for a sample of CF₃H at room temperature[‡]:

$$W = \frac{E}{\aleph'} \cdot 2.71 \cdot 10^5 \cdot \left(\frac{R_0}{\text{Å}} \right)^2 \text{ s}^{-1} \text{ mbar}^{-1} \quad (5.39)$$

The question is: what values of \aleph' and R_0 yield correct values for $\mathcal{R}_{12} = \kappa(12^* - 13)/\kappa(12^* - 12)$ and $\mathcal{R}_{13} = \kappa(13^* - 13)/\kappa(13^* - 12)$ (where $\kappa(X^* - Y)$ is the relaxation rate of an excited ^XCF₃H molecule on a ground state ^YCF₃H molecule) ?

[‡]The mean free path is given by $\lambda = RT/\sqrt{2}\pi R_0^2 N_A p$ where R is the molar gas constant, T the temperature, N_A the Avogadro constant and p the pressure. The average speed for a particle of a mass of 102 a.m.u. at a temperature of 20°C is 247 m s⁻¹ if the speed distribution follows the Maxwell-Boltzmann law.

We show in figure 5.12 the sets of R_0 and \aleph' which fit our experimental data well. They have been determined in order to fit best the values for excitation up to $v_{CH} = 3$ (any other procedure would yield similar results).

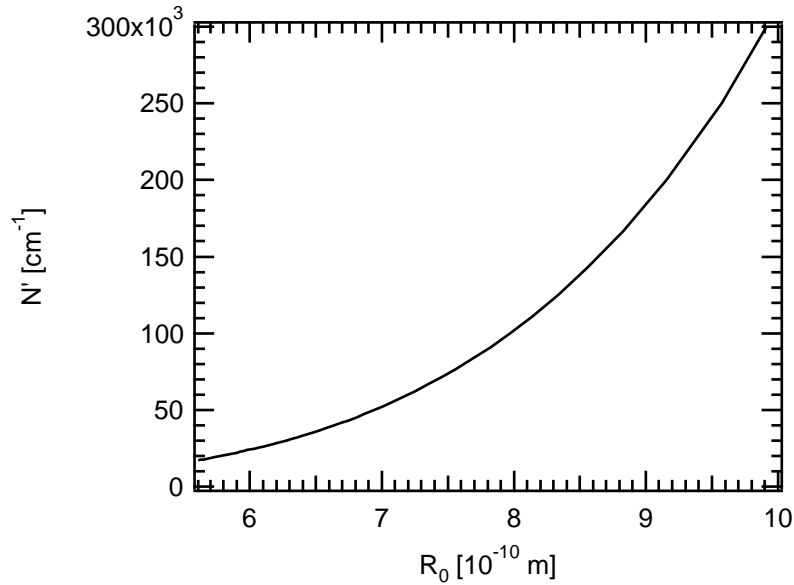


Figure 5.12: Pairs of R_0 and \aleph' which fit to the measured isotopic selectivity of the relaxation rates well.

Each of these sets yield the same values for *relative* relaxation rates, i.e. $\mathcal{R}_{12} = \kappa(12^* - 13)/\kappa(12^* - 12)$ and $\mathcal{R}_{13} = \kappa(13^* - 13)/\kappa(13^* - 12)$. We show in figure 5.13 the calculated relative relaxation rates \mathcal{R}_{12} and \mathcal{R}_{13} compared to our experimental data.

On figure 5.13 we can see that the experimental relative relaxation rates are very well reproduced, both qualitatively and quantitatively, which is a very nice result given that we work with only two fitting parameters, R_0 and \aleph' !

The *absolute* relaxation rates, which depend on the choice of the pair of R_0 and \aleph' , cannot be determined directly for the moment. In simulations presented later involving the whole laser isotope separation process including IRMPD (see section 5.3), we find the following values:

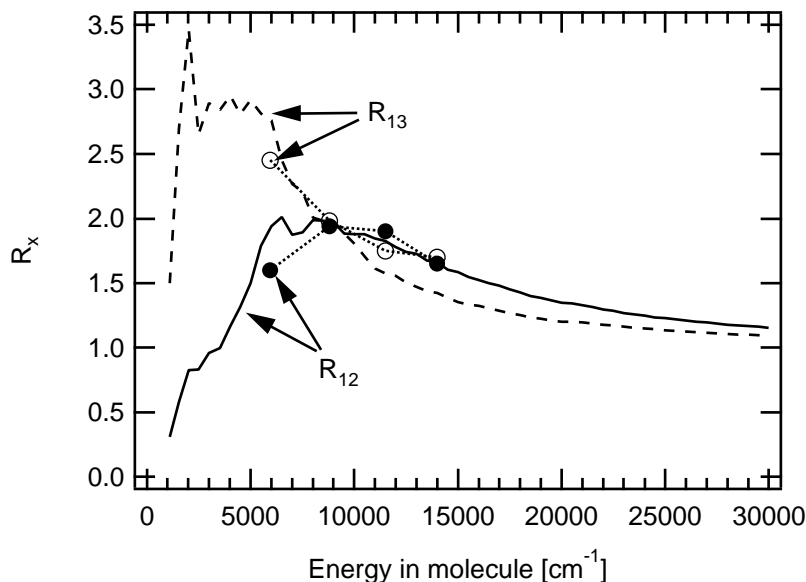


Figure 5.13: Calculated and experimental relative relaxation rates of vibrationally excited CF_3H on $^{12}\text{CF}_3\text{H}$ in the vibrational ground state.

● — $\kappa(12^* - 13)/\kappa(12^* - 12)$.

○ - - $\kappa(13^* - 13)/\kappa(13^* - 12)$.

$$R_0 = 7.4 \text{ \AA}$$

$$\aleph' = 6.8 \cdot 10^4 \text{ cm}^{-1}$$

Using these values, the absolute relaxation rates are computed and shown in figure 5.14. Furthermore, going back to section 5.2.3, we stated that if $R_0 \gtrsim 5 - 8 \text{ \AA}$, then the static picture can be used, its use is justified a posteriori.

The value for R_0 is very reasonable¹⁶ as one would expect typical values between 6 and 9 \AA ! The number of head-on collisions \aleph (with a mutual distance of $R < 7.4 \text{ \AA}$) such that $\sim 1000 \text{ cm}^{-1}$ is lost, is $6.8 \cdot 10^4 \text{ cm}^{-1} / E$ where E is the vibrational energy of the excited molecule. For example, a molecule with a vibrational energy of 8800 cm^{-1} (a molecule pre-excited via the 3_1 band) necessitates ~ 7.7 collisions ($R < 7.4 \text{ \AA}$) for the loss of $\sim 1000 \text{ cm}^{-1}$, or, in other words, every hard-sphere collision results in a transfer of $\sim 1000/7.7 \approx 130 \text{ cm}^{-1}$. Comparing this value with measured values for toluene and benzene ($\sim 300 \text{ cm}^{-1}$ per collision²⁴, see figure 2.16 on page 72), we see that this value

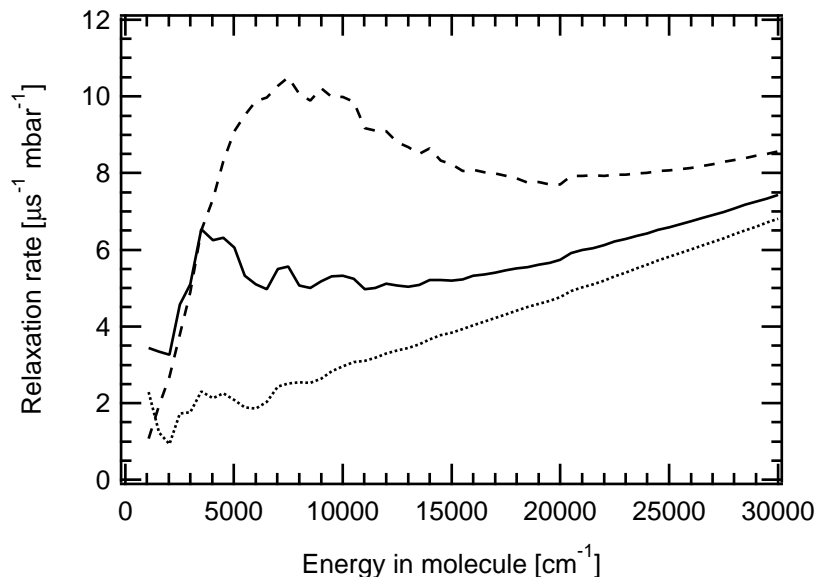


Figure 5.14: Relaxation rates as a function of the energy in the molecule (for $R'_0 = 7.4 \text{ \AA}$, $N' = 6.8 \cdot 10^4 \text{ cm}^{-1}$).

— self-relaxation rates

⋯ excited $^{13}\text{CF}_3\text{H}$ on ground state $^{12}\text{CF}_3\text{H}$

- - excited $^{12}\text{CF}_3\text{H}$ on ground state $^{13}\text{CF}_3\text{H}$

has the correct order of magnitude.

5.2.6 Conclusions

In this section we have described how we calculate collisional relaxation rates of excited CF_3H molecules on ground state CF_3H molecules. Under certain assumptions described at the beginning, we develop a theory for the calculation of relaxation rates for VET mediated by dipole-dipole interactions. We show that if we consider only these long-range interactions the calculated isotopic selectivity is too high, and we show that we necessitate non-selective collisional relaxation by head-on collisions in order to reproduce the experimental values of isotopic selectivity. The dependency of this selectivity on the vibrational energy of a molecule is very well reproduced (figure 5.13).

We have given a coherent picture of the process of the exchange of one quantum during the collision between an excited and a ground state CF_3H molecule. We have shown

that with a simple model we can correctly describe the experimentally observed isotopic selectivity. In particular, we have shown that for encounters between two molecules with an impact parameter $\gtrsim 7.4 \text{ \AA}$, near-resonant V-V energy transfer occurs and that for smaller mutual distances non-resonant V-V',T,R energy transfer occurs.

5.3 Numerical simulations of IRMPD in the presence of collisions

In this section we present numerical simulations of our molecular laser isotope separation (MLIS) process consisting of pre-exciting molecules to a vibrational overtone of the CH stretch-bend vibration, and then selectively dissociating only pre-excited molecules. The goal is twofold: first, we seek a better understanding of how different parameters affect our MLIS process and secondly we interested which mechanisms lead to the increase of isotopic selectivity upon an increase of the sample pressure. For this, these simulations are necessary as the IRMPD is a non-linear process with respect to the fluence of the CO₂ dissociation laser, which has been well confirmed by experiments and simulations before^{25, 26}. After a brief introduction to the subject, we briefly state the equations that have to be solved by the numerical code. Then we show how to evaluation the physical parameters of these equations. We finally present the results: here, we first compare our simulations with our experimental data and show that our model reliably describes the processes. This allows us to have a look at the mechanisms of and the influences of different physical parameters on our MLIS scheme.

5.3.1 Generalities

In our approach to the numerical simulations, we base ourselves on a statistical treatment presented earlier in this text (see section 2.2.3.B). Briefly, one bins the vibrational levels into coarse grained levels of width ΔE , i.e. all vibrational states with an energy E lying between $i\Delta E$ and $(i + 1)\Delta E$ belong to level i . This way one uses calculated transition rates for the population and depopulation of these bins. These transition rates are calculated averaging over all possible transitions between the members of the bins.

For the simulation of the whole MLIS process, we take these grained energy levels as a starting point, taking into account the following effects by which the molecule may lose or gain energy:

IR photon absorption/emission: by absorbing or emitting one quantum of energy $p\Delta E$ molecules are pumped up and down.

Unimolecular dissociation: if the molecules have enough energy, they can dissociate. For CF_3H the lowest dissociation channel is $\text{CF}_3\text{H} \rightarrow \text{CF}_2 + \text{HF}$.

Collisions: in collisions molecules can undergo vibrational relaxation and gain or lose energy.

Overtone pre-excitation: for the MLIS experiments a part of the molecules are promoted with a laser via an overtone of the CH stretch vibration into a vibrationally excited state.

In principle spontaneous emission could be included too, but it can be safely neglected²⁷ because the time-scale for such a process is typically milliseconds whereas we are working on time-scales of 100 ns - 1 μs . We show in figure 5.15 the main effects by which the molecules can gain or lose vibrational energy.

For all our calculations the ensemble of molecules is considered to be rotationally relaxed (in section 3.2 we have shown that at a pressure of $\gtrsim 1$ mbar rotational relaxation is complete). In principle uncomplete rotational relaxation could be treated by introducing some phenomenological parameters into the dissociation laser absorption steps characterising the degree of rotational relaxation²⁸, but as we work at pressures of typically ~ 1 mbar this problem is circumvented.

5.3.2 Formalisation of the problem: the master equation

For the numerical simulations we work with a large ensemble of molecules, each one having a certain internal energy E lying in a certain bin i . N_i is defined as the probability of a molecule having an energy corresponding to bin i and is a function of time. We have to consider only the first n bins, where n has to be large enough so that for the highest lying bin dissociation is very important compared to up- and down-pumping by

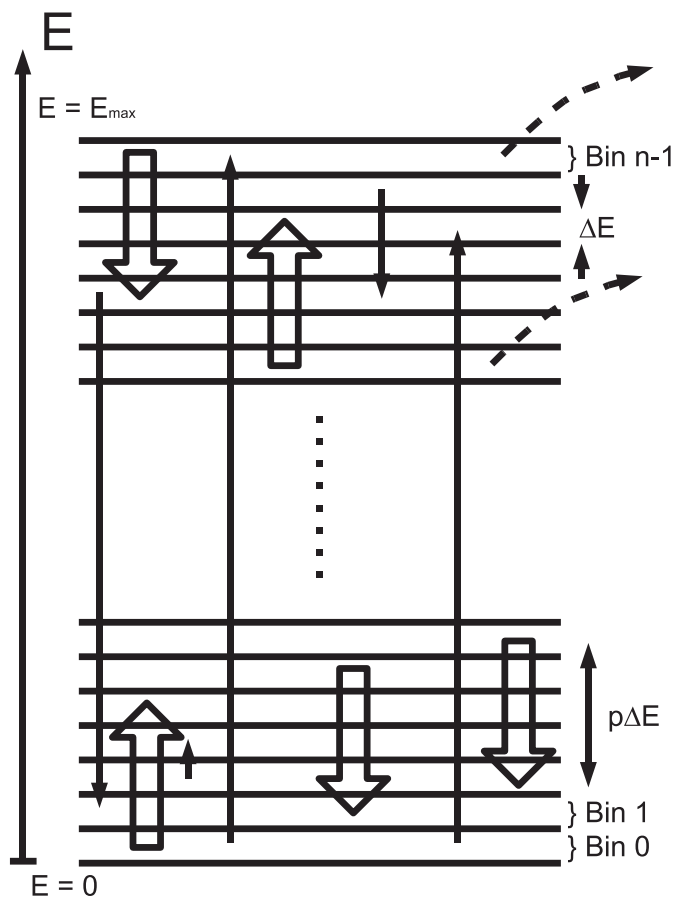


Figure 5.15: Energy level diagram: \uparrow and \downarrow are due to collisions; \Uparrow and \Downarrow are due to pumping by the CO_2 laser; \dashrightarrow are losses due to unimolecular dissociation of the molecules. The pre-excitation step is not shown.

the laser or by collisions.

We define

$$\mathcal{N} := \begin{pmatrix} N_0 \\ N_1 \\ N_2 \\ \vdots \\ N_{n-1} \end{pmatrix} \quad (5.40)$$

and the goal is to find equations describing the variation of \mathcal{N} as a function of time.

CO₂ laser pumping: The CO₂ laser photons make steps of p . The population and depopulation rates of the grained bins read

$$\frac{dN_i}{dt} = - ({}^{IR}k_{i+p,i} + {}^{IR}k_{i-p,i}) \cdot N_i + {}^{IR}k_{i,i-p} \cdot N_{i-p} + {}^{IR}k_{i,i+p} \cdot N_{i+p}, \quad (5.41)$$

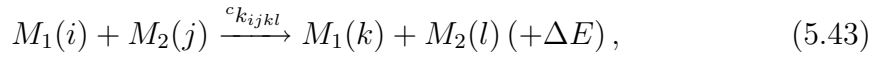
where ${}^{IR}k_{i\pm p,i}$ are the up- and down-pumping constants from level i to levels $i \pm p$.

Dissociation: Rates due to unimolecular dissociation read

$$\frac{dN_i}{dt} = - {}^d k_i \cdot N_i, \quad (5.42)$$

where ${}^d k_i$ is the dissociation rate of level i .

Collisions: Define ${}^c k_{ijkl}$ as rate of vibrational energy transfer via



where i, j, k, l are the labels of the energy bins of molecules 1 and 2. In that case, the rate equations read

$$\frac{dN_i}{dt} = - \sum_{j=0}^{n-1} {}^c k_{ij} \cdot N_i \cdot N_j + \sum_{j_1=0}^{n-1} \sum_{j_2=0}^{n-1} {}^c k_{j_1 j_2 i} \cdot N_{j_1} \cdot N_{j_2}, \quad (5.44)$$

where

$$\begin{aligned} {}^c k_{ijk} &:= \sum_{l=0}^{n-1} {}^c k_{ijkl} \\ {}^c k_{ij} &:= \sum_{k=0}^{n-1} \sum_{l=0}^{n-1} {}^c k_{ijkl} \quad . \end{aligned} \quad (5.45)$$

Overtone pre-excitation: The rates due to the pre-excitation laser read

$$\begin{aligned}\frac{dN_0}{dt} &= -{}^p k \cdot N_0 \\ \frac{dN_P}{dt} &= {}^p k \cdot N_0 \quad ,\end{aligned}\tag{5.46}$$

where level p is the level populated by the pre-excitation laser.

Note that ${}^{IR}k_{ij}$ and ${}^p k$ are time dependent.

This leaves us with the following master equation

$$\frac{d\mathcal{N}}{dt} = A_1 \mathcal{N} + A_2 \mathcal{N}^2,\tag{5.47}$$

where A_1 is a $(n \cdot n)$ matrix and A_2 is a $(n \cdot n \cdot n)$ tensor. Their elements are

$$(A_1)_{ij} = \begin{cases} -(d k_i + {}^{IR}k_{i,i+p} + {}^{IR}k_{i,i-p}) & (i = j) \\ {}^{IR}k_{i,j} & (i = j \pm p) \\ 0 & (\text{otherwise}) \end{cases} + \begin{cases} -{}^p k & (i = j = 0) \\ {}^p k & (i = P, j = 0) \\ 0 & (\text{otherwise}) \end{cases}\tag{5.48}$$

and[‡]

$$(A_2)_{ijk} = {}^c k_{jki} - \delta_j^i \cdot {}^c k_{ik}.\tag{5.49}$$

In order to simplify the equation to be solved, we assume the following:

- The large majority of the molecules are in the ground state.
- Vibrational relaxation leads to steps of p between different bins (because it is mainly mediated by one vibration, ν_5 in our case).

The first condition is well satisfied in our experiments. This allows for the following simplification: as $\forall t : N_0(t) \approx 1$ and $N_i(t) \ll 1 (\forall t, \forall i \geq 1)$ the relaxation rates can be embedded into A_1 . Secondly, only steps of p are done for vibrational relaxation: the excited molecule moves down by p bins, the ground state molecules move up by p bins. This way, the rates due to vibrational relaxation read:

$${}^\ddagger (A_2 \mathcal{N}^2)_k = ((A_2 \mathcal{N}) \mathcal{N})_k = \sum_{i=0}^{n-1} \sum_{j=0}^{n-1} (A_2)_{kij} N_i N_j$$

$$\begin{aligned}
\frac{dN_0}{dt} &= v_{k_j} \cdot N_p - F \cdot \sum_{j=1}^{n-1} v_{k_j} \cdot N_j \\
\frac{dN_i}{dt} &= -v_{k_i} \cdot N_i + v_{k_{i+p}} \cdot N_{i+p} \quad (i \geq 1, i \neq p) \\
\frac{dN_p}{dt} &= \left(F \cdot \sum_{j=1}^{n-1} v_{k_j} \cdot N_j \right) - v_{k_p} \cdot N_p + v_{k_{2p}} \cdot N_{2p} \quad ,
\end{aligned}
\tag{5.50}$$

where v_{k_j} is the relaxation rate of an excited molecule in bin j on ground state $^{12}\text{CF}_3\text{H}$ and F is the 0.99 for the $^{12}\text{CF}_3\text{H}$ molecule and 0.01 for the $^{13}\text{CF}_3\text{H}$ molecule, taking into account that there are also other relaxation partners in the sample other than the ones we are considering in the simulations. The implementation into A_1 is straightforward and analogous to the previously explained cases. We are left with the following simplified master equation

$$\frac{d\mathcal{N}(t)}{dt} = A_1(t) \cdot \mathcal{N}(t) \tag{5.51}$$

to be solved by a numerical code.

5.3.3 Evaluation of physical values for the master equation

In the previous section we gave the master equation in expression 5.51. The $(n \cdot n)$ matrix contains all rate constants that take into account the population and depopulation due to the pre-excitation and the dissociation lasers, unimolecular dissociation and V-V energy transfer. In the following sections we go into further detail regarding the numerical evaluation of the different terms of A_1 .

5.3.3.A Overtone pre-excitation

Here the absolute values are not important. It has to be evaluated in such a way that a small fraction of the molecules are pre-excited (typically $\sim 1-5\%$) in order to fulfill the assumption that relaxation occurs only on molecules in the vibrational ground state.

5.3.3.B Collisional relaxation

In section 5.2 we have calculated the *relative* relaxation rates, the absolute values are not known. We take the rates for collisional relaxation determined numerically (in

section 5.2) and introduce a scaling parameter that has to be fitted in our simulations.

5.3.3.C Unimolecular dissociation

In the absence of any experimental data the dissociation rates of molecules excited above the dissociation limit have to be calculated. The central equation for calculating the dissociation rate $k(E)$ is

$$k(E) = \frac{N^\ddagger(E - E_0)}{h\rho(E)}, \quad (5.52)$$

where N^\ddagger is the sum of states at the transition state, where the reaction coordinate remains fixed, ρ is the reactant density of states, E is the energy inside the molecule and E_0 is the energy at the transition state with respect to the ground state of the reactant. To apply this the existence of a transition state is a pre-requisite. This is a (unique) saddle point on the potential energy surface that the molecule necessarily has to cross to dissociate and which separates the bound state from the dissociated state.

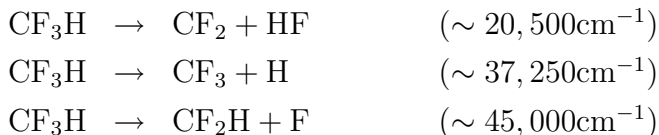
Different theories for the calculation of dissociation rates commonly admit equation 5.52, they differ in how N^\ddagger and ρ are evaluated. Popular theories include RRK and RRKM²⁹, SACM³⁰ (Statistical adiabatic channel model) or phase space theories (PST). We use the RRKM theory.

In the RRK (Rice-Ramsperger-Kassel) theory³¹⁻³³ the molecule is treated as a set of s independent harmonic oscillators which, however, freely exchange energy. This energy is statistically distributed over all vibrational degrees of freedom. Within this framework the evaluation of N^\ddagger and ρ is done by direct counting (including anharmonicity). The calculations are very straightforward, although some knowledge of the transition state (energy E_0 and vibrational frequencies) is necessary. In the RRKM (RRK-Marcus) theory³⁴⁻³⁷ the effect of rotational energy, angular momentum and zero-point energies are explicitly included.

(I) RRKM calculations for CF₃H

The unimolecular dissociation reaction of CF₃H has different channels, the three lowest

are³⁸



where the energies in brackets are evaluated by Shin³⁸ calculating the differences of the enthalpy H_f of CF_3H and the products³⁹. The dissociation level can lie higher if they go through an energetic maximum. In the case of the first dissociation channel, it lies at⁴⁰ $\sim 24,000 \text{ cm}^{-1}$.

For the calculation of the dissociation rates we use the dissociation energy E^{TS} and the vibrational frequencies ω_i^{TS} at the transition state computed by Shin³⁸ as shown in table 5.2.

E^{TS} / cm^{-1}	25,880
$\omega_i^{TS} / \text{cm}^{-1}$	2204, 1259, 1180, 1096, 877, 597, 302, 223

Table 5.2: Energy and vibrational frequencies at the transition state for the lowest dissociation channel $\text{CF}_3\text{H} \rightarrow \text{CF}_2 + \text{HF}$

For the RRK calculations we employ a code written in the group of Martin Quack.

The dissociation rates can be compared with experimental data as follows. Several studies of dissociation rates as a function of the *temperature* exist, and the conversion for energy dependent dissociation rates $k(E)$ to temperature dependent dissociation rates $k(T)$ is done with via the relation

$$k(T) = \int k(E)p(E, T)dE, \quad (5.53)$$

where $p(E, T)$ is the Maxwell Boltzmann distribution at a temperature T .

Figure 5.16 shows the temperature dependence of CF_3H dissociation measured by different authors⁴⁰⁻⁴⁴ and the rates we get using our energy dependent dissociation rates calculated with RRKM. One set of experimental data presented in the graph (dotted

line) lies quite far away from the others; furthermore these measured dissociation rates lie very high with respect to typical dissociation rates for the transition considered⁴⁵, so we can suppose that the latest of the three other measurements is the most reliable. It coincides well with our calculations.

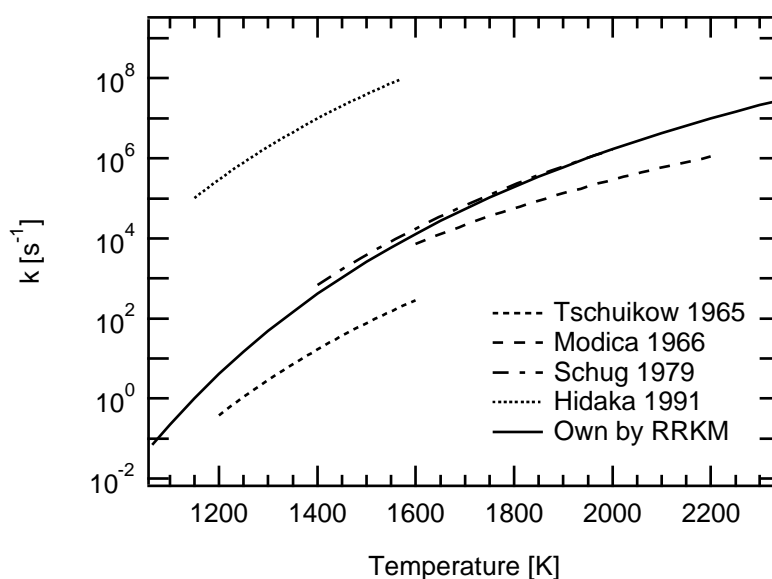


Figure 5.16: Arrhenius plots of experimental data for CF_3H measured by different authors.

For these reasons, we take our computed dissociation rates without any further modifications[‡].

(II) Isotopic influences on unimolecular dissociation

Unimolecular dissociation itself is isotopically selective due to two effects^{29, 46, 47}: there is a *critical energy effect* and a *statistical weight effect*. The first effect is due to a different zero point energy for different molecular isotopic species which makes the dissociation energy different. The second effect is that different density of states ρ due to different vibrational energies give different unimolecular dissociation rates.

[‡]The exact values for the dissociation rates are not crucial for the calculation of the final dissociation yield of an IRMPD experiment⁴⁵.

Performing some simple estimations of the isotopic influence on unimolecular dissociation rates leads us to the conclusion that it is on the order of magnitude of $\sim 0.05\%$ for the critical energy defect and $\lesssim 3\text{-}4\%$ for the statistical weight effect. These differences are relatively small and we exclude any isotopically different unimolecular dissociation rates for the purpose of the simulations.

5.3.3.D IR photon pumping

For our simulations we have to calculate the rates at which a molecule absorbs photons of a laser radiation field (or emits photons by stimulated emission). The concepts based on a statistical treatment^{27, 48, 49} are used (see section 2.2). In this approach close lying vibrational states of a molecule are binned into levels of a certain width ΔE which are characterised by its energy E . The expressions developed allow us to calculate these rates. The following expression for the up-pumping rate from level $I \rightarrow J$ has been developed earlier (see equation 2.27):

$$K_{I,J} = 1.511 \cdot \frac{(G/pm^2) (I/MW cm^{-2}) \rho'_I}{(\Delta/cm^{-1}) \rho_I}, \quad (5.54)$$

where

- G : Integrated band intensity of the pumped IR-chromophore
- I : dissociation laser intensity
- ρ_I : Density of effective coupled states at level M
- ρ'_I : Density of states where the degree of freedom corresponding to the pumped vibration is removed from the count
- Δ : Effective coupling width (adjustable parameter)

The rates for down-pumping are given as follows (see also table 2.12 on page 47):

$$\begin{array}{l} \text{Case B :} \\ \text{Case C :} \end{array} \quad \frac{K_{J,I}}{\frac{\delta_J}{\delta_I} \cdot K_{I,J}} \quad (5.55)$$

$$\frac{\delta_J}{\delta_I} \cdot \frac{2\delta_J}{\pi\sqrt{3}|V|} \cdot K_{I,J}$$

where δ_X is the the average spacing between the vibrational states in bin X, and $|V|$ is the average coupling between the states in the upper and lower bin via the laser radiation. The “Case B” refers to regions of high density of states, where the states within a grained level are all coupled amongst each other, and “Case C” refers to regions of low density of states, where the states within a grained level are uncoupled amongst each others, and couple only via the laser radiation to levels in the other bin.

We would like to introduce two generalisations, which are presented in this section:

1. Equations 5.54 and 5.55 give the expressions for the up and down-pumping rates of excited molecules. In particular, we give values for the case of pumping through regions of low densities of states (the “case C”). These results however are explicitly given using the assumption that the upper level is and stays essentially unpopulated compared to the lower level during the whole experiment. This condition is reasonably well met for the calculation of IRMPD of molecules in the ground state. However, in our simulations, where we pre-excite molecules to a certain level and then also pump them down by the CO₂ laser, we have the inverse situation. This necessitates a certain generalisation of the formulae. We show in appendix A how the pumping rates are developed, and we show also that a direct generalisation is not possible in the framework of our master equations presented here. We propose the following pragmatic solution: for each couple of bins between which molecules can be pumped up and down, we first determine which of the two states is more populated. If this is the lower state, we use the pumping rates as described in equation 5.55. In the opposite case, the calculation of the pumping rates is inverted. The general statement of pumping through low density of states is: “Up-pumping through a low density region is slow”. We would like to add: “... down-pumping too !”.
2. A second and very important improvement is to introduce a dependence of the pumping-rates on the isotopic species and the vibrational energy of the molecule and the wavelength of the pumping laser. The value of G/Δ in equation 5.54 gives the absorption cross-section and is an average over multiple absorption steps (figure 5.17-I). We propose generalising equation 5.54 by replacing G/Δ by a calculated absorption cross-section which depends on the laser frequency ν , the vi-

brational energy E of the molecule and the isotopic species of the molecule (figure 5.17-II).

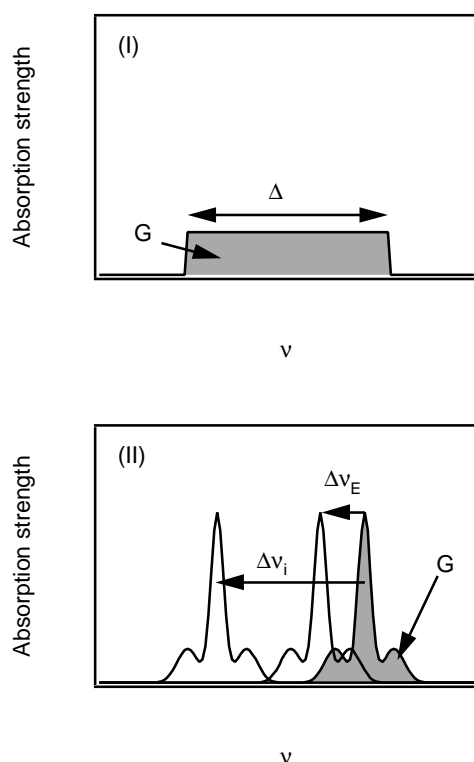


Figure 5.17: Absorption spectrum for calculations based on a statistical treatment.

(I) In commonly used models a constant cross-section σ for the absorption of an IR photon is implied.

(II) We generalise the pumping-rates by replacing a constant cross-section by a calculated cross-section $^X\sigma_E(\nu)$ which depends on the vibrational energy ($\Delta\nu_E$) and the isotopic species of the molecule ($\Delta\nu_i$).

For this we need to be able to calculate the absorption/emission spectra of excited molecules. We have discussed this issue in section 5.1, and we can use the calculated absorption and emission spectra to replace G/Δ in equation 5.54.

5.3.4 Results

5.3.4.A Some characteristics of the numerical code

Our numerical code is written in fortran 90 and contains roughly a thousand lines. It is compiled on a PC with `Plato v 2.11c` from Salford Software, UK. The code can be found in appendix E.

Basically, the code solves the master equation given in expression 5.51, which reads

$$\frac{d\mathcal{N}(t)}{dt} = A(t) \cdot \mathcal{N}(t), \quad (5.56)$$

where \mathcal{N} is a vector with n elements containing the populations of the individual levels and $A(t)$ is a $(n \cdot n)$ matrix incorporating all pumping, relaxation and dissociation rates. To solve this, the code uses the fourth order Runge-Kutta⁵⁰ method, advancing by steps Δt in time. Each step is calculated twice, once advancing using a step Δt , once using two steps of $\Delta t/2$. If the two results are the same within some given maximum error, the step is accepted. Otherwise, the code redefines $\Delta t \mapsto \Delta t/2$ and redoes the particular step. This procedure is repeated until the results converge. For this reason, the time steps can change within one simulation. A typical value for a starting point for Δt is 2 ns.

For convenience a vibrational energy E_d is defined above which all molecules dissociate rapidly and can never be pumped or relaxed down to the ground state. Typically, we define $E_d = 28,000 \text{ cm}^{-1}$.

A single run simulates a three laser experiment, i.e. with pre-excitation, dissociation and LIF lasers. It calculates the evolution of \mathcal{N} for both isotopic species simultaneously. The LIF laser is taken into account by stopping the simulations at the time when this LIF laser intervenes and evaluating the number of dissociated molecules. The following physical parameters can be chosen as input:

- Fluence of the dissociation laser
- Wavelength of the dissociation laser
- Pressure of sample

- Pre-excitation energy
- Timing of lasers (pre-excitation $\xrightarrow{\Delta t_{PE-IRMPD}}$ dissociation $\xrightarrow{\Delta t_{IRMPD-LIF}}$ LIF)

The temporal shapes of the pre-excitation and dissociation lasers, the unimolecular dissociation rates and the relaxation rates are given in separate input files. Optionally, an experiment can be run twice, once with and once without pre-excitation, in order to evaluate how much of the dissociated molecules are due to ground state dissociation (analogous to our experimental setup). There are some other input parameters concerning the calculation procedure itself, such as some convergence criteria for the calculations, the size of the energy bins, and so on. Typically, for rough calculations bins of 1000 cm^{-1} are used. For the results presented in this text, we use bins of 200 cm^{-1} .

The code stores the number of dissociated molecules in a single experiment in a file. Optionally it can also store the number of dissociated molecules and the distribution of vibrational energies of the molecules as a function of time. Figure 5.18 shows an example of the number of dissociated molecules as a function of time, and figures 5.19 and 5.20 the distribution of the molecules at different moments for the same experiment.

The time for the calculation of a single three laser experiment varies as a function of the parameters chosen, in particular the size of a bin. Typically, for calculations shown in this document, half a minute is spent on a calculation of a single IRLAPS experiment by a standard laptop (1.5 GHz, Intel Centrino) running Windows XP.

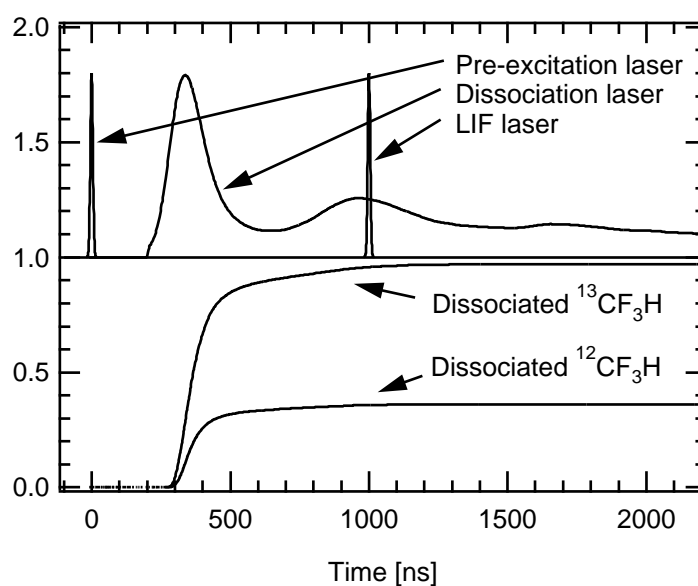


Figure 5.18: Example of a simulated three laser experiment with molecules pre-excited via the 3_1 band at $t = 0$. At $t = 200$ ns there is the onset of the dissociation laser with a total fluence of 6 J cm^{-2} . The pressure of the sample is 0.2 mbar. The top curves show the temporal shapes of the three lasers. The bottom panel shows the amount of dissociated $^{12}\text{CF}_3\text{H}$ and $^{13}\text{CF}_3\text{H}$.

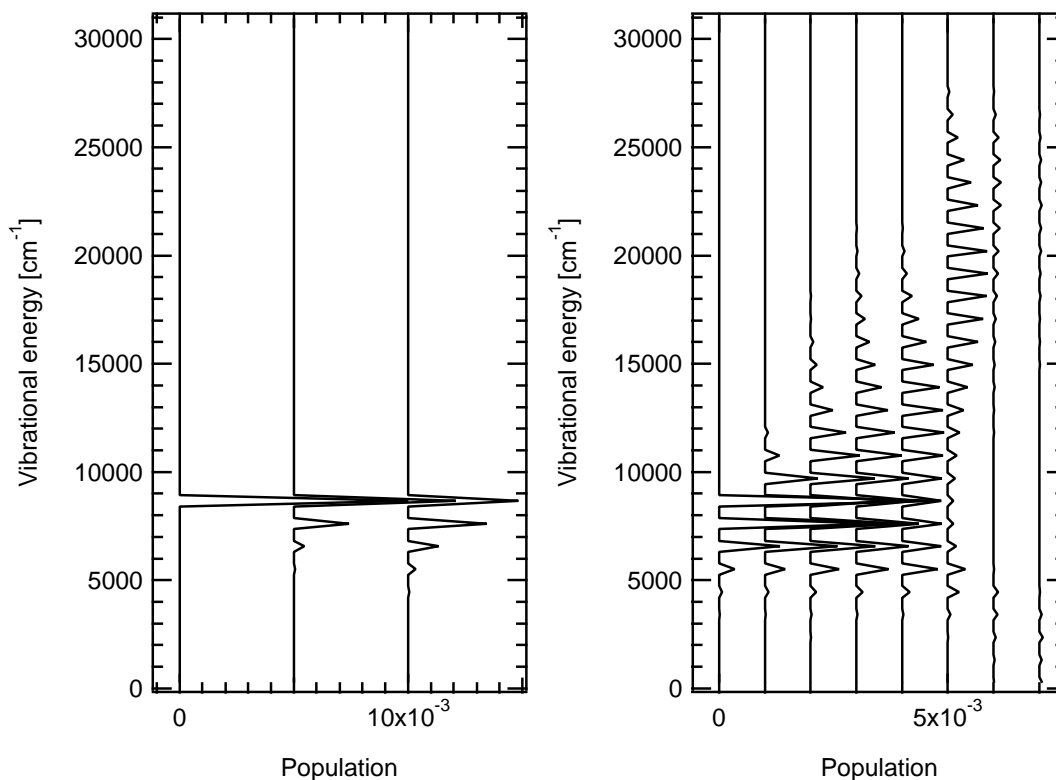


Figure 5.19: Energy distributions for the example shown in figure 5.18, for the $^{13}\text{CF}_3\text{H}$ isotopomer. The population in the ground state is cut away for clarity.

- ▶ Left graph, from left to right: $t = 0, 100$ and 200 ns (vibrational relaxation).
- ▶ Right graph, from left to right: $t = 200, 220, 240, 250, 260, 300, 500, 1000$ ns (IRMPD).

The different curves have different offsets for clarity. Binwidths of $\nu_0/5$ have been chosen (where $\nu_0 = 1048 \text{ cm}^{-1}$ is the frequency of the CO_2 dissociation laser). Through absorption or emission of a photon such as vibrational relaxation, only steps of 5 bins are done, which explains why the population distribution goes back to 0 in four out of five bins.

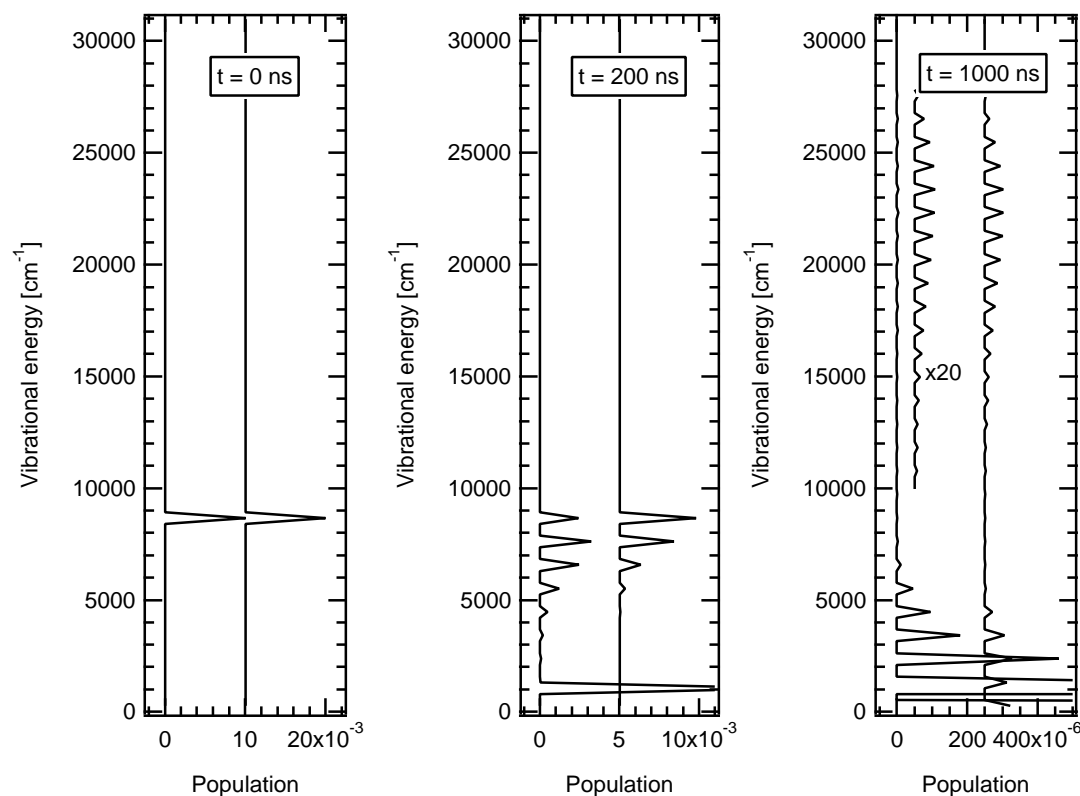


Figure 5.20: Dynamics of energy level populations calculated for CF_3H (left curve on a graph: $^{12}\text{CF}_3\text{H}$, right curve on a graph: $^{13}\text{CF}_3\text{H}$), at $t = 0, 200$ and $t = 1000$ ns for the same experimental conditions as in figures 5.18 and 5.19. The curves for $^{13}\text{CF}_3\text{H}$ are offset for clarity. At $t = 0$, the molecules are pre-excited at an energy of 8800 cm^{-1} (left graph). On the graph in the centre isotopically selective collisional relaxation is put to evidence, in the right graph the higher pumping efficiency for the $^{13}\text{CF}_3\text{H}$ isotopomer. Note that in the case of $^{12}\text{CF}_3\text{H}$ the population at $\sim 1000 \text{ cm}^{-1}$ is rapidly populated due to the warming up of molecules in the ground state by collisions with excited molecules.

5.3.4.B Comparison with experiments

In this section we present some comparisons between our experimental data and our simulations. We also compare our simulations with data reported elsewhere^{51, 52}. In particular we compare our simulations with data presented in sections 4.3 (photofragment excitation spectra of vibrationally excited molecules and dissociation selectivity at low pressures), 4.4 (Measurements of the decay rates as a function of the dissociation laser fluence and frequency). The simulations have only a single fitting parameter: a multiplicative constant for collisional relaxation, all other parameters are kept fixed.

Sections (I) and (II) concern the collision-free situations, and we show that our simulations represent the experimental data well. In section (III) we present calculations with which we can scale vibrational relaxation rates, and we finally present in section (IV) simulations including the scaled vibrational relaxation rates.

(I) Simulation of photofragment spectra

To begin with, we present comparisons of the measured and calculated photofragment spectra for molecules pre-excited via the 3_1 band. In these experiments we measured the total dissociation probability D as a function of the frequency and the fluence of the dissociation laser, always keeping a zero time-delay between the pre-excitation and the dissociation lasers. For convenience, we describe the photofragment spectrum by the function 4.1, which reads

$$D(\nu) = 1 - \exp \left(-B \cdot \exp \left(- \left(\frac{\nu - \nu_0}{\omega} \right)^2 \right) \right), \quad (5.57)$$

where D is the dissociation probability, ν is the frequency of the dissociation laser, and B , ν_0 and ω are fitting parameters.

At the first step, we show simulated and measured dissociation yields at a particular dissociation laser frequency, as a function of the fluence of the dissociation laser. Two examples, for dissociation laser frequencies of 1083 cm^{-1} and 977 cm^{-1} are shown in figure 5.21 for the dissociation of $^{13}\text{CF}_3\text{H}$.

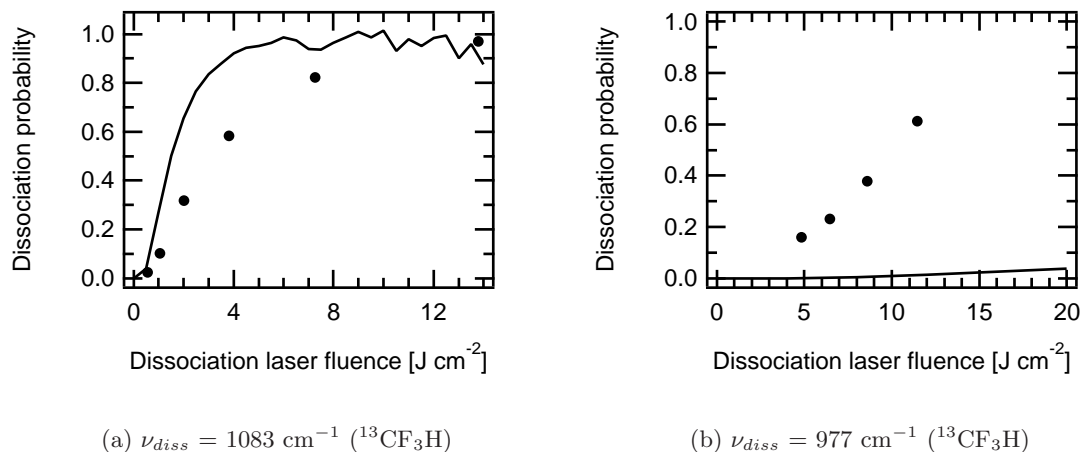


Figure 5.21: — Simulated and • measured dissociation yields.

Considering that the experiments are performed at 0.4 mbar, where rotational relaxation is not complete, we cannot compare the experiments and the simulated values directly. For a pressure of 1 mbar, where rotational relaxation is more complete, the dissociation probability is larger. Experimentally we have determined that at a dissociation laser fluence of $\sim 3 \text{ J cm}^{-2}$ and a pressure of 0.4 mbar the dissociation yield is $\sim 50\%$ of what it would be if rotational relaxation were complete (see figure 3.8 on page 99). In light of this, our simulation shown in figure 5.21-a fits very well to the experimental data, without a single fitting parameter !

Figure 5.21-b shows the same dependence for an off-resonant dissociation laser wavelength. Here, our simulations predict essentially no dissociation, whereas it is experimentally clearly observed. In what follows we will try to find an explanation for this discrepancy.

A possible reason is that vibrations other than the ν_5 mode can absorb photons. For example, depositing two quanta into the ν_6 vibration could enhance absorption of lower frequency photons. The band origin of the first overtone of the ν_6 vibration is at 1014 cm^{-1} for molecules in the ground state⁵³. We show in figure 5.22 the calculated absorption spectrum of a molecule at 8800 cm^{-1} ($\nu_{CH} = 3$) due to the absorption of two quanta in ν_6 . The splitting due to the double degeneracy of the ν_6 vibration is

neglected for simplicity.

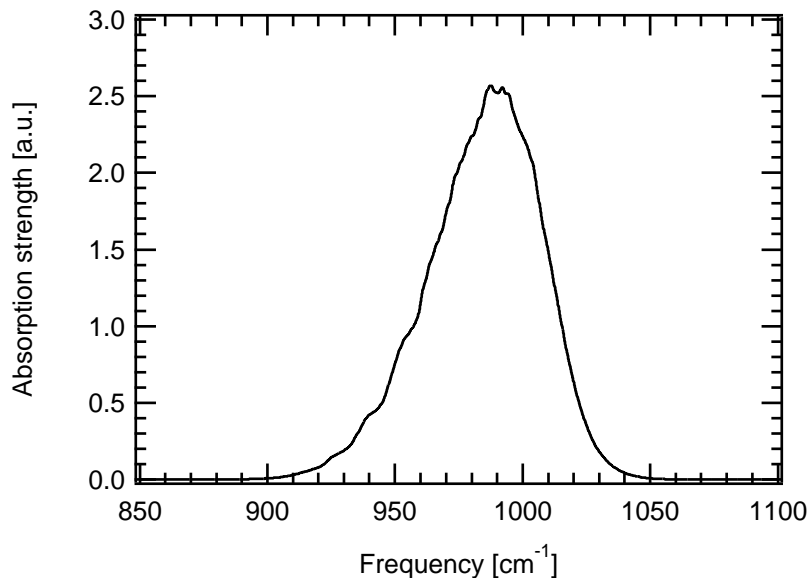


Figure 5.22: Absorption spectrum of two quanta in the ν_6 vibration for molecules with a vibrational energy of 8800 cm^{-1} .

The absorption spectrum has been calculated in the same way as for the case of a single photon absorption. The matrix elements scale as follows⁶:

$$\langle v | q^2 | v + 2 \rangle = \frac{1}{2} \cdot \sqrt{(v + 1) \cdot (v + 2)} \quad (5.58)$$

or, in other words, $\sigma(v \rightarrow v + 2) = (v + 2) \cdot (v + 1) \cdot \sigma(0 \rightarrow 2)$ where σ is the absorption strength.

We can incorporate the absorption of two quanta of ν_6 in the code, and recalculate the dependence of the dissociation yield on the fluence at a frequency of the dissociation laser of 977 cm^{-1} (figure 5.21-b). The result is shown in figure 5.23.

It is clearly visible that the inclusion of $2\nu_6$ reproduces the experimental values very well, once again without any fitting procedure.

For all of the following calculations, absorption through the ν_6 band is included for

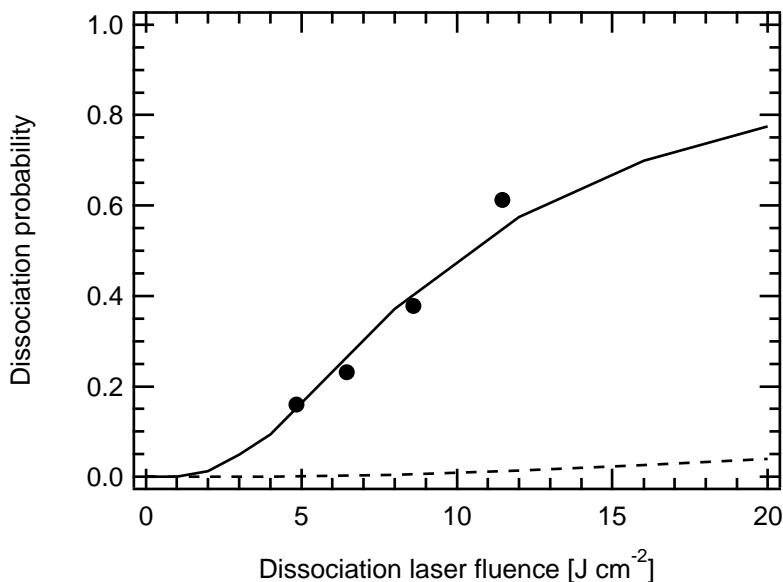


Figure 5.23: Dissociation yield of molecules pre-excited via the 3_1 band, with a dissociation laser frequency of 977 cm^{-1} .

- Experiments
- Calculations using only the ν_5 vibration for the absorption of photons
- Calculations using the ν_5 and ν_6 vibrations for the absorption of photons.

completeness, although for typical frequencies in the 1050 cm^{-1} region this has no appreciable influence. We show in figure 5.24 the photofragment spectra for $^{12}\text{CF}_3\text{H}$, comparing experimental and simulated values for a sample at 1 mbar and a fluence of 5 J cm^{-2} , for off-resonant dissociation laser frequencies.

It clearly demonstrates the necessity of including the possibility of absorption of a photon via $\nu_6 \rightarrow \nu_6 + 2$. We fit the function 5.57 to our calculated data. Although the overall photofragment spectra correspond reasonably well to each other, there are some discrepancies of the exact values for B and ω . There is a relatively good correspondence of the fitted values of ν_0 (centre of dissociation curves) which is shown in figure 5.25.

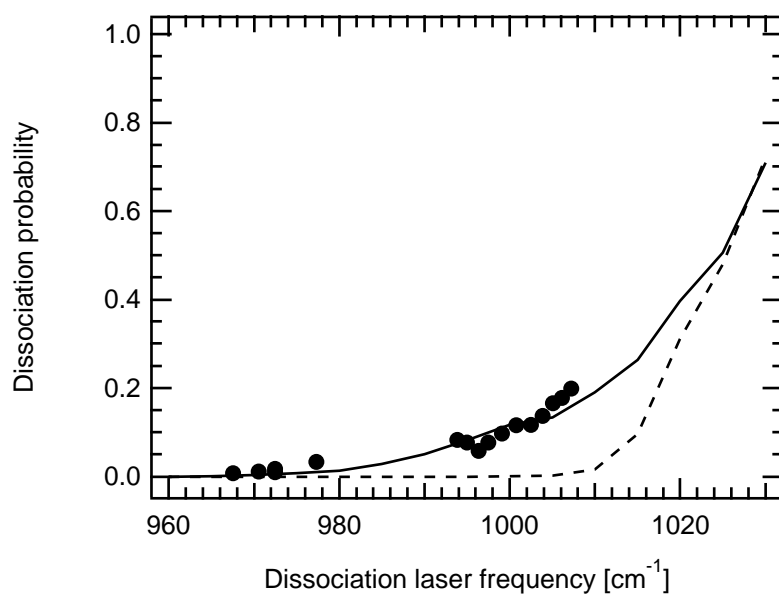


Figure 5.24: Photofragment spectra of vibrationally excited $^{12}\text{CF}_3\text{H}$ for off-resonant dissociation laser frequencies, at a dissociation laser fluence of 5 J cm^{-2} , for a sample pressure of 1 mbar.

- Experimental data.
- calculation with absorption via the ν_5 and the ν_6 modes.
- - calculation with absorption via the ν_5 mode.

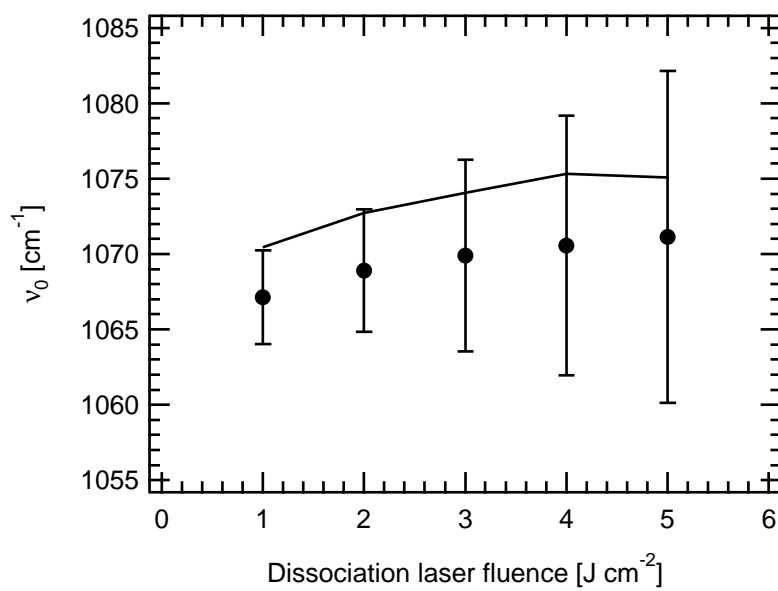


Figure 5.25: • Measured and — calculated centres ν_0 of the photofragment spectra of vibrationally excited $^{12}\text{CF}_3\text{H}$.

(II) Simulation of the dissociation selectivity

We now consider the data presented in sections 4.3.3. We measured the ratio of dissociation probabilities for the two isotopic species pre-excited via the 3_1 band for different dissociation laser wavelengths and fluences. This ratio, $S_d = {}^{13}D/{}^{12}D$, where ${}^x D$ is the dissociation probability of the ${}^x\text{CF}_3\text{H}$ molecule, is called the dissociation selectivity. We have also measured S_d for one particular dissociation laser wavelength for molecules pre-excited via the 2_1 band.

Figure 5.26 shows the measured and simulated dissociation selectivities for a dissociation laser frequency of 1047 cm^{-1} , for molecules pre-excited via the 2_1 (left graph) and the 3_1 (right graph) bands.

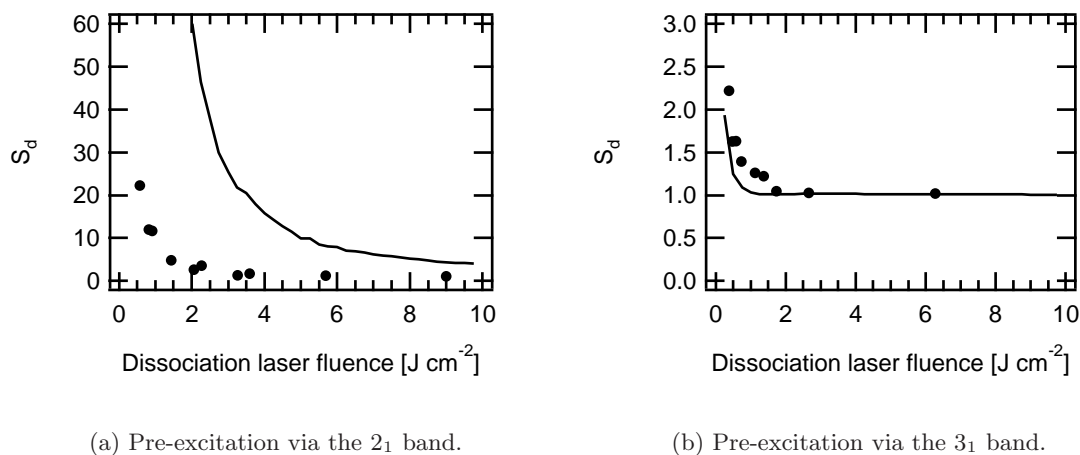


Figure 5.26: — Simulated and • measured dissociation selectivities for a sample at 0.4 mbar.

The graphs show that the simulations for pre-excitation via the 3_1 band describe the experimental data very well taking into account the complexity of the problem. For molecules pre-excited via the 2_1 band, this is however not true: there is only a qualitative correspondence, but quantitatively the values differ considerably (figure 5.26-a). Computed values for S_d lie too high, which means that either the dissociation yield of ${}^{13}\text{CF}_3\text{H}$ is overestimated or the dissociation yield of ${}^{12}\text{CF}_3\text{H}$ is underestimated. We believe that the latter is true because ${}^{12}\text{CF}_3\text{H}$ molecules at $v_{CH} = 2$ are off-resonant

with respect to the dissociation laser field. For such far off-resonant pumping the computation becomes very sensitive to details of absorption spectra, which is difficult to account for accurately. The problem that common theories underestimate IR photon absorption rates when they are out of resonance, was already noticed some time ago. Some ideas of how to circumvent this problem have been proposed⁵⁴. As these ideas cannot be directly transposed to our simulations, we simply have to note that our simulations do not work well whenever relatively weak (off-resonant) transitions are being considered (i.e. either energetically low-lying molecules or a dissociation laser frequency lying far from resonance). As a result our computed pumping rates may underestimate the real ones. We conclude that for vibrational levels close to and above $v_{CH} = 3$ our dynamic equations are a good description, but at $v_{CH} = 2$ and below, they do not describe our experiments quantitatively, although still truly reflecting qualitative trends.

(III) Simulation of the selectivity as a function of the sample pressure

In a next step we compare some data presented in the thesis by Mikhail Polianski^{51, 55}. In figure 3.17 of his thesis he presents the selectivity upon an increase of the pressure for molecules pre-excited via the 3_1 band. The two laser pulse shapes, such as their mutual timing used in his experiments, are shown in figure 5.27. For the initial pre-excitation of the molecules a pulsed Alexandrite laser (PAL) with a length of ~ 100 ns length has been used in this experiment.

We present in figure 5.28 the comparison between his experimental data and our simulations. With these simulations the vibrational relaxation rates can be scaled correctly.

In his experiments, M. Polianski pre-excites the molecules at the Q-branch of the $^{13}\text{CF}_3\text{H}$ isotopomer. The isotopic ratio of the products is measured by mass spectrometry after irradiation of the sample during typically tens of minutes. The selectivity he measures incorporates the pre-excitation selectivity, i.e. the selectivity gained by the pre-excitation step only. However, the pre-excitation selectivity is not well characterised, as it depends on the precise pre-excitation energy. From photo-acoustic overtone spectra we estimate a pre-excitation selectivity which may lie anywhere between 300 and 900. Here, we take a pre-excitation selectivity of 360 such that the the overall selectivity at

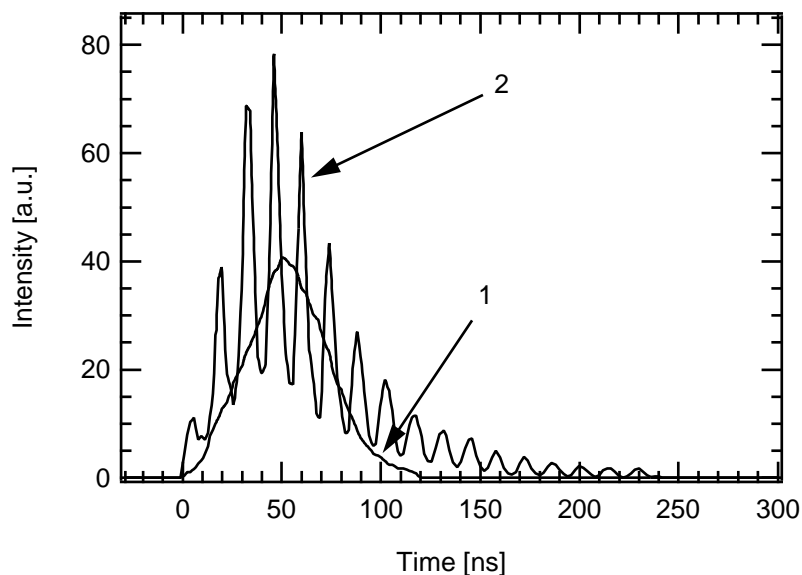


Figure 5.27: Laser pulses used for the experiments elsewhere^{51, 52}.

- 1 - pre-excitation laser
- 2 - dissociation laser.

a zero pressure corresponds to the experiments. We see that the overall selectivity can be well reproduced.

(IV) Simulation of relaxation experiments

Finally, we propose comparing decay rates measured and presented in section 4.4 with our numerical simulations. In this section we presented decay rates k for the two isotopomers, for different dissociation laser wavelengths and fluences. Figure 5.29 shows two graphs with such comparisons.

For all our measurements with fluences below, about, 5 J cm^{-2} , a single exponential function, $Y = Y_0 \cdot \exp(-k\Delta t)$, fits the data well (but not for higher fluences). In our simulations the fluence, where single exponentials no longer fit the data well lies slightly lower.

Once again, the correspondence between experimentally and numerically determined

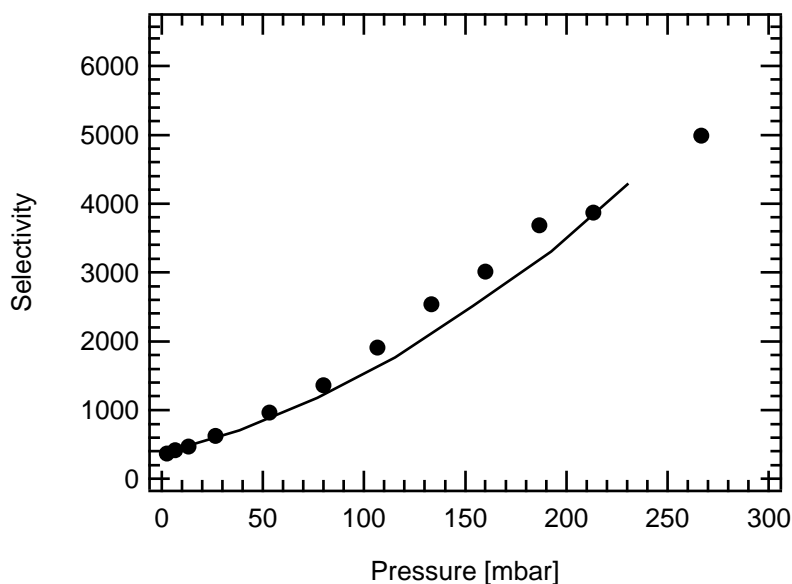
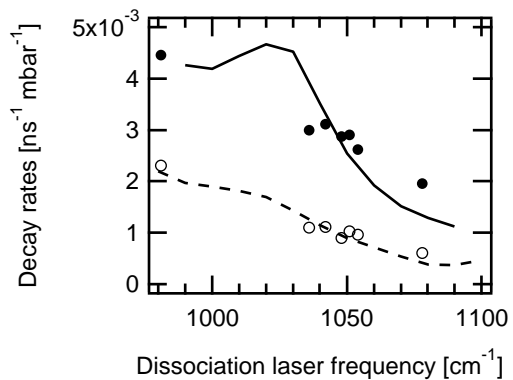
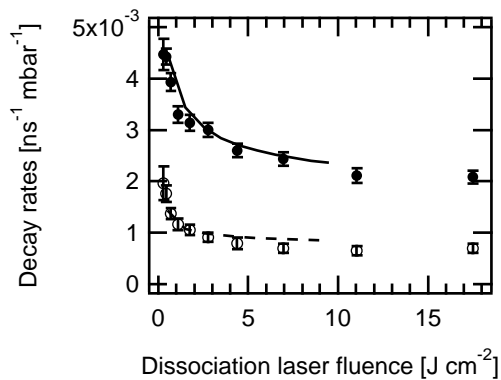


Figure 5.28: Overall selectivity of the dissociation yields as a function of the pressure of the sample.

● Experiments⁵¹ — Simulations.



(a) Decay rates for a dissociation laser fluence of 3 J cm^{-2}



(b) Decay rates for a dissociation laser frequency of 1047 cm^{-1} .

Figure 5.29: Measured and calculated decay rates for ● — $^{12}\text{CF}_3\text{H}$ ○ - - $^{13}\text{CF}_3\text{H}$.

decay rates k is not bad.

(V) Conclusions

In this section we have presented simulations of some of our experiments. Our simulations reproduce the experimental data well, considering the complexity of the processes and the fact that we have only one single fitting parameter (a multiplicative constant for collisional relaxation). Because of this we believe that our model of the collisional and IRMPD processes describe the processes in an adequate manner. Nevertheless we have to note that IRMPD does, on a quantitative level, not adequately describe weak pumping transitions, as we have shown for the simulations of the dissociation selectivity for molecules pre-excited via the 2_1 band.

Now we are able to use our codes to make practical predictions for the laser isotope separation process. This is presented in the next sections.

5.3.4.C Isotopic selectivity at high pressures

We now dispose of a model of our MLIS system that is coherent with our experimental results. In most cases, the model can reproduce the experiments quantitatively, in a few cases the correspondence is only on a qualitative level. In particular, the simulations for molecules pre-excited via the 3_1 band yield very good results. For this reason we use our model to look at the mechanisms of the process upon increasing the sample pressure, where collisional vibrational relaxation and IRMPD occur simultaneously.

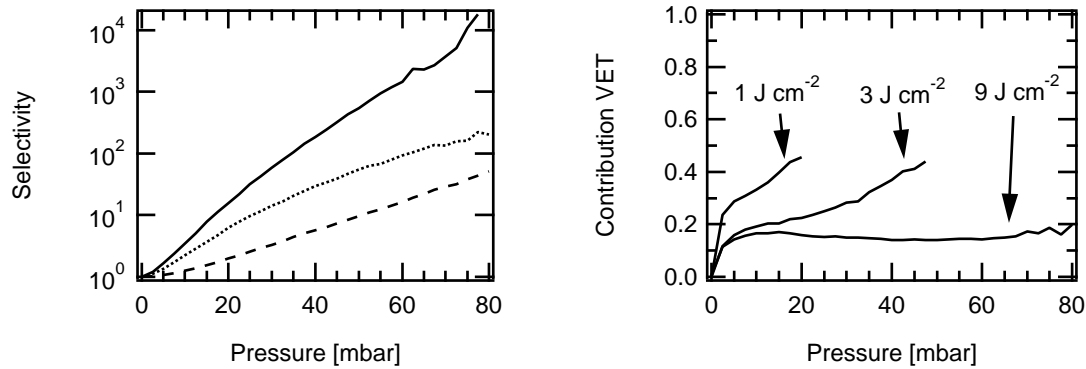
In these simulations we look at the special case where the frequency of the dissociation laser is set to 1047 cm^{-1} , as this is typically used in our MLIS process. One of the goals of this thesis is to determine the contribution of isotopically selective collisional relaxation and the influence of different IR photon absorption strengths to the enhancement of isotopic selectivity upon an increase of the sample pressure. In order to separate these two influences, we perform a set of simulations where we:

1. determine the isotopic selectivity S_{total} upon the increase of the pressure,
2. the same as in (1), but setting the vibrational relaxation rates to be equal (set the relaxation rates of both isotopomers to be the average of the calculated relaxation

rates), thus determining the isotopic selectivity S_{IRMPD} due to different IRMPD rates,

- the same as in (1), but setting the photon absorption rates to be equal (set the IR photon absorption/emission rates of both isotopomers to be the average of the calculated IR photon absorption rates), thus determining the isotopic selectivity S_{VET} due to different vibrational relaxation rates.

This way, the different influences of the mechanisms can be evaluated, as $S_{total} \approx S_{VET} \cdot S_{IRMPD}$ (there is at most a difference of $\sim 30\%$ between S_{total} and $S_{VET} \cdot S_{IRMPD}$). We present in figure 5.30 this separation. We show the isotopic selectivity of our MLIS process as a function of the sample pressure and show the respective influences of isotopically selective collisional relaxation and different IR absorption strengths of the two isotopomers.



(a) Isotopic selectivity for a fluence of 9 J cm^{-2} of the dissociation laser.

— overall selectivity.

⋯ due to different IRMPD efficiencies.

-- due to isotopically selective collisional relaxation.

(b) Relative contribution of isotopically selective IRMPD for 1, 3 and 9 J cm^{-2} .

Figure 5.30: Numerical evaluation of the contributions of the different mechanisms to the increase of isotopic selectivity, for a frequency of the dissociation laser of 1047 cm^{-1} .

In figure 5.30-b we plot the relative importance of the two mechanisms. We defined this “importance” \mathcal{I} (or “contribution”) earlier (see equation 4.10) which we recall here

$$\mathcal{I}_x := \frac{S_x - 1}{\sum_i (S_i - 1)}, \quad (5.59)$$

where S is the selectivity, $x =$ due to isotopically selective vibrational relaxation / due to IRMPD and i sums over the two possible x . We see in figure 5.30-b that for low pressures all selectivity S is due to different IRMPD rates (which is expected, because there is no collisional relaxation taking place). As the pressure is increased, the relative influence of collisional relaxation increases. For 3 J cm^{-2} both effects are equally as important at ~ 50 mbar, for higher fluences the influence of different IR absorption strengths stays predominant.

5.3.4.D IRMPD properties of vibrationally pre-excited CF_3H

In a previous section we have shown that our model describes the experiments in a satisfying manner. We are interested in having a general feeling of the dependency of the dissociation yield for different pre-excitation energies as a function of different parameters such as the pressure and the CO_2 dissociation laser fluence and frequency.

Figure 5.31 shows an example of a calculated dissociation probability as a function of the pre-excitation energy, for a given fluence and frequency of the dissociation laser and for a given sample pressure. The timing of the lasers is kept fixed (zero time-delay between pre-excitation (YAG) and CO_2 dissociation lasers).

We show in figure 5.32 dissociation probabilities for a set of different parameters.

5.3.4.E Predictions for MLIS

We can employ this proven model to make some predictions useful for molecular laser isotope separation (MLIS). For this, we depart from the MLIS scheme presented elsewhere^{51, 52} where the pre-excitation laser and the dissociation laser are temporally overlapped (see figure 5.27 on page 212). Experimentally, this configuration has been determined to be at least close to the ideal configuration. Here, we vary numerically different parameters in order to determine their relative influences.

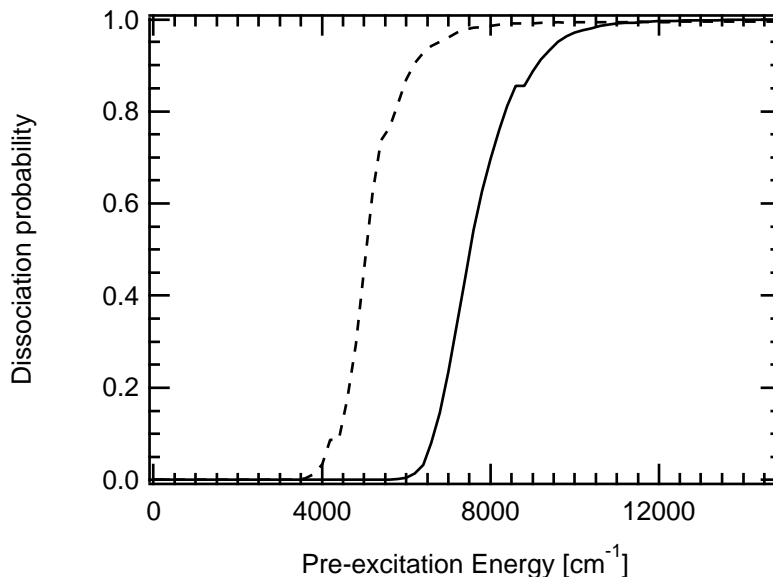


Figure 5.31: Simulated dissociation probability for — $^{12}\text{CF}_3\text{H}$ and - - $^{13}\text{CF}_3\text{H}$ molecules, for a dissociation laser frequency $\nu = 1047 \text{ cm}^{-1}$, a dissociation laser fluence $\Phi = 3 \text{ J cm}^{-2}$ and a sample pressure $p = 1 \text{ mbar}$.

In figure 5.33 we show the dissociation selectivity and yield as a function of the pressure for pre-excitation via the second and the third overtone of the CH stretching bending vibration[‡].

It can be seen that for this MLIS scheme (overlapped pulses and high pressure) that the second overtone of the CH stretching bending vibration is better suited than the third overtone as far as the selectivity of the dissociation step is concerned. For the same pressure, the dissociation probabilities are the same for the $^{13}\text{CF}_3\text{H}$ species, but the dissociation selectivity is higher for the lower pre-excitation level. Figure 5.34 shows analogous data for different CO_2 laser fluences.

The figures demonstrate the problem of choosing the correct dissociation laser fluence: for low fluences, the dissociation selectivity increases which is, however, accompanied by a simultaneous drop of the absolute dissociation yield. From the data shown here it

[‡]Simulations for pre-excitation via the first overtone are left away, as we have shown that those results are only qualitatively correct, not quantitatively.

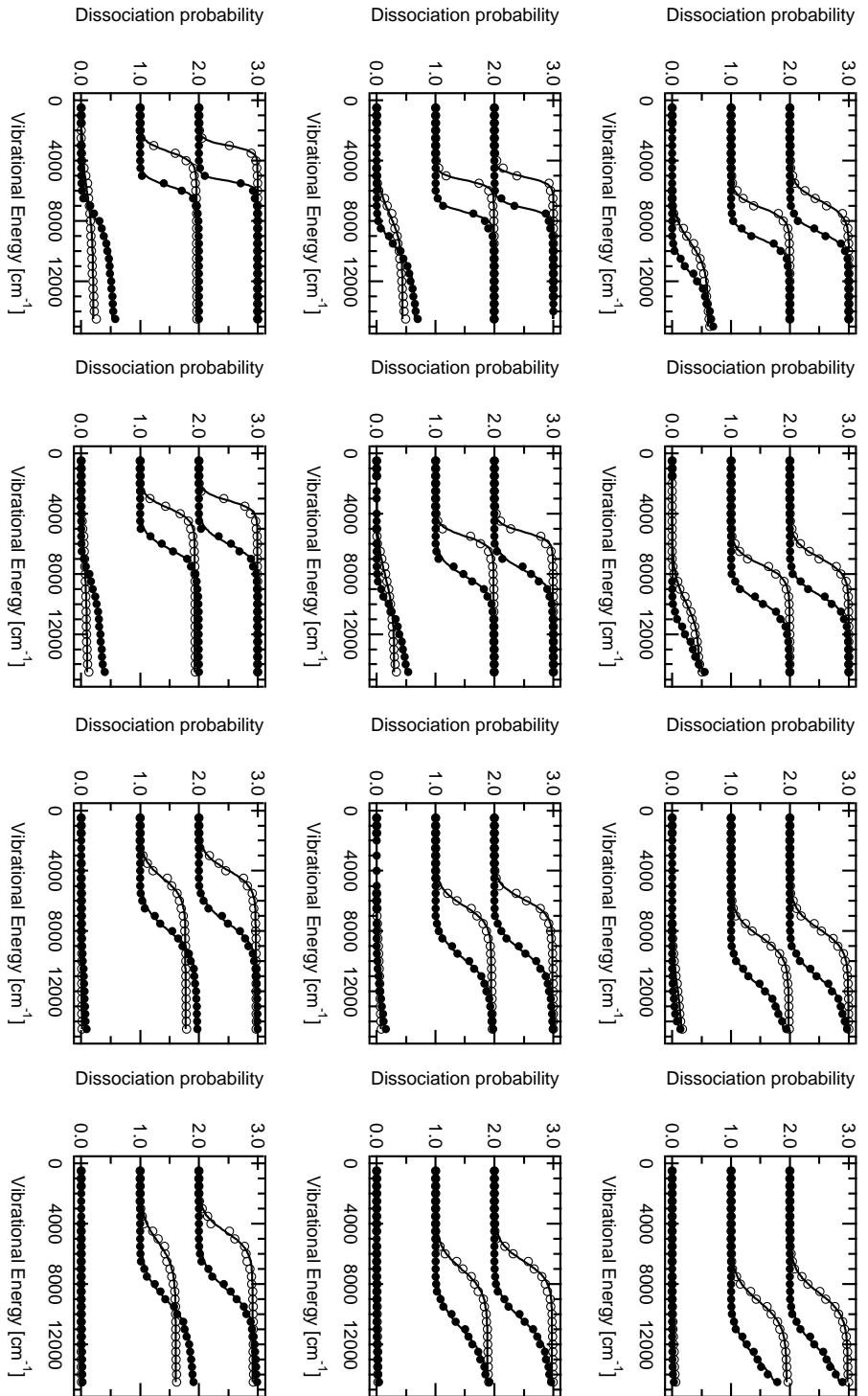


Figure 5.32: Calculated dissociation probabilities: \bullet $^{12}\text{CF}_3\text{H}$ \circ $^{13}\text{CF}_3\text{H}$. Some curves are offset for clarity.

- ▶ Dissociation laser fluence: on one single graph, $\Phi = 0.5, 3$ and 5.5 J cm^{-2} (from bottom to top).
- ▶ Dissociation laser frequency: $\nu = 1028 \text{ cm}^{-1}$ (top line), 1048 cm^{-1} (centre line), 1068 cm^{-1} (bottom line)
- ▶ Sample pressure: $p =$ collision-less (left column), 1 mbar (middle left column), 5 mbar (middle right column), 9 mbar (right column)

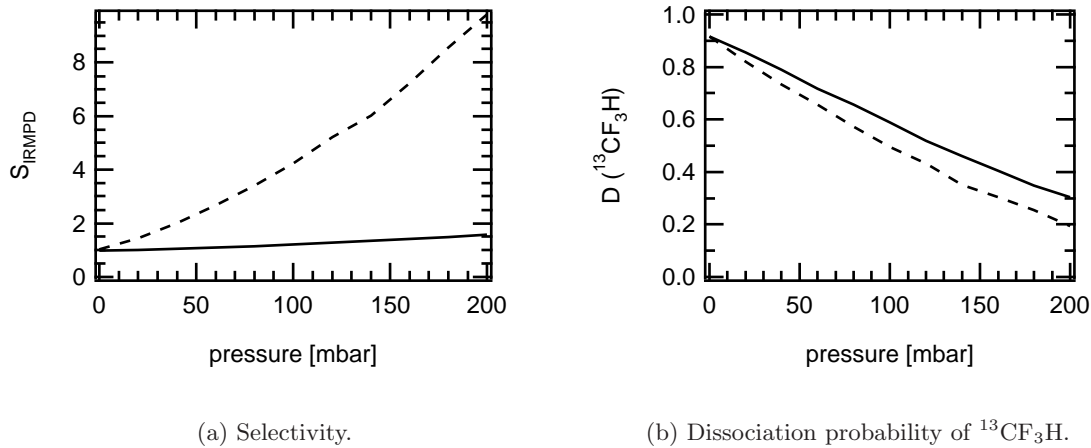


Figure 5.33: Dissociation selectivity and yield for pre-excitation via the - - 3_1 and the — 4_1 bands, for a dissociation laser frequency of 1044 cm^{-1} and fluence of 3 J cm^{-2} .

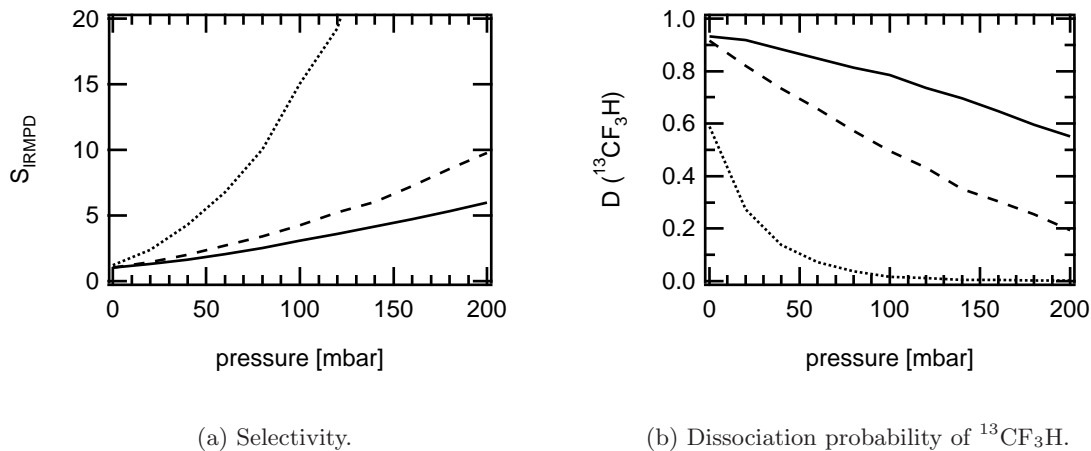


Figure 5.34: Dissociation selectivity and yield for a dissociation laser fluence of $\cdots 1$, - - 3 and — 5 J cm^{-2} , for pre-excitation via the 3_1 band and a dissociation laser frequency of 1044 cm^{-1} .

can be seen that a fluence of 3 J cm^{-2} is a good compromise if one desires a relatively high dissociation probability. Finally, figure 5.35 shows analogous data for different CO_2 laser frequencies.

From this figure it can be seen, that *by changing the dissociation laser fluence from*

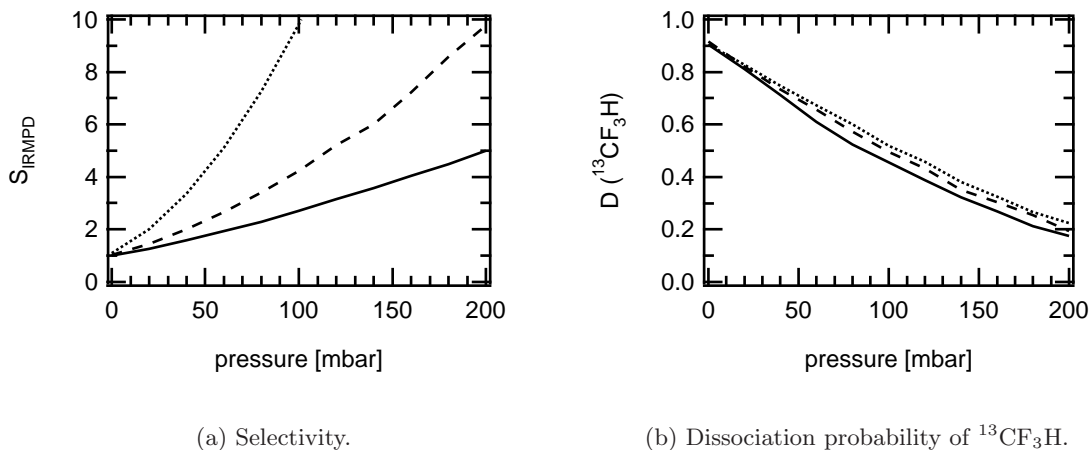


Figure 5.35: Dissociation selectivity and yield for a dissociation laser frequency of \cdots 1039, $- -$ 1044 and $—$ 1049 cm^{-1} , for pre-excitation via the 3_1 band and a dissociation laser fluence of 3 J cm^{-2} .

1044 cm^{-1} down to 1039 cm^{-1} , some selectivity (a factor of 2-3 for typical pressures of 50-100 mbar) can be gained without any significant change of the productivity. For this reason, we propose that for a potential industrial application the dissociation laser frequency should be chosen as far to the red as possible within the 9P emission band of the CO_2 laser ($\sim 1039 \text{ cm}^{-1}$). For the next emission band of the dissociation laser ($\sim 970\text{-}980 \text{ cm}^{-1}$), the absolute yields however are too low to be industrially interesting.

5.3.5 Summary and discussion

Section 5.3 was devoted to simulations of the IRMPD process of pre-excited CF_3H molecules in the presence of collisions. In section 5.3.1 we introduced the basic ideas of our simulations, in section 5.3.2 we developed the master equation which has to be solved numerically and in section 5.3.3 we explained how to evaluate physically reasonable values for the different rate coefficients needed in our master equation. Basically, for the interaction of a molecule with the field of the dissociation laser we applied a statistical theory presented in section 2.2, for vibrational relaxation we used the numerical results obtained in section 5.2 and for unimolecular dissociation we applied RRKM theory. The pumping rates due to the dissociation laser have been generalised by introducing a dependency on the dissociation laser frequency, the excitation level of the

molecule and its isotopic species.

In section 5.3.4 we presented our results. After a first general introduction, we presented a comparison between the numerical simulations and experiments:

- We simulated photofragment spectra which have been measured experimentally (see section 4.3). We noticed the necessity of introducing absorption of IR photons by increasing the number of quanta in the ν_6 vibration by two. In this case, there is an excellent agreement between experiments and numerical simulations.
- Simulations of dissociation selectivities (experiments presented in sections 4.3.3) showed an excellent agreement for molecules pre-excited via the 3_1 band. For molecules pre-excited via the 2_1 band the agreement is only on a qualitative level. We explained that the discrepancy is because in this case $^{12}\text{CF}_3\text{H}$ molecules are very much out of resonance with the dissociation laser field, and in such cases the absorption rates are underestimated.
- We calculated the dissociation selectivity of pre-excited CF_3H molecules as a function of the sample pressure in order to scale the vibrational relaxation rates.
- Also simulated decay rates fit very well with experimental data. The only discrepancy is that single exponentials do not fit absolutely well to simulated decay curves as opposed to experimental data. However, using such exponentials for the fit, the decay rates k correspond astonishingly good to the experimental data.

In these simulations, we worked with one single fitting parameter, a multiplicative constant for the vibrational relaxation rates. This scaling factor has been determined by fitting our results to different types of experiments.

With this set of simulations we are convinced that our model is a good and *necessary* model and that it describes reality in a satisfactory manner. With this, we were able to perform simulations in which we can observe the mechanisms of the OP-IRMPD process, and we can also perform simulations that have not been or cannot be performed experimentally.

Two sets of numerical experiments have been performed. First, in section 5.3.4.C we have shown how we determined the following:

At higher working pressures, isotopically selective collisional relaxation and different IR photon absorption rates both contribute to the enhancement of isotopic selectivity of the dissociation yield. For typical conditions we propose, the main contribution comes from different IRMPD rates.

We performed simulations where we evaluate the dissociation yield as a function of different experimental conditions such as the fluence and the frequency of the dissociation laser and the pressure of the sample. We have found that, in general, for an optimal dissociation selectivity in a real MLIS process, pre-excitation has to be done up to the first or the second overtone of the C-H stretch vibration, depending on different experimental parameters.

We have given some general features of the OP-IRMPD process. For a practical application at higher pressures and with overlapped pre-excitation and dissociation lasers⁵² we propose to use a dissociation laser frequency on the red side of the 9P emission band of the CO₂ laser.

Bibliography

- [1] Aleksei Stuchebrukhov, Stanislav Ionov, and Vladilen Letokhov. IR Spectra of Highly Vibrationally Excited Large Polyatomic Molecules and Intramolecular Relaxation . *J. Phys. Chem.*, 93:5357–5365, 1989.
- [2] A. L. Malinovsky, I. Yu. Petrova, E. A. Ryabov, A. A. Makarov, and V. S. Letokhov. Transition Spectra in the Vibrational Quasicontinuum of Polyatomic Molecules: Raman Spectra of Highly Excited SF₆ Molecules . *J. Phys. Chem. A*, 102:9353–9359, 1998.
- [3] V. N. Likhman, A. N. Petin, E. A. Ryabov, and V. S. Letokhov. Transition Spectra in the Vibrational Quasicontinuum of Polyatomic Molecules: IR Multiple-Photon

- Absorption in SF₆. 1. Experimental Studies . *J. Phys. Chem. A*, 103:11293–11298, 1999.
- [4] V. N. Lokhman, A. A. Makarov, I. Yu. Petrova, E. A. Ryabov, and V. S. Letokhov. Transition Spectra in the Vibrational Quasicontinuum of Polyatomic Molecules: IR Multiple-Photon Absorption in SF₆. 1. Theoretical Simulation and Comparison with Experiment . *J. Phys. Chem. A*, 103:11299–11309, 1999.
- [5] A. A. Kosterev, A. A. Makarov, A. L. Malinovsky, I. Yu. Petrova, E. A. Ryabov, and V. S. Lethokov. Transition Spectra in the Vibrational Quasicontinuum of Polyatomic Molecules: Raman Spectra of Highly Excited UF₆ Molecules . *J. Phys. Chem. A*, 104:10259–10264, 2000.
- [6] S. Califano. *Vibrational States*. John Wiley and Sons, 1976.
- [7] Philip R. Bunker and Per Jensen. *Molecular Symmetry and Spectroscopy*. Ottawa : NRC Research Press, 1998.
- [8] Günter Klatt, Andrew Willetts, Nicholas C. Handy, Riccardo Tarroni, and Paolo Palmieri. An Improved Anharmonic Potential for CHF₃ . *J. Molec. Spectrosc.*, 176:64–74, 1996.
- [9] O. V. Boyarkin, M. Kowalczyk, and T. R. Rizzo. Collisionally Enhanced Isotopic Selectivity in Multiphoton Dissociation of vibrationally excited CF₃H . *J. Chem. Phys.*, 118(1):93–103, 2003.
- [10] N. J. Fyke, P. Lockett, J. K. Thompson, and P. M. Wilt. The Infrared Spectra of HCF₃ and DCF₃ . *J. Molec. Spectrosc.*, 58:87–101, 1975.
- [11] G. Graner and G. Guelachvili. Fluoroform: the Polyad at 8-9 μm . *J. Molec. Spectrosc.*, 107:215–228, 1984.
- [12] A. Amrein, M. Quack, and U. Schmitt. High-Resolution Interferometric Fourier-Transform Infrared- Absorption Spectroscopy in Supersonic Free Jet Expansions - Carbon-Monoxide, Nitric-Oxide, Methane, Ethyne, Propyne, and Trifluoromethane . *J. Phys. Chem.*, 92(19):5455–5466, 1988.
- [13] J. P. Champion and G. Graner. Fluoroform - A new analysis of the polyad at 8-9 μm . *Molec. Phys.*, 58(3):475–484, 1986.

- [14] Andreas Amrein, Martin Quack, and Ulrich Schmitt. High resolution interferometric Fourier transform infrared absorption spectroscopy in a supersonic free jet expansion - The interacting states ν_2 , ν_5 and $\nu_3 + \nu_6$ of trifluoromethane . *Molec. Phys.*, 60(1):237–248, 1987.
- [15] Gerhard Herzberg. *Molecular Spectra and Molecular Structure. II. Infrared and Raman Spectra of Polyatomic Molecules*. Krieger Publishing Company: Malabar, Florida, 1991.
- [16] Alexander Makarov (ISAN Troitsk Russia). Private communication .
- [17] V. T. Platonenko and N. A. Sukhareva. On vibrational energy exchange between strongly excited polyatomic molecules . *Sov. Phys. JETP*, 51(6):1065–1071, 1980.
- [18] V. T. Platonenko and N. A. Sukhareva. Vibrational relaxation of strongly excited polyatomic molecules . *Sov. Phys. JETP*, 54(3):454–459, 1981.
- [19] V. M. Akulin. Singularities of collisional vibrational relaxation processes in strongly excited spectrally complex polyatomic molecules . *Sov. Phys. JETP*, 57(4):774–780, 1983.
- [20] Bruce H. Mahan. Resonant Transfer of Vibrational Energy in Molecular Collisions . *J. Chem. Phys.*, 46(1):98–101, 1967.
- [21] R. D. Sharma and C. A. Brau. Near-Resonant vibrational energy transfer in N_2 - CO_2 Mixtures . *Phys. Rev. Lett.*, 19(22):1273–1275, 1967.
- [22] R. D. Sharma and C. A. Brau. Energy Transfer in Near-Resonant Molecular Collisions due to Long-Range Forces with Application to Transfer of Vibrational Energy from ν_3 Mode of CO_2 to N_2 . *J. Chem. Phys.*, 50(2):924–930, 1969.
- [23] R. D. Sharma. Vibration-to-Vibration energy transfer in CO-CO collisions . *Chem. Phys. Lett.*, 30(2):261–266, 1975.
- [24] Beatriz M. Toselli and John R. Barker. Isotope effects in the vibrational deactivation of large molecules . *J. Chem. Phys.*, 97(3):1809–1817, 1992.
- [25] M. Quack and G. Seyfang. Frequency-dependent non-linear intensity dependence in the IR Photochemistry of CF_3I . *Chem. Phys. Lett.*, 93(5):442–447, 1982.

- [26] P. Dietrich, M. Quack, and G. Seyfang. Quantitative Infrared Photochemistry with CO₂ laser of different temporal shape: dissociation of CF₃I with nanosecond pulses . *Infrared Phys.*, 29(2-4):517–523, 1989.
- [27] Martin Quack. Master Equations for Photochemistry with Intense Infrared Light . *Ber. Bunsenges. Phys. Chem.*, 83:757–775, 1979.
- [28] M. L. Azcárate and E. J. Quel. Isotopic Selectivity and Collisional Deactivation in the Infrared Multiple-Photon Dissociation of CDCl₃ in Equimolar CDCl₃/CHCl₃ Mixtures . *J. Phys. Chem.*, 93:697–702, 1989.
- [29] K. A. Holbrook, M. J. Pilling, and S. H. Robertson. *Unimolecular Reactions*, chapter Kinetic Isotope Effects in Unimolecular Reactions. Wiley: Chichester, 1996.
- [30] M. Quack and J. Troe. Specific rate constants of unimolecular processes. 2. Adiabatic Channel model . *Ber. Bunsenges. Phys. Chem.*, 78(3):240–252, 1974.
- [31] Oscar Knefler Rice and Herman C. Ramsperger. Theories of unimolecular gas reactions at low Pressures . *J. Am. Chem. Soc.*, 49(7):1617–1629, 1927.
- [32] Oscar Knefler Rice. The Quantum Theory of Quasi-Unimolecular Gas Reactions . *Proc. Natl. Acad. Sci. U.S.A.*, 14(2):113–118, 1928.
- [33] L. S. Kassel. Studies in Homogeneous Gas Reactions. II. Introduction of Quantum Theory . *J. Phys. Chem.*, 32(7):1065–1079, 1928.
- [34] R. A. Marcus. Lifetimes of Active Molecules. I. . *J. Chem. Phys.*, 20(3):352–354, 1952.
- [35] R. A. Marcus. Lifetimes of Active Molecules. II. . *J. Chem. Phys.*, 20(3):355–359, 1952.
- [36] R. A. Marcus. Unimolecular Dissociations and Free Radical Recombination Reactions . *J. Chem. Phys.*, 20(3):359–364, 1952.
- [37] R. A. Marcus. Recombination of Methyl Radicals and Atomic Cracking of Ethyl Radicals . *J. Chem. Phys.*, 20(3):364–368, 1952.

- [38] Dong Nam Shin, Yong Sim Yoo, Chul Woong Park, Jae Won Hahn, and Kihyung Song. Kinetic study for the unimolecular dissociation of CF_3H : RRKM and PST calculations on an ab initio potential energy surface . *Chem. Phys. Lett.*, 258:613–619, 1996.
- [39] S. W. Benson. *Thermochemical kinetics*. Wiley, New York, 1976.
- [40] E. Tschuikow-Roux and J. E. Marte. Thermal Decomposition of Fluoroform in a Single-Pulse Shock Tube. I . *J. Chem. Phys.*, 42(6):2049–2056, 1965.
- [41] E. Tschuikow-Roux. Thermal Decomposition of Fluoroform in a Single-Pulse Shock Tube. II. Pressure Dependence of the Rate . *J. Chem. Phys.*, 42(10):3639–3642, 1965.
- [42] A. P. Modica and J. E. LaGraff. Mass-Spectrometer and UV Absorption Study of CHF_3 Decomposition behind Shock Waves . *J. Chem. Phys.*, 44(9):3375–3379, 1966.
- [43] K. P. Schug, H. Gg. Wagner, and F. Zabel. Gas Phase α , α Elimination of Hydrogen Halides from Halomethanes. I. Thermal Decomposition of Chlorodifluoromethane, Trifluoromethane, and Trichloromethane Behind Shock Waves . *Ber. Bunsenges. Phys. Chem.*, 83:167–175, 1979.
- [44] Yoshiaki Hidaka, Takuji Nakamura, and Hiroyuki Kawano. High temperature pyrolysis of CF_3H in shock waves . *Chem. Phys. Lett.*, 187(1,2):40–44, 1991.
- [45] Georg Seyfang (ETH Zurich Switzerland). Private communication .
- [46] Lars Melander. *Isotope Effects on Reaction Rates*. Ronald Press Company: New York, 1960.
- [47] Keith J. Laidler. *Chemical Kinetics*, chapter Isotope Effects. Harper & Row, New York, 1987.
- [48] Martin Quack. Theory of unimolecular reactions induced by monochromatic infrared radiation . *J. Chem. Phys.*, 69(3):1282–1307, 1978.
- [49] Martin Quack. Master Equations for Photochemistry with Intense Infrared Light (IV). A Unified Treatment of Case B and Case C Including Nonlinear Effects . *Ber. Bunsenges. Phys. Chem.*, 85:318–330, 1981.

-
- [50] John Charles Butcher. *The numerical analysis of ordinary differential equations : Runge-Kutta and general linear methods*. Chichester a.o. : Wiley, 1987.
- [51] Mikhail N. Polianski. *Overtone pre-excitation - Infrared Multiple Photon Dissociation Under Collisional Conditions. New Potential for Laser Isotope Separation*. PhD thesis, Ecole polytechnique fédérale de Lausanne, Switzerland, 2004.
- [52] M. Polianski, O. V. Boyarkin, and T.R. Rizzo. Collisionally-assisted, highly-selective laser isotope separation of carbon-13 . *J. Chem. Phys.*, 121(23):11771–11779, 2004.
- [53] A. Ceausu-Velcescu, H. Bürger, and G. Graner. High-resolution infrared spectra of HCF_3 in the ν_6 (500 cm^{-1}) and $2\nu_6$ (1000 cm^{-1}) regions: rovibrational analysis and accurate determination of the ground state constants C_0 and D_K^0 . *J. Molec. Spectrosc.*, 220:298–305, 2003.
- [54] V. S. Letokhov and A. A. Makarov. “Leakage” effect as an Exciting Mechanism of High Vibrational Levels of Polyatomic Molecules by a Strong Quasi-Resonant Laser IR Field . *Optics Comm.*, 17(3):250–253, 1976.
- [55] M. Polianski, O. V. Boyarkin, and T. R. Rizzo. to be published . 2005.

Chapter 6

Conclusions and Outlook

The goal of this thesis was to explain the increase of isotopic selectivity in our OP-IRMPD molecular laser isotope separation process upon increasing the sample pressure or the time-delay between the two lasers. We have performed a set of experiments and numerical simulations and we are able to give a coherent picture of this enhancement. Furthermore, we have directly observed isotopically selective collisional vibrational relaxation of highly excited medium-sized polyatomic molecules which is, to the best of our knowledge, the first in its kind. We have proposed a model including both short-distance and long-distance interactions between two CF_3H molecules which is in a satisfying agreement with our experimental findings.

6.1 Isotopically selective collisional vibrational relaxation

We have performed experiments where we measure the total dissociation yield using the OP-IRMPD process as a function of the time-delay between the pre-excitation and dissociation laser. By letting either excited $^{12}\text{CF}_3\text{H}$ or $^{13}\text{CF}_3\text{H}$ relax on ground state $^{12}\text{CF}_3\text{H}$ or $^{13}\text{CF}_3\text{H}$ we were able to measure relative relaxation rates of self and cross-relaxation ($^{13}\text{CF}_3\text{H}$ on $^{12}\text{CF}_3\text{H}$ and vice versa). The finding is that in general the molecules relax roughly 1.5-2.5 as fast on $^{13}\text{CF}_3\text{H}$ than on $^{12}\text{CF}_3\text{H}$ (see figure 4.26). Table 6.1 summarises the final result.

There is a small uncertainty as to the absolute relaxation rates, because our detection via IRLAPS senses molecules over an energy region which is not a priori well known.

Pre-excitation energy	$\kappa(12^* - 12) : \kappa(12^* - 13) : \kappa(13^* - 13) : \kappa(13^* - 12)$
5950 cm^{-1}	1.00 : 1.60 : 1.00 : 0.41
8800 cm^{-1}	1.00 : 1.94 : 1.00 : 0.51
11,530 cm^{-1}	1.00 : 1.90 : 1.00 : 0.57
14,000 cm^{-1}	1.00 : 1.65 : 1.00 : 0.59

Table 6.1: Summary of relative relaxation rates of excited CF_3H on ground state CF_3H . $\kappa(X^* - Y)$ is the relaxation rate of excited ${}^X\text{CF}_3\text{H}$ on ground state ${}^Y\text{CF}_3\text{H}$.

We have proposed a numerical model for the explanation of these results. In this model, vibrational energy transfer is mediated by (a) the repulsive part of the (short-range) interaction potential of the two molecules and (b) the long-range dipole-dipole interactions. Collisional relaxation due to (a) is very difficult to handle, which is why we treat this part as an adjustable parameter. For the vibrational relaxation rate W due to part (b) relatively precise calculations can be done based on the Fermi golden rule $W = 2\pi|V|^2\rho/\hbar$. Here, V can be related to the IR absorption spectra of molecules in the ground state, and ρ can be related to the overlap of the absorption spectra of molecules in the ground state and emission spectra of the excited molecules. These emission spectra had to be calculated, taking into account a so-called “statistical inhomogeneous broadening”¹ due to large intramolecular mode mixing. Our model resembles those proposed by Mahan² and Sharma and Brau³⁻⁵, where a similar distinction between long-range and short-range interactions has been made. At some point these authors have to assume a certain value for the cut-off distance that separates long-range and short-range interactions, and they also have to assume a certain vibrational energy transfer probability mediated by short-range interactions. As we possess a set of measurements with isotopically substituted molecules, we *fit* these parameters rather than assuming certain values. The fitted values, $\sim 7.4 \text{ \AA}$ for the cut-off radius, and $\sim 6.8 \cdot 10^4/E$ the number of collisions for the molecule to lose 1000 cm^{-1} in short-range interactions, are physically reasonable, which makes our model credible. To our knowledge, this is the first time that such calculations have been performed for highly excited polyatomics where such extensive mixing has to be taken into account.

6.2 Enhancement of isotopic selectivity in our MLIS process

We have performed a series of experiments to determine the mechanism of the enhancement of isotopic selectivity by increasing the time-delay *at low pressures*. Basically, two questions have to be answered. First, is this phenomenon specific to CF_3H molecules pre-excited via the 3_1 band and due to some accidental resonances of this band with others? And secondly, if not, what mechanisms apply?

By changing the pre-excitation energy to different rovibrational bands, we have determined unambiguously that the phenomenon is not specific to the pre-excited rovibrational state, but general, and may hence be used for other molecules. In a set of experiments we have determined the respective influence of isotopically selective collisional relaxation and different absorption strengths of IR photons for different pre-excitation energies and fluences of the dissociation laser. Interestingly enough, both mechanisms contribute in general roughly 50 % to the enhancement of isotopic selectivity.

In a second step we developed numerical master equations for the description and calculation of the OP-IRMPD process. We showed in a set of simulations, that our experimental data is relatively well reproduced, which makes our simulations credible. With this, we could simulate experiments at higher pressures, and we could show, that for a fluence of 3 J cm^{-2} and a frequency of 1047 cm^{-1} of the CO_2 dissociation laser both mechanisms contribute significantly to the enhancement of isotopic selectivity, although the influence of different IRMPD rates is predominant.

In view of finding an ideal parent molecule for MLIS via collisionally assisted OP-IRMPD, different criteria must be met. There are some chemical constraints which were not subject of this thesis. These constraints include the capacity of the dissociation product recombining with each other or with a scavenger gas to form a stable product. From a point of view of efficiently and selectively bringing the molecules to dissociate, we summarise the key properties that such a molecule should have:

1. Large absorption coefficient for an overtone of a certain mode. This is typically achieved in molecules with a C-H bond which is in general very anharmonic, and as a consequence the absorption is relatively strong.

2. A well resolved isotopic shift for pre-excitation.
3. A large isotopic shift for the mode that has the largest transition dipole moment (for V-V relaxation to be as selective as possible). Ideally, the intra- and intermode anharmonicity for this vibration should be as small as possible (in order to conserve isotopic selectivity of VET upon excitation of the molecule).
4. A well absorbing vibration to the blue of the dissociation laser such that an efficient discrimination between ground state molecules and excited molecules can be done for IRMPD, and a large isotopic shift for this particular vibrational mode.

For the case that this scheme should ever be employed in an industrial laser isotope separation plant, we propose the use of a (strong) CO₂ laser line at the low frequency end of the 9P emission band of CO₂ ($\sim 1039 \text{ cm}^{-1}$).

Bibliography

- [1] Aleksei Stuchebrukhov, Stanislav Ionov, and Vladilen Letokhov. IR Spectra of Highly Vibrationally Excited Large Polyatomic Molecules and Intramolecular Relaxation . *J. Phys. Chem.*, 93:5357–5365, 1989.
- [2] Bruce H. Mahan. Resonant Transfer of Vibrational Energy in Molecular Collisions . *J. Chem. Phys.*, 46(1):98–101, 1967.
- [3] R. D. Sharma and C. A. Brau. Near-Resonant vibrational energy transfer in N₂-CO₂ Mixtures . *Phys. Rev. Lett.*, 19(22):1273–1275, 1967.
- [4] R. D. Sharma and C. A. Brau. Energy Transfer in Near-Resonant Molecular Collisions due to Long-Range Forces with Application to Transfer of Vibrational Energy from ν_3 Mode of CO₂ to N₂ . *J. Chem. Phys.*, 50(2):924–930, 1969.
- [5] R. D. Sharma. Vibration-to-Vibration energy transfer in CO-CO collisions . *Chem. Phys. Lett.*, 30(2):261–266, 1975.

APPENDICES

Appendix A

Development of formulae for pumping molecules through a low density regime (“case C”)

The formulae for the up- and down-pumping constants $K_{J,I}$ for the case of essentially uncoupled levels within an energy bin (“case C”) are given in table 2.12. Here we first give some qualitative explanations of how the formulae have been calculated (section A.1). Quantitative explanations can be found in section A.2.

The case C calculations are explicitly given for the initial condition that the upper level J is not populated at $t = 0$ and stays sparsely populated throughout the experiment. This condition is reasonably well fulfilled for IRMPD of ground state molecules. In our case however, we populate a certain level with the pre-excitation laser (overtone of C-H stretch vibration). If we look at the up and down-pumping rates between this populated level (\equiv level J) and a level lying $\sim 1,050 \text{ cm}^{-1}$ (energy of CO_2 laser photon) below it (\equiv level I) the situation is inverted. The upper level is initially populated and the lower level is unpopulated. We hence have to generalise the formulae for case C or at least adapt it to our calculations. Section A.3 treats this problem.

A.1 Qualitative explanations

In case C the states within both grained levels I and J are not anharmonically coupled between each other, but there is a pairwise interaction due the IR field between members of levels I and J (figure A.1)[‡].

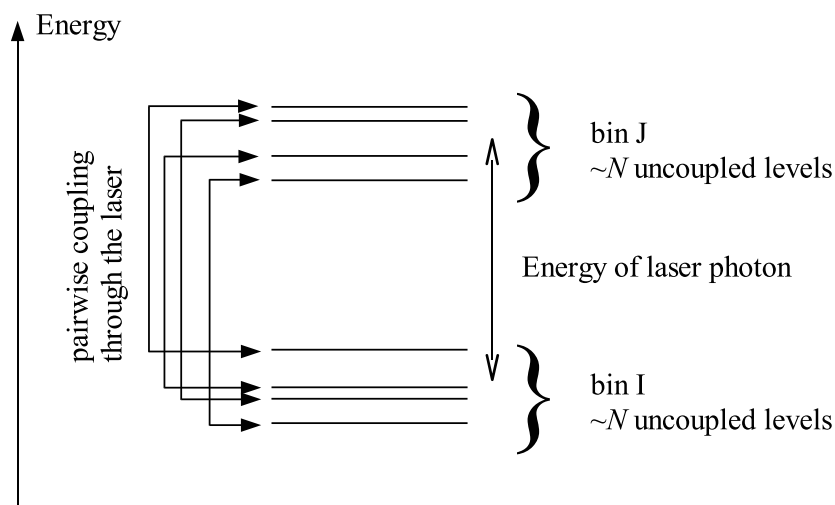


Figure A.1: In case C, the states in both the upper and lower bins are uncoupled amongst each other. Coupling occurs only between members of bin I and bin J via laser radiation.

The total evolution of population corresponds hence to the average of the population evolutions between the individual couple of states.

For each pair of coupled states i and j ($p_i(t = 0) = 1$ and $p_j(t = 0) = 0$), the population evolution is described by Rabi-oscillations. The amplitude of these oscillations is mainly given by the off-resonance shift $D = \omega - (E_j - E_i)$ where ω is the energy of a laser photon and E_i and E_j are the energies of the upper and the lower levels respectively. The smaller D , the larger the amplitude of oscillations (in the limiting case of $D = 0$

[‡]Unfortunately there is a small inconsistency in the theory: on the one hand one assumes that the states within a bin are uncoupled, but on the other hand one sums over all couples of states, therefore assuming that the states are equally populated. This inconsistency has to be accepted if one wants to apply the master equation calculations.

there is a complete population transfer $i \rightarrow j \rightarrow i \rightarrow j \rightarrow \dots$). The frequency of the population transfer also depends, although weaker, on D . Figure A.2 demonstrates this population transfer.

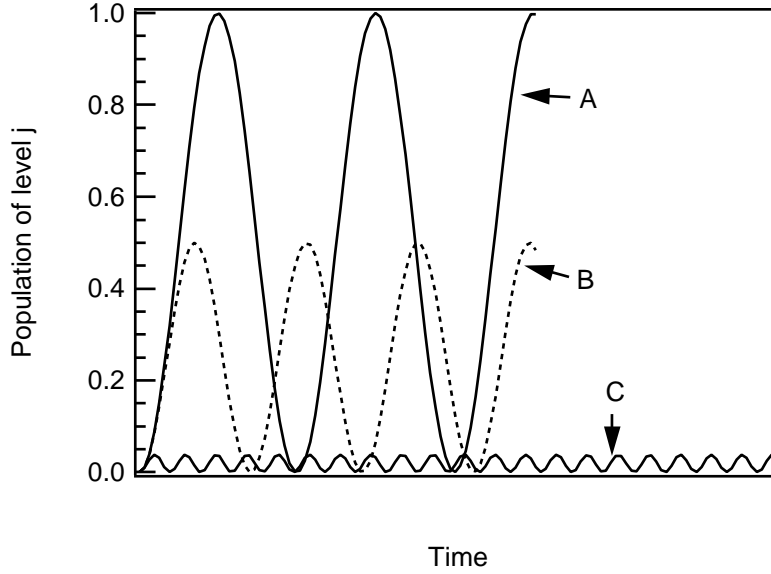


Figure A.2: Rabi-oscillations for different strengths of coupling between the two states. The curves show the population of the upper level j which is initially unpopulated. A measure of the coupling is given by D/V where D is the off-resonance shift between the laser field and the difference in energy of the two states and V is the strength of the laser field.

- (A) Strong coupling ($D \ll V$).
- (B) Intermediate coupling ($D \approx V$).
- (C) Weak coupling ($D \gg V$).

The total population in a bin is obtained after averaging over all members of this bin:

$$p_J(t) = \frac{\sum_{i=1}^N p_{j_i}(t)}{N}, \quad (\text{A.1})$$

where N is the number of coupled pairs of states (analogously for bin I). Here small i, j 's refer to single states in a bin, and capital I, J 's refer to the bins themselves. With some assumptions about how D_i and V_i (strength of coupling via the laser) are

distributed the averaged population $p_J(t)$ can be well approximated by doing master equation calculations with the rate constants given in table 2.12 which we recall to be $K_{J,I} = 2\pi \frac{|V|^2}{\delta_J}$ and $K_{I,J} = K_{J,I} \cdot \left(\frac{\delta_J}{\delta_I}\right) \left(\frac{2\delta_J}{\pi\sqrt{3}|V|}\right)$ (for details see section A.2).

A.2 Calculations details

If we look at a single interacting pair of levels i and j the transfer of population is described by a Rabi-oscillation. If initially only the lower level i is populated the evolution is described by

$$\begin{aligned} p_j(t) &= \frac{V^2}{V^2+D^2} \sin^2\left(\frac{t}{2}\sqrt{V^2+D^2}\right) \\ p_i(t) &= 1 - p_j(t) \end{aligned} \quad (\text{A.2})$$

where $\Omega = \sqrt{V^2 + D^2}$ is the so-called “generalised Rabi frequency”. V is the coupling matrix element between the levels i and j and D is the off-resonance shift (figure A.3).

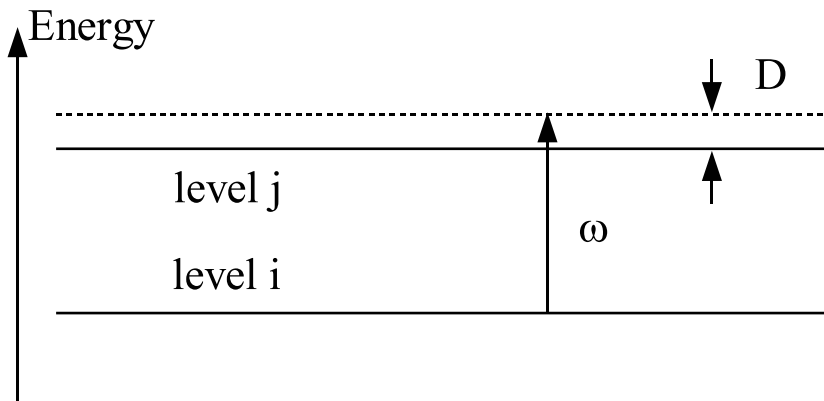


Figure A.3: D is the off-resonance shift between the difference of energy of the two levels and the frequency of the electromagnetic field.

If initially all states in the grained level I are equally populated the total population in the upper grained level J is described as

$$p_J(t) = \frac{1}{N} \sum_{k=1}^N \frac{V_k^2}{V_k^2 + D_k^2} \sin^2\left(\frac{t}{2}\sqrt{V_k^2 + D_k^2}\right). \quad (\text{A.3})$$

If there are a lot of coupled levels ($N \rightarrow \text{large}$) the sum can be replaced by integrals over V and D which read

$$p_J(t) = \frac{\int_{-\infty}^{\infty} dD F(D) \int_{-\infty}^{\infty} dV G(V) \frac{V^2}{V^2+D^2} \sin^2\left(\frac{t}{2}\sqrt{V^2+D^2}\right)}{\int_{-\infty}^{\infty} dD F(D) \int_{-\infty}^{\infty} dV G(V)}, \quad (\text{A.4})$$

where, however, F and G are completely unknown.

This equation is not easy to evaluate, even if some special forms of $F(D)$ and $G(V)$ are assumed. One can however evaluate the behaviour as $t \rightarrow \infty$ and for the special case of square functions of F and G

$$F(D) = \begin{cases} C_D & -D_m \leq D \leq D_m \\ 0 & \text{otherwise} \end{cases} \quad (\text{A.5})$$

$$G(V) = \begin{cases} C_V & -V_m \leq V \leq V_m \\ 0 & \text{otherwise} \end{cases}$$

With this equation A.4 becomes

$$p_J(t) = \frac{1}{D_m V_m} \int_0^{D_m} dD \int_0^{V_m} dV \sin^2\left(\frac{t}{2}\sqrt{V^2+D^2}\right) \frac{V^2}{V^2+D^2}. \quad (\text{A.6})$$

As $t \rightarrow \infty$ the expression $\sin^2\left(\frac{t}{2}\sqrt{V^2+D^2}\right)$ will be on average $1/2$ and p_J is readily evaluated

$$p_J(t \rightarrow \infty) = \frac{1}{2D_m V_m} \int_0^{D_m} dD \int_0^{V_m} dV \frac{V^2}{V^2+D^2} \quad (\text{A.7})$$

Because in case C the coupling between the states is assumed to be small, we have $D_m \gg V_m$ and the above integral becomes

$$p_J(t \rightarrow \infty) = \frac{\pi V_m}{8D_m} + \frac{1}{4} \left\{ 1 - \left[\frac{V_m^2 + D_m^2}{V_m D_m} \right] \arctan(V_m/D_m) \right\} \approx \frac{\pi V_m}{8D_m}. \quad (\text{A.8})$$

Also, if equation A.4 is evaluated for $D_m^{-1} \ll t \ll V_m^{-1}$, which is the most interesting region, one gets

$$p_J(t) \approx \frac{V_m^2}{4D_m} t. \quad (\text{A.9})$$

By setting¹ $V_m^2 = 12|V|^2$ and $D_m = \delta/2$ where $|V|$ is the average interaction defined in table 2.11 and δ is the average spacing between effectively coupled levels we get

$$p_J(t) = \begin{cases} \frac{\pi\sqrt{3}|V|}{2\delta_J} & t \rightarrow \infty \\ \frac{6|V|^2}{\delta_J} t & D_m^{-1} \ll t \ll V_m^{-1} \end{cases} . \quad (\text{A.10})$$

In our calculations we do not consider the individual coupling between states, but we seek to describe the evolution of the population of a bin with master equations using pumping rates. We can set pumping rates between a lower level I and an upper level J of

$$\begin{aligned} K_{J,I}^C &= 2\pi|V|^2/\delta_J \\ K_{I,J}^C &= (\pi\sqrt{3}|V|/2\delta_J)^{-1} \cdot (\delta_J/\delta_I) \cdot K_{J,I} \ , \end{aligned} \quad (\text{A.11})$$

where we used the approximation that $2\pi \approx 6$ and by setting $\delta = \delta_J^2/\delta_I$. This way we get a population evolution similar to the one described above. The initial slope and the final relaxed distributions are the same as described in equation A.10. This is illustrated in figure A.4. The value for $K_{J,I}^C$ corresponds to the up-pumping value of cases A and B, the down-pumping rate $K_{I,J}^C$ is the same as for case B with a correction factor of $(\pi\sqrt{3}|V|/2\delta_J)^{-1}$.

For these calculations we made a certain number of approximations and assumptions. One of these is that G and F are square functions. If they would have been assumed e.g. gaussians, the evolution would be slightly different. This is also shown in figure A.4.

A.3 Attempts to generalise case C calculations

All the calculations presented above hold true as long as the upper level J is initially unpopulated and that on average the coupling V is small, so that the upper level essentially remains unpopulated at all times. A generalisation of case C calculations is

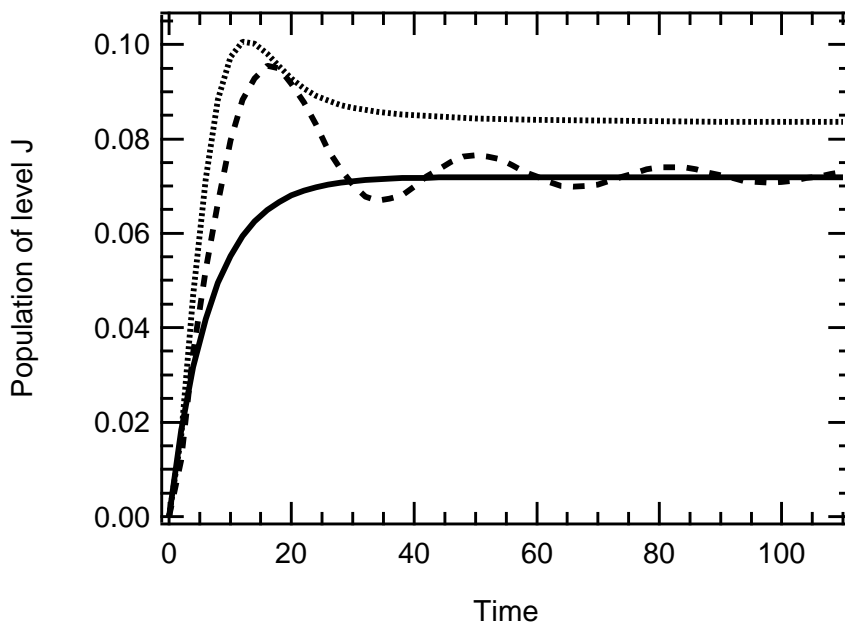


Figure A.4: Evolution of upper level J (solution to equation A.4).

-- G, F are square functions (equation A.5).

... G, F are gaussian functions.

— Approximative solution to the case of $G, F =$ square functions by master equations (pumping rates in A.11).

difficult, because in our approach to use the master equation we characterise the population distribution by their energy and not by the state (we only store $|\langle \Psi_i | \Psi(t) \rangle|^2$ in form of $p_i(t)$ ($i = 0, 1, 2, \dots$) and not $|\Psi(t)\rangle$ itself, where $|\Psi_i\rangle$ is the state associated with bin i , $|\Psi(t)\rangle$ is the state of the molecule). This is not sufficient if we want to generalise these calculations.

We decide to take a pragmatic approach to this problem: when calculating the pumping-rates, we first determine for each pair of states the one which is more populated. If the lower state is more populated, then the formulae developed by Quack will be applied, in the inverse situation, the formulae will be correctly inverted. This may lead to some problems in regions where molecules in the ground state heated up by collisions and/or IR photons absorption “meet” molecules pre-excited having lost energy due to collisions and/or stimulated emission. However, it turns out, that the influence is marginal.

Bibliography

- [1] Martin Quack. Master Equations for Photochemistry with Intense Infrared Light (IV). A Unified Treatment of Case B and Case C Including Nonlinear Effects . *Ber. Bunsenges. Phys. Chem.*, 85:318–330, 1981.

Appendix B

Collisional quenching of LIF

At the pressures used in our experiments, CF_2 fragments in an excited electronic state may not only spontaneously emit a photon (LIF), but can undergo non-radiative collisional deactivation. As long as we are performing experiments at a constant pressure, this correction is simply a scaling factor having no influence on our results, since we are only interested in relative values. However, in the experiments where we measure pressure dependencies, the LIF signal has to be corrected for the quenching.

To determine a correction factor we measure the decrease of the LIF signal as a function of time for different pressures. This decrease is characterised by a relaxation rate K_p which can be expressed as

$$K_p = \frac{1}{\tau_0} + q \cdot p, \quad (\text{B.1})$$

where τ_0 is the radiative lifetime of an excited state, p is the pressure of the quenching gas and q is the quenching constant. q is measured by fitting an exponent to the tail of the LIF signal (at the beginning some scattered light contributes to the LIF signal). Figure B.1 shows a sample LIF signal and the region fitted.

The radiative life-time has been determined to be $\tau_0 = (64 \pm 2) \cdot 10^7$ ns and the quenching constant $q = (1.10 \pm 0.09) \cdot 10^5$ (mbar s)⁻¹ (see fig B.2). The value for τ_0 compares well with the literature¹⁻⁴ which which cites values of 59, 61 ± 3 , 55 and 62 ± 4 ns. The quenching rate q of CF_2 on CF_3H has not been measured to our knowledge, but for CF_2HCl and for CF_4 they have been determined to be $6.6 \cdot 10^5$ and $8.8 \cdot 10^4$ (mbar s)⁻¹.

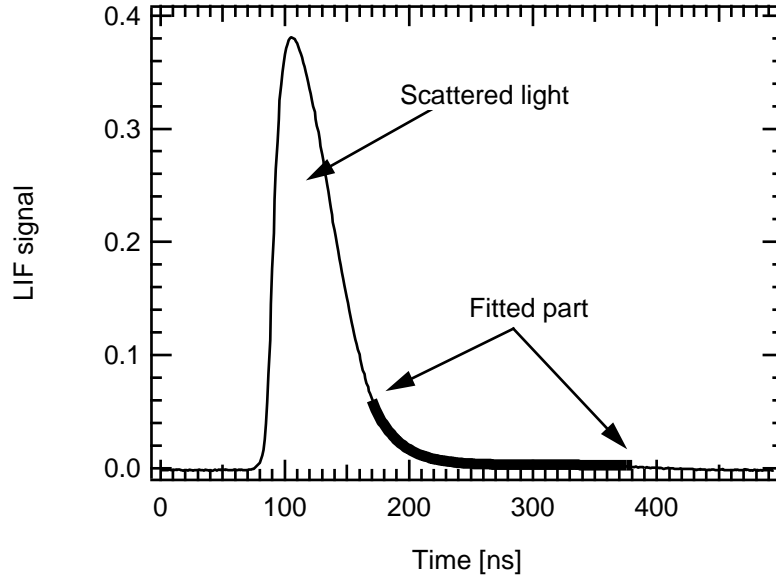


Figure B.1: Sample LIF signal at 47.8 mbar. The first large peak is due to scattered light, the exponential fit has been done on the tail of the signal.

One could expect that the CF_3H quenching rate lies between the rates for CF_2HCl and for CF_4 , which is the case.

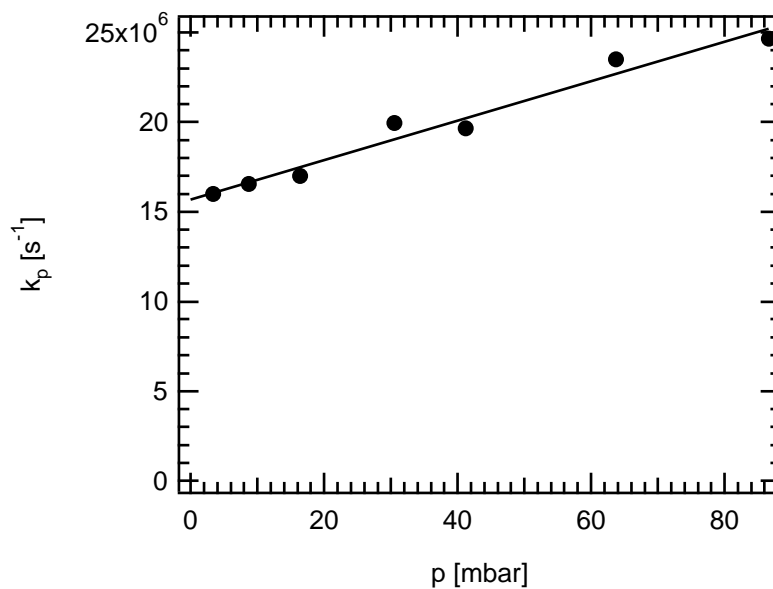
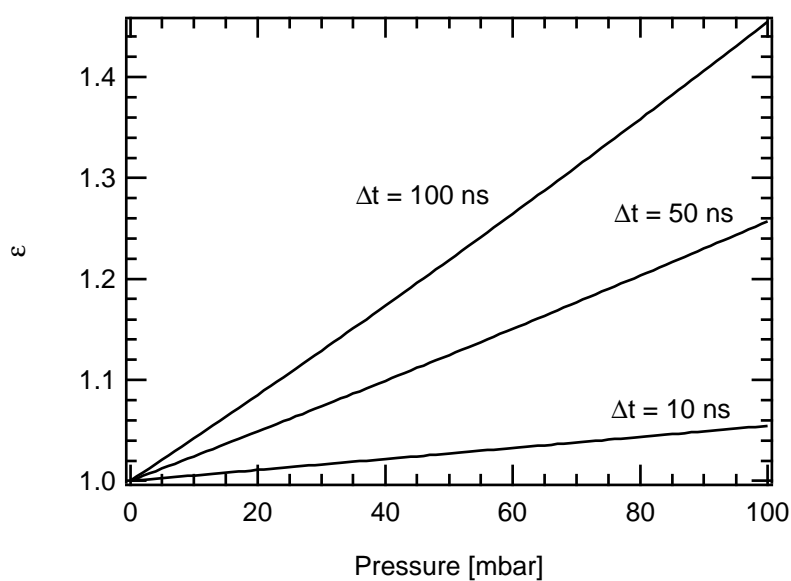
In an experiment the LIF signal is integrated from t_0 to t_1 , i.e.

$$\begin{aligned} S_p &= \int_{t_0}^{t_1} \eta \cdot \exp(-k_p t) dt \\ &= \frac{\eta \exp(-k_p t_0)}{k_p} \cdot (1 - \exp(-k_p (t_1 - t_0))) \quad , \end{aligned} \quad (\text{B.2})$$

where η is the transmission by the detection system. The signal S_0 that would be measured in the absence of collisions, is related to the signal S_p measured at a finite pressure p by

$$S_0 = \frac{k_p}{k_0} \cdot \exp((k_p - k_0) \cdot t_0) \cdot \frac{1 - \exp(-k_0 \Delta t)}{1 - \exp(-k_p \Delta t)} \cdot S_p = \varepsilon \cdot S_p, \quad (\text{B.3})$$

where $k_0 = 1/\tau_0$ and $\Delta t = t_1 - t_0$. Figure B.3 shows the values of ε for different integration times Δt (10, 50 and 100 ns), for $t_0 = 0$ ns. As Δt becomes shorter the correction becomes less important.

Figure B.2: Quenching of CF_2 on CF_3H .Figure B.3: Correction factors ϵ for the dissociation yield.

Bibliography

- [1] F. B. Wampler, J. J. Tiee, W. W. Rice, and R. C. Oldenberg. UV laser photochemistry of CF_2Br_2 . *J. Chem. Phys.*, 71(10):3926–3930, 1979.

-
- [2] David S. King, Peter K. Schenck, and John C. Stephenson. Spectroscopy and Photophysics of the $\text{CF}_2\tilde{A}^1B_1 - \tilde{X}^1A_1$ System . *J. Molec. Spectrosc.*, 78:1–15, 1979.
- [3] W. Hack and W. Langel. Photophysics of CF_2 ($\tilde{A}^1B_1(0, 6, 0)$) excited by a KrF laser at 248nm. I: Quenching of $\text{CF}_2(\tilde{A})$ by its common precursors . *J. Photochem.*, 21:105–110, 1983.
- [4] L. Rubio, M. Santos, and J. A. Torresano. Laser induced fluorescence detection of CF, CF_2 and CF_3 in the infrared multiphoton dissociation of C_3F_6 . *J. Photochem. Photobiol. A: Chem.*, 146:1–8, 2001.

Appendix C

CO₂ laser fluence control and measurement

C.1 Attenuation of the CO₂ laser beam

We have considered different schemes for the attenuation of the CO₂ laser beam in order to make fluence dependent measurements: by clipping the beam with an iris, by changing the output energy of the laser by adjusting the voltage of the CO₂ laser, by passing the laser beam through an absorption cell filled with CFH₃ or by attenuating the beam by teflon sheets. The most reliable and convenient way is the latter, which is described in more detail below.

A small system has been built in which a variable number of 0.1 mm thick teflon sheets can be mounted on a small motor that spins the teflon sheets so that the laser always hits a different place in order to avoid melting of the teflon. Every teflon sheet absorbs ~50% of the energy. The attenuation of the CO₂ laser beam can be calculated by Beer's Law

$$\Phi = \Phi_0 \cdot \exp(-\varepsilon n), \quad (\text{C.1})$$

where Φ_0 and Φ are the initial and final fluences, n is the number of teflon sheets and ε is an absorption coefficient for a single teflon sheet. The value of ε is wavelength dependent. It can be determined by taking an FTIR scan of teflon in the region of the

CO₂ laser output. This is shown in figure C.1.

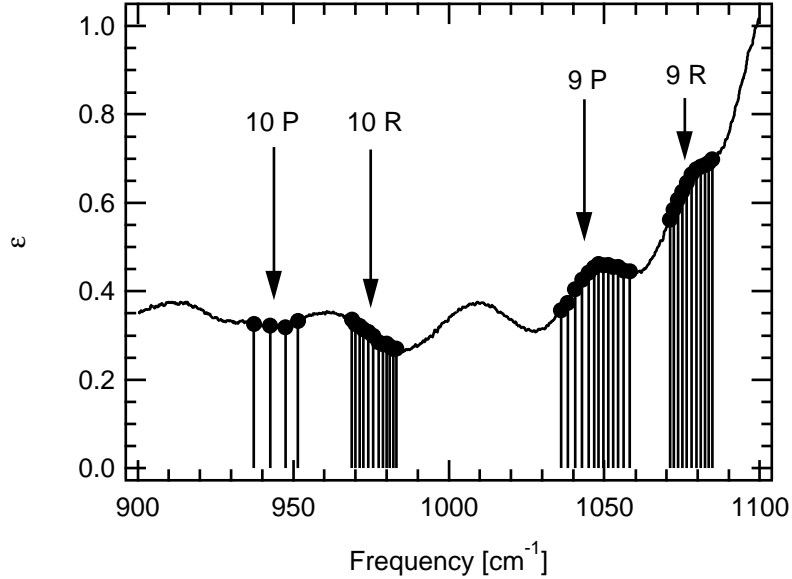


Figure C.1: Absorption spectrum of teflon. The frequencies of emitted radiation by the CO₂ laser are shown in the graph (10R, 9P and 9R laserlines, a couple for 10P as we rarely used these frequencies).

C.2 Calculation of the fluence

The fluence is defined to be the total energy per unit area. Its dimension is hence energy / surface, we typically use J cm⁻². The fluence of a laser beam varies across the beam. In the case of a perfect TEM₀₀ beam it follows a Gaussian distribution. When we give values for the fluence Φ of the CO₂ laser it is referred to the *centre* of the beam. We calculate Φ as follows

$$\Phi = E \cdot f_1 \cdot f_2 \cdot \exp(-\varepsilon n) \cdot \frac{1}{\pi r_0^2}, \quad (\text{C.2})$$

where E is the total power of the beam, f_1 is the fraction of energy that passes the Pellin-Broca prism and the BaF₂ windows of the cell, f_2 is the fraction of the CO₂ laser pulse used before the LIF laser pulse and r_0 is the FWHM / $\sqrt{\ln 2}$, where the FWHM is taken from the CO₂ laser intensity at the centre of the cell. The dependence of f_1 , f_2

and r_0 on the frequency of the CO₂ laser are shown in figures C.2 - C.5.

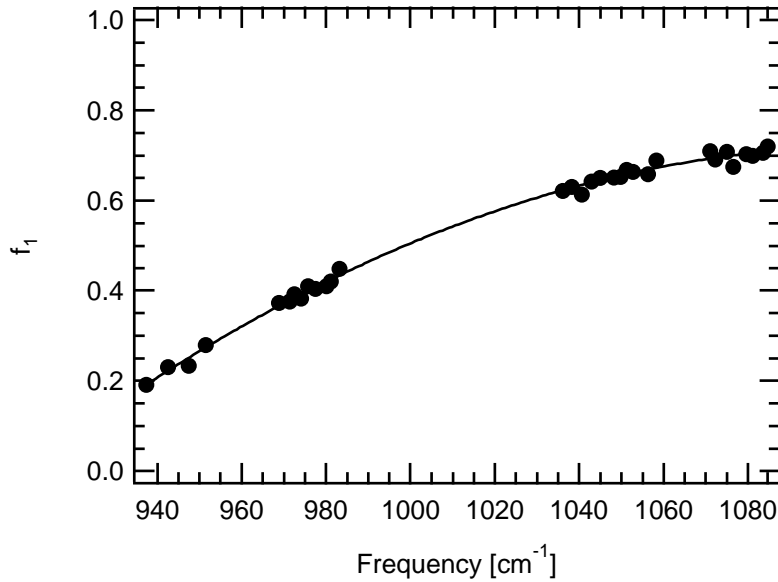


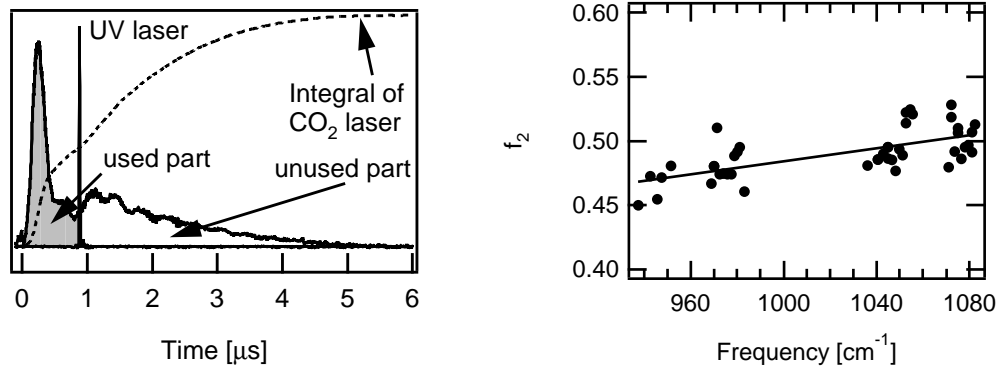
Figure C.2: Amount of transmitted light f_1 by the Pellin-Broca prism and the BaF₂ windows of the cell.

The absorption of the CO₂ laser light by the Pellin-Broca prism and the BaF₂ window depends smoothly on the CO₂ laser frequency. An ad hoc second order polynomial dependence can be easily fitted to the data points. f_1 includes absorption by a Pellin-Broca prism just in front of the cell. This is done because of space limitations after the Pellin-Broca prism for the measurement of the energy in the laser beam.

The fraction f_2 of the laser shot which is effectively used in our experiments lies between 45 and 53%, although no smooth dependence can be observed. For our data analysis we took the values obtained by doing a linear fit to the experimental data points.

We measure the FWHM by scanning a small slit at the focal point and measuring the energy let through it as a function of the displacement x . This is shown in figure C.4.

If the beam profile is Gaussian, the measured energy E' let through is given by



(a) Not the whole CO₂ laser pulse is effectively used for LIF detected dissociated molecules.

(b) On average (48 ± 5) % of the beam is used.

Figure C.3: Measurements of f_2 , the amount of the CO₂ laser shot used.

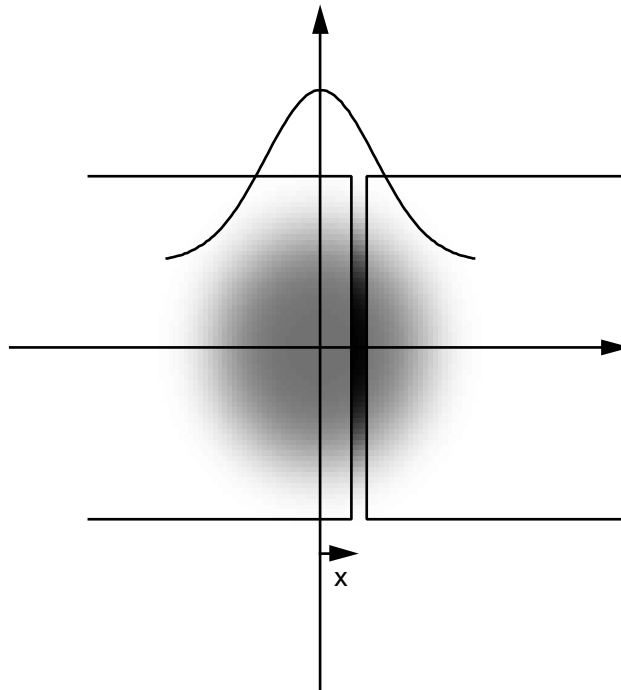


Figure C.4: By scanning a slit over the beam we measure a Gaussian dependence of the energy let through as a function of the displacement.

$$\begin{aligned}
E'(x) &= \int_{-\infty}^{\infty} \frac{E_0 \cdot \Delta x}{\omega \sqrt{\pi}} \cdot \exp\left(-\left(\left(\frac{x}{\omega_x}\right)^2 + \left(\frac{y}{\omega_y}\right)^2\right)\right) dy \\
&\propto \exp\left(-\left(\frac{x}{\omega_x}\right)^2\right)
\end{aligned} \tag{C.3}$$

and analogous for $E'(y)$, where E_0 is the energy in the total beam, Δx is the size of the slit and $\omega_x = 2r_0$. The widths in the horizontal and vertical directions are not the same, there is a small distortion because of the Pellin-Broca prism. We show in figure C.5 the data points we measure.

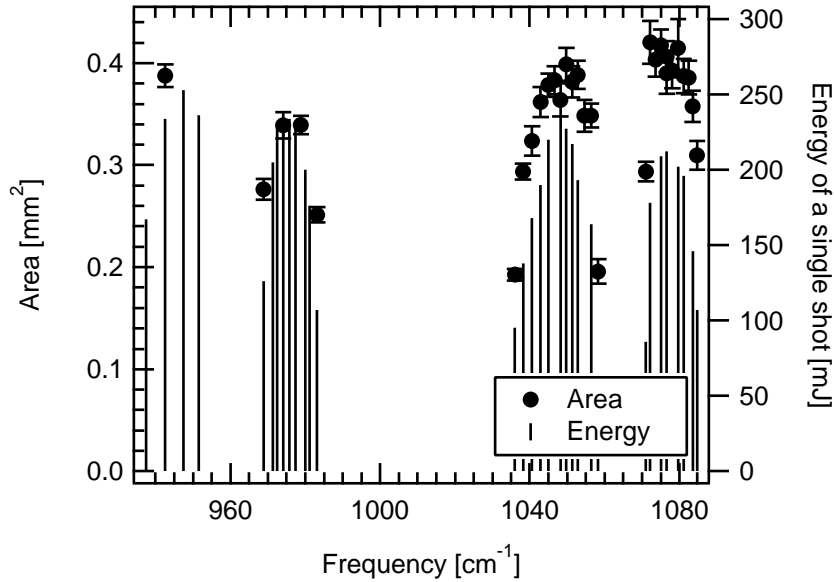


Figure C.5: Cross-section of the CO₂ laser beam at the focal point (left axis) and output energy of pulse (right axis).

There is a correlation between the area of the focal spot and the total energy of the laser shot (see figure C.5): the higher the energy of a pulse, the larger the area. We believe that this is because in the case of a high energy pulse it is not a clean TEM₀₀ pulse. These modes are less well focused than the TEM₀₀ mode, which broadens the area. As most of the measurements have been done with laser lines at the centre of the emission bands of the CO₂ laser we always use 0.4 mm² as area.

With the measurements of ε , f_1 , f_2 and r_0 as a function of the CO₂ laser frequency

we have now all instruments at our hand to accurately calculate the fluence[‡] of the CO₂ laser radiation.

[‡]Often called the “effective fluence” if we want to stress the fact that f_2 , the fraction of the CO₂ laser radiation actually used, is included.

Appendix D

CO₂ laser fluence dependence of the decay rate

There is a surprising effect one can observe: the measured decay rate k as a function of the dissociation laser fluence goes through a maximum and drops for both the high fluence and the low fluence limit. We show in figure D.1 an example of how the decay rate k behaves as a function of the dissociation laser fluence.

The values of the decay rates k in figure D.1 go through a maximum at $\sim 1 \text{ J cm}^{-2}$. This behaviour is often observed for different measurements. How can this be explained? We give an explanation of this phenomenon.

In a typical experiment where we scan the delay between the pre-excitation and the dissociation lasers, our system first selectively dissociates pre-excited molecules with the CO₂ laser, then the photofragments are detected via LIF. We do not exclusively detect molecules still having all their initial vibrational energy at the onset of the dissociation laser, but also molecules having lost a part of it. Because they have lost vibrational energy, their dissociation probability drops.

We show in figure D.2 qualitatively the dissociation probability for a low, an intermediate and a high fluence of the dissociation laser.

The arrows in the figure show a typical amount of energy a molecule has to lose until the

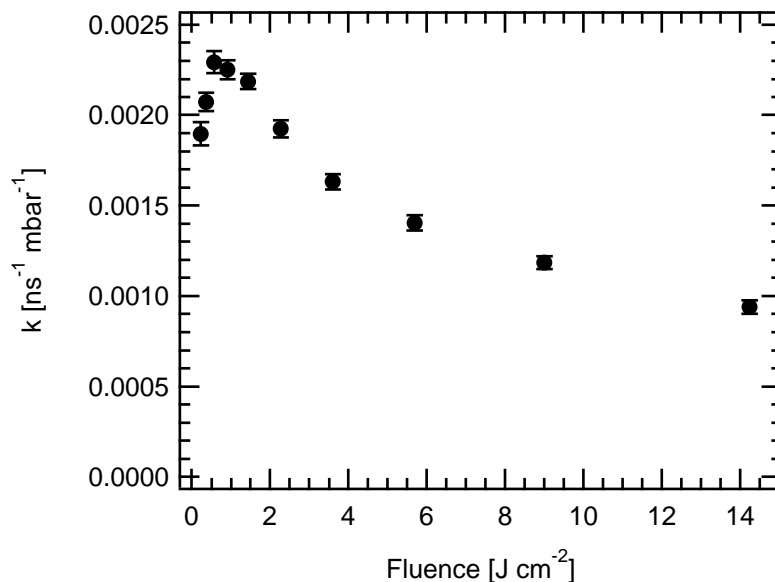


Figure D.1: Example of a measurement of k as a function of the fluence of the dissociation laser, for the $^{13}\text{CF}_3\text{H}$ isotopomer pre-excited via the 2_1 band, at a dissociation laser frequency of 1047 cm^{-1} , with 75% $^{13}\text{CF}_3\text{H}$ and 25% $^{12}\text{CF}_3\text{H}$ in the sample.

dissociation laser does not dissociate them efficiently any more. An “efficient” dissociation is defined with respect to the dissociation probability at the pre-excitation energy. It can be seen that the smallest energy window probed by the dissociation laser is not in the zero fluence limit, but at an intermediate fluence. In both the low and the high fluence limits the windows grow again. This is a consequence of how the dissociation probability changes with the vibrational excitation of the molecule.

It turns out, that in general this fluence lies around $1\text{-}2 \text{ J cm}^{-2}$.

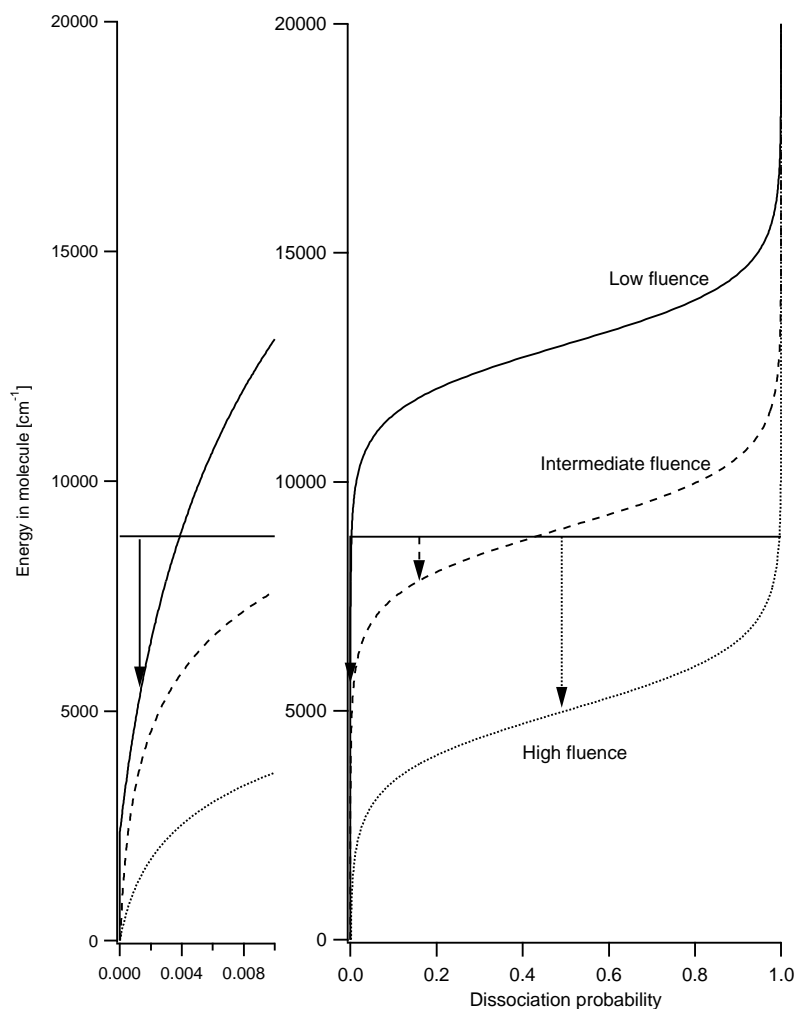


Figure D.2: Illustration of why k goes through a maximum as a function of the fluence of the dissociation laser (the curves on the left are the ones on the right enlarged). The three curves show qualitatively the dissociation probability of an excited molecule at a given vibrational energy for three different fluences. The arrows represent the energy a molecule has to lose in order to move out of the window of where they are still effectively dissociated compared to the initial dissociation probability at the pre-excitation energy.

Appendix E

The numerical codes for the calculation of IRMPD in the presence of collisions

E.1 Generalities

We show in figure E.1 the rough principle of our code. The code has been written in fortran 90.

A couple of input files are necessary for the code to work correctly:

1. A file `input.files.txt` containing the list of files with the description of a single experiment to calculate (we design one set of pre-excitation, dissociation and LIF lasers as “one experiment”).
2. The files designated in `input.files.txt`. These files contain all relevant information for the calculations such as the physical parameters (timing of lasers, fluence of CO₂ laser, sample pressure, etc).
3. A file `input.rho.txt` containing the density of states of CF₃H. This has been calculated by direct counting.
4. A file `input.rrkm.txt` containing the dissociation rates as calculated by the RRKM method. This has been calculated with a code from the group around

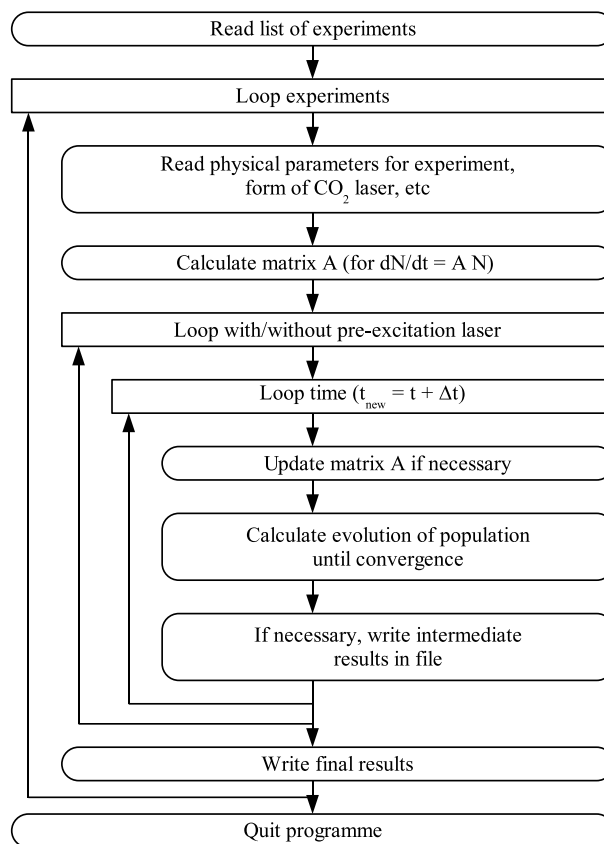


Figure E.1: Principle of our code

Martin Quack in Zurich.

5. A file `input.oelaser.txt` and a file `input.co2laser.txt` containing the forms of the pre-excitation and dissociation lasers. If the pre-excitation laser is a YAG pumped dye laser, the excitation step is quasi instantaneous; for this case an option for instantaneous excitation exists in the code.
6. A file `input.vvet.txt` containing the (relative) vibrational relaxation rates. They have been calculated with an other code performing the calculations described in section 5.2.

E.2 The code

See next page.


```

character (LEN=150) :: identifier
real :: f11, f12, f13, f14, f15, f16, f17 ! Values of physical parameters
real :: initialt, finalt
real :: photon_energy
real :: fluence
integer :: bins_per_photon
real :: level_excited
real :: fraction_excited1
real :: fraction_excited2
real :: pressure
integer :: bg_substr
integer :: instant_excitation

real :: timedelay1
real :: timedelay2
real :: E_max
real :: E_lim
real :: ratio_max
real :: deltaT_min
real :: deltaT_max
integer :: store_general
integer :: store_popindiv
integer :: print_deltaT
character (LEN=50) :: filename_rho
character (LEN=50) :: filename_rrkm
character (LEN=50) :: filename_co2laser
character (LEN=50) :: filename_oelaser
character (LEN=50) :: filename_vvnet
real :: wa
real :: wb
real :: E0a1
real :: E0a2
real :: E0b
real :: A0
real :: ibi
real :: amount_species2

! Identifier for experiment
! Timing
! Frequency of CO2 laser
! Fluence of CO2 laser
! Bins per photon
! Pre-excitation level
! Fraction of 12CF3H excited
! Fraction of 13CF3H excited
! Sample pressure
! 1 = automatic background subtraction
! otherwise = no
! 1 = YAG laser
! otherwise = take profile from
! filename_oelaser
! Time-delay between pre-excitation and
! CO2 lasers
! Time-delay between CO2 and LIF lasers
! Maximum vibrational energy considered
! Energy above which the dissociation rate
! is >> MPA
! Maximum error for calculation with
! Runge-Kutta
! Minimum time-step [not incorporated in
! the code]
! Maximum time-step
! 1 = store results
! 1 = store population.xxxx.txt
! Save results every ... ns in file
! Filename with density of states
! Filename with RRMK values
! Filename with form of CO2 laser
! Filename with form of pre-excitation
! laser
! Filename with vibrational relaxation
! rates
! (*)
! (*)
! (*)
! (*)
! (*)
! (*)
! (*)
! (*)
! Integrated band intensity (ground state)
! Amount of carbon-13 in the sample

! The absorption spectrum of an excited CF3H molecule with a vibrational energy E
! is:

```

$$\sigma(\nu) = (1+A0 \cdot E) \cdot \frac{\exp\left(-\sqrt{\omega - \nu_0}\right)}{\sqrt{\omega - \nu_0}}$$

```

! where
! \nu_0 = E0a + E0b \cdot E
! with
! E0a1 for carbon-12
! E0a2 for carbon-13
! If you have problems reading \LaTeX, refer to equation 5.7 in the thesis
! (and learn LaTeX !!)
! file 'rho.txt'
real, dimension (:), allocatable :: rho, rho0
integer, dimension (:), allocatable :: rho_count, rho0_count
integer :: rho_nlines, rho_nlines0
! file 'rrkm.txt'
real, dimension (:), allocatable :: rrkm
integer, dimension (:), allocatable :: rrkm_count
integer :: rrkm_nlines
! file 'vvnet.txt'
real, dimension (:), allocatable :: vvnet
integer, dimension (:), allocatable :: vvnet_count
integer :: vvnet_nlines
! file 'co2laser.txt'
real, dimension (:), allocatable :: co2laser
real :: co2laser_dt
integer :: co2laser_nlines
! file 'OELaser.txt'
real, dimension (:), allocatable :: oelaser
real :: oelaser_dt
integer :: oelaser_nlines
! General parameters calculated from input parameters
real :: dE_bin ! binwidth
integer :: n ! number of levels
real, dimension (:), allocatable :: absorb ! Absorption intensity in function
! of the pre-excitation energy

```

```

! *****
!
! BEGIN CODE
! *****
write (*,*) "*****"
write (*,*) "Running simulation *"
write (*,*) "*****"
write (*,*)

! *****
! Read input file
! *****
fileNumber = 0
open (16, file="input.files.txt", status="old")
do
    fileNumber = fileNumber + 1
    read (16,*) filenameinput
    if (trim(filenameinput) == "NOFILESLEFTOVER") exit
    write (*,*) "File : " // trim(filenameinput)

    open (10, file="inputfiles/" // trim(filenameinput), status="old")
! Identification
    read (10, *) fl1, fl2, fl3, fl4, fl5, fl6, fl7
    read (10, *) identifier
! Physical properties
    read (10, *) photon_energy
    read (10, *) fluence
    read (10, *) pressure
    read (10, *) amount_species2
    read (10, *) level_excited
    read (10, *) fraction_excited1
    read (10, *) fraction_excited2
    read (10, *) instant_excitation
! Background subtraction
    read (10, *) bg_subtr
! timing
    read (10, *) initial
    read (10, *) timedelay2
    read (10, *) timedelay1
! Absorption spectrum of excited state
! *****
! Matrices A1
real, dimension (:,:), allocatable :: a1_rkm, a1_up, a1_down, a1_coll
real, dimension (:,:), allocatable :: a1_downB, a1_downC, a1_downB_noirt
real, dimension (:,:), allocatable :: a1_downC_noirt, a1_down
real, dimension (:,:), allocatable :: a1_oe_noirt, a1_oe
real, dimension (:,:), allocatable :: a1_1, a1_2, a1_3, a1_4, a1_5
real :: co2laser_value, oelaser_value
real :: co2laser_value_store, oelaser_value_store

! Calculation of timeevolution
real, dimension (:,:), allocatable :: pop, pop1, pop2, pop3, pop4, newpop, poptot
real, dimension (:,:), allocatable :: pop_onestep, pop_twosteps, error_pop
integer :: co2laser_position, oelaser_position
real :: changes_matrix
real :: co2_intensity
real :: deltat
real :: ratio
integer :: lastprinttime
real :: time
integer :: oe_excitation_done
integer :: bg

! Dissociationprobability
real :: d12, d13

! *****
!
! INTERFACE FOR FUNCTIONS
! *****
interface
    function deriv (a1, pop)
        real, intent (in), dimension (:,:) :: pop
        real, intent (in), dimension (:,:) :: a1
        real, dimension (1:size(pop)) :: deriv
    end function deriv

    function intochar (i)
        integer, intent (in) :: i
        character (LEN=10) :: intochar
    end function intochar
end interface

```

```

read (10, *) wa
read (10, *) wb
read (10, *) E0a1
read (10, *) E0a2
read (10, *) E0b
read (10, *) A0
read (10, *) ibi
! Numerical details
read (10, *) ratio_max
read (10, *) deltaT_min
read (10, *) deltaT_max
read (10, *) E_max
read (10, *) E_lim
read (10, *) bins_per_photon
! output in file
read (10, *) store_general
read (10, *) store_popindiv
read (10, *) print_deltaT
close (10)
if (bg_subtr /= 1) bg_subtr = 0
filename_rho = "input_rho.txt"
filename_rrkm = "input_rrkm.txt"
filename_co2laser = "input_co2laser.txt"
filename_olaser = "input_olaser.txt"
filename_vvet = "input_vvet.txt"
! *****
!
! CALCULATE PARAMETERS NECESSARY FOR THE SIMULATIONS, AND LOAD EXTERNAL FILES
! *****
dE_bin = photon_energy / bins_per_photon
n = int (E_max/dE_bin) + 1
finalt = timedelay1 + timedelay2
allocate (rho (0:2*n-1))
allocate (rho0 (0:2*n-1))
allocate (rho_count (0:2*n-1))
allocate (rrkm (0:2*n-1))
allocate (rrkm_count (0:2*n-1))
allocate (vvet (0:2*n-1))
allocate (vvet_count (0:2*n-1))
allocate (absorb (0:2*n-1))

rho = 0.
rho0 = 0.
rho_count = 0
rrkm = 0.
rrkm_count = 0
vvet = 0.
vvet_count = 0
absorb = 0.

! Density of states
open (10, file=trim(filename_rho), status="old")
read (10, *) tmp_char
read (10, *) tmp_char
read (10, *) tmp_char
read (10, *) rho_nlines
do i=1, rho_nlines
read (10, *) energy, value
energy = energy * 1000
bin = int(energy/dE_bin)
if (bin < n) then
rho (bin) = rho (bin) + 10**value
rho_count (bin) = rho_count (bin) + 1
endif
enddo

read (10, *) rho_nlines0
do i=1, rho_nlines0
energy = energy * 1000
bin = int(energy/dE_bin)
if (bin < n) then
rho0 (bin) = rho0 (bin) + 10**value
rho0_count (bin) = rho0_count (bin) + 1
endif
enddo

close (10)
where (rho_count /= 0) rho = rho / rho_count
where (rho0_count /= 0) rho0 = rho0 / rho0_count
deallocate (rho_count)
deallocate (rho0_count)

```

```

! Calculate relative absorption strengths
do i=0, n-1
  energy = (i+0.5)*dE_bin
  abscentre = E0a1 + E0b * energy
  abswidth = sqrt (wa**2 + (wb * energy)**2)
  absint = (1 + a0 * energy)
  absorb (i) = absint * exp ( - ((( photon_energy - abscentre ) / abswidth )**2)) &
    / (abswidth*sqrt(3.1415))
! Absorption by 2nu6
  abscentre = 1024.1 - 0.0039206 * energy
  abswidth = sqrt (wa**2 + (wb * energy)**2)
  absint = (5.0253e-5 * energy + 3.8577e-9 * energy * energy) / 0.0282095
  absorb (i) = absorb (i) + &
    2.75e-4*absint * exp ( - ((( photon_energy - abscentre ) / abswidth )**2)) &
    / (abswidth*sqrt(3.1415))
enddo
do i=n, 2*n-1
  energy = ((i-n)+0.5)*dE_bin
  abscentre = E0a2 +E0b * energy
  abswidth = sqrt (wa**2 + (wb * energy)**2)
  absint = (1 + a0 * energy)
  absorb (i) = absint * exp ( - ((( photon_energy - abscentre ) / abswidth )**2)) &
    / (abswidth*sqrt(3.1415))
! Absorption by 2nu6
  abscentre = 1024.1 - 0.0039206 * energy
  abswidth = sqrt (wa**2 + (wb * energy)**2)
  absint = (5.0253e-5 * energy + 3.8577e-9 * energy * energy) / 0.0282095
  absorb (i) = absorb (i) + &
    2.75e-4*absint * exp ( - ((( photon_energy - abscentre ) / abswidth )**2)) &
    / (abswidth*sqrt(3.1415))
enddo
! Read CD2 laser profile
open (10, file=trim(filename_co2laser), status="old")
read (10, *) co2laser_nlines, co2laser_dt
allocate (co2laser (0:co2laser_nlines-1))
rho (n:2*n-1) = rho (0:n-1)
rho0 (n:2*n-1) = rho0 (0:n-1)
! RKM dissociation
open (10, file=trim(filename_rrkm), status="old")
read (10, *) rrkm_nlines
do i=1, rrkm_nlines
  read (10, *) energy, value
  bin = int(energy/dE_bin)
  if (bin < n) then
    rrkm (bin) = rrkm (bin) + value
    rrkm_count (bin) = rrkm_count (bin) + 1
  endif
enddo
close (10)
where (rrkm_count /= 0) rrkm = rrkm / rrkm_count
rrkm = rrkm / 10E9
deallocate (rrkm_count)
rrkm (n:2*n-1) = rrkm (0:n-1)
! V-V energy transfer
open (10, file=trim(filename_vvet), status="old")
read (10, *) vvet_nlines
do i=1, vvet_nlines
  read (10, *) energy, value12, value13
  bin = int(energy/dE_bin)
  if (bin < n) then
    vvet (bin) = vvet (bin) + value12
    vvet (bin+n) = vvet (bin+n) + value13
    vvet_count (bin) = vvet_count (bin) + 1
    vvet_count (bin+n) = vvet_count (bin+n) + 1
  endif
enddo
close (10)
where (vvet_count /= 0) vvet = vvet / vvet_count
vvet = vvet * 1e-3
deallocate (vvet_count)

```

```

do i = 0, co2laser_nlines-1
  read (10, *) tmp_real, co2laser (i)
enddo
co2laser = co2laser / sum (co2laser)
close (10)

! Read pre-excitation laser profile (for PAL laser)
open (10, file=trim(filename_oelaser), status="old")
read (10, *) oelaser_nlines, oelaser_dt
allocate (oelaser (0:oelaser_nlines-1))
do i = 0, oelaser_nlines-1
  read (10, *) tmp_real, oelaser (i)
enddo
oelaser = oelaser / sum (oelaser)
close (10)

! *****
! Calculate Matrices
! *****
allocate (A1_rrkm (0:2*n-1,0:2*n-1))
allocate (A1_downB_point (0:2*n-1,0:2*n-1))
allocate (A1_downC_point (0:2*n-1,0:2*n-1))
allocate (a1_oe_point (0:2*n-1,0:2*n-1))
allocate (a1_coll (0:2*n-1,0:2*n-1))

A1_rrkm = 0.
A1_up_point = 0.
A1_downB_point = 0.
A1_downC_point = 0.
a1_oe_point = 0.
a1_coll = 0.

! Pre-excitation matrix
a1_oe_point(int(level_excited/dE_bin),0) = fraction_excited1
a1_oe_point(0,0) = - a1_oe_point(int(level_excited/dE_bin),0)

do i = 0, co2laser_nlines-1
  read (10, *) tmp_real, co2laser (i)
enddo
co2laser = co2laser / sum (co2laser)
close (10)

! Read pre-excitation laser profile (for PAL laser)
open (10, file=trim(filename_oelaser), status="old")
read (10, *) oelaser_nlines, oelaser_dt
allocate (oelaser (0:oelaser_nlines-1))
do i = 0, oelaser_nlines-1
  read (10, *) tmp_real, oelaser (i)
enddo
oelaser = oelaser / sum (oelaser)
close (10)

! *****
! Calculate Matrices
! *****
allocate (A1_rrkm (0:2*n-1,0:2*n-1))
allocate (A1_downB_point (0:2*n-1,0:2*n-1))
allocate (A1_downC_point (0:2*n-1,0:2*n-1))
allocate (a1_oe_point (0:2*n-1,0:2*n-1))
allocate (a1_coll (0:2*n-1,0:2*n-1))

A1_rrkm = 0.
A1_up_point = 0.
A1_downB_point = 0.
A1_downC_point = 0.
a1_oe_point = 0.
a1_coll = 0.

! Pre-excitation matrix
a1_oe_point(int(level_excited/dE_bin),0) = fraction_excited1
a1_oe_point(0,0) = - a1_oe_point(int(level_excited/dE_bin),0)

do i=0, n-1
  a1_rrkm(i,i) = - rrrkm (i)
  a1_rrkm(i+n,i+n) = - rrrkm (i)
enddo

! RRKM matrix
if (instant_excitation == 1) a1_oe_point = 0.

a1_oe_point(n*int(level_excited/dE_bin),n) = fraction_excited2
a1_oe_point(n,n) = - a1_oe_point(n*int(level_excited/dE_bin),n)

if (instant_excitation == 1) a1_oe_point = 0.

! RRKM matrix
do i=0, n-1
  a1_rrkm(i,i) = - rrrkm (i)
  a1_rrkm(i+n,i+n) = - rrrkm (i)
enddo

! Upumping matrix
do i=0, 2*n-1
  if (rho (i) /= 0.) then
    a1_up_point(i,i) = - 1.511 * ibi * absorb (i) * rho0 (i) / rho (i)
    if (i<n-i-bins_per_photon) &
      a1_up_point(i+bins_per_photon,i) = - a1_up_point(i,i)
    if (i<2*n-1-bins_per_photon .and. (i>n)) &
      a1_up_point(i+bins_per_photon,i) = - a1_up_point(i,i)
    endif
  endif
enddo

! Downpumping matrix case B (high density of states)
do i=bins_per_photon, 2*n-1
  if (rho(i)/=0.) then
    if (i<n-1 .or. (i>n+bins_per_photon)) then
      A1_downB_point(i,i) = - 1.511 * ibi * rho0 (i-bins_per_photon) &
        * absorb (i-bins_per_photon) / rho (i)
      A1_downB_point(i-bins_per_photon,i) = - A1_downB_point(i,i)
    endif
  endif
enddo

! Downpumping matrix case C (low density of states)
do i=bins_per_photon, 2*n-1
  if ((rho (i-bins_per_photon)/=0.) .and. (rho(i)/=0.) .and. &
    (rho0(i-bins_per_photon)/=0.)) then
    if (i<n-1 .or. (i>n+bins_per_photon)) then
      A1_downC_point(i,i) = - (2./ (3.141592 * (3**0.5))) * &
        ( 1.511 * ibi * absorb (i-bins_per_photon) &
          * rho0 (i-bins_per_photon) * rho (i-bins_per_photon) / &
            (rho (i)**3) )**0.5
    endif
  endif
enddo

```

```

A1_downC_noint(i-bins_per_photon,i) = - A1_downC_noint(i,i)
endif
endif
enddo
! V-V Energy transfer
do i=bins_per_photon, 2*n-1
  if ((i<n-1).or.(i>n+bins_per_photon)) then
    ! Assume large majority of molecules in gs
    A1_coll(i,i) = - vvet(i) * pressure
    A1_coll(i-bins_per_photon,i) = - A1_coll(i,i)
    a1_coll(0,i) = a1_coll(0,i) + A1_coll(i,i)
    ! Assume large majority of molecules C12
    a1_coll(bins_per_photon,i) = a1_coll(bins_per_photon,i) - A1_coll(i,i)
  endif
enddo
! *****
! Perform calculations
! *****
! Initialise variables
allocate (pop (0:2*n-1))
allocate (newpop (0:2*n-1))
allocate (pop1 (0:2*n-1))
allocate (pop2 (0:2*n-1))
allocate (pop3 (0:2*n-1))
allocate (pop4 (0:2*n-1))
allocate (poponestep (0:2*n-1))
allocate (pop_twosteps (0:2*n-1))
allocate (error_pop (0:2*n-1))
allocate (a1_1 (0:2*n-1,0:2*n-1))
allocate (a1_2 (0:2*n-1,0:2*n-1))
allocate (a1_3 (0:2*n-1,0:2*n-1))
allocate (a1_4 (0:2*n-1,0:2*n-1))
allocate (a1_5 (0:2*n-1,0:2*n-1))
allocate (a1_up (0:2*n-1,0:2*n-1))
! *****
! *****
! *****
allocate (a1_downB (0:2*n-1,0:2*n-1))
allocate (a1_downC (0:2*n-1,0:2*n-1))
allocate (a1_down (0:2*n-1,0:2*n-1))
allocate (a1_oe (0:2*n-1,0:2*n-1))
allocate (poprot (0:2*n-1))
! *****
! *****
! Loop: with/without pre-excitation laser
! *****
do bg=0, bg_subtr
  if (bg=1) then
    fraction_excited1 = 0.
    fraction_excited2 = 0.
    a1_oe_noint = 0.
  endif
! *****
! Initialisations
! *****
pop = 0.
pop(0) = 1.-amount_species2
pop(n) = amount_species2
time = initialt
lastprinttime = int((time-initialt) / print_delta) - 1
delta = 1.
oe_excitation_done = 0
if (store_general == 1) then
  if (bg == 0) then
    open(20, file="results/p." // trim(identifier) // ".txt")
  else
    open(20, file="results/p.bg." // trim(identifier) // ".txt")
  endif
endif
! *****
! *****
! Loop: time evolution
! *****

```

```

do
    if (abs (A1_downC (k*n+j,k*n+j)) > abs (A1_downB (k*n+j,k*n+j))) &
        then
        A1_down (k*n+j,k*n+j) = A1_downC (k*n+j,k*n+j)
        A1_down (k*n+j-bins_per_photon,k*n+j) = &
            A1_downC (k*n+j-bins_per_photon,k*n+j)
        if (pop (k*n+j) > pop (k*n+j-bins_per_photon)) then
            ! Generalisation case C
            tmprate = A1_up (k*n+j-bins_per_photon,k*n+j-bins_per_photon)
            A1_up (k*n+j-bins_per_photon,k*n+j-bins_per_photon) = &
                A1_down (k*n+j,k*n+j)
            A1_down (k*n+j,k*n+j) = tmprate
            tmprate = A1_up (k*n+j,k*n+j-bins_per_photon)
            A1_up (k*n+j,k*n+j-bins_per_photon) = &
                A1_down (k*n+j-bins_per_photon,k*n+j)
            A1_down (k*n+j-bins_per_photon,k*n+j) = tmprate
        endif
    endif
enddo

al_oe = al_oe_noint * oelaser_value / oelaser_dt
if (i==1) al_1 = al_oe + al_up + al_down + al_rrkm + al_coll
if (i==2) al_2 = al_oe + al_up + al_down + al_rrkm + al_coll
if (i==3) al_3 = al_oe + al_up + al_down + al_rrkm + al_coll
if (i==4) al_4 = al_oe + al_up + al_down + al_rrkm + al_coll
if (i==6) al_5 = al_oe + al_up + al_down + al_rrkm + al_coll
enddo

! Do calculation RUNGE-KUTTA
pop1 = deltat * deriv (al_1, pop)
pop2 = deltat * deriv (al_3, pop+0.5*pop1)
pop3 = deltat * deriv (al_3, pop+0.5*pop2)
pop4 = deltat * deriv (al_5, pop+pop3)
pop_onestep = pop + (pop1 + 2.*(pop2+pop3) + pop4) / 6.
pop1 = pop1 / 2.
pop2 = deltat * deriv (al_2,pop+0.5*pop1) / 2.
pop3 = deltat * deriv (al_2,pop+0.5*pop2) / 2.
pop4 = deltat * deriv (al_3,pop+pop3) / 2.
pop_twosteps = pop + (pop1 + 2.*(pop2+pop3) + pop4) / 6.
pop1 = deltat * deriv (al_3,pop_twosteps) / 2.

do i=1, 5
    co2laser_position = (time+(i-1)*deltat/4.)-timedelay1 / co2laser_dt
    oelaser_position = (time+(i-1)*deltat/4.) / oelaser_dt
    if ((co2laser_position>0.) .and. &
        (co2laser_position<1.*(co2laser_nlines-1))) &
        then
        co2laser_value = (co2laser_position - 1.*int (co2laser_position)) &
            * co2laser (int(co2laser_position)+1) + (1. + &
            1.*int(co2laser_position) - co2laser_position) * &
            co2laser(int(co2laser_position))
        else
        co2laser_value = 0.
        endif
    if ((oelaser_position>0.) .and. (oelaser_position<1.*(oelaser_nlines-1))) &
        then
        changes_matrix = 1
        oelaser_value = (oelaser_position - 1.*int (oelaser_position)) &
            * oelaser (int(oelaser_position)+1) + (1. + &
            1.*int(oelaser_position) - oelaser_position) * &
            oelaser(int(oelaser_position))
        else
        oelaser_value = 0.
        endif
    if (i==3) then
        co2laser_value_store = co2laser_value
        oelaser_value_store = oelaser_value
        co2_intensity = fluence * co2laser_value / (co2laser_dt*1E-9*1E6) !Check
        al_up = al_up_noint * co2_intensity
        al_downB = al_downB_noint * co2_intensity
        al_downC = al_downC_noint * sqrt(co2_intensity)
        al_down = al_downB
    do j=0, n-1
        do k=0,1

```



```

pop2 = deltat * deriv (a1_4*pop_twosteps+0.5*pop1)/2.
pop3 = deltat * deriv (a1_4*pop_twosteps+0.5*pop2)/2.
pop4 = deltat * deriv (a1_5*pop_twosteps+pop3) / 2.
pop_twosteps = pop_twosteps + (pop1 + 2.*(pop2+pop3) + pop4) / 6.

! The following step is not a strictly correct thing to do, but necessary
! It turns out that for high Energies, where RRKM values >> other values
! (IR pumping, collisions) the timesteps chosen by the code are too large
! to get consistent results. (i.e. timesteps in the ns region give
! apparently values which are within the error region defined - in fact
! the values for N_i grow for high E instead of decreasing). Correctly one
! should advance with much smaller time steps (e.g. 0.001 ns), but this
! would considerably increase the time for the calculations.
! We chose a more pragmatic approach: by defining a certain value e_lim
! for which we consider the unimolecular dissociation to be >> than any
! other process, we will simply say that every molecule with E > e_lim
! will have no chance whatsoever to get down to the g.s. Hence all values
! for pop with E > e_lim will be set to 0.
! The value e_lim has to be carefully chosen by hand.

do i=int (E_lim/dE_bin)+1, n-1
  pop_onestep (i) = 0.
  pop_twosteps (i) = 0.
  pop_onestep (i+n) = 0.
  pop_twosteps (i+n) = 0.
enddo

error_pop = (pop_onestep - pop_twosteps)
ratio = maxval (abs(error_pop))

if (ratio /= 0.) then
  deltat = deltat * (ratio_max / ratio)**0.2
else
  deltat = deltat_max
endif

if (deltat > deltat_max) deltat = deltat_max

if (ratio <= 1.1*ratio_max) exit
enddo

pop = pop_twosteps

where (pop < 0.) pop = 0. ! RRKM rates may be very fast, and they have not
! been taken into account when evaluating the
! timestep delta t.

```

```

if (time >= 0).and.(instant_excitation == 1).and. &
  (oe_excitation_done == 0)) then
  oe_excitation_done = 1
  pop (int(level_excited/dE_bin)) = pop (int(level_excited/dE_bin)) &
    + fraction_excited1*pop (0)
  pop (0) = (1-fraction_excited1)* pop (0)
  pop (n+int(level_excited/dE_bin)) = pop (n+int(level_excited/dE_bin)) &
    + fraction_excited2*pop (n)
  pop (n) = (1-fraction_excited2)* pop (n)
endif

! Write results
if (store_general == 1) then
  write (20,'(5s15.5)') time+deltat/2., &
    1.-(sum(pop(0:n-1))/(1.-amount_species2)), &
    1.-(sum(pop(n:2*n-1))/amount_species2), &
    co2_intensity, oelaser_value_store
endif

if (store_popindiv == 1) then
  if (lastprinttime /= int ((time-initial) / print_deltat)) then
    lastprinttime = int ((time-initial) / print_deltat)

    if (store_general == 1) then
      if (bg == 0) then
        open (21, file="results/p." // trim(identifier) // ". " // &
          trim(introchar (int(time+deltat/2)-initial))) // ".txt")
      else
        open (21, file="results/p.bg." // trim(identifier) // ". " // &
          trim(introchar (int(time+deltat/2)-initial))) // ".txt")
      endif
    endif
  endif
  do i=0, n-1
    write (21, '(f15.5,2e14.5)') &
      i*dE_bin, pop(i)/(1.-amount_species2), pop(i+n)/amount_species2
  enddo
  close (21)
endif
endif

time = time + deltat
if (time >= finalt) exit

```

```

enddo
if (store_general == 1) close (Z0)
if (bg==0) poptot = pop
enddo
! *****
! Write final results
! *****
if (bg_subtr=0) then
  d12 = 1.-(sum(pop(0:n-1))/(1.-amount_species2))
  d13 = 1.-(sum(pop(n:2*n-1))/amount_species2)
else
  d12 = (sum(pop(0:n-1))-sum(poptot(0:n-1)))/(1.-amount_species2)
  d13 = (sum(pop(n:2*n-1))-sum(poptot(n:2*n-1)))/amount_species2
endif

if (filenumber == 1) then
  open (Z0, file="results/d.all.txt")
else
  open (Z0, file="results/d.all.txt", position="append")
endif

write (Z0,*) f11, f12, f13, f14, f15, f16, f17, d12, d13
close (Z0)
! *****
! END
! *****
deallocate (rho)
deallocate (rho0)
deallocate (rrkm)
deallocate (absorb)
deallocate (co2laser)
deallocate (A1_rrkm)
deallocate (A1_up_noimt)
deallocate (A1_downB_noimt)
deallocate (A1_downC_noimt)
deallocate (pop)

deallocate (A1_up)
deallocate (A1_downB)
deallocate (A1_downC)
deallocate (A1_down)
deallocate (oe_laser)
deallocate (a1_oe_noimt)
deallocate (newpop)
deallocate (pop1)
deallocate (pop2)
deallocate (pop3)
deallocate (pop4)
deallocate (pop_onestep)
deallocate (pop_twosteps)
deallocate (error_pop)
deallocate (a1_1, a1_2, a1_3, a1_4, a1_5)
deallocate (a1_oe)
deallocate (vvet)
deallocate (a1_coll)
deallocate (poptot)

enddo

close (16)

end program IRLAPS
! *****
! FUNCTIONS
! *****
function deriv (a1,pop)
  implicit none
  real, intent (in), dimension (:) :: pop
  real, intent (in), dimension (:,:) :: a1
  real, dimension (1:size(pop)) :: deriv
  integer :: n
  n=size(pop)
  deriv = matmul (a1, pop)
end function deriv
function intochar (i)
  integer, intent(in) :: i
  integer :: i_part

```

```

character :: i_part_char
character (LEN=10) :: intochar, intocharp
integer :: j, dim, ip

ip = i
if (i > 0) then
    dim = i+int(log10(ip*1.0))
    intocharp = ""
    do j=1, 4-dim
        intocharp = trim(intocharp) // "0"
    enddo
    do j=1, dim
        i_part = int(ip/(10**(dim-j)))
        ip = int(ip - (10**(dim-j))*i_part)
        select case (i_part)
            case (1)
                i_part_char = "1"
            case (2)
                i_part_char = "2"
            case (3)
                i_part_char = "3"
            case (4)
                i_part_char = "4"
            case (5)
                i_part_char = "5"
            case (6)
                i_part_char = "6"
            case (7)
                i_part_char = "7"
            case (8)
                i_part_char = "8"
            case (9)
                i_part_char = "9"
            case (0)
                i_part_char = "0"
        end select
        intocharp = trim(inttocharp) // i_part_char
    enddo
    else
        intocharp = "0000"
    endif
    intochar = intocharp
end function intochar

```


Notations, constants and abbreviations

Notations and constants		
\vec{d}	Dipole moment	Eq. 5.22
d_{hs}	Hard sphere diameter	Eq. 2.47
f	Fraction of $^{13}\text{CF}_3\text{H}$ in sample	Section 4.5.2
f_1	Amount of transmitted light by optical system, for dissociation laser	Eq. C.2, fig. C.2
f_2	Amount of pulse used for the dissociation of molecules	Eq. C.2, fig. C.3
$g_{tt'}$	Anharmonicity constants	Eq. 2.2, table 2.3
g_i	Degeneracy of a vibrational mode i	Eq. 5.8
h	Planck constant	$\sim 6.626 \cdot 10^{-34}$ J s
k	Decay rate	
\bar{k}	$k \cdot p$	
${}^x k$	Pumping rates for calculations due to x	Section 5.3.2
k_B	Boltzmann constant	$\sim 1.380 \cdot 10^{-23}$ J K $^{-1}$
n	Amount of teflon sheets used	Eq. C.1
$\langle n \rangle$	Average occupation number in a mode	Eq. 5.8
p	Pressure	

Continued on next page

Notations and constants		
p	Change of bins per absorbed / emitted photon (calculations)	Section 5.3.1
p_I	Population of grained level I	Table 2.11
q	Quenching constant	Eq. B.1
q	Vibrational coordinate operator	
q_6	Interaction constant	Eq. 5.11
r	Distance between molecules	Eq. 2.34
r_0	Radius of dissociation laser in focal point	Eq. C.2, fig. C.5
r_0	Impact parameter in collisions (closest distance)	Eq. 2.38
r_c	See definition \rightarrow	Eq. 2.42
r_{hs}	Hard sphere radius	Eq. 2.42
s	Number of oscillators in a molecule	Eq. 5.8
s'	Number of independent oscillators in a molecule	Eq. 5.8
Δt	Time-delay between pre-excitation and dissociation lasers ($\Delta t_{PE-IRMPD}$) and dissociation and LIF lasers ($\Delta t_{IRMPD-LIF}$)	
v	Relative velocity of two molecules	Eq. 2.30
v	Set of vibrational quantum numbers (v_1, v_2, \dots, v_6)	Page 23
v_x	Quantum number in mode x	
x_{ij}	Anharmonicity constants	Eq. 2.2, table 2.3
x, y	See definition \rightarrow	Fig. 2.11
A	Increase of integral absorption strength upon excitation of molecule	Eq. 5.36
A_{KJ}	Hönl-London factors	Eq. 5.13
A_p	Integral absorption strength of absorption spectrum of an excited molecule	Eq. 5.7

Continued on next page

Notations and constants

A_1, A_2	Matrices for master equation calculations	Eq. 5.47
B	Rotational constant	Eq. 2.13
C	Rotational constant	Eq. 2.13
D	Dissociation probability	
D	Off-resonance shift for photon absorption	Page 238
E	Enhancement of selectivity	Eq. 1.2
E	Energy	
ΔE	Width of a bin for the calculations	Section 5.3.1
E_d	Cut-off level over which dissociation is complete	Page 199
E^{TS}	Energy of the transition state	Section 5.3.3.C
\vec{E}	Electrical field	Eq. 2.20
F	Rotational energy	Eq. 2.13
F_X	Rovibrational absorption spectrum of molecule X	Eq. 2.46
F	See definition \rightarrow	Section A.2, eq. A.5
G	See definition \rightarrow	Section A.2, eq. A.5
G	Integrated band intensity	Eq. 2.1
H	Molecular Hamiltonian	Eq. 2.19
I	Intensity of dissociation laser	Eq. 2.27, eq. 5.54
J	Rotational quantum number	Eq. 2.13
K	Rotational quantum number	Eq. 2.13
$K_{I,J}$	Transition rate from level I to level J	Table 2.11
K_p	Relaxation rate in collisional quenching	Eq. B.1
M	Rotational quantum number	Page 167
$P(E, E')$	Energy transfer probability from $E' \rightarrow E$	Page 61

Continued on next page

Notations and constants		
P	Probability that a head-on collision results in energy transfer	Page 182
P_{if}	Transition probability	Eq. 2.30
P	Number of pre-excited molecules	Eq. 4.3
Q	Set of vibrational coordinate operators	
R	Scaling factor for collisional relaxation	Section 5.3.3.B
R_c	Impact parameter of collision	Fig. 5.5
R_0	Cut-off distance between two molecules, where dipole-dipole interaction stop prevailing	Page 167
R_{AB}	Distance between two molecules	Eq. 2.46
S	Dissociation selectivity	Eq. 1.1
S_{IRMPD}	Dissociation selectivity due to isotopically selective IRMPD	Section 5.3.4.C
S_{VET}	Dissociation selectivity due to isotopically selective collisional relaxation	Section 5.3.4.C
T	Temperature	
V	Coupling between levels	Table 2.11
V_d	Interaction energy due to dipole-dipole interactions	Eq. 5.22
W	Average coupling between two states	
W	Transition rate	Eq. 5.17
W	Coupling between states	Page 36
W_f	Interaction constant	Eq. 5.11
Y	Dissociation yield	
Z_{hs}	Hard sphere collision rate	Eq. 2.47
α	See definition \rightarrow	Eq. 2.14
α	See definition \rightarrow	Eq. 2.51
δ_I	Spacing between individual levels in grained level I	Table 2.11

Continued on next page

Notations and constants

δ_i^p	Kronecker symbol	
δ	Width of a gaussian	
δ	Density of effectively coupled states	Page 240
η	Transmission of LIF signal through the detection system	Page 108
ϵ	Dissociation efficiency (rotational relaxation)	Eq. 3.3
ε	Absorption coefficient of teflon	Eq. C.1, fig. C.1
ε_0	Permittivity of free space	$\sim 8.85 \cdot 10^{-12}$ $\text{C}^2 \text{N}^{-1} \text{m}^{-2}$
κ	relaxation rate	
$\bar{\kappa}$	$\kappa \cdot p$	
ω	Energy of a photon	Table 2.11
ω	Width of absorption spectrum	
ω	Fundamental frequencies	Eq. 2.2, table 2.3
ω^{TS}	Vibrational frequencies at the transition state	Table 5.2
μ	Reduced mass	Eq. 2.30
μ	Transition dipole moment ($ \langle 1 \vec{d} 2 \rangle $)	Pages 21 and 60
ν	Frequency of a laser	
ν_x	Vibrational mode x	
ν_p	Pumped vibration	
ν_0	Band origin	
$\delta\nu_p$	Width of absorption feature of an excited molecule	Eq. 5.7
$\Delta\nu_p$	Shift of absorption feature of an excited molecule	Eq. 5.7
$\Delta\nu$	Linewidth of a laser	Page 36

Continued on next page

Notations and constants		
$\Delta\nu$	Splitting of vibrational states	Section 2.1.2.B
ν_0	band origin	Eq. 2.2
ϕ	Orientation in space	Eq. 2.34
ρ	Density of states	
ρ'	Density of states without the one absorbing IR photons	Section 2.2.3.B
ϱ	Completeness of rotational relaxation	Eq. 3.2
$\sigma_E(\nu)$	Absorption spectrum of an excited molecule at an energy E	Eq. 5.7
σ	Transition strength	Eq. 5.5, eq. 5.58
τ_{IVR}	Time-scale for IVR	Section 2.1.2.A
τ_0	Time for spontaneous emission of excited molecule	Eq. B.1
τ_d	Time for the molecule to reach the dissociation limit	Eq. 1.5
θ	Orientation in space	Eq. 2.34
ξ	Interaction constant	Eq. 5.11
Δ_I	Width of grained level I	Table 2.11
Δ	Adjustable coupling width for IR absorption/emission (calculations)	Section 2.2.3.B
Γ	Transition rate	
Ω	Generalised Rabi Oscillation frequency	Page 238
Φ	Fluence of dissociation laser	Eq. C.2
\hbar	$h / 2\pi$	
\mathcal{A}_r	Ground state rovibrational absorption spectrum	Eq. 5.18
\mathcal{C}	Weighted average over J and K of \mathcal{C}_{JK}	
\mathcal{C}_{JK}	See definition \rightarrow	Eq. 5.27

Continued on next page

Notations and constants

\mathcal{E}_r	Excited state rovibrational emission spectrum	Eq. 5.18
\mathcal{E}	Excited state SIB emission spectrum	Eq. 5.18
\mathcal{I}	Importance of a mechanisms for isotopic selectivity	Eq. 4.10
\mathcal{N}	Vector of populations	Eq. 5.40
\mathcal{P}	Probability that a molecule has not relaxed	Eq. 5.29
\mathcal{R}_{12}	See definition \rightarrow	Eq. 4.13
\mathcal{R}_{13}	See definition \rightarrow	Eq. 4.13
\mathcal{R}_E	See definition \rightarrow	Eq. 4.15
\mathcal{S}	Decay selectivity	Page 108
\mathcal{S}_{IRMPD}	Decay selectivity due to isotopically selective IRMPD	Eq. 4.9
\mathcal{S}_{VET}	Decay selectivity due to isotopically selective collisional relaxations	Eq. 4.8

Abbreviations

ADC	Analog to digital converter
BRW	Biased random walk
CAMAC	Computer automated measurement and control
CET	Collisional energy transfer
CRISLA	Chemical reaction by isotope selective laser activation
CVET	Collisional vibrational energy transfer
CI-IVR	Collisionally induced IVR
DFM	Difference frequency mixing
DOS	Density of states
E.T.	Energy Transfer
EPFL	École polytechnique fédérale de Lausanne
FGR	Fermi Golden Rule

Continued on next page

Abbreviations

FTIR	Fourier Transform Infrared Spectroscopy
IC	Internal conversion
IP	Ionisation potential
IRF	Infrared Fluorescence
IRLAPS	Infrared laser assisted photofragment spectroscopy
IRMPA	Infrared multiple photon absorption
IRMPE	Infrared multiple photon excitation
IRMPD	Infrared multiple photon dissociation
IVR	Intramolecular vibrational energy redistribution
KCSI	Kinetically controlled Selective Ionisation
LCPM	Laboratoire de chimie physique moléculaire
LIF	Laser induced fluorescence
LIS	Laser isotope separation
MLIS	Molecular laser isotope separation
MPA	Multiple photon absorption
MPD	Multiple photon dissociation
OPA	Optical parametric amplification
OP-IRMPD	Overtone Pre-excitation - Infrared Multiple Photon Dissociation
PA	Photo-acoustic
PAL	Pulsed alexandrite laser
P-E	Pre-excitation
PES	Potential energy surface
PMT	Photo multiplier tube
PST	Phase space theory
QMS	Quadrupole mass spectrometer
RRK	Rice-Ramsperger-Kassel
RRKM	RRK-Marcus
RS	Raman shifter
RS	Raman scattering
SACM	Statistical adiabatic channel model
SHG	Second harmonic generation

Continued on next page

Abbreviations

SIB	Statistical inhomogeneous broadening
SEP	Stimulated emission pumping
SSH	Schwartz, Slawsky and Herzfeld
TDL	Tunable diode laser absorption
TEA	Transversely Excited Atmospheric
TDTL	Time dependent thermal lensing
TRIRDR	Time-resolved infrared double-resonance
UBT	Urea breath test
UVA	Ultraviolet absorption
VET	Vibrational energy transfer
WFQA	Weak field quasi-resonant approximation

List of Tables

2.1	Normal modes and symmetry in $^{12}\text{CF}_3\text{H}$ and $^{13}\text{CF}_3\text{H}$	20
2.2	Transition dipole moment between the ground state and the fundamentals.	21
2.3	Anharmonic constants for CF_3H	24
2.4	Constants for the CH chromophore in CF_3H	28
2.5	Band origins of the members of the polyads created by $ N\nu_1\rangle$, $ (N - 1)\nu_1 + 2\nu_4\rangle$, . . . $ 2N\nu_4\rangle$	29
2.6	Values of $c_{N,J}^i$	30
2.7	Integrated band strengths G	31
2.8	$\alpha_i \cdot 10^3$ for B and C for CF_3H	33
2.9	Tiers of states in CF_3H	37
2.10	“Slow” IVR in CF_3H	39
2.11	Notation used for the statistical treatment.	46
2.12	Pumping rates for the different cases A-D.	47
2.13	Three approaches how to deal with the problem of the divergence of $P(r_0, v)$	59
2.14	Dependence of σ on the relative velocity of the two molecules and of $\langle\langle P \rangle\rangle$ on the temperature T , for the different models.	59
4.1	Four schemes for the investigation of the mechanisms of the enhancement of isotopic selectivity varying different parameters.	107
4.2	Decay rates for molecules excited via the 5_2 vibrational mode with molecules excited via another (unidentified) band	113
4.3	Relative contributions of isotopically selective collisional relaxation and isotopically selective IRMPD to the enhancement of isotopic selectivity.	131
4.4	Experimentally measured ratio of relaxation rates.	143

4.5	Results obtained for the separation of IRMPD and vibrational relaxation for a dissociation laser frequency of 1047 cm^{-1} and fluence of 3 J cm^{-2} . . .	149
5.1	Shifts, widths and intensity of the SIB spectra.	161
5.2	Energy and vibrational frequencies at the transition state for the lowest dissociation channel $\text{CF}_3\text{H} \rightarrow \text{CF}_2 + \text{HF}$	194
6.1	Summary of relative relaxation rates of excited CF_3H on ground state CF_3H	230

List of Figures

1.1	IRLAPS detection scheme.	5
1.2	Spectrum of the 3_1 transition in CF_3H	7
1.3	Observed effect we study in this thesis.	8
1.4	Collisions between the lasers and during IRMPD lower the vibrational energy of the molecules	9
2.1	Normal modes in CF_3H (frequencies for $^{12}\text{CF}_3\text{H}$).	21
2.2	FTIR scan of CF_3H at room temperature.	22
2.3	Anharmonic coupling between dark and bright states.	26
2.4	Integrated absorption strengths of $0 \rightarrow \nu_{\text{CH}} = N$	32
2.5	IVR	34
2.6	Multiple time-scales showing up in an absorption spectrum.	38
2.7	Calculated redistribution of vibrational energy in a CF_3H molecule initially in the $\nu_1 = 3$ state.	40
2.8	The two qualitatively distinct regions in IRMPD.	42
2.9	Basic idea of the statistical treatment.	45
2.10	Behaviour of up- and down-pumping rates between different bins.	51
2.11	Model for hard collisions.	55
2.12	Experimental data demonstrating the dependency of the probability of energy transfer between an excited CO_2 molecule and an N_2 molecule in the ground state under the effects of long-range and short-range interaction forces.	62
2.13	Average energy transferred $\langle \Delta E \rangle$ in a collision of excited azulene at an energy E , for different bath gas molecules.	65

2.14	Example of the dependence of the vibrational relaxation rate on the vibrational excitation, for the case of excited O ₂ relaxing on N ₂	68
2.15	Temperature dependency for CO(00 ⁰ 1)+CO(00 ⁰ 0) → CO(00 ⁰ 0)+CO(00 ⁰ 1) and for CO(00 ⁰ 1)+N ₂ (<i>v</i> =0) → CO(00 ⁰ 0)+N ₂ (<i>v</i> =1) collisions.	70
2.16	Average energy $\langle\langle\Delta E\rangle\rangle$ transferred between an excited molecule and the same unexcited species.	72
3.1	General energy level diagram used in our experiments.	88
3.2	Optical setup of the experiments.	90
3.3	Timing of pre-excitation, dissociation and LIF lasers.	93
3.4	Generation of the laser beam for pre-excitation of CF ₃ H molecules via the 2 ₁ band.	94
3.5	Generation of the laser beam for pre-excitation of CF ₃ H molecules via the 2 ₁ band.	95
3.6	The decay rate <i>k</i> goes up as <i>p</i> goes down, indicating that molecules flying out of the reaction volume falsify the experimental measurement.	97
3.7	Measurements for rotational relaxation.	98
3.8	Completeness of rotational relaxation.	99
3.9	Initial setup for the production of ¹³ C enriched CF ₃ H.	100
3.10	Procedure for the synthesis of ¹³ CF ₃ H.	101
3.11	Comparison of measured and literature mass-spectra for the identification of the gas.	102
3.12	Mass spectrum of the final products of the ¹³ CF ₃ H synthesis.	103
4.1	General experimental procedure.	106
4.2	Successive measurements of the decay rate <i>k</i>	109
4.3	Energy scheme used in the experiments for the determination state specificity of relaxation rates.	111
4.4	Experiments to test the influence of the rotational identity of the pre-excited state on the decay rates.	112
4.5	Experiments to test the influence of the vibrational identity of the pre-excited state on the decay rates.	113
4.6	Energy scheme used in the experiments for the determination of photofragment excitation spectra of excited molecules.	115

4.7	Sample curves of measured dissociation yields.	116
4.8	Sample curves of measured dissociation probability.	117
4.9	ν_0 , ω and B found for the photofragment spectra of excited $^{12}\text{CF}_3\text{H}$ and $^{13}\text{CF}_3\text{H}$ for different fluences of the CO_2 laser.	118
4.10	An IRLAPS action spectrum around the Q-branch of the 3_1 band in $^{13}\text{CF}_3\text{H}$ is split into two parts due to the two different isotopomers.	120
4.11	Example of a measurement of the dissociation selectivity S_{IRMPD}	121
4.12	Dissociation selectivity S_{IRMPD} for 3 J cm^{-2} and for 9 J cm^{-2}	122
4.13	Dissociation selectivity S_{IRMPD} for molecules pre-excited via the 3_1 and via the 2_1 bands for a dissociation laser frequency of 1047 cm^{-1}	123
4.14	Comparison of experimental and predicted dissociation yields.	125
4.15	Energy scheme used in the experiments for the relaxation experiments changing the wavelength of the dissociation laser.	128
4.16	Sample measurements of the decay rate k	129
4.17	Decay rate k for $^{12}\text{CF}_3\text{H}$ and $^{13}\text{CF}_3\text{H}$ at a fluence of $\Phi = 3 \text{ J cm}^{-2}$ as a function of the dissociation laser frequency.	130
4.18	\mathbb{S}_{IRMPD} and \mathbb{S}_{VET} determined by changing the wavelength of the CO_2 dissociation laser.	131
4.19	Importance \mathcal{I} of a mechanism for the enhancement of isotopic selectivity upon leaving a time-delay between the pre-excitation and the dissociation lasers.	132
4.20	Energy scheme used in the experiments for the relaxation experiments using $^{13}\text{CF}_3\text{H}$ as relaxation partner of excited CF_3H	135
4.21	Example of measurement of the decay rate k for different isotopic composition of the sample for $^{12}\text{CF}_3\text{H}$ and $^{13}\text{CF}_3\text{H}$	136
4.22	Values for $k(x^* - y)$ for molecules pre-excited via the 3_1 band.	137
4.23	Values for $k(x^* - y)$ for molecules pre-excited via the 2_1 , 4_1 and 5_2 bands.	138
4.24	Schematic absorption and emission spectra of $^{12}\text{CF}_3\text{H}$ and $^{13}\text{CF}_3\text{H}$ for molecules in the ground state and with 8800 cm^{-1} vibrational energy.	140
4.25	Values for \mathcal{R}_{12} and \mathcal{R}_{13} for different pre-excitation energies and dissociation laser conditions.	142
4.26	Relative relaxation rates \mathcal{R}_{12} and \mathcal{R}_{13}	144
4.27	Interpretation of our results obtained with isotopically enriched samples.	145

4.28	Measured values of S_{IRMPD}	146
4.29	Contributions of isotopically selective collisional relaxation and different IRMPD efficiencies to the increase of isotopic selectivity, for different pre-excitation levels and fluences.	147
4.30	Experimentally determined ratio of relaxation rates.	150
5.1	Absorption spectra for CF_3H molecules at 0, 2500, 5000, 7500, . . . , 20,000 cm^{-1}	158
5.2	SIB absorption spectra for ν_2 , ν_3 and ν_6	159
5.3	The transition spectra of excited molecules shift, broaden and get more intense as the energy of the molecules increase.	160
5.4	For the calculation of the whole absorption spectrum the SIB spectrum is convoluted with a rotational contour.	164
5.5	The calculation of the transition rate is done by integrating over the trajectory.	171
5.6	Absolute vibrational energy transfer rates for V-V relaxation mediated by the ν_5 mode.	174
5.7	Relaxation rates associated with a particular mode.	175
5.8	The shift between absorption and emission spectra as a function of the energy of the donor molecule.	176
5.9	Parts (I) and (II) of equation 5.37 and the total relaxation rate (relative values).	177
5.10	Contribution of ν_5 to the V-V energy transfer process.	180
5.11	Results for \mathcal{R}_{12} and \mathcal{R}_{13} where only vibrational energy transfer via long range dipole-dipole interactions are considered.	180
5.12	Pairs of R_0 and \mathcal{N}' which fit to the measured isotopic selectivity of the relaxation rates well.	184
5.13	Calculated and experimental relative relaxation rates of vibrationally excited CF_3H on $^{12}CF_3H$ in the vibrational ground state.	185
5.14	Relaxation rates as a function of the energy in the molecule (for $R_0 = 7.4 \text{ \AA}$, $\mathcal{N}' = 6.8 \cdot 10^4 \text{ cm}^{-1}$).	186
5.15	Energy level diagram for master equation calculations.	189

5.16 Arrhenius plots of experimental data for CF_3H measured by different authors.	195
5.17 Absorption spectrum for calculations based on a statistical treatment. . .	198
5.18 Example of a simulated three laser experiment.	201
5.19 Energy distributions for the example shown in figure 5.18.	202
5.20 Dynamics of energy level populations calculated for $^{12}\text{CF}_3\text{H}$ and for $^{13}\text{CF}_3\text{H}$.	203
5.21 Simulated and measured dissociation yields.	205
5.22 Absorption spectrum of two quanta in the ν_6 vibration for molecules with a vibrational energy of 8800 cm^{-1}	206
5.23 Dissociation yield of molecules pre-excited via the 3_1 band, with a dissociation laser frequency of 977 cm^{-1}	207
5.24 Photofragment spectra of vibrationally excited $^{12}\text{CF}_3\text{H}$ for off-resonant dissociation laser frequencies.	208
5.25 Measured and calculated centres ν_0 of the photofragment spectra of vibrationally excited $^{12}\text{CF}_3\text{H}$	209
5.26 Simulated and measured dissociation selectivities for a sample at 0.4 mbar.	210
5.27 Laser pulses used for the experiments elsewhere.	212
5.28 Overall selectivity of the dissociation yields as a function of the pressure of the sample.	213
5.29 Measured and calculated decay rates for $^{12}\text{CF}_3\text{H}$ and $^{13}\text{CF}_3\text{H}$	213
5.30 Numerical evaluation of the contributions of the different mechanisms to the increase of isotopic selectivity, for a frequency of the dissociation laser of 1047 cm^{-1}	215
5.31 Simulated dissociation probability for $^{12}\text{CF}_3\text{H}$ and $^{13}\text{CF}_3\text{H}$ molecules. . .	217
5.32 Calculated dissociation probabilities.	218
5.33 Dissociation selectivity and yield for pre-excitation via the 3_1 and the 4_1 bands.	219
5.34 Dissociation selectivity and yield for a dissociation laser fluence of 1, 3 and 5 J cm^{-2}	219
5.35 Dissociation selectivity and yield for a dissociation laser frequency of 1039, 1044 and 1049 cm^{-1}	220

A.1	In case C, the states in both the upper and lower bins are uncoupled amongst each other.	236
A.2	Rabi-oscillations for different strengths of coupling between the two states.	237
A.3	D is the off-resonance shift between the difference of energy of the two levels and the frequency of the electromagnetic field.	238
A.4	Evolution of upper level J	241
B.1	Sample LIF signal.	244
B.2	Quenching of CF_2 on CF_3H	245
B.3	Correction factors ε for the dissociation yield.	245
C.1	Absorption spectrum of teflon.	248
C.2	Amount of transmitted light f_1 by the Pellin-Broca prism and the BaF_2 windows of the cell.	249
C.3	Measurements of f_2 , the amount of the CO_2 laser shot used.	250
C.4	By scanning a slit over the beam we measure a Gaussian dependence of the energy let through as a function of the displacement.	250
C.5	Cross-section of the CO_2 laser beam at the focal point and output energy of pulse.	251
D.1	Example of a measurement of k as a function of the fluence of the dissociation laser.	254
D.2	Illustration of why k goes through a maximum as a function of the fluence of the dissociation laser.	255
E.1	Principle of our code	258

Acknowledgements

This thesis would not have been possible without the help of many people.

First of all, I would like to thank my thesis advisor Prof. Tom Rizzo for his confidence in me and in giving me the opportunity to perform the research under his direction. His guidance and motivation were always of great help.

My deep gratitude and appreciation goes to Dr. Oleg Boyarkin, my supervisor, for guiding me through the wonder- and colourful world of laser spectroscopy and for his continuous support during all these years.

A special thank you goes to Dr. Mikhail Polianski with whom I shared the lab and with whom I spent hours in front of the black board developing models on laser isotope separation and vibrational energy transfer. Thanks also for the great help in every day problems in the lab (e.g. fixing lasers I broke before).

I wish to thank my colleagues Plinio Maroni and Thanh Tung Dang, with whom Misha and I shared the office during several years. A great thank you to all of you guys for the lovely time we spent together, for your humour, your joy and the coffee breaks ! Thank you for supporting me in moments of fluctuating mood (especially when I was writing up the thesis !).

Thanks are due to present and former LCPM members: Dr. Rainer Beck, Dr. Andreas Braun, Dr. Andrea Callegari, Rachele Chianese, Dr. Marcel Drabbels, Prof. Tino Gäumann, Monia Giudi, Anthi Kamariotis, Dr. Aziz Kasimov, Dr. Monika Kowalczyk, Evgeniy Loginov, Dr. Joachim Makowe, Pavel Maksyutenko, Sébastien Mercier, An-

toine Milon, Dr. Dimitrios Papageorgopoulos, Dr. Julia Rebstein, Dr. David Rueda, Marco Sacchi, Dr. Mathieu Schmid, Dr. Patrice Theulé.

A special thanks goes to Amanz Ruf who helped me with the synthesis of $^{13}\text{CF}_3\text{H}$ (poor guy having to teach chemistry to a physicist !) and a very special thanks goes to Marianne Dang whose support went well beyond administrative matters.

I am grateful to all my physicist- and mathematician-friends: Céline, Yvonne, Christian, Dominique (“Grüessech !”), Fabien (who does not appreciate jam together with Gruyères cheese on bread), Gilles (moi je pense pas que t’es de mauvaise foi), Loic (my “coloc”), Pierre (who managed to finish his thesis before me.... grrr !), Raphael and Reda (if you want to know where the best strawberries come from... he knows !). A particular thanks to Séverine for her continuous support, her joy and her advice. And for equation (3.13).

A very special thanks goes to my very special friends Myriam and Daniel, for all the great time we spent together and for all their support during darker moments of my life.

I am forever indebted to my parents for their support and encouragement when it was most required. Without their support, I would not be where I am now. An enormous hug and thanks goes to my most beloved sister Olivia, for her humour and her support. Thank you also for the time trying to explain chemistry to your “brudder”.

Last, but not least, I wish to tenderly thank Valérie for having shared the past couple of years with me, for all her love, her understanding and patience also in difficult moments.

Curriculum vitae: Richard Bossart

Rue St-Roch 5
1004 Lausanne
Switzerland
richard.bossart@a3.epfl.ch



Birthdate and -place: 25 December 1974, Winterthur

Swiss and British Citizenship.

Marital status: Single

2005	Research&Development at Rolex, Geneva
2000-05	PhD thesis in physical chemistry, EPFL, Switzerland supervised by Prof. Tom Rizzo “On Isotopically Selective Collisional Energy Transfer and Infrared Multiple Photon Absorption by Vibrationally Highly Excited Molecules”
2000	Masters thesis in cluster physics, EPFL, Switzerland supervised by Prof. Christian Félix “Development of a source of silver clusters with the pick-up method”
1997/98	Year at Imperial College, London
1995-2000	Studies in physics at EPFL, Switzerland
1995	Maturtätszeugnis Realgymnasium Bern-Kirchenfeld, Switzerland